



HAL
open science

Contact and macroscopic aging in dense suspensions at the colloidal edge

Francesco Bonacci

► **To cite this version:**

Francesco Bonacci. Contact and macroscopic aging in dense suspensions at the colloidal edge. Materials Science [cond-mat.mtrl-sci]. Université Paris-Est, 2019. English. NNT: 2019PESC2047. tel-02491157

HAL Id: tel-02491157

<https://theses.hal.science/tel-02491157>

Submitted on 25 Feb 2020

HAL is a multi-disciplinary open access archive for the deposit and dissemination of scientific research documents, whether they are published or not. The documents may come from teaching and research institutions in France or abroad, or from public or private research centers.

L'archive ouverte pluridisciplinaire **HAL**, est destinée au dépôt et à la diffusion de documents scientifiques de niveau recherche, publiés ou non, émanant des établissements d'enseignement et de recherche français ou étrangers, des laboratoires publics ou privés.

CONTACT AND MACROSCOPIC AGING IN COLLOIDAL SUSPENSIONS

A THESIS PRESENTED BY

FRANCESCO BONACCI

TO

UNIVERSITÉ PARIS EST

ÉCOLE DOCTORALE SCIENCES, INGÉNIEURIE ET
ENVIRONNEMENT

IN PARTIAL FULFILLMENT OF THE REQUIREMENTS FOR THE DEGREE OF
DOCTOR OF PHILOSOPHY IN

MATERIALS SCIENCE AND ENGINEERING

COMMITTEE MEMBERS:

M.	XAVIER CHATEAU	THESIS SUPERVISOR
M.	LUCA CIPELLETTI	THESIS REVIEWER
M.	GUILLAUME OVARLEZ	THESIS REVIEWER
M.	ERIC M. FURST	JURY PRESIDENT
M.	PASCAL BOUSTINGORRY	THESIS EXAMINER
MME.	JULIE GOYON	THESIS CO-SUPERVISOR
M.	ANAËL LEMAÎTRE	THESIS CO-SUPERVISOR

CHAMPS-SUR-MARNE, FRANCE, 26 NOVEMBER 2019

ABSTRACT

TODAY, THE AGING BEHAVIOR OF DENSE SUSPENSIONS OR PASTES IS NEARLY SYSTEMATICALLY ATTRIBUTED TO STRUCTURAL EVOLUTION. HERE, WE BRING EXPERIMENTAL EVIDENCE THAT, IN CONTRAST, DENSE AQUEOUS SILICA AND POLYMER LATEX SUSPENSIONS AGE EVEN AFTER THEIR MICROSTRUCTURE IS FROZEN BY THE FORMATION OF ATTRACTIVE, THERMALLY IRREVERSIBLE, INTERPARTICLE CONTACTS. BY PERFORMING THREE POINT FLEXURAL TESTS WITH LASER TWEEZERS ON PARTICLE RODS, WE ACCESS THE BENDING RIGIDITY OF CONTACTS AND SHOW THAT IT GROWS ESSENTIALLY LOGARITHMICALLY IN TIME. WE THUS SHOW THAT THE SHEAR MODULUS AND YIELD STRESS OF THESE DENSE SUSPENSIONS AGE SOLELY DUE TO THE PROGRESSIVE STIFFENING OF CONTACTS. CONTACT-CONTROLLED MECHANICAL AGING APPEARS TO BE A GENERIC AGING MECHANISM, THAT SHOULD BE AT WORK IN A WIDE CLASS OF MATERIALS, SUCH AS CEMENTS, SOILS, OR 3D INKS.

RESUMÉ

LA MAJORITÉ DES ÉTUDES SUR LE VIEILLISSEMENT DES SUSPENSIONS COLLOÏDALES DENSES ATTRIBUE CELUI-CI À UNE ÉVOLUTION STRUCTURELLE. DANS CE TRAVAIL, NOUS APPORTONS DES PREUVES EXPÉRIMENTALES DE L'INVALIDITÉ DE CETTE HYPOTHÈSE DANS LE CAS DE SUSPENSIONS AQUEUSES DE PARTICULES DE SILICE ET PMMA: CELLES-CI VIEILLISSENT BIEN QUE LEUR MICROSTRUCTURE SOIT FIGÉE PAR LA FORMATION DE CONTACTS ADHÉSIFS ENTRE LES PARTICULES, IRRÉVERSIBLES PAR AGITATION THERMIQUE. EN EFFECTUANT DES TESTS DE FLEXION À TROIS POINTS AVEC DES PINCES OPTIQUES SUR DES CHAINES DE PARTICULES, NOUS MESURONS LA RIGIDITÉ EN FLEXION DES CONTACTS ET NOUS MONTRONS QU'ELLE AUGMENTE QUASI-LOGARITHMIQUEMENT AU COURS DU TEMPS. NOUS MONTRONS AINSI QUE LE MODULE DE CISAILLEMENT ET LA CONTRAINTE-SEUIL DE CES SUSPENSIONS DENSES VIEILLISSENT UNIQUEMENT EN RAISON DU RENFORCEMENT DES CONTACTS. LE VIEILLISSEMENT MÉCANIQUE CONTRÔLÉ PAR LES CONTACTS SEMBLE ÊTRE UN MÉCANISME DE VIEILLISSEMENT GÉNÉRALISÉ, QUI DEVRAIT SE MANIFESTER DANS UNE LARGE GAMME DE MATÉRIAUX TELS QUE LES CIMENTS, LES SOLS OU LES ENCRE 3D.

Contents

1	Introduction	9
1.1	General context and motivations	10
1.2	Outline of the thesis	11
I	Part I	13
2	State of the Art	15
2.1	Colloidal suspensions	16
2.2	Colloidal interactions	17
2.2.1	van der Waals (vdW) forces	18
2.2.2	Electrostatic interactions	20
2.2.3	DLVO theory	25
2.2.4	non-DLVO interactions	27
2.2.5	Time-dependent interactions	28
2.3	Phase diagrams of model systems	28
2.3.1	The hard sphere system (HSS)	28
2.3.2	The square-well system (SWS)	30
2.3.3	Arrested states at low volume fractions (gels)	31
2.3.4	Phase separation inhibition	33
2.3.5	Fractal gels	35
2.4	Aging and thixotropy	35
2.4.1	Colloidal glasses and gels	35
2.4.2	Thixotropy	36
2.4.3	Aging	37
2.4.4	General remarks	44
3	Materials and Methods	47
3.1	Suspension preparation and characterization	48
3.1.1	Stöber synthesis	48
3.1.2	PMMA particles	50
3.1.3	Particle size analysis	50

3.1.4	Zeta potential	52
3.1.5	Particle interactions	55
3.1.6	Suspension preparation	58
3.2	Macroscopic characterization: Rheometry	61
3.2.1	Rheometry in Couette geometry	62
3.2.2	Oscillatory rheology	63
3.2.3	Experimental procedure	64
3.2.4	Shear modulus	66
3.2.5	Yield stress	66
3.2.6	Rheometry cycle	67
3.2.7	Main results: silica suspensions	68
3.2.8	Main results: PMMA suspensions	70
3.2.9	Elastic modulus vs yield stress	72
3.3	Structural characterization: Confocal Microscopy	76
3.3.1	Working principle	76
3.3.2	Experimental limitations	79
3.3.3	Results	80
3.3.4	Aging	88

II Part II 91

4	Three-Point Bending Tests with LTs	93
4.1	Laser Tweezers (LTs)	94
4.1.1	Optical traps	94
4.1.2	Setup	96
4.1.3	AOD calibration	99
4.1.4	Force calibration	99
4.2	Experimental procedure	102
4.2.1	Materials	102
4.2.2	Sample cell	102
4.2.3	Assembly of particle rods	103
4.2.4	Three-point bending experiments	106
4.2.5	Loading cycle	109
4.3	Elasticity of particle rods	110
4.3.1	SiO ₂ particle rods	110
4.3.2	PMMA particle rods	115
4.4	Yielding of particle rods	117
4.4.1	SiO ₂ particle rods	117
4.5	Interpretation of the results	121
4.5.1	JKR and DMT models	121
4.5.2	Pantina-Furst model	123
4.5.3	Dominik-Tielens model	127
4.5.4	Contact aging	130

5	Three-Point Bending Tests: Behind the Scene	135
5.1	Rigid body rotation	136
5.1.1	Force-deflection curves	136
5.1.2	Simulated motion of the rods in 3D	137
5.1.3	Misalignment correction	140
6	From Micro to Macro	143
6.1	Elastic modulus	144
6.1.1	SiO ₂ particle suspensions	144
6.1.2	PMMA particle suspensions	148
6.2	Yield stress	151
6.3	Elastic modulus vs yield stress	153
6.4	Discussion	156
7	Conclusions and Perspectives	159
Appendices		
	Appendix A Dynamic Light Scattering	165
	Appendix B Scanning Electron Microscopy	169
	Appendix C Particle tracking	171
	Appendix D Relation between k_r and k_0	175
	Appendix E Equilibrium shape of a bent chain of particles	179

Introduction

Contents

1.1	General context and motivations	10
1.2	Outline of the thesis	11

1.1 General context and motivations

Dense colloidal suspensions (or pastes) constitute a broad class of materials found in areas ranging from environmental systems (e.g. silts, clays), to industry (ceramics, drilling muds, slurries), construction (plaster, cements), foodstuff, cosmetics, pharmaceuticals (toothpaste, medical ceramics). Their most remarkable feature is thixotropy: a slow evolution of their mechanical properties when switching from rest to flow (at fixed density, in the absence of drainage). Thus, their viscosity under flow, or their shear modulus and yield stress at rest, depend both on time and strain history [45, 40, 144, 143, 87, 73]. Thixotropy enables these systems to switch reversibly between solid- and liquid-like states with sharply contrasted properties. At rest, it is usually accompanied with aging —slow, non-exponential dynamics at long times.

Understanding thixotropy and aging is of tremendous importance in many practical applications, because these phenomena are often at play in situations when materials have to be processed. To appreciate this fact, consider for example fresh cement pastes (i.e. in the dormant period of the hydration reaction). They are suspensions of irregularly shaped particles with a typical size ranging from 100 nm to about 100 μm and they can, thus, exhibit properties inherent to dense colloidal suspensions. The placing of a concrete and/or its spreading on solid surfaces, is an important operation which largely determines the quality of the final product [139]. Rheology is a key parameter of concrete *workability*. For example, a time- and/or shear-dependent viscosity may affect the time and pumping pressure required to fill a formwork or empty a truck. The magnitude of the yield stress, i.e. the stress that should be overcome to initiate flow from quiescent conditions, determines whether sedimentation of the coarsest elements may occur [168]. In shotcrete, the ability of the material to recover solid-like properties after flow arrest is crucial in determining whether the material remains on the wall or flow down after spraying [168]. Aging also leads to a phenomenon often described in concrete industry as *workability loss*, since the yield stress steadily increases with resting time.

In recent decades, tremendous progress has been made towards understanding the dynamics of so-called “stabilized” suspension, in which the formation of inter-particle adhesive contacts is fully avoided by tuning inter-particle interactions (via double-layer polarization, or polymer depletion effects) [53, 54, 50, 159, 121, 208]. Confocal microscopy was instrumental to such progresses, yet may only be applied to transparent, i.e. nearly index matched, systems, hence is limited to systems in which van der Waals forces are absent. Meanwhile, studies of “non-stabilized” suspensions have tended to focus on very dilute systems (i.e. packing fractions at most a few percent) where a structural evolution (the formation of flocs) could be imaged and thus analyzed, e.g., using light scattering techniques [35, 16, 37].

The tremendous success of these studies has created an observational bias as, today, classical works on suspensions only mention structural dynamics as the root cause of thixotropy [9, 130]. But the pastes of civil and environmental engineer-

ing, are dense and generally contain significant concentrations of ions; these screen Coulombic repulsion and allow attractive van der Waals forces to bring particles into solid-solid contacts, which are likely to impact macroscopic properties and their evolution by a number of mechanisms. Indeed, it is well-known that, the macroscopic response of non-colloidal granular materials [89], is affected by contact friction, which is time-dependent [51, 152, 11]. In cements, the formation of hydrate gels between grains, which determines the late-time strength and mechanical properties of solid concrete [201, 97], was proposed to play a role in thixotropy [169]. Contact aging [123] was also proposed to play a role in highly dilute (0.02%) gels of nanometric particles in microgravity—a situation rather far from real pastes. But in the general context of attractive suspensions, this idea seems reserved to reactive systems (cements) where the suspending fluid evolves, or refers to frictional forces, and a direct relation between contact and macroscopic aging has never been established.

In fact, it remains unclear how solid-solid contacts may affect just the rheology of colloidal systems. By designing an optical-trap three-point bending test, Pantina and Furst [146, 147] showed that beams of PMMA and polystyrene particles present a finite flexural rigidity, which entails that the contacts formed between particles resist rotation. The flexural rigidity of polystyrene particle rods was later shown to evolve [129]. Besides, a recent work on model pastes of strongly attractive spherical and crushed silica particles provided evidence that mechanical aging was not accompanied by an evolution of the microstructure [73]. All these elements lead us to ask whether time-dependent physical bonding in dense, ionic pastes could be responsible for their mechanical aging, without invoking structural changes in the particle network.

This work aims to investigate the potential existence of a link between contact and macroscopic aging. To achieve it, we study the aging behavior of model dense colloidal suspensions, composed of silica (SiO_2) and PMMA particles in divalent electrolyte aqueous solutions, and combine measurements performed at the particle level, through optical-trap three-point bending tests and confocal microscopy, and at the macroscopic scale, through rheometry. The use of model ionic systems enables us to carefully control a number of parameters expected to affect the rheology of real suspensions in the dense regime, such as the volume fraction, the size and the shape of the particles and the magnitude of the interactions.

1.2 Outline of the thesis

In [Chapter 2](#), after briefly introducing the reader to colloidal phenomena, we focus on the forces acting between charged colloids in water, and rapidly discuss the limitations of the existing theories (i.e. DLVO). Then, we review the general literature on colloidal phase transitions, thixotropy, aging and structural evolution in arrested states (glasses and gels). In [Chapter 3](#), we describe the materials and experimental methods used to assess mechanical aging. We present the procedure of synthesis of silica particles, the characterization of their properties in water and electrolyte solutions, and investigate their time-dependent rheology in dense suspen-

sions. **Part I** ends with the characterization of the microstructure of the suspensions under a confocal microscope.

In **Part II** we study aging at the particle scale. **Chapter 4** is first devoted to the description of the tweezers experiments. We outline the basic concepts of optical trapping techniques, the tweezers setup used in this work and its calibration. We then focus on the experimental procedure used to carry out three-point bending tests on particle rods, the main features of acquisition and processing of the data, and illustrate how the existence of contact aging at the nanoscale is revealed. We also review models for resistance to rolling motion in adhesive contacts, apply them to our micro-sized particles, and briefly discuss the literature on contact aging, with particular regard on silica. A short chapter, **Section 5.1**, will then show in detail how the raw data and the subsequent data analysis are used to interpret and “correct for misalignment” the tweezers tests, in order to accurately study the micro-mechanics of the rods under bending. Thereafter, we review the main results of our work and illustrate how we are able to establish a quantitative link between macroscopic and contact aging, **Chapter 6**. The implications of our findings in terms of bulk rheology, such as the effects of the particle size, ionic strength and packing fraction, are analyzed. **Chapter 7** comprises some concluding remarks and perspectives on future works.

Part I

Part I

Contents

2.1	Colloidal suspensions	16
2.2	Colloidal interactions	17
2.2.1	van der Waals (vdW) forces	18
2.2.2	Electrostatic interactions	20
2.2.3	DLVO theory	25
2.2.4	non-DLVO interactions	27
2.2.5	Time-dependent interactions	28
2.3	Phase diagrams of model systems	28
2.3.1	The hard sphere system (HSS)	28
2.3.2	The square-well system (SWS)	30
2.3.3	Arrested states at low volume fractions (gels)	31
2.3.4	Phase separation inhibition	33
2.3.5	Fractal gels	35
2.4	Aging and thixotropy	35
2.4.1	Colloidal glasses and gels	35
2.4.2	Thixotropy	36
2.4.3	Aging	37
2.4.4	General remarks	44

2.1 Colloidal suspensions

The term colloidal suspension refers to a class of heterogeneous mixtures in which the dispersed phase —the colloid —has a specific size range with respect to the size of the typical constituents comprising the continuum phase. Unlike a solution where solute and solvent constitute only one phase, on the one hand, in a colloidal dispersion the two phases remain separated; the suspended particles are insoluble and macroscopic, in the sense that their size is significantly larger than the size of the solvent molecules. This ensures that, from the “particle point of view”, the suspending medium behaves as a continuum (i.e., characterized by continuum properties such as viscosity, refractive index, dielectric constant, etc.). Unlike a granular system, on the other hand, the size of a colloid must be small enough that thermal energy $k_B T$ is the fundamental energy scale, so that thermal forces (Brownian motion) allow the particles to rapidly sample the accessible configuration space [130].

Gravitational Peclet Number The border between a colloidal system and a non-colloidal one can be located through the gravitational Peclet number, which compares the effects of thermal motion and gravitational forces, and is calculated as the ratio between the characteristic sedimentation and diffusion times of the colloids. The characteristic time taken for a particle of radius a and density ρ_p to sediment its own size, in a solvent of density ρ_s and viscosity η_0 , is

$$t_{\text{sed}} = \frac{2a}{v_{\text{sed}}} = \frac{9\eta_0}{2(\rho_p - \rho_s)ga} \quad (2.1)$$

where g is the gravitational acceleration. The characteristic diffusion time of the same particle can be expressed as a function of the diffusion coefficient D :

$$t_{\text{diff}} = \frac{6\pi\eta_0 a^3}{k_B T} \quad (2.2)$$

The gravitational Peclet number Pe is then

$$Pe = \frac{t_{\text{sed}}}{t_{\text{diff}}} = \frac{3k_B T}{4\pi(\rho_p - \rho_s)ga^4} \quad (2.3)$$

When the Peclet number is $\gg 1$, thermal agitation dominates over sedimentation and the system has a strictly colloidal behavior. Conversely, colloidal effects are negligible when $Pe \ll 1$. The transition occurs around $Pe \simeq 1$. For a silica particle ($\rho_p \sim 2 \text{ g/cm}^3$) in pure water and ambient temperature, we obtain:

$$a_{\text{tran}} = \left(\frac{3k_B T}{4\pi(\rho_p - \rho_s)g} \right)^{\frac{1}{4}} \approx 0.55 \mu\text{m} \quad (2.4)$$

Colloids, thus, must have a size range midway between the nanometer and micrometer scales, $a \in [0.01, 10] \mu\text{m}$. Due to their small size, colloidal particles possess a high surface-to-volume ratio and are thus sensitive to surface-mediated interactions.

Another intrinsic parameter in colloidal suspensions is the particle concentration, or packing fraction ϕ , defined as the ratio between the volume occupied by the particle Ω_p and the total volume Ω_{tot} of the suspension.

$$\phi = \frac{\Omega_p}{\Omega_{\text{tot}}} = \frac{\Omega_p}{\Omega_p + \Omega_{\text{solv}}} \quad (2.5)$$

where Ω_{solv} is the solvent volume.

Colloidal suspensions have many features in common with atomic systems, and, for this reason, they are usually considered as models to elucidate some fundamental phenomena in the atomic counterparts. The striking advantage of using colloids is twofold: on the one hand, their interactions can be finely tuned, by functionalizing their surface or changing the solution composition by addition of polymers and/or salts, and they can be controlled and manipulated rather easily by external fields, such as electric and magnetic fields or optical traps [122]. On the other hand, because of their size close to (or larger than) the wavelength of visible light, colloids can be studied by many optical techniques such as confocal microscopy [79, 53, 54, 159, 121], total-internal-reflection microscopy [205] and light scattering [35, 16], which (i) allows for direct comparisons with analytical and numerical results and (ii) leads to a close and fruitful interplay between theory, computer simulation, and experiments.

2.2 Colloidal interactions

Numerous phenomena in colloidal suspensions are determined by the strength and range of the interactions between the particles. Two or more particles can interact via different forces, that can be classified into 4 main groups, according to their nature: hydrodynamic, dispersion, surface, and depletion forces [130]. A cartoon of the various forces at play in colloidal dispersions is reported in [Figure 2.1](#). Hydrodynamic interactions originate from long-range flow perturbations induced by the motion of the particles in the fluid, and will be ignored when studying aging and thixotropy in quiescent conditions. Dispersion forces are ubiquitous in colloidal systems, since they are quantum mechanical in nature; they arise from the existence of permanent and/or fluctuating electric dipole in the atoms of the particles. Surface forces include electrostatic and steric forces, which arise respectively from the presence of charges and adsorbed polymers at the particle surface. These repulsive forces usually tend to stabilize the suspension preventing flocculation. Colloidal particles can also experience attractive forces associated with the presence of *depletants*, *viz.* non-adsorbing polymers or nanoparticles. The attraction arises from the increase in the osmotic pressure occurring when the particles get so close that the *depletants* are unable to access the space between them.

For the scope of our study, here we focus on the specific situation of similar, electrically charged particles in aqueous solvents, in the absence of added polymers. In these conditions, the interactions are usually described by the classical theory of Derjaguin, Landau, Verwey, and Overbeek (DLVO) [47, 203], for which the net

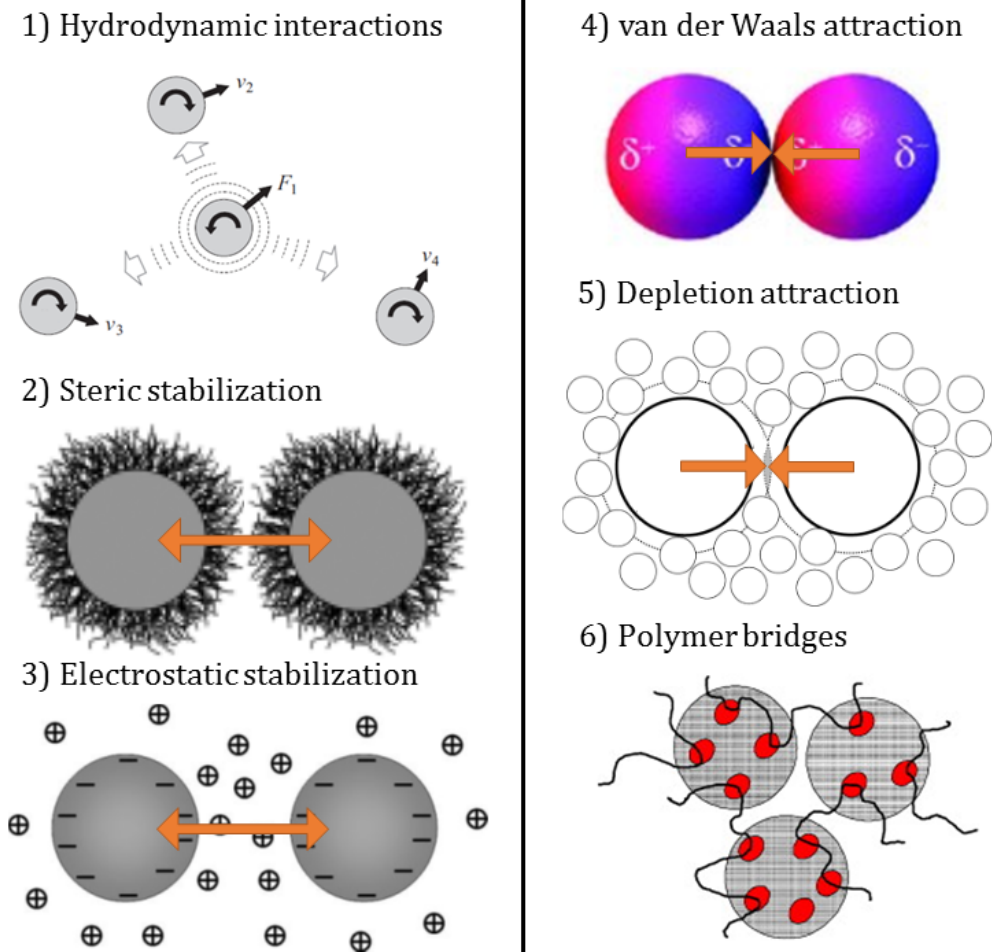


Figure 2.1 – A diagram of typical colloidal interactions.

pair interaction is modeled as a combination of two main contributions: a purely electrostatic repulsive part due to residual surface charges, and an attraction term due to van der Waals forces. DLVO theory has been instrumental in characterizing the stability of colloidal dispersions, but in recent years, the presence of additional non-DLVO contributions has emerged among the scientific community to explain specific experimental and theoretical issues.

2.2.1 van der Waals (vdW) forces

van der Waals forces between molecules The van der Waals forces between atoms and/or molecules are caused by the interaction between electrical dipoles, due to the presence of fluctuating and/or permanent asymmetries in the electron density of the interacting media. The electron density shift can be permanent; this is the case of polar molecules (e.g. water), where the dipole arises from the difference in electronegativity between the atoms. Nonpolar molecules can possess a transient dipole due to spontaneous and/or induced electron density fluctuations; these molecules behave as fluctuating/induced dipoles. These forces can be expressed, in the most general form, as a contribution of three different types of dipole-dipole interactions:

1. Keesom or *permanent dipole - permanent dipole* interactions. They originate from the alignment of the rotating dipoles and involve polar molecules.
2. Debye or *permanent dipole - induced dipole* interactions. They depend on the angular orientations of the molecules, like for the Keesom interactions, and are caused by the interaction between a polar and a nonpolar molecule.
3. London or *induced dipole - induced dipole* interactions. Also known as dispersion forces, they represent perhaps the most important contribution to the total van der Waals force between atoms and molecules, because they are always present.

For short separations, each of these contributions has an interaction free energy which varies with the inverse sixth power of the distance between the interacting atoms/molecules r , so that the (attractive) interaction potential can be written as:

$$V_{vdW} = -\frac{C_{vdW}}{r^6} \quad (2.6)$$

where C_{vdW} is a constant dependent on the electric properties of the given system and is expressed in Jm^6 .

van der Waals forces between macroscopic bodies To calculate the interaction energy between two macroscopic bodies, Hamaker [90] proposed to perform a pair-wise summation over all the atoms in the bodies. The “two-body” potential is obtained by summing (i.e. integrating) the energy of all atoms in one body with the energy of all atoms in the other. With this assumption, the vdW interaction energy per unit area of two semi-infinite parallel plates at separation h reads:

$$W_{vdW} = -\frac{A_H}{12\pi h^2} \quad (2.7)$$

where A_H is called the Hamaker constant and accounts for all the properties of the two materials and the interacting medium, but is independent from the geometrical properties embodied in the calculation. The Hamaker approximation is very useful in colloidal systems; an explicit calculation of the vdW forces between two colloidal particles of equal radii a at center-to-center separation $r = 2a + h$, leads to [171]:

$$V_{vdW} = -\frac{A_H}{6} \cdot \left(\frac{2a^2}{r^2 - 4a^2} + \frac{2a^2}{r^2} + \log \left(\frac{r^2 - 4a^2}{r^2} \right) \right) \quad (2.8)$$

When the surface-to-surface separation is small with respect to the radius of the particles ($h \ll 0.01a$), we can approximate the above expression with

$$V_{vdW} = -\frac{A_H a}{12h} \quad (2.9)$$

Even though the Hamaker pair-wise additivity represents a good approximation, it ignores the influence of neighboring atoms on the interaction between any pair of atoms. Lifshitz [116] presented an alternative, more rigorous, approach, where

each body is treated as a continuum —thus neglecting its atomic structure —and the forces are derived in terms of dielectric bulk properties of the media. In the Lifshitz computation, the vdW forces arise from fluctuations in the electromagnetic field and can be estimated by treating the interaction as standing waves which only occur at certain frequencies. The expression for the potential in the Lifshitz theory remains the same as in the Hamaker theory, but the many-body effects are automatically incorporated in the Hamaker constant, which now can be calculated from the knowledge of the frequency-dependent permittivities and refractive indexes of the interacting media.

When the surface-to-surface distance between the two bodies increases, the time taken for the electromagnetic waves emitted from the oscillating dipoles to interact can become comparable with the period of fluctuation of the dipole itself, and the van der Waals attraction is reduced [100]. This phenomenon, called *retardation effect*, is usually taken into account by modifying the expression of A_H at large separations ($h \gg 5 \text{ nm}$). Since we are mainly interested in interactions at contact, i.e. at short distances, we will neglect retardation effects in the remainder of this work.

2.2.2 Electrostatic interactions

In many real systems, coalescence of the suspended particles induced by van der Waals interactions is hindered by long-range repulsive forces, which prevent particles from coming into direct contact. In aqueous solutions and in absence of added polymers, these forces originate from the presence of electric charges at the particle surface. In mineral colloids such as silica, for instance, the charge density is provided by the ionization or dissociation of the surface functional groups $\text{SiOH} \rightarrow \text{SiO}^- + \text{H}^+$. The region in proximity of a charged surface is generally described by the *diffusive double-layer model* [82, 27, 185]. According to the model, the ionic concentration profile around a charged surface, with charge density $\sigma < 0$, can be essentially split into two main regions, as shown in [Figure 2.2\(a\)](#). In the vicinity of the (negative) charged plane, the (positive) counterions are bound, usually transiently, to the surface, and form the so-called Stern-Helmholtz layer. Far away from it, instead, the unbound cations can undergo Brownian motion, and thus form a broader region called diffusive layer. Perhaps surprisingly, this charge distribution arises from an osmotic effect acting between the counterions, to the detriment of the Coulombic forces that tend to minimize the charge asymmetry. What maintains the diffusive layer is thus an entropic effect; the mutual repulsion between the counterions forces them to diffuse in solution and increase their configurational entropy. Note also that the osmotic pressure brings about the repulsive forces between two macroscopic charged surfaces, as we will see shortly. The reason is that, on bringing two such surfaces together, one is forcing the counterions back onto the surfaces against their osmotic repulsion.

No added electrolytes Here we consider the case where the counterions in solution are provided only by the dissociation of the surface. We consider two negative charged planes of equal surface charge density — $\sigma < 0$ —separated a distance h in water, as shown in [Figure 2.2\(b\)](#). The electrostatic potential Φ and equilibrium

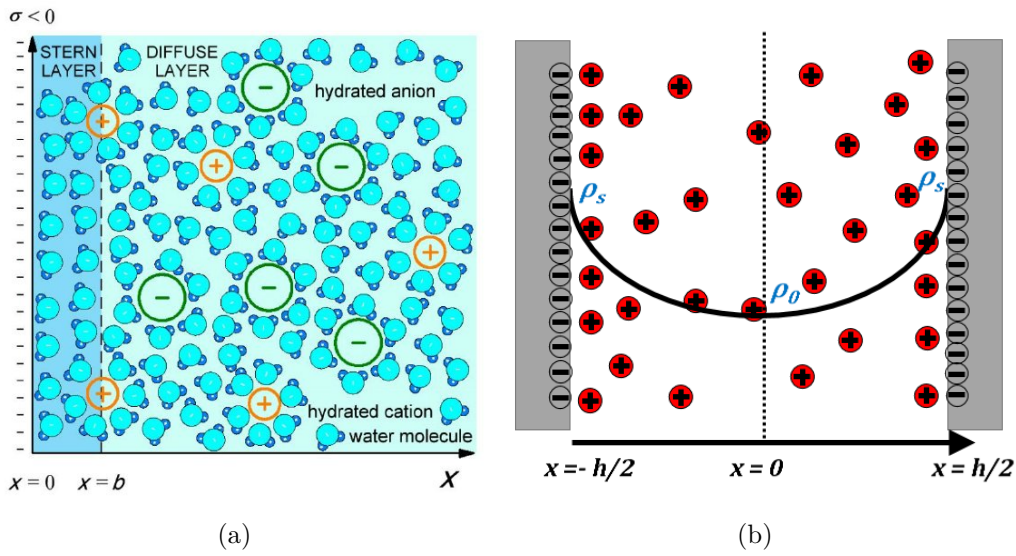


Figure 2.2 – (a) The double layer around an isolated charged plane. The Stern layer is located in a region $0 < x < b$, where b also defines the outer Helmholtz plane OHP (see later text). (b) The ionic distribution in the vicinity of two charged planes at a distance h . Solid black curve is the cation density profile ρ (ions/m³) in the gap, with ρ_s and ρ_0 the contact and the mid-plane values, respectively.

ion concentration ρ in the gap can be calculated via the Poisson-Boltzmann (PB) equation:

$$\frac{d^2\Phi}{dx^2} = -\frac{ze\rho_0}{\epsilon_0\epsilon} \cdot \exp\left(\frac{-ze\Phi(x)}{k_bT}\right) \quad (2.10)$$

The PB equation originates from the well-known Poisson equation and the equilibrium requirement of constant chemical potential everywhere in the gap, which gives a Boltzmann distribution of counterions at any point x :

$$\rho(x) = \rho_0 \cdot \exp\left(\frac{-ze\Phi(x)}{k_bT}\right) \quad (2.11)$$

In [Equations \(2.10\)](#) and [\(2.11\)](#), e is the elementary charge, z the ion valency, $\epsilon_0\epsilon$ is the permittivity of the solution, k_bT the thermal energy and ρ_0 the ion concentration at the mid-plane. Let us note that:

- (i) by symmetry, the electric field must vanish at the mid-plane $E_0 = -(d\Phi/dx)_{x=0} = 0$.
- (ii) the system is electrically neutral (total charge of the counterions in the gap equal to the total charge on the surfaces).

From these two conditions, it can be shown that the surface values of the electric field and counterions concentration are related to σ through:

$$E_s = -\sigma/\epsilon_0\epsilon \quad (2.12)$$

$$\rho_s = \rho_0 + \frac{\sigma^2}{2\epsilon_0\epsilon k_b T} \quad (2.13)$$

Since in this case there are no electrolyte ions in the bulk solution $\rho_0(h = \infty) = 0$, the equilibrium osmotic pressure in the gap depends only on the contact values of the counterions concentration. This holds as long as there is no interaction between the counterions and the surfaces (no adsorption) so that σ is constant regardless the gap separation (we will see that this is not generally true). The pressure buildup on bringing two plane surfaces together from infinity ($x = \infty$ where $P = 0$) to a separation $x = h$ at constant temperature can be calculated as:

$$P(h) = k_b T \rho_0(h) = k_b T [\rho_s(h) - \rho_s(\infty)] \quad (2.14)$$

As anticipated before, the repulsive pressure between two approaching charged planes is proportional to the increase of counterion concentration with respect to its infinite-separation value ($\rho_s(h) > \rho_s(\infty)$).

Added electrolytes We now consider an isolated surface in an electrolyte solution (Figure 2.2(a)), i.e, a solution which already contains different types of ions i (of valency z_i). We note that all the fundamental equations derived in the previous sections are still applicable, providing that one takes into account the correct charge density $\sum_i z_i e \rho_i(x)$ and the number density $\sum_i \rho_i(x)$. We rewrite the Boltzmann distribution of the ions i at x :

$$\rho_i(x) = \rho_{\infty i} \cdot \exp\left(\frac{-z_i e \Phi(x)}{k_b T}\right) \quad (2.15)$$

where $\rho_{\infty i} = \rho_i(x = \infty)$ is the ionic concentration of ions i in the bulk where $\Phi(x = \infty) = 0$. The Poisson-Boltzmann equations now reads:

$$\frac{d^2 \Phi}{dx^2} = -\frac{\sum_i z_i e \rho_{\infty i}}{\epsilon_0 \epsilon} \cdot \exp\left(\frac{-\sum_i z_i e \Phi(x)}{k_b T}\right) \quad (2.16)$$

In analogy with Equation (2.13), if the surface brings a constant charge density σ , we also have:

$$\sum_i \rho_{si} = \sum_i \rho_{\infty i} + \frac{\sigma^2}{2\epsilon_0\epsilon k_b T} \quad (2.17)$$

where, now, $\rho_{si} = \rho_i(x = 0)$ is the surface ionic concentration of species i . Substitution of Equation (2.15) into Equation (2.17) leads to the Grahame equation, which expresses the relationship between surface charge density and surface potential $\Phi_s = \Phi(x = 0)$:

$$\sigma = \left(2\epsilon_0\epsilon k_b T \sum_i \rho_{\infty i} \left(e^{-z_i e \Phi_s / k_b T} - 1\right)\right)^{1/2}. \quad (2.18)$$

Debye-Huckel approximation Far from the solid-liquid interface, the ion concentration and the electrostatic potential are given by the solution of the PB equation. Equation (2.16) is a non-linear differential equation and can be solved analyti-

cally only in the case of symmetric electrolytes $z : z$. However, when the electrostatic energy is small everywhere in the gap compared to the thermal energy (approximately when $\Phi_s \ll 25$ mV), we can expand the exponential term $e^{-x} = 1 - x$ (Debye-Huckel approximation). The Grahame equation simplifies to:

$$\sigma = \varepsilon_0 \epsilon \kappa \Phi_s \quad (2.19)$$

where

$$\kappa = \left(\frac{\sum_i \rho_{\infty i} e^2 z_i^2}{\varepsilon_0 \epsilon k_b T} \right)^{1/2} \quad (2.20)$$

Note that [Equation \(2.19\)](#) is akin to the equation of a parallel plate capacitor relating the charge density on the plates to the voltage across a gap of length κ^{-1} . This length is called the *Debye length* and can be thought of as a measure of the “thickness of the double layer” [94]. The Debye length is one of the most important parameter for characterizing the electrostatic interactions between colloids. Indeed, it sets the spatial extent of the electrostatic forces. This is more evident if one solves the PB equation in the Debye-Huckel approximation, because in this case the potential takes a very simple form:

$$\Phi(x) \sim e^{-\kappa x} \quad (2.21)$$

Therefore, away from the surface, Φ decreases exponentially with a characteristic decay length equal to κ^{-1} . For a given electrolyte, the Debye length, and hence the decay length of the electrostatic potential, depends only on the amount of ions in solution, and not on any property of the surface such as its charge or potential (see [Equation \(2.20\)](#)). More precisely, the range of the repulsive forces shrinks when adding salt to the solvent, since it is inversely proportional to ρ .

Electrostatic potential energy In analogy with [Equation \(2.14\)](#), the osmotic pressure between two surfaces at distance h in an electrolyte solution can be calculated from the total ionic concentration at the mid-plane (ρ_0):

$$P(h) = k_b T \left[\sum_i \rho_{0i}(h) - \sum_i \rho_{0i}(\infty) \right] \quad (2.22)$$

The last equation can be solved analytically only for a symmetric electrolyte. The result is:

$$P(h) = 64 k_b T \rho_{\infty} \gamma^2 e^{-\kappa h} \quad (2.23)$$

where $\gamma = \tanh(ze\Phi_s/4k_bT)$. The energy per unit area is obtained by a simple integration with respect to h :

$$W(h) = \frac{64 k_b T \rho_{\infty} \gamma^2}{\kappa} e^{-\kappa h} \quad (2.24)$$

The interaction potential for two spheres of radius a can be calculated by applying the Derjaguin approximation [46]:

$$V(h) = \frac{64 \pi k_b T a \rho_{\infty} \gamma^2}{\kappa^2} e^{-\kappa h} \quad (2.25)$$

In the case of an asymmetric electrolyte, analytic approximated solutions are available only in the Debye-Huckel approximation; the interaction potential per unit area of two planar surfaces reads [99]:

$$W(h) = 2\epsilon_0\epsilon\kappa\Phi_s^2 e^{-\kappa h} \quad (2.26)$$

and for two equal spheres:

$$V(h) = 2\pi a\epsilon_0\epsilon\Phi_s^2 e^{-\kappa h} \quad (2.27)$$

In the above expressions, Φ_s and σ are related by Equation (2.19).

Finite Size effects Let us note that in the derivation of the potential energy between charged surfaces, two strong assumptions are made:

- (i) the electrolyte ions are treated as point-like charges,
- (ii) at small distances, the solvent permittivity does not change.

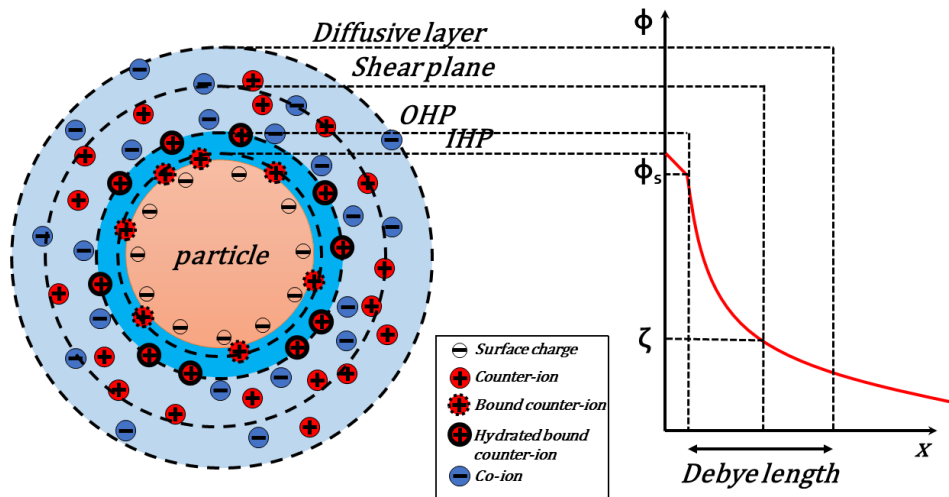


Figure 2.3 – Double layer and electrostatic potential in the proximity of an isolated charged particle. The electrostatic potential decays linearly within the Stern layer and exponentially in the diffusive region. Its value at the shear plane is called zeta potential ζ .

Clearly, in a region of few Å from the surface plane, these two assumptions are likely to break down. First, we note that the counterions in the neighborhood of the plane of charge can be bound and/or physisorbed to the surface; moreover, they can be in the dehydrated, partially hydrated, or fully hydrated state. In all cases, their finite size certainly limits their distance of closest approach to the surface, and hence their maximum concentration. Finite size effects are usually described by virtually separating the Stern layer into two additional regions: the Inner Helmholtz Plane (IHP), which passes through the centers of the bound cations, i.e. those ions which have lost their solvation shell, and the Outer Helmholtz Plane (OHP), which

passes through the centers of the physisorbed (hydrated) cations, at the distance of their closest approach to the plane ($x = b$ in [Figure 2.2\(a\)](#)) [185]. The OHP plane, thus, defines the region past which the ionic atmosphere begins to obey the Poisson-Boltzmann equation. A more detailed representation of the double layer, comprising the Stern and diffusive regions along with the corresponding electrostatic potential drop, is illustrated in [Figure 2.3](#). The shear layer, defined as the plane integral with the surface during a relative motion between the surface and the liquid, is also reported. The potential surface at the shear plane is called zeta potential ζ . Note that, in general, ζ does not coincide with the surface potential Φ_s , defined at the OHP. Since within the Stern layer (i) the potential does not obey the PB equation and (ii) the high electric fields must produce some ordering of solvent dipoles, leading to a change in the local dielectric permittivity, [Equations \(2.24\) to \(2.27\)](#) are accurate only for surface separations beyond the Stern layer.

Charge regulation We recall that [Equations \(2.13\) and \(2.17\)](#) have been obtained assuming a constant surface charge density, regardless the gap between the surfaces. Yet, in real situations, when two planes are forced into molecular contact, the surface charge density may decrease and the repulsion fall below that calculated on the assumption of constant σ , [Equation \(2.22\)](#). This phenomenon, known as *charge regulation*, affects the shape of the potential for very short separations. In general, neither σ nor Φ_s remain constant and hence the “true” potential lies between the curves calculated using a constant surface potential (charge) and a variable charge (surface potential). The charge regulation effect can be incorporated in the double layer theory by considering explicitly both the surface association and dissociation constants of the adsorbing ions [99], or by constant regulation approximations [13]. A more detailed description of charge regulation models can be found in [26, 13, 199].

2.2.3 DLVO theory

In the DLVO theory (Derjaguin, Landau [47] and Verwey, Overbeek [203]) the net interaction between two isolated particles is described by the sum of the attractive vdW and repulsive electrostatic double layer forces:

$$V_{DLVO}(h) = V_{vdW}(h) + V_{el}(h) \quad (2.28)$$

Let us consider the situation of two microspheres of radius a interacting between an electrolyte solution containing a divalent salt. In these conditions, the potential energy of the pair, as a function of their surface-to-surface separation h , can be written thanks to [Equations \(2.8\) and \(2.27\)](#):

$$V_{DLVO}(h) = -\frac{A_H}{6} \left[\frac{2a^2}{h(h+4a)} + \frac{2a^2}{(h+2a)^2} + \ln \left(\frac{h(h+4a)}{(h+2a)^2} \right) \right] + 2\pi a \epsilon_0 \epsilon \Phi_s^2 e^{-\kappa h} \quad (2.29)$$

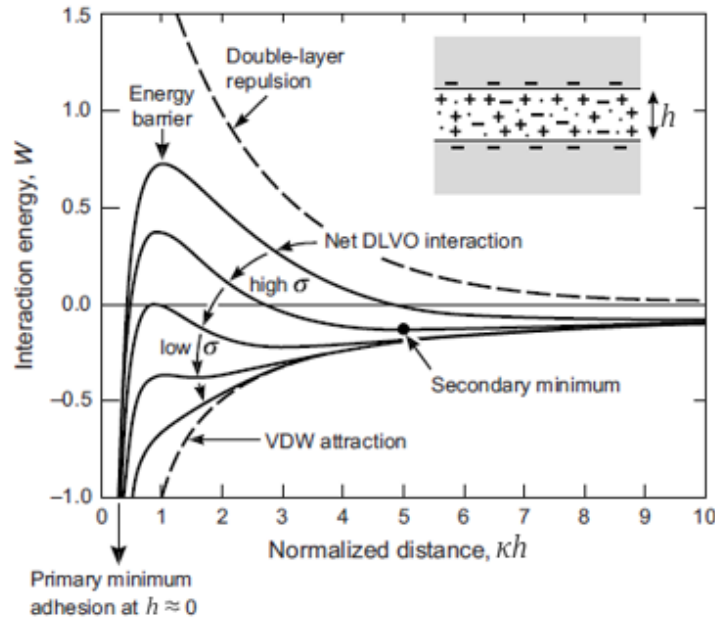


Figure 2.4 – The DLVO interaction energy (per unit area) of two charged planes in electrolyte solutions, versus reduced distance κh . Figure taken from [99].

or through the simplified expression, Equation (2.9):

$$V_{DLVO}(h) = -\frac{A_H a}{12h} + 2\pi a \epsilon_0 \epsilon \Phi_s^2 e^{-\kappa h} \quad (2.30)$$

Note that the vdW interactions are almost insensitive to the pH and salt concentration of the solution, while, as we have seen, the latter strongly influences the electrostatic term. As a consequence, the net DLVO interaction is essentially determined by variations in the double-layer forces, as shown in Figure 2.4. At small surface-to-surface separations, $h \rightarrow 0$, the vdW forces must dominate due to the $1/h$ divergence, whereas the electrostatic term remains finite. Hence, particles are expected to establish direct contact once h is sufficiently small. The potential energy minimum at contact is known as the primary minimum. However, when the surface charge density σ is high—in absence of added electrolyte or far from the iso-electric point IEP (where the surface charge is zero)—the DLVO theory predicts that the electrostatic contribution dominates at large distances, resulting in the emergence of an energy barrier for h just beyond the primary minimum, as shown in Figure 2.4. The amplitude of the barrier can be several times the thermal energy of the particles: in this case the latter are thus unable to establish contact by thermal activation. Variations in electrolyte concentration and pH reduce the amplitude (through Φ_s) and extent (through κ) of the double-layer forces, leading to a progressive decrease of the energy barrier. In moderate electrolyte concentrations, the DLVO potential may present a shallow secondary minimum at intermediate distances (few nm); in this case the particles are weakly bound and may escape from the well by thermal agitation. If the energy barrier is still high, the particles remain dispersed in the solution for periods exceeding any reasonable measuring time; the suspension

is said to be stable. At high salt concentrations, the energy barrier can be further lowered, and two situations may arise: if the barrier is of few or fraction of k_bT , the particles weakly bound in the secondary minimum can flocculate (fall into the deep energy minimum) by thermal activation in a measurable time period. Above a critical electrolyte concentration, the barrier disappears, and particles immediately establish contact upon collision; in these conditions the suspension is unstable, and flocculation is irreversible.

2.2.4 non-DLVO interactions

Recently, DLVO theory has been found unable to fully predict the behavior of colloids in aqueous suspensions [147, 149, 204, 128, 26, 199, 13]. One critical feature of the model is that it treats the suspending phase only as a transmitting medium, neglecting its structure. It is reasonable to believe that, especially at low h , the water structure participates in a more significant way. Indeed, diverse phenomena such as polarization effects induced by the high electric fields at the interface, existence of adsorbed layers of hydrated cations, image-charge effects caused by the difference in dielectric constants, formation and breakage of hydrogen bonds between water and surface functional groups, and geometric constraining effects, lead in general to the formation of ordered liquid layers [98, 83]. The overlap of these structured layers gives rise to additional repulsive non-DLVO forces, known as solvation (hydration) forces, which typically decay exponentially with distance [98].

In inorganic colloids such as silica, hydration forces are usually associated to strong hydrogen bonding networks, since these materials typically possess hydroxy- and oxy-surface groups. The magnitude and range of the repulsion typically vary with the concentration and type of electrolyte, and the solution pH. Quite generally, solvation forces are important at low salt contents, whereas they disappear on increasing the salinity [128, 26]. By surface force apparatus (SFA) experiments on silica sheets, Chapel [26] found a positive correlation between the reduction in the repulsive forces and the increase in the hydrated radius of the cations. The author explained the observed behavior by assuming that each adsorbed cation breaks the network of hydrogen bonds, and thus reduces the strength and range of the repulsion. Note that this “structure-breaker” capability is stronger for cations with larger hydrated size, because they bring along more water molecules. This behavior is in contrast to that found by Pashley and Israelachvili [149] for mica surfaces. They observed that an increase of the numbers of water molecules in the first shell around the cations, induces a larger repulsion between the surfaces. Here, the cation plays the role of a “structure-maker”. More recently, Borgovec et al. [199, 13] found that the interactions between spherical silica surfaces were well described by DLVO theory, but only down to few nm. Deviations were observed at smaller separations for different monovalent and multivalent metal ions; the forces usually became strongly repulsive, whereas vdW attraction was expected. Interestingly, an additional non-DLVO attraction at moderate multivalent cation concentrations was observed.

The physical origin of the short-ranged repulsion in silica, however, remains an open question. Indeed, these forces have been also attributed to steric interactions

between gel (hairy) layers of polysilicic acid $(-(\text{OH})_2-\text{O}-\text{Si}(\text{OH})_2-\text{OH})$ —see Vigil et al. [204]. Similarly, Bitter and co-workers [17] developed a model based on DLVO theory plus a steric repulsion attributed to silica gel layers that can eventually shrink at high electrolyte concentrations. Yaminsky et al. [211] affirmed that the complex behavior of colloidal silica can be totally ascribed to these polysilicic acids, which can undergo many transformations, such as swelling, gelation and condensation when exposed to different physio-chemical conditions.

Sometimes, the measured force profiles show an additional short-ranged non-DLVO attraction, usually attributed to charge fluctuations, ion-correlation and/or image charge effects. Ion correlation is described as a vdW-type force caused by the polarization of the ions in the gap between the two interacting surfaces [67]. The effect may be significant only at separation well beyond few nm and its amplitude may increase with the surface charge density and the valency of the cations. Interestingly, many works report the existence of cation-dependent non-DLVO attractive interactions [199, 55, 198], especially when divalent and multivalent metal cations are used to screen the double layer forces. Formation of ion bridges may explain such forces [147].

2.2.5 Time-dependent interactions

Interestingly, it is relatively well known that the interaction strength between colloidal particles may increase with the time of stationary contact [98]. However, the study of time-dependent interactions remains scarce. Time-dependent forces have been ascribed to different phenomena. Vigil et co workers [204] attributed them to an interfacial consolidation of the overlapping polysilicic gel layers, when the surfaces are forced into contact. Other authors claimed that they are caused by the formation of an hydrogen bonds network between the surfaces [127]. Vakarelski et al. [198] observed time dependent adhesion and related it to a protracted breaking of interfacial structured water layers, whose kinetics is controlled by the hydration enthalpy of the adsorbed cations. Time-dependent interactions and contact aging will be treated in more detail later in the manuscript.

2.3 Phase diagrams of model systems

Like atomic systems, colloidal suspensions exhibit phase transitions [93]. More generally, one could find colloids in liquid, gel, pasty, crystalline and even glassy states. This complex phase behavior stems from the combined effects of thermal motion, particle interactions and packing fraction. All of these parameters also determine the mechanical (rheological) response of the suspension under external stresses.

2.3.1 The hard sphere system (HSS)

The colloidal system with the simplest phase diagram is the hard sphere suspension (HSS), in which particles interact only through an infinite repulsion on contact.

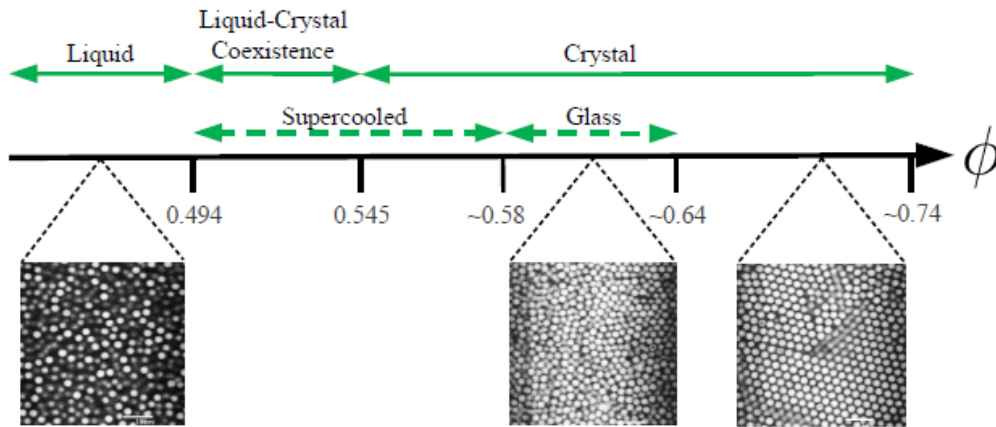


Figure 2.5 – Phase diagram of monodisperse hard spheres as a function of volume fraction. Equilibrium states are indicated with solid green arrows, while non-equilibrium ones with dashed arrows. Figure taken from [93].

This is equivalent to say that particles are infinitely stiff; the interaction energy V as a function of r , the center-to-center distance between the colloids, can thus be expressed as

$$V(r) = \begin{cases} \infty, & \text{if } r \leq d \\ 0, & \text{otherwise} \end{cases} \quad (2.31)$$

where d is the particle diameter. Since only excluded volume effects are present, the free energy of the system is determined only by entropy, and the HS phase diagram depends only on the packing fraction ϕ [93]. As illustrated in Figure 2.5, despite the absence of any attractive part in the potential, several equilibrium and out-of-equilibrium states may be present. The two thermodynamic equilibrium phases are the liquid one, which is found for $\phi < 0.494$ and the crystalline one, which is found for $\phi > 0.545$. Note that in between these two limits, the two phases may coexist. Interestingly, the HS crystallization arises from an entropic effect; when spheres arrange into a crystalline lattice, indeed, the configurational entropy reduction is balanced by an increase in vibrational entropy, since the volume in which particles can rattle without leaving the configuration is higher in the crystalline state than in the liquid one.

In practice, crystallization is often not observed and the suspension remains a fluid for $0.545 < \phi < 0.58$. This is usually caused by the presence of a small polydispersity in the particle size distribution, which hampers nucleation of crystalline regions [217]. In such situations, the liquid is termed supercooled. On increasing ϕ above 58%, the dynamics slows down enough that the suspension can be considered essentially frozen for times of the order of typical observation times, and the system usually exhibits a dramatic increase in viscosity. The resulting kinetically arrested phase is called a colloidal (repulsive) glass [164]. The upper bound of the glassy region is located at the maximum concentration at which spheres can be randomly packed, $\phi_{\text{rcp}} \sim 0.64$.

The glass transition has been widely studied in last decades by theory [200, 215, 174], numeric simulations [217] and experiments [164, 200, 85]. Nearly ideal HS colloids have been made experimentally using poly-(methyl methacrylate) (PMMA) particles, sterically stabilized with a layer of poly-(12-hydroxystearic acid) to minimize aggregation due to van der Waals forces, and suspended in a refractive index and density matched mixture of cis-decalin and cycloheptyl bromide (CHB) [163].

Particle motion in a supercooled liquids is found to be in accordance with the mode-coupling theory (MCT) [81], which predicts a two step decay of the density correlation function: a fast relaxation (β -relaxation) due to the rattling of the particles inside the cage formed by their neighbors, and a slow decay (α -relaxation) due to thermally activated cage break-up processes [36]. On approaching the glass transition line, MCT predicts a power-law divergence of the α -relaxation time, *viz.* a complete dynamical arrest. Several studies have shown that MCT is able to predict the phase behavior of hard spheres systems with an accuracy of 20% [174].

2.3.2 The square-well system (SWS)

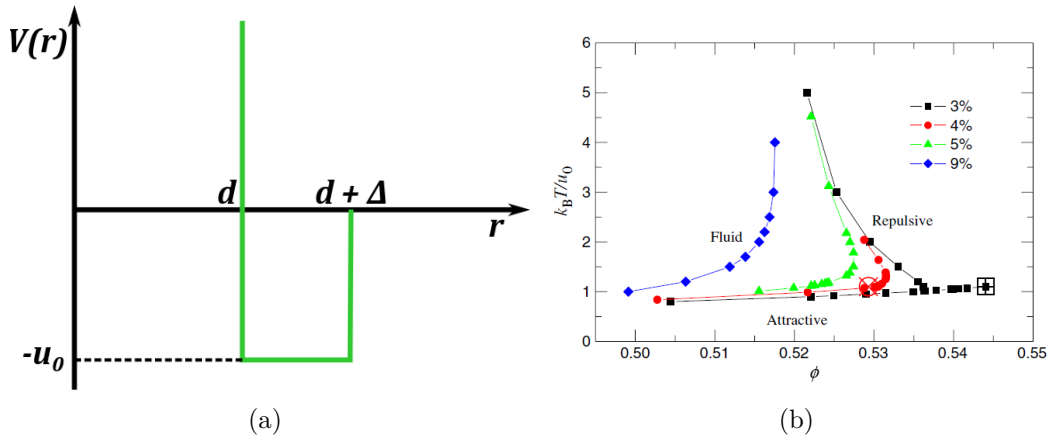


Figure 2.6 – (a) Square-well potential. A repulsive hard core at contact is complemented by an attractive well with finite depth u_0 and small width Δ . (b) The ideal MCT phase diagram of square-well glasses, in the high- ϕ branch. Glass lines with different colors represent various attraction widths, parametrized by the ratio $R = \Delta / (d + \Delta)$, ranging from 3 to 9%. Reducing R leads to a more pronounced re-entrant shape (see text for details). Figure taken from [36].

Arrested states can also form if one introduces an attractive part in the interaction potential, while keeping constant the volume fraction. The simplest model that has become a paradigm for the study of colloidal suspensions with short range attractions is the square-well system (SWS), for which the interaction potential consists of a hard-core repulsion for $r < d$ and a constant attraction well $-u_0$ for $d < r < d + \Delta$,

as shown in [Figure 2.6\(a\)](#).

$$V(r) = \begin{cases} \infty, & \text{if } r \leq d \\ -u_0, & \text{if } d < r < d + \Delta \\ 0, & \text{otherwise} \end{cases} \quad (2.32)$$

The phase diagram is now parameterized by three quantities, namely ϕ , $k_B T/u_0$ and $\delta = \Delta/d$, the latter being the range of the attractive potential in units of particle radius. MCT theory has been used to characterize the phase diagram of SW colloidal suspensions in the high concentration regime $\phi \gg 0.40$ [42], where the cage effect remains substantial for the dynamics [174]. At high ϕ and for short-range attraction widths (few per cents of d), the theory predicts two main phenomena: (i) at intermediate attraction strengths, the formation of bonds locally reduces the inter-particle distances and leads to a more inhomogeneous distribution of voids than in the repulsion-driven glass, thus it shrinks the local cage size and allows to the melting of the glass; (ii) if the strength of the attraction is increased further, however, a new arrested phase, called attractive glass, is formed, since now the bonds are so long lived to prevent structural rearrangements [14, 42]. Thus, in the dense regime, the phase diagram displays a re-entrant shape, as illustrated in [Figure 2.6\(b\)](#). At constant ϕ , the SWS can be in the repulsive, attractive or ergodic fluid phase, depending on the strength of the attraction. These expectations have been demonstrated recently through numerical simulations [214] and experiments on model square-well suspensions [154, 59]; the latter consist of hard spheres (e.g. sterically stabilized PMMA particles in cis-decalin) to which nonadsorbing polymers (e.g. polystyrene) acting as depletant agents, are added. In these conditions the strength of attraction is determined by the amount of polymer in solution, whereas the range is of the order of the polymer radius of gyration, as predicted by the Asakura–Oosawa potential $V^{AO}(r)$ [4].

2.3.3 Arrested states at low volume fractions (gels)

We have seen that much effort has been devoted to provide a framework for dynamical arrest at large packing fractions (the liquid-glass transition). It is known, however, that colloidal dispersions may form disordered arrested states—the gels—at lower ϕ (down to a few percent). Gel formation is associated to the emergence of a rigid percolating network of bonds, that gives to the gel solid-like properties (elastic modulus, yield stress) and allows it to support its own weight under gravity.

The gelation mechanism is still a matter of debate. Numerous descriptions have been proposed to explain gel formation in the limit of small Δ , such as models based on percolation theory [74], diffusion limited aggregation with finite bond breakage probability [43], mode-coupling theory extended to lower volume fractions or applied to clusters of particles [109], and thermodynamic approaches based on liquid–gas phase separation [213, 194, 121]. Quite generally, gelation should be controlled by the lifetime of the bonds [213]. In chemical gels like epoxy resin and rubber, on the one hand, the network is made of chemical (covalent) bonds that have an infinite

lifetime. In these systems, hence, gelation is well described in terms of percolation theory [64], since the gel point exactly coincides with the emergence of an infinite network spanning over the sample. In colloidal gels with interparticle interaction energy of the order of $k_B T$, on the other hand, the bonds are characterized by a finite lifetime; since the space-spanning structure can be lost by rupture of a single bond belonging to the percolated network, percolation is usually transient and does not coincide with gelation, although it is a necessary condition to form a gel.

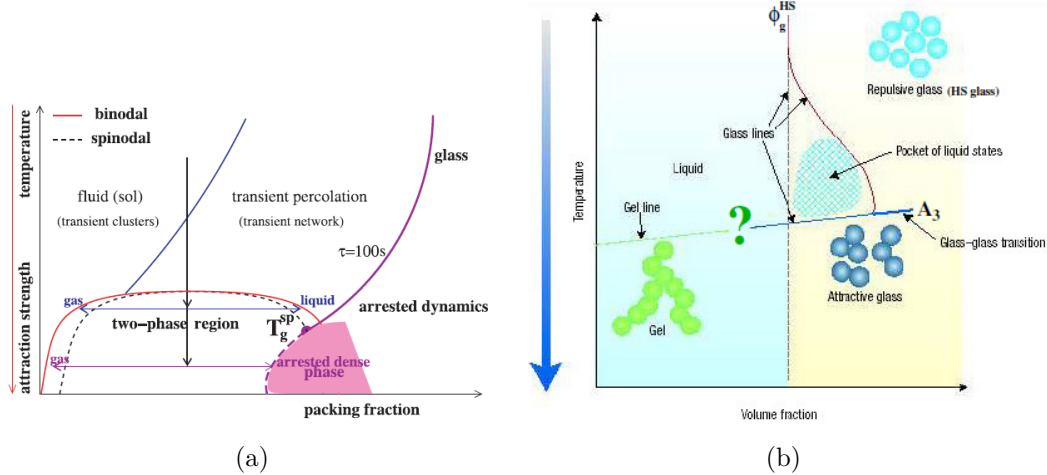


Figure 2.7 – (a) Representation of the phase diagram of SWS with a short-range well depth potential, including the percolation (blue), spinodal (red) and glass lines (magenta), as calculated from numerical studies. Arrested spinodal decomposition occurs when the dense phase meets the glass line in the high ϕ branch. This happens when the quench into the two-phase region is performed at a temperature below the intersection T_g between the spinodal and the extrapolated glass line. (b) The gel line as the extension to low ϕ of the attractive-glass line. Figures taken from [213]

Increasing the interaction strength and hence the bond lifetime, however, may lead to phase separation [173, 213]. This is the case of spherically symmetric attractive potentials such as the square-well model. When the range of the attractive potential is small (few per cent of the particle diameter), the phase diagram of different systems does not depend on the shape of the potential, as predicted by the Noro Frenkel extended law of corresponding states [141]. This is true down to the Baxter’s limit —the adhesive hard sphere (AHS) system —which is the limit of the SW potential for $\Delta \rightarrow 0$, $u_0 \rightarrow \infty$ such as the second virial coefficient remains finite. Thus, the SW phase diagram can be represented by the Baxter’s model, which has been carefully evaluated via grand-canonical Monte Carlo techniques by Miller and Frenkel [132, 133]. The calculations do predict a metastable (with respect to the gas–crystal transition) liquid–gas coexistence (spinodal) region, as depicted with a red line in Figure 2.7(a). In such conditions, many works suggest that gel formation is a non-equilibrium process, and can be described in terms of arrested phase separation, or spinodal decomposition [43, 65, 173]. The mechanism underlying this gelation route can be understood as follows. Under a quench at low ϕ (black arrow in Figure 2.7(a)), the system crosses the spinodal phase separation boundary, and

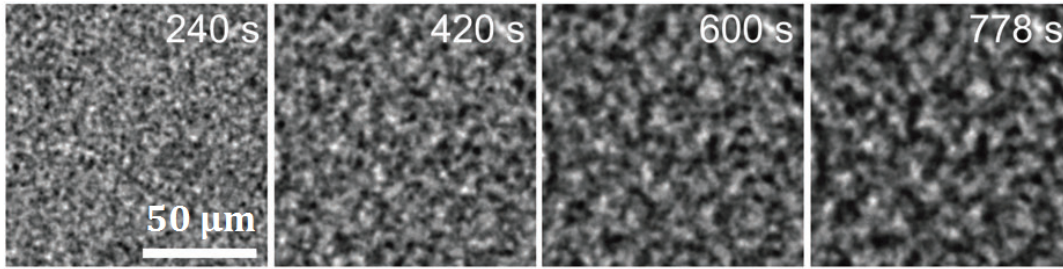


Figure 2.8 – Spinodal decomposition of an oil-in water nanoemulsion after the system is quenched into the gel state. Figure taken from [78].

colloid-rich and colloid-poor domains start to form. During this coarsening process, the volume fraction of the colloid-rich domains steadily increases, and phase separation arrests when an attractive glass transition occurs within this denser phase. For short-ranged, low-energy attractive potential, various experimental works [78, 121] have indeed confirmed this scenario. Typical optical microscopy images during spinodal decomposition are reported in Figure 2.8 for an oil-in water nanoemulsion at $\phi = 33\%$, in which the interactions between droplets can be approximated with a square well potential, with fixed width and temperature-dependent depth [78]. The structural changes of the microstructure are reflected in the time evolution of the structure factor $S(q)$: during coarsening, first a peak in $S(q)$ appears at low q , indicating the presence of dense regions with a characteristic size $1/q$; then a drift with time of the peak towards lower and lower q -values is observed. At some point, the coarsening process arrests and $S(q)$ does not evolve any further [121].

An alternative interpretation, based on the ideal mode-coupling theory for short-ranged attractive potentials applied to low ϕ [15, 14], suggests that the phase separation line is preempted by the attractive glass line; dynamical arrest can be approached from the fluid phase before the coexistence curve is reached, hence the gel-line is nothing but the extension to low ϕ of the attractive-glass line, as shown schematically in Figure 2.7(b). Numeric simulations [65] however, are at variance with this picture, inasmuch the glass line is predicted to always ends on the right side of the spinodal, even for very low $k_B T/u_0$ down to the Baxter’s limit.

2.3.4 Phase separation inhibition

We now discuss a situation that may be relevant for colloidal suspensions in aqueous solvents, i.e. when the short range vdW attraction is complemented by a weak long-range repulsion due to residual charges onto colloidal particles (see later in the text). In this case, due to these competing forces, particles may prefer to aggregate in clusters with a finite size, usually with low coordination number [173, 213]. On increasing the attraction strength, a stable cluster phase can be generated, and gelation may be mediated by (i) the percolation of the clusters, instead of the particles themselves, and (ii) the residual “effective” cluster–cluster interaction. In these conditions, the phase separation line is pushed towards higher attraction strength and/or is replaced by an equilibrium cluster phase (microphase separation), while the gel and glass lines may merge into a single curve, as shown in Figure 2.9(a).

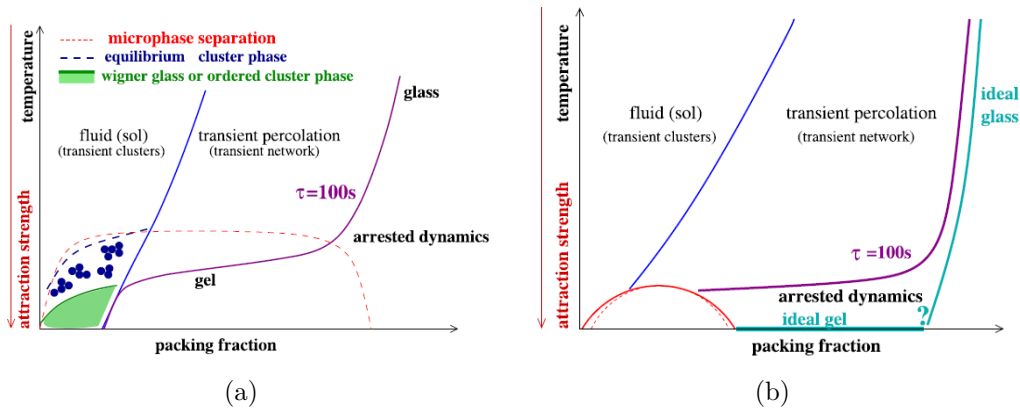


Figure 2.9 – Phase diagram for SWS when an additional long-range repulsion (a) or directional interactions (b) are considered. Phase separation is hindered, and at high attraction strengths and intermediate ϕ , gelation is caused by percolation of the equilibrium clusters with limited coordination. Figures taken from [213].

Note that the microphase separation usually results in the appearance of a pre-gel low q peak in the static structure factor [176], which does not evolve with time upon gelation. This scenario has been partially confirmed by Sedgwick et al. [175], as shown in Figure 2.10, for density-matched charged PMMA particles with depletion interactions.

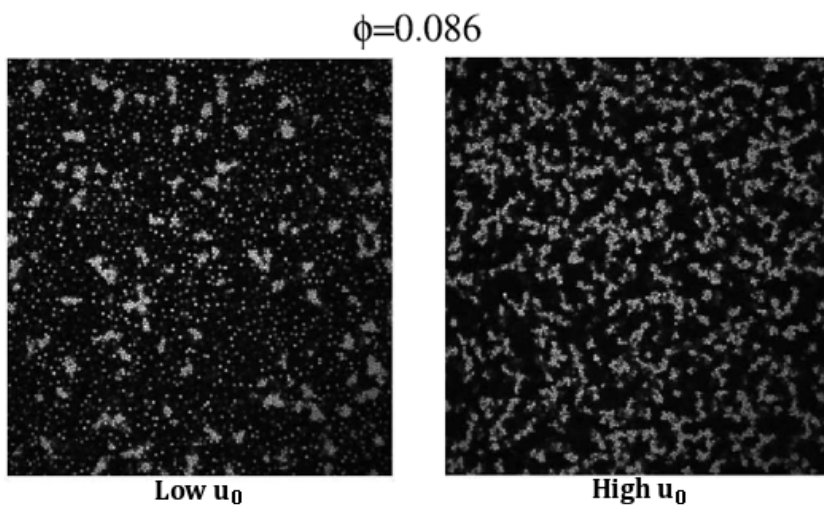


Figure 2.10 – Equilibrium cluster phase (fluid) at low attraction energy (left panel) and arrested phase (gel), due to cluster percolation, for increasing attraction strength (right panel). Figure taken from [175].

A similar modification of the phase diagram is found for systems in which particles interact through directional forces, e.g. for patchy-like particles. It can be shown that, in this case, not only the phase separation boundary is pushed towards increasing attraction strengths, but it is also shifted towards lower volume fractions [213], as shown in Figure 2.9(b). The existence of an energetically preferred cluster size, and

its effects on the corresponding phase diagram, have been addressed numerically [173] in the framework of the square well system, using a toy model in which a (*ad hoc*) constraint on the maximum particle number per cluster N_{\max} is introduced (maximum valency models). It has been confirmed that, for low N_{\max} , there exists a window of intermediate packing fractions for which it is possible to cool down the fluid without encountering phase separation (Figure 2.9(b)). In this case, since phase separation is not intervening, the route to the gelled state may proceed through a series of equilibrium states. At infinite attraction strength, the bonds are so long-lived that there are no time scales whereby the system can relax due to bond rearrangements. So, the dynamical arrest state is not strictly connected to the observation time window, and the gel is termed ideal. For a recent review of this and related topics, see [213] and references therein.

2.3.5 Fractal gels

In the presence of sufficiently strong attractive forces, colloidal dispersions may form gels also at extremely low volume fractions ($< 1\%$). In this case, the suspension consists of clusters (flocs) with average size ξ , that pack to form a sample-spanning microstructure. The microstructure of such diluted gels can be described by fractal theory, according to which the radius of gyration ξ of a floc made of N particles with radii a scales as $\xi = aN^{1/d_f}$, where d_f is the fractal dimension. The fractal dimension depends on the kinetics of aggregation [112]. When aggregation is not hindered by energy barriers, one expects particles to stick immediately upon contact, so that flocculation is essentially determined by diffusion (diffusion-limited cluster aggregation or DLCA). In this case, one usually obtains $d_f \sim 1.8$. More compact clusters (higher $d_f \sim 2.1$) are found in the reaction-limited cluster aggregation (RLCA), for which several collision events have to occur before stable bonds are formed. The presence of a characteristic length scale ξ results in the emergence of a pronounced peak at very low q in the static structure factor, whose magnitude steadily increases over time, reflecting the growth of the clusters. The suspension is usually said to have gelled when the peak ceases to evolve in time [35].

2.4 Aging and thixotropy

2.4.1 Colloidal glasses and gels

In the last section we have seen that colloidal suspensions can undergo a transition from a liquid to a solid state as a function of the particle volume fraction and the strength and nature of the colloidal interactions. We found that two types of solid (or jammed) state exist in colloidal suspensions: glasses and gels. We also note that a qualitative distinction between the two is based on the mechanism of dynamical arrest [189, 216]. In the former the constituent particles are trapped “topologically” by the cages formed by the nearest-neighbors, while in the latter the arrested state is due to interparticle bonds. Glasses and gels, hence, may exhibit substantial differences. For instance, the mechanical strength of the gels is determined by the percolated infinite network of particles, while in a glass it stems from caging

effects. A gel is usually inhomogeneous due to the formation of large aggregates made of many particles, while a glass is relatively homogeneous over length scales of few times the particle size. However, since both gelation and glass transitions are thought to have a kinetic, rather than thermodynamic, origin [213], some have argued that gels and glasses should display similar features [189]. On approaching the fluid-to-solid transition in both systems, for example, it has been shown [176] that density correlations typically relax in a two-step fashion, with the final relaxation time diverging when the critical volume fraction ϕ_c is reached.

These observations led to the suggestion that a wide variety of systems, including colloidal suspensions, and granular and molecular systems, could be described in an unifying framework in terms of a jamming phase diagram [118], whereby the phase behavior is set by the density ρ (or particle volume fraction ϕ), the temperature T (or reduced temperature $k_B T/u_0$, where u_0 is the attraction energy), and the applied external stress σ [193]. According to the jamming phase diagram, there would be three ways to transform a liquid-like colloidal suspensions into a jammed solid-like one; increasing ϕ , increasing u_0 or decreasing σ . While we have investigated in some detail the effect of packing fraction and attraction strength, this approach suggests that also a mechanical stress should play an important role in determining the fluid-to-solid transition. Since, in general, a sufficiently large stress causes a solid sample to yield, it is the yield stress σ_y —the minimum stress needed to induce flow from quiescent conditions —that defines the phase boundary [193]. Although the jamming scenario provides an unifying description of the fluid-solid transition for a wide variety of materials, time-dependent effects are not considered explicitly in this approach. Indeed, it is known that many jammed systems, such as colloidal glasses and gels, exhibit aging phenomena, i.e. a continuous evolution of their mechanical properties with time, usually associated to the material relaxation towards equilibrium [36]. Moreover, during flow, a thixotropic response is commonly found; shearing the sample causes a gradual decrease in viscosity with time, with the characteristic time to reach a steady state flow that depends on the previous flow history. It is well established that changes in the material properties as a function of shear history are intimately linked to structural changes [9, 130]. In recent years, hence, a considerable effort has been devoted to studying the relationship between the structure of the suspension under stationary flow and its time-dependent mechanical properties.

2.4.2 Thixotropy

An archetype of our current interpretation of thixotropy is perhaps provided by the illustration given by Barnes in his seminal paper [9], that we report in [Figure 2.11](#). When left at rest, the structure of the material under investigation evolves over time due to thermal fluctuations, which allow the particles to continually explore different configurations and to reorganize in more energetically favorable states. As a consequence, the material is expected to strengthen over time. This structural evolution, however, can be erased by vigorously shearing the system, so that the material can be brought back to a reference, unstructured state. Often, the term “structuration” is used to refer to the fact that the “structural state” of the material varies with the flow history. Phenomenological approaches aiming to include time-dependent rheological

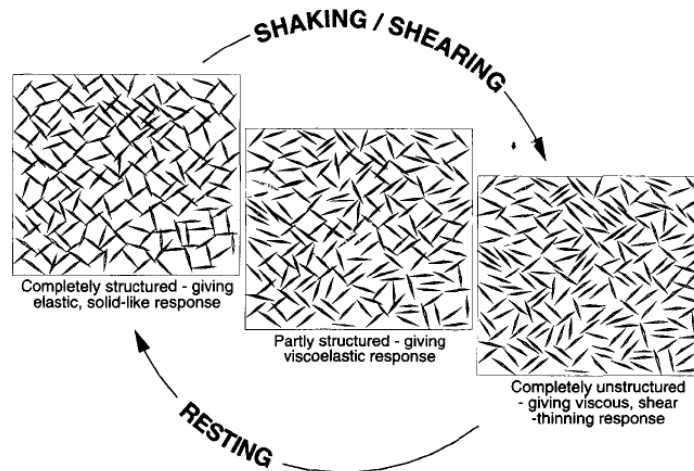


Figure 2.11 – Structural evolution of a thixotropic material under flow (up arrow) and quiescent (down arrow) conditions. Figure taken from [9].

effects, indeed, commonly use empirical kinetic models based on this idea [130]; “structuration” is mathematically described by a single dimensionless parameter λ : $\lambda = 0$ for “minimum” structure and $\lambda = 1$ for “maximum” structure. This is exactly the scenario expressed visually by the arrows in Figure 2.11. Observe also that the latter suggest a reversible process; the structure can be indefinitely brought back and forth between the “completely structured” and “completely unstructured” state. Since thixotropy appears macroscopically reversible, it comes as no surprise that reversible, microscopic phenomena, such as particle flocculation and deflocculation, are typically invoked. The concept of maximum and minimum microstructure is however rather vague, and does not correspond to any physical quantity [169].

2.4.3 Aging

We have seen that when a thixotropic material is left at rest, one usually observes an increase of its mechanical strength, associated with a structural evolution. The time-dependence of mechanical properties are also indicative of systems that age; for these materials, for instance, the yield stress and the elastic modulus are typically found to grow with resting time [45, 143]. It is conceivable, thus, to think that aging phenomena are related to an evolution of the structure.

Quite generally, the aging time is counted starting when the sample is first quenched from the fluid-like to the solid-like state. From a macroscopic perspective, it is defined by the onset of an elastic mechanical response. Since colloidal suspensions can solidify under a wide variety of conditions, however, the choice of the zero aging time depends on the specific system under consideration. In dilute systems with large attraction strengths, the zero of the aging time is taken as the percolation time, i.e. when the low- q peak in the static structure factor ceases evolving in time [35]. For weakly attractive gels at intermediate ϕ , on the contrary, there is a delicate in-

terplay between aggregation, dynamical arrest and phase separation [25], and it may not be straightforward to distinguish between aging and gelation [144]. In colloidal glasses, the quench usually coincides with the cessation of a mechanical shear, the latter being used to randomize the structure. The same procedure is used in concentrated, pasty suspensions, since aggregation rapidly results in gelation [169, 73]. In thermoreversible dense systems aggregation is induced “*in situ*”, by rapidly decreasing the temperature. In these conditions, a clear latency period is observed, in which the viscous part of the complex modulus is higher than the elastic one, and the aging time can be inferred by pinpointing the moment in which the moduli cross [87].

We now review how aging phenomena are interpreted in terms of structural evolution for these different systems: dilute non-stabilized gels, stabilized depletion gels at intermediate packing fractions, repulsive and weakly attractive glasses and pasty systems.

Aging in dilute, non-stabilized gels

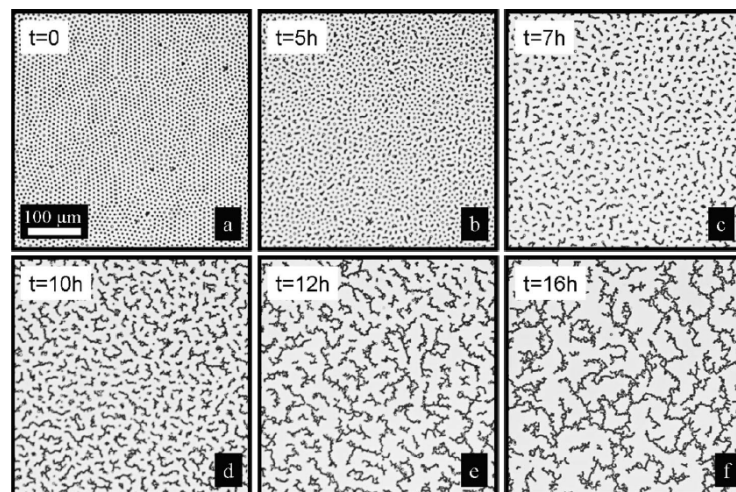


Figure 2.12 – Microstructure recovery after flow arrest for a bi-dimensional colloidal suspensions. Figure taken from [124].

At low volume fractions and for $k_B T/u_0 \ll 1$, irreversible aggregation leads to the formation of fractal clusters, which jam to form an elastic solid with a hierarchic structure. In these systems, the gel point can be related to the formation of such a space-filling network of flocs. One of the most striking example of the gelation “kinetics” in dilute conditions has been provided by the group of Vermant and co-workers [124], who studied structure breakage and recovery for a colloidal suspension of polystyrene particles confined in two-dimensions (Figure 2.12).

Dynamic light scattering has been used to study aging long after the gel point was reached, in a wide variety of materials at low ϕ , including diluted ($\phi \approx 10^{-4}$) fractal colloidal gels [16, 32, 37, 58] and semi-concentrated suspensions of clay particles [7, 32]. Usually, a non-exponential decay of the intermediate scattering

function (density correlations) at very large timescales is observed:

$$f(q, t) \sim \exp[-(t/\tau_r(q, t_w))^p] \quad (2.33)$$

where $\tau_r(q, t_w)$ is the relaxation time and $p \sim 1.5$ the relaxation shape factor. In addition, these systems usually exhibit a $\tau_r(q) \sim q^{-1}$ scaling, indicating that the dynamics is “ballistic” rather than diffusive, since the average particle displacement grows linearly with time. According to Cipelletti et al. [35] and Bouchaud [20], such a behavior may be caused by the presence of randomly distributed internal stress sources within the sample, whose response is that of an elastic solid. This physical interpretation can be understood as follows. When a particle suddenly changes its position (micro-collapse), it creates a long-range dipole force. Since the material reacts elastically, each rearrangement induces a tensile strain field in its vicinity, which further causes the motions of other particles belonging to the network. In this context, aging arises from an increase of the energy barrier for further collapses, due to previous rearrangements.

Internal stresses may arise during the quench into the solid state, as the particles are rapidly kinetically trapped into an out-of-equilibrium configuration; the micro-collapses, thus, correspond to the yielding of regions where higher than average tensile stresses have been frozen-in during the solidification. One cannot exclude, however, that internal stresses may develop after the fluid-solid transition. For laponite suspensions, Bandyopadhyay and co-workers [7] imputed the emergence of internal stresses to a steadily increase of the interparticle repulsion with time, as suggested by variations in the conductivity of the suspensions, probably due to the dissociation of ions at the surface of the particle. Similarly, for diluted colloidal gels made of strongly attractive particles, Cipelletti et al. [35] and Manley et al. [123] have suggested that tensile stresses may build up as a result of the decrease of the average interparticle distance, due to syneresis. These works nicely indicate that material aging is intimately related to the microscopic origin of elasticity and nature of particle-particle interactions.

Stress redistribution after particle rearrangements Recently, the interplay between thermal energy, interactions strength and material relaxation has been also addressed in numerical works. In [21], for example, Bouzid et al. studied the dynamic structure factor of a dilute gel, where micro-collapses are introduced manually to speed up the computation. Depending on the ratio between thermal energy $k_b T$ and interactions strength u_0 , they observed significant variations in the gel dynamics, which they imputed to changes in the mechanism of stress redistribution within the material after particle rearrangements. Remarkably, close to the athermal regime $k_b T/u_0 = 0$, the intermediate scattering function $f(q)$ decreases as a compressed exponential with $p = 1.5$, in excellent agreement with the internal stress relaxation model of Cipelletti [35] and Bouchaud [20], and experiments on non-stabilized dilute colloidal gels [35, 37, 58]. On increasing the ratio $k_b T/u_0$, the authors found a gradual transition of $f(q)$ from a compressed ($p > 1$) to a stretched ($p < 1$) exponential decay, and a concomitant change of the dynamics from super-diffusive, with $\tau_r(q) \sim q^{-1}$, to sub-diffusive, with $\tau_r(q) \sim q^{-2}$. These observations suggest

a transition towards a more glass-like dynamics when the attraction energy between the particles is reduced.

Gelation and aging in stabilized, depletion gels



Figure 2.13 – Structural evolution during aging of a tenuous depletion gel. Figure taken from [126].

Structural evolution has been also proposed to be at the origin of gelation and aging observed in weakly attractive depletion gels [144]. In these index- and density-matched systems, the structure and dynamics have been “easily” investigated through confocal microscopy. For gels with $\phi > 0.25$, Varadan and Solomon [202] observed a short-range structure similar to that found in dense liquids. However, for large length scales, they found significant heterogeneities due to the formation of large voids and dense clusters. Structural heterogeneity as a function of polymer concentration c_p (i.e. attraction strength) has been investigated also in [50]. On increasing c_p , a transition from an immobile clusters liquid structure to a gelled state was found, accompanied by a non-monotonic evolution of the contact number distribution, and by an increasingly heterogeneous dynamics and a stronger localization of single particle motion.

Non density-matched depletion gels usually exhibit a delayed collapse induced by gravity [162, 24]. A recent investigation of the phenomenon has been carried out by Kilfoil and co-workers [126] using a combination of time-dependent measurements of vertical concentration profiles, and standard confocal microscopy imaging. The direct observation of microstructure coarsening during the delayed sedimentation phenomenon, as shown in Figure 2.13, was interpreted as a clear manifestation of aging; the coarsening leads to structural instabilities under gravity, until the gel sudden collapses under its own weight.

Slow dynamics in aging colloidal glasses

One of the most comprehensive study of aging in colloidal glasses was carried out by the research group of Weeks and co-workers [93, 39, 33, 34]. With a fast scanning confocal microscope, they were able to track in three-dimensions the trajectories of several thousand individual particles, and compute their mean square displacement

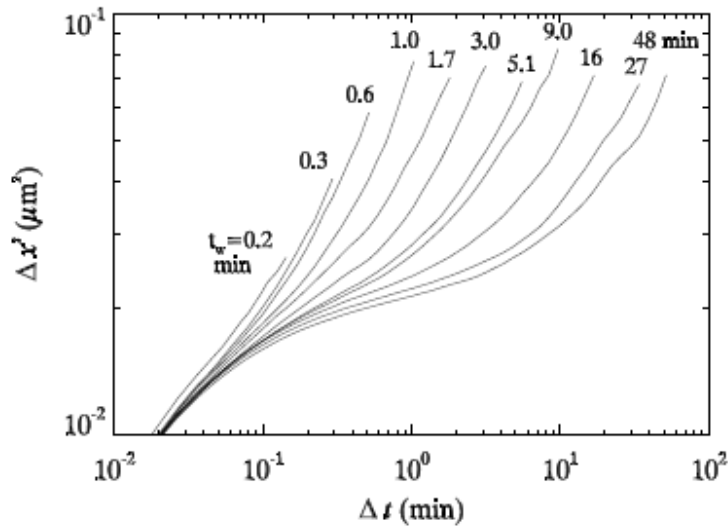


Figure 2.14 – Mean square displacement at different resting times, in a repulsive (hard sphere) colloidal glass. Figure adapted from [93].

(MSD). Figure 2.14 displays the MSDs of a repulsion-driven glass as a function of lag time Δt , for different times of rest. As the system ages, the plateau observed at intermediate Δt , a landmark signature of the cage effect, extends to increasingly longer times, indicating a slowing down of particle motion. Conversely, no dependence of the mean square displacement with age was detected for a supercooled liquid, despite a minute difference in ϕ . Interestingly, local cage rearrangements lead to an upturn in Δx^2 at the end of the plateau, in contrast with the expected divergence of the α -relaxation time predicted by mode-coupling theory. This suggests that ergodicity may be restored, probably by thermally activated processes (hopping) involving groups of cooperative particles [36]. Another intriguing fact emerging from these experiments is that no correlations between the age and the structure of the glass is clearly observable [33, 34]. Although the dynamics is spatially and temporally heterogeneous, the experiments do not show neither a coarsening of the less mobile domains nor significant variations in the structure factor as the glass ages.

Aging in attractive glasses has been less investigated in experiments [106]. Nevertheless, various numerical works [161, 66] suggest that the overall dynamics should be qualitatively similar to that seen in repulsion-driven glasses. Some differences should occur, however. In particular, one expects a stronger localized motion of the particles than in repulsive systems, due to bond formation. A more detailed investigation of aging in glasses is given in [36].

Aging in pasty systems

Dense suspensions or pastes, especially in the presence of strong van der Waals and double-layer forces, have received little attention because they pose tremendous problems for imaging and thus analysis. For this reason, their aging behavior has been preferentially studied via rheometry. Aging has been characterized for

pastes made of polymer coated particles, in which direct contact is thus avoided. Derec and co-workers [45] studied dense ($\phi \approx 40\%$) suspensions of polyethylene oxide-protected silica particles (sterically stabilized). Using small shear oscillations in the linear regime, they found a logarithmic growth of G' . At the same time, by performing start-up flow experiments at fixed $\dot{\gamma}$ and various resting times, they found that the stress at the overshoot —a measure of the stress stored in the material before the onset of flow (σ_y) —was larger in the older samples.

In the last few years, octadecyl-coated silica nanoparticles dispersed in tetradecane (or decalin) have received great attention due to their peculiar ability to switch from hard- to sticky-sphere behavior in response to a small change in temperature. Guo et al. [87] combined rheometry and XPCS experiments to compare the temporal evolution of the macroscopic elasticity and of the microstructure. They found a good agreement between the aging of G' , as measured by rheometry, and (i) the increasingly restricted short-range motion of the colloids and (ii) the steady rise in the fraction of localized particles over time, as extrapolated from the analysis of the dynamic structure factors. Interestingly, as pointed out by the authors, these two phenomena are compatible with an increase in the attraction strength between the silica colloids over time. A different interpretation is given in [80], where the authors used time-resolved rheo-SANS to study the aging of similar thermoreversible silica gels. They proposed an empirical relationship between an order parameter extracted from scattering measurements (in analogy with thixotropy kinetic models discussed above), and the shear modulus growth during aging. According to the authors, the correlation between increasing elasticity and evolution of the structural parameter support the interpretation of aging as a monotonically evolution of the microstructure, due to particle rearrangements.

Pastes of civil and environmental engineering have been less investigated. Ovarlez and Coussot [144] studied the time evolution of the elastic moduli of Na-bentonite suspensions in the semi-dense regime. Mechanical aging was assessed through a thorough study of the time evolution of G' in various packing fractions and temperature conditions. After a careful rescaling of the data, they concluded that aging may result from structural rearrangements driven by thermally activated processes, despite they did not gather direct proofs for that. A similar interpretation for the strengthening of the elastic modulus, observed in three different suspensions, namely a bentonite suspension, a mustard and a hair gel, was proposed in [40]. Recently, Fusier et al. [73] studied aging in strongly attractive dense suspensions of spherical and crushed silica particles, by investigating the linear elastic (G') and non-linear (σ_y) response versus time. They found that the overall rheological properties of the material increased strongly with time, despite confocal microscopy observation provided evidence that their time-evolution cannot be ascribed to changes in the particle network.

The *soft glassy rheology* (SGR) model In the early 2000, Sollich and co-workers [184] proposed a general, phenomenological model to interpret the rheology and aging of soft systems. According to the model, the systems is divided

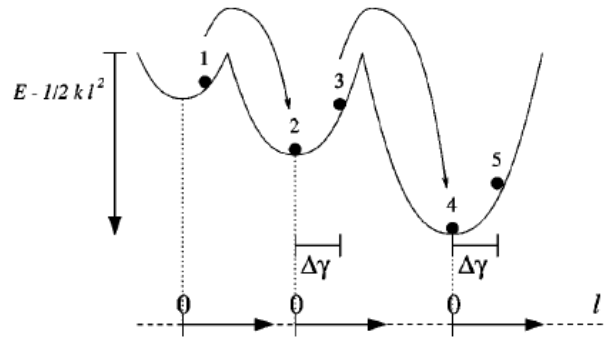


Figure 2.15 – Sketch of the aging (hopping) dynamics in the soft glassy rheology (SGR) model of Sollich and co-workers. Figure taken from [184].

into mesoscopic elements which, at rest, have an average zero local strain $l = 0$. Under an external macroscopic strain γ , each element can strain relative to its local equilibrium state and eventually yield above a critical yield strain l_y , thus relaxing stress (Figure 2.15). The model assumes that the deformation is locally affine, that is, it follows the macroscopically imposed strain, $l = \gamma$. Associated to the local critical deformation, one can define a yield energy $E_y = k/2 \cdot l_y^2$, where k is an elastic constant of the isolated elements. Next, the energy landscape of a material at any time t is assumed to consist of a spatially uncorrelated, time-invariant distribution of traps $\rho(E_y, t)$. The use of a distribution of well depths, instead of a single value, is assumed to mimic the inherent disorder of the microstructure. Finally, the evolution of the probability, $P(E_y, t)$, for a given element to be in a trap of depth E_y at time t is governed by thermally activated hopping. This means that, when activated, each element can “hop” to another trap, as shown in Figure 2.15. The hopping mechanism deserves special attention. Under an external strain γ , the hopping frequency

$$\tau = \tau_0 e^{\frac{E_y - k/2 \cdot l^2}{x}} \quad (2.34)$$

is controlled by $E_y - k/2 \cdot l^2$, the local activation energy barrier, and by (indirect) interactions between different elements, modeled by an effective temperature x . Aging effects are found when the distribution of traps, $\rho(E_y, t)$, have an exponential tails, analogous to Bouchaud’s model for aging dynamics in glassy systems. Observe that in the SGR model, the uncorrelated distribution of well depths implies that there is no direct interactions (i.e. mediated by an interaction potential) between the particles/aggregates. Note also that the term “thermally activated hopping” is somewhat misleading. Thermal energy can be small compared to typical trap depths E_y —in this case, the dynamics is triggered by elastic interactions within the sample, and not by pure thermal motion: a rearrangement (bond breakage) somewhere propagates and causes rearrangements elsewhere. Hence, also when thermal fluctuations are weak, stress heterogeneities frozen-in upon quench can still partially relax through elastically driven rebounds.

2.4.4 General remarks

We have reviewed the general literature on gelation, thixotropy and aging, and we have seen that structural evolution (i) is a quite general phenomenon to explain the time-dependence of the mechanical properties of colloidal suspensions, and (ii) has been an active and important field of research in the last decades. The classical literature on thixotropy and aging, perhaps surprisingly, rarely mentions the possible time-evolution of thermally irreversible interparticle contacts, despite the fact that systems with strong interactions are ubiquitous in industrial processes (concrete casting, drilling muds etc.) and natural phenomena (debris flows etc.). Although the idea that other physical phenomena which do not occur at the particle scale, such as frictional aging, may also produce mechanical aging [123], this possibility has not been yet explored deeply.

The currently prevailing viewpoint, we think, follows from the considerable progresses made in recent decades in studies that access structural evolution in dense suspensions where the attraction energy between the particles is absent, or of the order of $k_B T$. Initially, this progress has been possible thanks to the interplay between the advancement in imaging techniques, e.g. confocal microscopy, and in the design of well characterized index-matched model systems. Among them, the hard sphere system of Pusey and van Megen [163] (sterically stabilized PMMA particles in index- and density-matched organic solvent) and, subsequently, the colloid-polymer attractive system, have been instrumental in shaping our current view on glasses, because they have facilitated the direct comparison between experiments, theory and simulations. Analogously, our comprehension on dynamical arrest at lower packing fractions ($\phi \sim 10 - 40\%$) has benefited from the works on these index-matched depletion gels [50, 159, 162], where vdW forces and contact formation are fully suppressed. For these weakly attractive systems, particle bonds can reversibly break and form many times during the course of an experiment, and time-dependent mechanical responses and aging can be easily associated to structural evolution.

Turbid suspensions, where strong van der Waals forces are at play, are not suited to be imaged with a confocal microscope. For such systems, hence, other techniques are called for. Despite recent improvements on light scattering techniques, such as dynamic light scattering (DLS) [35, 1, 58], multi-sparkle diffusing wave spectroscopy (MSDWS) [16], and x-ray photon correlation spectroscopy (XPCS) [32], have allowed the study of aging in concentrated suspensions to some extent, their application for packing fraction around $\phi = 30\%$ remains scarce and limited to sterically stabilized suspensions [87, 80]. Experiments on very dilute systems have demonstrated that the dynamics keeps evolving in time also long after solidification [35, 16, 37, 58], but these range of particle concentrations is quite far from the packing fractions we are interested in ($\phi > 30\%$), for which no exhaustive characterization of aging and structural evolution exists.

Hence, at intermediate ϕ , roughly between 20% and 50%, the conditions under which gels form, and how the dynamical transition and the solid-like rheology are connected, remain to be elucidated. For glassy suspensions, this relationship is usually well described by mode-coupling theory [174]. In dilute gels, it can be interpreted in terms of fractal models [158] and by analyzing the thermal fluctuation of the normal modes of the aggregates [107]. However, the extension of both approaches for

dense suspensions is questionable. Additionally, aging phenomena are non explicitly considered, and the existence of an analogy between the dynamics of moderately concentrated suspensions and glassy systems is not fully clarified [87].

Materials and Methods

Contents

3.1	Suspension preparation and characterization	48
3.1.1	Stöber synthesis	48
3.1.2	PMMA particles	50
3.1.3	Particle size analysis	50
3.1.4	Zeta potential	52
3.1.5	Particle interactions	55
3.1.6	Suspension preparation	58
3.2	Macroscopic characterization: Rheometry	61
3.2.1	Rheometry in Couette geometry	62
3.2.2	Oscillatory rheology	63
3.2.3	Experimental procedure	64
3.2.4	Shear modulus	66
3.2.5	Yield stress	66
3.2.6	Rheometry cycle	67
3.2.7	Main results: silica suspensions	68
3.2.8	Main results: PMMA suspensions	70
3.2.9	Elastic modulus vs yield stress	72
3.3	Structural characterization: Confocal Microscopy . .	76
3.3.1	Working principle	76
3.3.2	Experimental limitations	79
3.3.3	Results	80
3.3.4	Aging	88

3.1 Suspension preparation and characterization

3.1.1 Stöber synthesis

In 1968, Stöber and co-workers showed that, by means of hydrolysis of alkyl silicates and subsequent condensation of silicic acid in alcoholic solutions, monodisperse silica particles in the colloidal size range can be easily produced [186]. The method consists in the hydrolysis and condensation of tetraethyl orthosilicate (TEOS) with water/ethanol solutions in the presence of ammonia as a catalyst. During the reaction, small seed nanoparticles form and gradually aggregate to form larger, macroscopic, usually porous particles. In the original synthesis protocol [186], a single growth step is performed by a one-step addition of TEOS into a solution of ethanol, ammonium hydroxide and deionized water. The vessel is placed in a constant temperature bath and fitted with a magnetic stirrer. This yields particles with maximum size in the submicrometric range (few hundred of nm) and usually with a broad size distribution [56]. As large monodisperse particles (typically above 1 μm) are difficult to synthesize by this procedure, alternative methods have been proposed in the last 50th years. Bogush et al. [18] used a seeded growth technique for preparing larger particles and increasing solids mass fraction. The technique lies in the consecutive addition of TEOS to a suspensions already containing silica nanoparticles (seeds), prepared as described above. Particle size up to 900 nm, with a narrow size distribution, can be easily achieved, but the extension of the method to higher sizes is limited by the presence of secondary nucleation, which leads to bidisperse samples. To avoid the formation of a second population, it is necessary to add TEOS by small fractions over a long period of time, which further complicates and lengthens the experiments. To overcome these difficulties, a so-called semibatch process (continuous addition), in which the system reactants feed into a reactor at a constant flow rate, is also applied [18, 117, 104, 56, 142]. This technique drastically reduces the synthesis time. Moreover, because of the slow rate of reaction of hydrolysis, the continuous addition is claimed to give greater control over the resulting particle size, shape, and size distribution [56, 142]. Precipitation parameters, such as reaction temperature [18, 117], TEOS/EtOH/H₂O concentration ratios used in the recipe [76], reaction time [56] and rate of addition [142] affect the resulting particle size, size distribution and morphology. In practice, hence, the Stöber synthesis may be affected by a great number of experimental conditions. In order to reduce the number of free parameters and to produce particle above 1 μm , a semibatch process, wherein one controls only the rate of addition of TEOS, seems to be the far most simple and straightforward technique.

Experimental protocol

Here, we use a fast semibatch synthesis proposed in [104]. This procedure permits a reduction of the time of physical contact between reactants and the plastic of the vessel, and guarantees the production of important amount of silica solid mass fraction.

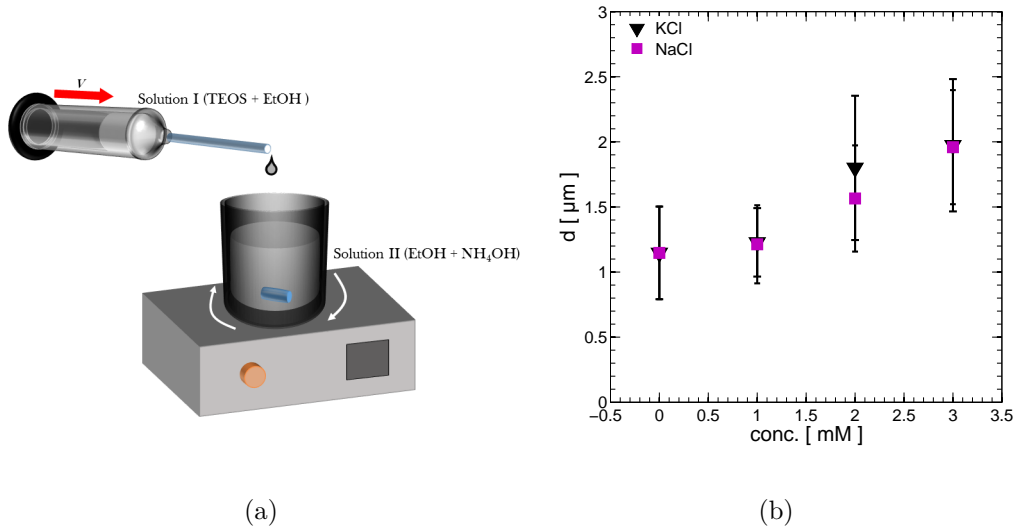


Figure 3.1 – (a) Schematic representation of the device used to synthesize silica particles. (b) Particle size versus electrolyte concentration, for two different cations and same rate of addition 1.1 mL/min. The other experimental conditions are held fixed (Table 3.1).

Table 3.1 – Experimental conditions according to [104].

Product	solution I (mL)	solution II (mL)
TEOS	80	0
EtOH	230	800
NH ₄ OH	0	170

TEOS ($\text{Si}(\text{OC}_2\text{H}_5)_4$, 99%, Aldrich Chemical Co.), ethanol (EtOH, Analar NORMAPUR, 99.9% v/v), and ammonia hydroxide (NH_4OH , 28%, Analar NORMAPUR) are used as reactant materials without any further purification. Two solutions, I (TEOS in ethanol) and II (ammonia in ethanol), are prepared separately. By means of a syringe pumps (Harvard Apparatus), the solution I is added at a constant flow rate into a plastic vessel that contains solution II, under stirring. A diagram of the apparatus is shown in Figure 3.1(a). After the end of the withdrawal, the solution is left under stirring 2 hours until total consumption of the reactants. All the experiments are performed at ambient temperature, yet the reaction temperature is not precisely controlled due to experimental difficulties. The product concentrations in the recipe are reported in Table 3.1.

According to Nowaza and co-workers [142], the final particle size is primarily controlled by the rate of addition of TEOS, all other parameters being constant:

$$d \simeq A \cdot v^{-0.32} \quad (3.1)$$

where d is the particle diameter in μm , v the velocity of addition in mL/min and A a temperature dependent constant. Since the flow rate can be carefully controlled by the syringe pump, we tentatively follow Equation (3.1) to produce particles in the

desired range. Surprisingly, although monodisperse particles are always produced, we are not able to control the final size by changing the flow rate of the reactants, while fixing the other experimental conditions. Furthermore, for any given addition rate, the results are hardly reproducible and appear to do not correlate with variations in room temperature. As a consequence, we decide to keep v constant at 1.1 mL/min, as originally proposed in [104]. In these conditions, each synthesis yields a monodisperse particle batch, with a size ranging between 0.8 and 1.2 μm . At the end of the synthesis, particles are washed by centrifugation (5000 rpm during 5 min) several times with ethanol 96% (GPR Rectapur VWR) and with de-ionized water (Aquadem 18M) to eliminate impurities and solvents. They are finally dried at 60 °C for 12h and sorted according to their measured size.

In order to systematically produce particles above 1.2 μm , we employ a recent semibatch technique which consists in adding of small amounts of salt into solution II [137]. The salt promotes particle coagulation in early reaction stage by reducing their surface potential due to cation adsorption. We add small amount of KCl and NaCl to our solutions, in the range 1-4 mM, whilst fixing the other parameters. The results of the synthesis, versus electrolyte concentration, are shown in Figure 3.1(b). As illustrated, the particle diameter (measured by DLS), increases with the amount of salt introduced in solution II, for both cations. As a drawback, adding more and more salt leads to an increase in particle polydispersity, as already noted in [137]. However, we anticipate that the error bars in Figure 3.1(b) are significantly overestimated. This is caused by spurious effects (sedimentation, presence of aggregates) that lead to erroneous estimates of the size distribution in the dynamic light scattering measurements (see section Section 3.1.3). The final diameters are little affected by the salt type, suggesting that cation hydrated radius does not play a major role in the kinetic of particle growth, in contrast with the expectations of Nakabayashi and co-workers [137].

3.1.2 PMMA particles

PMMA particles are purchased from MicroBeads (Spheromers CA3). Particle sizes are distributed around 3 μm with a 15% polydispersity. The particles are washed several times with ethanol and deionized water before use.

3.1.3 Particle size analysis

Dynamic light scattering (DLS)

Dynamic light scattering (DLS) is a non-invasive technique for measuring the size of sub-micron particles and macro-molecules. DLS is based on the dynamic analysis of coherent light scattered by particles in dilute suspensions. For a particle undergoing Brownian motion, the intensity of the scattered light fluctuates at a rate that depends upon its size. By measuring the decay of the intensity autocorrelation function of the fluctuating light, the diffusion coefficient of the particles can be extracted, and the average (hydrodynamic) radius a measured through the

Stokes-Einstein equation:

$$D = \frac{k_b T}{6\pi\eta a} \quad (3.2)$$

where $k_b T$ is the thermal energy and η the solvent viscosity (refer to [Appendix A](#) for more details).

We use a standard DLS instrument ZetaSizer Nano, supplied by Malvern. Silica particles are diluted in deionized water at a low volume fraction $\phi < 0.01\%$ to avoid multiple scattering. The suspensions are placed in standard disposable size cuvettes and illuminated by the laser.

As discussed in [Appendix A](#), DLS results can be affected by various effects like sedimentation and presence of aggregates. Sedimentation, in particular, is expected to be important in our measurements, especially for particles above $1\ \mu\text{m}$, due to the strong density mismatch between silica and water. To limit sedimentation effects, we performed several measurement runs, each of them comprising at least 5 short data acquisitions of typical duration of 60 s. For each batch of particles, the data obtained from different runs are then averaged. To limit the effects of particle aggregation, we analyze the data in terms of number density distribution (see [Appendix A](#)).

Particle sizes in the range $0.5\text{-}1.9\ \mu\text{m}$ are produced and then analyzed through DLS. Quite generally, the technique returns an average polydispersity ranging from $\sim 10\%$ to $\sim 20\%$ as the size of the particles increases. However, we do not attribute this trend only to an intrinsic result of the Stöber synthesis, but rather to an increasingly effect of sedimentation, which introduces a drift velocity to the motion of the particles. In addition, the technique itself has an inherent $10\text{-}15\%$ band spreading, which leads to an overestimation of the polydispersity [96].

Scanning Electron Microscope (SEM)

We also use scanning electron microscopy (SEM) to estimate the size of our silica particles. Due to the high resolution of the instrument (up to few nm), the size distribution can be characterized with high accuracy.

The particles are firstly diluted in water at low volume fraction. They are then deposited by drop-casting technique onto a conductive substrate, which is placed inside the SEM chamber after complete evaporation of the solvent. SEM analysis is performed by field-emission gun SEM (Zeiss Neon 40 EsB FIB-SEM), equipped with an Everhart-Thornley detector for collection of secondary electrons (SEs). To prevent charge accumulation at the surface, dielectric samples are usually sputter-coated with a conductive layer prior to be loaded in the SEM chamber. Here we adopted a different strategy, consisting in an electron bombardment carried out at low primary electron energies. In these conditions, it can be shown that charge accumulation is drastically reduced [19]. As explained in [Appendix B](#), we use a beam energy close to the first crossover energy E_1 —around 1 keV for Stöber silica—which is more efficient than E_2 in preventing charging under a constant electron beam.

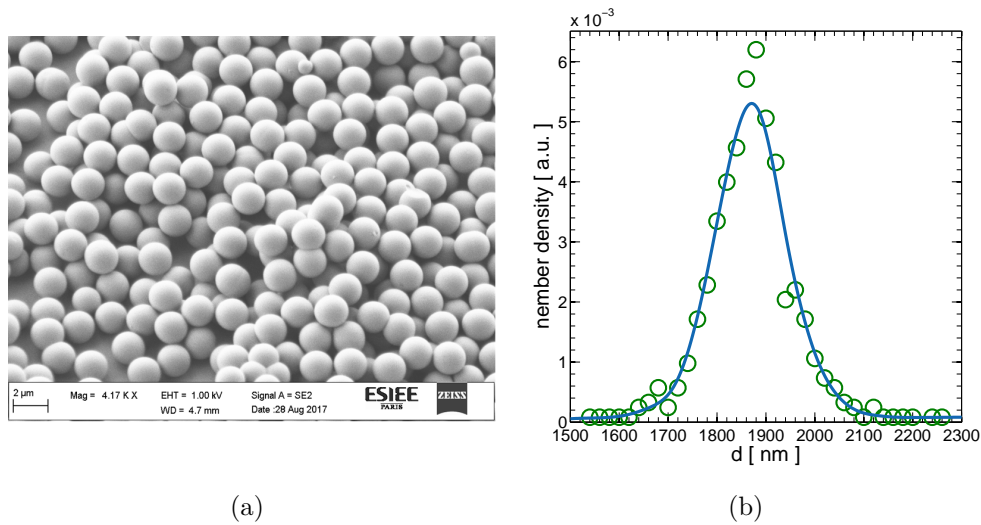


Figure 3.2 – (a) SEM micrograph of 1.9 μm silica particles. (b) Size distribution measured by analysis of SEM images.

To measure the size of the particles, several SEM snapshots are acquired and then analyzed by means of a standard Matlab algorithm (function *imfindcircles*, <https://fr.mathworks.com/help/images/ref/imfindcircles.html>). The script directly returns the center and the radius of each particle within the field of view. We report in Figure 3.2(a) a typical SEM micrograph of the largest particles used in this work. As illustrated in Figure 3.2(b), by analysis of this and additional images, we find a mean particle diameter of $d = (1860 \pm 90)\text{nm}$, corresponding to a polydispersity of $\sim 5\%$. We then compare the corresponding size distribution with the dynamic light scattering estimate, $d = (1950 \pm 350)\text{nm}$, corresponding to a polydispersity of $\sim 18\%$. Although the mean value is approximately the same, the results clearly show that DLS overestimates the polydispersity, especially for particles above 1 μm.

3.1.4 Zeta potential

We now investigate the surface properties of isolated silica particles in saline solutions containing CaCl_2 . In Section 2.2.2, we explained that there exist an electric double layer around a charged particle in solution. Consider now the liquid adjacent to that particle under the influence of an external electric field. The electric field will generate a motion of the ions in opposite directions; if the particle is negatively charged, the positive counterions will move towards the anode, while the negative co-ions towards the cathode. This causes the particle to move, and this motion virtually defines a plane of shear, at a distance δ_s from the surface, which separates the stationary layer of fluid attached to the dispersed particle and the rest of the solution. The zeta potential ζ is defined as the electric potential at the location of this shear plane, relative to the bulk solution. It quantifies only the charge inside δ_s and not its absolute surface charge, and therefore it does not coincide neither with the Stern potential —at the outer Helmholtz plane (OHP)—nor with the double layer potential (at the boundary between the double layer and the bulk). Nevertheless,

there is a considerable body of evidence that the shear plane lies very close to the OHP [94], so that ζ is good estimate for the surface potential Φ_s . This approximation will be used to calculate the interaction energy between our particles.

The zeta potential is a key indicator of the stability of a colloidal suspensions because it indicates the degree of electrostatic repulsion between the charged particles. It depends strongly on the ionic strength and pH of the solution, since both a change in the ion concentration and in the degree of surface dissociation affect the charge density at the particle surface. It is usually measured by means of electrophoresis experiments, *viz.* by recording the (electrophoretic) mobility μ_m of the particles under a known external electric field. Assuming equilibrium between electrostatic and viscous forces, and a Boltzmann distribution for the ions around the particles, it can be shown that [183]:

$$\mu_m = -\frac{\epsilon_0 \epsilon \zeta}{\eta} \quad (3.3)$$

where η is the viscosity of the solvent.

We measure ζ with a Zetasizer nano ZS supplied by Malvern. The instrument uses electrophoretic light scattering to assess the mobility of the particles, through Laser Doppler Velocimetry (LDV) technique. Silica particles are diluted in deionized water at various salt concentrations and very low volume fractions $\phi < 0.01\%$ to avoid multiple scattering. The suspensions are injected into disposable cuvettes equipped with two electrodes at either end, allowing for the application of an external electric field. The rate of intensity fluctuations of the scattered light is measured and afterwards related to the particle velocity, in analogy with DLS. In Figure 3.3

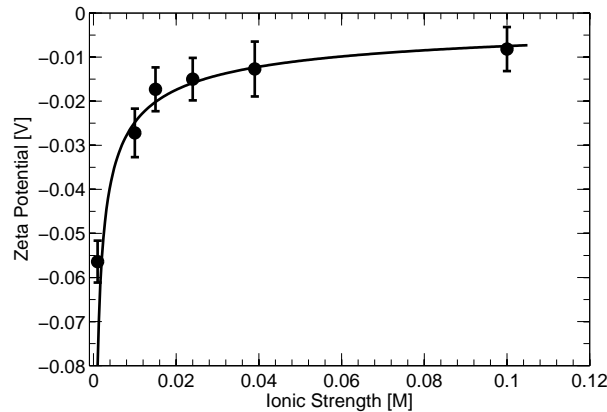


Figure 3.3 – Zeta potential for 1 μm silica particles versus ionic strength, in CaCl_2 solutions. The solid line is a fit of the linearized Stern equation to the data.

we report the zeta potential versus CaCl_2 concentration. The latter is expressed in terms of ionic strength I , defined as

$$I = \frac{1}{2} \sum_i c_i \cdot z_i^2 \quad (3.4)$$

where c_i and z_i are the molar concentration and valence of ion i , respectively. As

illustrated, ζ is strongly affected by even a small amount of salt. Above $I = 0.05$ M, the potential saturates to small values around -10 mV. At this and higher electrolyte content, the conductivity of the solution increases and the applied voltage is automatically lowered by the instrument to values < 10 V, to prevent damages of the electrodes. In addition, according to Equation (3.3), the mobility of the particles is strongly reduced as the surface potential decreases. In these conditions, both electroosmosis flow and sedimentation dominate the motion of the particles and hence perturb the results. We are thus forced to limit the measurement to I below 0.1 M.

The trend in Figure 3.3 can be approximately explained by considering the adsorption of Ca^{++} cations to the silica surface. To proceed, we use a linearized Stern equation, as in [147]. First, we recall that the surface charge density is related to the potential by the Grahame equation (Equation (2.18)). Since in our range of ionic strengths $|\zeta| < 25$ mV almost everywhere, the Debye-Huckel approximation holds, and predicts:

$$\sigma = \left(\frac{e\zeta}{k_b T} \right) \sqrt{2000 N_a \epsilon_0 \epsilon k_b T \cdot I} \quad (3.5)$$

where N_a is the Avogadro number (σ now denotes the charge density within the shear plane, where we define the zeta potential). Next, we assume a Langmuir adsorption isotherm where each Ca^{++} is adsorbed to the deprotonated silanols according to [95]:



As a result, the particle surface can be considered as a two dimensional array of discrete positive SiOCa^+ , neutral SiOH , and negative SiO^- sites. The Langmuir adsorption can be written in term of the concentration of cations $[\text{Ca}^{++}]$ at the particle surface, the surface density of unoccupied sites $\{\text{S}^-\}$ and the intrinsic association constant K :

$$\{\text{C}^{++}\text{S}^-\} = K[\text{Ca}^{++}] \{\text{S}^-\} \quad (3.7)$$

where $\{\text{C}^{++}\text{S}^-\}$ is the surface density of associated states bringing a positive charge +1. The total number of negative adsorption sites is the sum of occupied and unoccupied sites:

$$\{\text{S}\}_{\text{tot}} = \{\text{C}^{++}\text{S}^-\} + \{\text{S}^-\} \quad (3.8)$$

and the total charge at the surface is

$$\sigma = e(\{\text{C}^{++}\text{S}^-\} - \{\text{S}^-\}) \quad (3.9)$$

Like in the charge regularization scheme, we further assume a Boltzmann distribution for the cations

$$[\text{Ca}^{++}] = [\text{Ca}^{++}]_{\infty} e^{-2e\zeta/k_b T} \quad (3.10)$$

where $[\text{Ca}^{++}]_{\infty}$ is the bulk cation concentration. Using again the Debye-Huckel approximation and combining Equations (3.7) and (3.8) we obtain:

$$\sigma = \frac{e\{\text{S}\}_{\text{tot}} (K \cdot I(1 - 2e\zeta/k_b T) - 3)}{3 + K \cdot I(1 - 2e\zeta/k_b T)} \quad (3.11)$$

Equations (3.5) and (3.11) are used together to extract ζ as a function of the ionic strength. The experimental data are then fitted with $\{S\}_{\text{tot}}$ and K as fitting parameters, and the result is reported in Figure 3.3 (solid black line). The model captures quite well the zeta potential versus I behavior; the fit returns $\{S\}_{\text{tot}} = (0.04 \pm 0.02)\text{nm}^{-2}$. This value can be compared to the maximum silanol density of fully hydrated silica $\approx 4\text{nm}^{-2}$ [95]. The fraction of dissociates sites is thus small, around $\alpha = 1\%$. Using the mass action equation [99] for the dissociation constant of silanol in water at $pH \approx 7$

$$K_d = \frac{\alpha}{1 - \alpha} \cdot 10^{-pH} \cdot e^{-e\zeta_0/k_bT}, \quad (3.12)$$

and the measured ζ_0 value at vanishing divalent salt concentration, it follows that $K_d = 10^{-7.5}\text{M}$ ($pK = 7.5$), a reasonable value [157]. The calculation suggests that only a small fraction of silanols dissociates at normal pH conditions, the rest of which probably forms a strong network of hydrogen bonds with water molecules [26, 222].

3.1.5 Particle interactions

The first part of this section is devoted to the estimate of the forces between our silica particles when dispersed in electrolyte solutions.

DLVO potential in CaCl_2 solutions

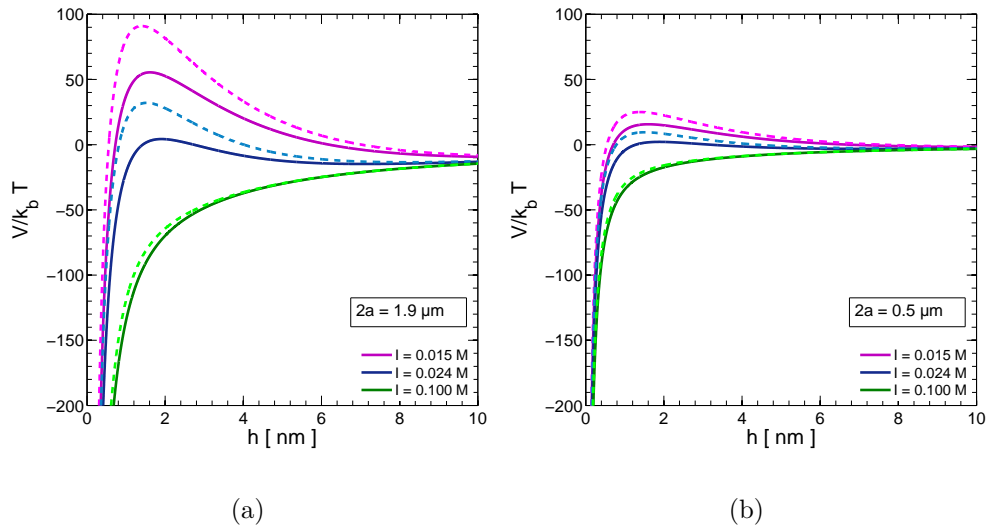


Figure 3.4 – DLVO potentials for our silica particles with (a) $2a = 1.9 \mu\text{m}$ and (b) $2a = 0.5 \mu\text{m}$ for different I values (colors). The curves are computed with either offset $h_{\text{off}} = 0$ (solid) and $h_{\text{off}} = 5 \text{ \AA}$ (dashed).

We have seen that, in the absence of contact, i.e. beyond distances of order a nanometer, the pair interaction between two colloidal particles of equal radius a in

asymmetric electrolytes is known to be captured by the DLVO expression [98]:

$$V_{DLVO}(h) = -\frac{A_H}{6} \left[\frac{2a^2}{h(h+4a)} + \frac{2a^2}{(h+2a)^2} + \ln \left(\frac{h(h+4a)}{(h+2a)^2} \right) \right] + 2\pi a \epsilon_0 \epsilon \Phi_s^2 e^{-\kappa h} \quad (3.13)$$

where $A_H = 8.3 \cdot 10^{-21} \text{J}$ [86, 128] is the non-retarded Hamaker constant, h the gap between particle surfaces, Φ_s the surface potential, approximated with the zeta potential ζ [94], and $\kappa^{-1} = 0.304/\sqrt{I}$ the Debye length in nm. This expression is valid in the Debye-Huckel approximation, which requires the electrostatic energy to be small compared to the thermal energy, i.e. $|\Phi_s| \ll 25 \text{mV}$.

The particle charges have been measured by zetametry using electrophoretic light scattering and the results are reported in Section 3.1.4 for ionic strengths up to $I = 0.1 \text{M}$. Such figure shows that $|\Phi_s|$ rapidly decreases with increasing I and that $|\Phi_s| \simeq 25 \text{mV}$ when $I = 0.015 \text{M}$, so that the Debye-Huckel approximation is reasonable for this and higher ionic strengths. Equation (3.13) is thus reported in Figure 3.4 for the largest and smallest silica particles used in this work. In the left figure we plot the DLVO calculation for $2a = 1.9 \mu\text{m}$ particles using $I = 0.015, 0.024$ and 0.1M and approximating the surface potentials with the measured zeta potential values (solid colored lines). At small I this interaction displays a peak that limits contact formation; at the largest ionic strength, however, the peak disappears and the interaction is attractive at all distances. In Figure 3.4(b) we report similar interaction potential computations for the smaller particles, $2a = 0.5 \mu\text{m}$. The plots clearly show that energy barriers are absent for $I > 0.1 \text{M}$.

Many studies pointed out the possible existence of non-DLVO short-range repulsive contributions to the interaction potential [204, 26, 149, 199, 13]. These additional forces are ascribed either to solvation or steric hindrance due to protruding hydrated silica hairs at the particle surface. They are usually accounted for by considering that the outer Helmholtz plane (OHP), i.e. the plane of origin of the electrostatic interactions, is located a few \AA outward from the contact plane, $h = 0$ [204]. To test for this effect, we also report in Figure 3.4 the DLVO interaction as computed using an offset $h_{\text{off}} = 5 \text{\AA}$ (dashed curves in corresponding colors), a reasonable upper value. We see that the uncertainty about the offset values does not change the fact that the barrier that limits contact formation is absent for $I = 0.1 \text{M}$, and hence for all higher I values.

DLVO potential in glycerol/water mixtures

Suspensions of silica particles in water are opaque due to the strong refractive index mismatch between silica ($n = 1.458$) and pure water ($n = 1.333$). Part of the aging characterization of the suspensions will be performed via imaging of their structure under a confocal microscope. For such experiments the index mismatch will preclude imaging beyond a few particle layers inside the material. In order to increase the suspension transparency, the interstitial fluid index will be modified by addition of glycerol ($n=1.475$). We thus investigate, here, the forces acting between our silica particles in water/glycerol mixtures. To proceed, we need to know how the Hamaker constant A_H of silica across the mixtures is modified by the presence of glycerol, as

Table 3.2 – Some properties of water, glycerol, silica and PMMA at ambient temperature. From left to right: density, refractive index, relative permittivity and viscosity.

System	ρ (g/mL)	n	ϵ_r	η (Pas)
Water	0.998	1.333	78.4	$0.98 \cdot 10^{-3}$
Glycerol	1.261	1.475	47	1.17
Silica	1.94 ± 0.05	1.458	3.9	/
PMMA	1.18	1.490	3.6	/

Table 3.3 – The Hamaker constant of silica particles interacting across a glycerol-water mixture as a function of glycerol mass concentration.

C_m (%)	0	30	40	50
A_H (J)	$9.1 \cdot 10^{-21}$	$5.9 \cdot 10^{-21}$	$4.9 \cdot 10^{-21}$	$4.0 \cdot 10^{-21}$

a function of its mass concentration C_m . We first estimate the refractive index and relative permittivity of the interstitial fluid using the Lorentz-Lorenz equations:

$$\frac{n_m^2 - 1}{n_m^2 + 2} = (1 - \phi_g) \cdot \frac{n_w^2 - 1}{n_w^2 + 2} + \phi_g \cdot \frac{n_g^2 - 1}{n_g^2 + 2} \quad (3.14)$$

where ϕ_g is the glycerol volume fraction, n_m , n_w and n_g are the refractive indexes of the mixture, water and glycerol, respectively. Equation (3.14) is evaluated using common values for n_w and n_g , taken from standard databases. These values, and other constants used in this work, are reported in Table 3.2. Note that the density of silica has been measured through pycnometer method. To calculate the Hamaker constant A_H , we then use an approximate expression based on the Lifshitz theory (see [98]):

$$A_H = \frac{3}{4} k_b T \left(\frac{\epsilon_s - \epsilon_m}{\epsilon_s + \epsilon_m} \right)^2 + \frac{3h\nu_e}{16\sqrt{2}} \frac{(n_s^2 - n_m^2)^2}{(n_s^2 + n_m^2)^{3/2}} \quad (3.15)$$

where $h\nu_e = 3 \cdot 10^{-18}$ J, ν_e being a typical atomic vibration frequency, ϵ_s and n_s are the relative permittivity and index of refraction of silica, respectively. Equation (3.15) is evaluated at various C_m , and the results reported in Table 3.3. As expected, A_H decreases as the glycerol mass content increases. The lowering of the Hamaker constant implies a reduced amplitude in the vdW attraction. We also note that A_H calculated at vanishing glycerol content is close to the value used previously in pure water, $8.3 \cdot 10^{-21}$ J [86, 128].

We plot in Figure 3.5(a) the DLVO potential energy for $I = 0.1$ M, calculated according to the Hamaker constants in Table 3.3 and assuming that the electrostatic interactions are not substantially affected by the presence of glycerol [3]. We compare the results with the potential energy obtained in the pure water case (solid line). Clearly, for this specific I , the reduced strength of vdW attraction only slightly changes the potential energy profile, which remains attractive for all separations (no energy barriers). This remains true even if an offset of 0.5 \AA is added in the electro-

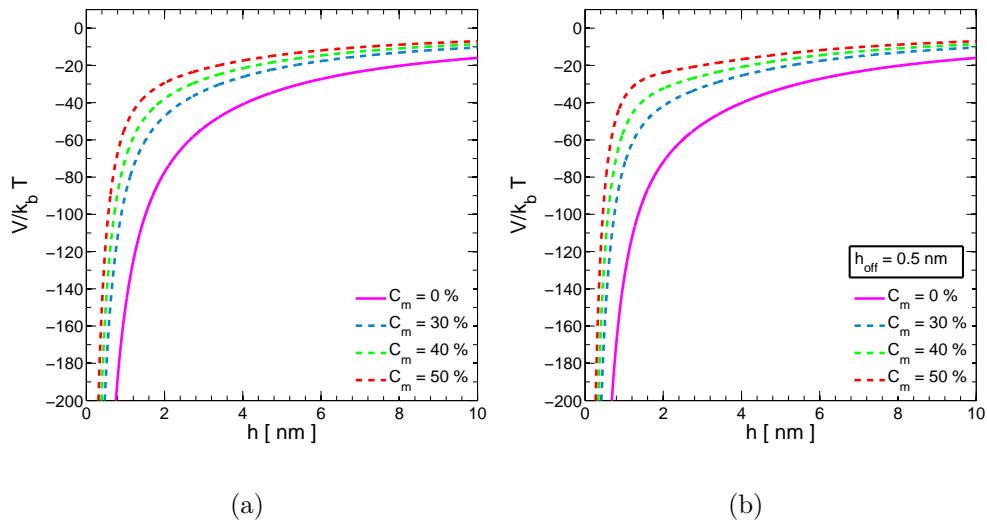


Figure 3.5 – DLVO potentials for silica particles in pure water (magenta solid line) and with increasing glycerol concentrations (dashed lines), for $I = 0.1 \text{ M}$ and $\zeta = -8 \text{ mV}$. (a) Without and (b) with a 0.5 \AA shift of the origin plane of the electrostatic double layer interactions.

static part of the potential, as discussed in Section 3.1.5 and shown in Figure 3.5(b). When the glycerol content varies in the range $[30, 50]\%$, hence, flocculation is not hindered by energy barriers for $I > 0.1 \text{ M}$.

3.1.6 Suspension preparation

Silica suspensions

The studied suspensions are thixotropic, their mechanical properties depend on the shear history and the time elapsed since their preparation in a given reference state. To aid experimental reproducibility, hence, they must be prepared following a rigorous protocol. This is achieved by applying the following procedure [73]:

- I) A small amount of dry silica powder (of known weight) is dispersed and left under stirring for several hours in large amount of deionized water (typically 200 g of water for 15 g of silica) to ensure full hydration of the particle surface.
- II) The dilute dispersion is then centrifugated at 5000rpm for 5min to eliminate the gross part of water.
- III) The necessary amount of water is added to the sediment according to the target packing fraction ϕ ; the suspension is then vigorously mixed by vortexer.
- IV) By means of a micro-pipette, a small amount of a batch salt solution ($[C] = 1 \text{ M}$) is added to reach the target ionic strength I . The suspension is again homogenized by stirring.
- V) To remove bubbles, the suspension is left in ultrasound bath for 3min.

The exact volume fraction is measured by weighting dry extract of small amount of each sample dried at $60 \text{ }^\circ\text{C}$ in an oven. A similar procedure is used for the

formulation of the suspensions in water-glycerol mixtures.

PMMA suspensions

A slightly different procedure is required for PMMA suspensions, as the hydrophobicity of the PMMA surface [111] complicates the dispersion process:

- I) The particles are dispersed in a great quantity of deionized water, left under stirring for 2 days to ensure a complete hydration of the surface and then allowed to sediment over night.
- II) The majority of the excess water along with some hydrophobic particles adsorbed at the air-liquid interface are removed with a syringe.
- III) The final volume fraction is reached by centrifugation of the sediment at 5500 rpm for 20 minutes, whereupon the proper amount of salt is added as described above.
- IV) Finally, after homogenization of the suspensions, 2 minutes of sonification are used to remove bubbles.

The removal of particles at the air-liquid interface (point II) usually leads to little control over the final volume fraction, which however only slightly departs from the desired one. For this reason, it was difficult to compare suspensions with different I and same ϕ .

Glycerol-water suspensions

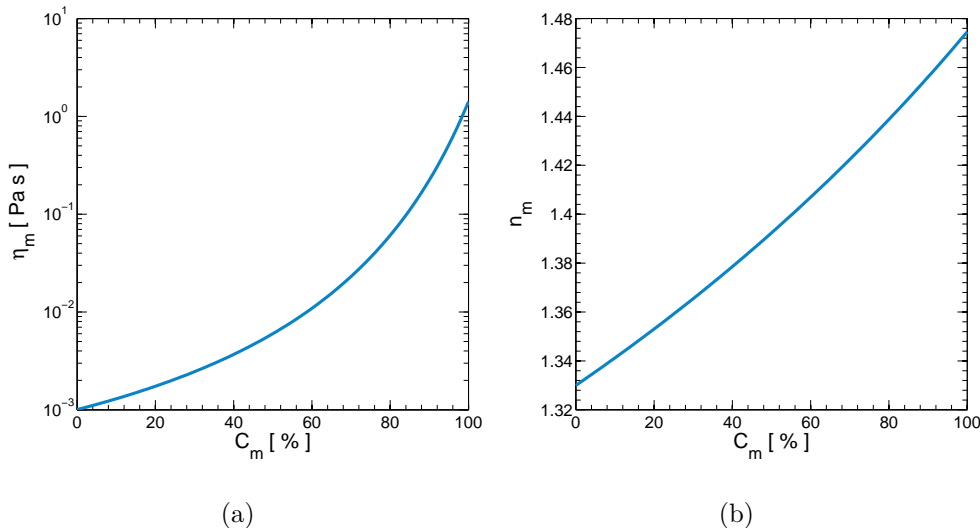


Figure 3.6 – Variation of viscosity (a) and refractive index (b) of water/glycerol mixtures as a function of glycerol mass concentration at ambient temperature.

In this part, we analyze the change in viscosity of water/glycerol suspensions as a function of the glycerol mass content. For the calculation, we use an empirical formula provided by Cheng [31], which compares well with experimental values [177].

According to the author, the viscosity η_m of the mixture is related to those of the two components by a power law:

$$\eta_m = \eta_w^\alpha \eta_g^{1-\alpha} \quad (3.16)$$

where α depends simultaneously on the glycerol mass concentration C_m and the temperature T :

$$\alpha = 1 - C_m + \frac{abC_m(1 - C_m)}{aC_m + b(1 - C_m)} \quad (3.17)$$

The parameters a and b vary with T according to

$$a = 0.705 - 0.0017 \cdot T \quad (3.18a)$$

$$b = (4.9 + 0.036 \cdot T)a^{2.5}, \quad (3.18b)$$

while the variations of the viscosity with temperature are approximated respectively as:

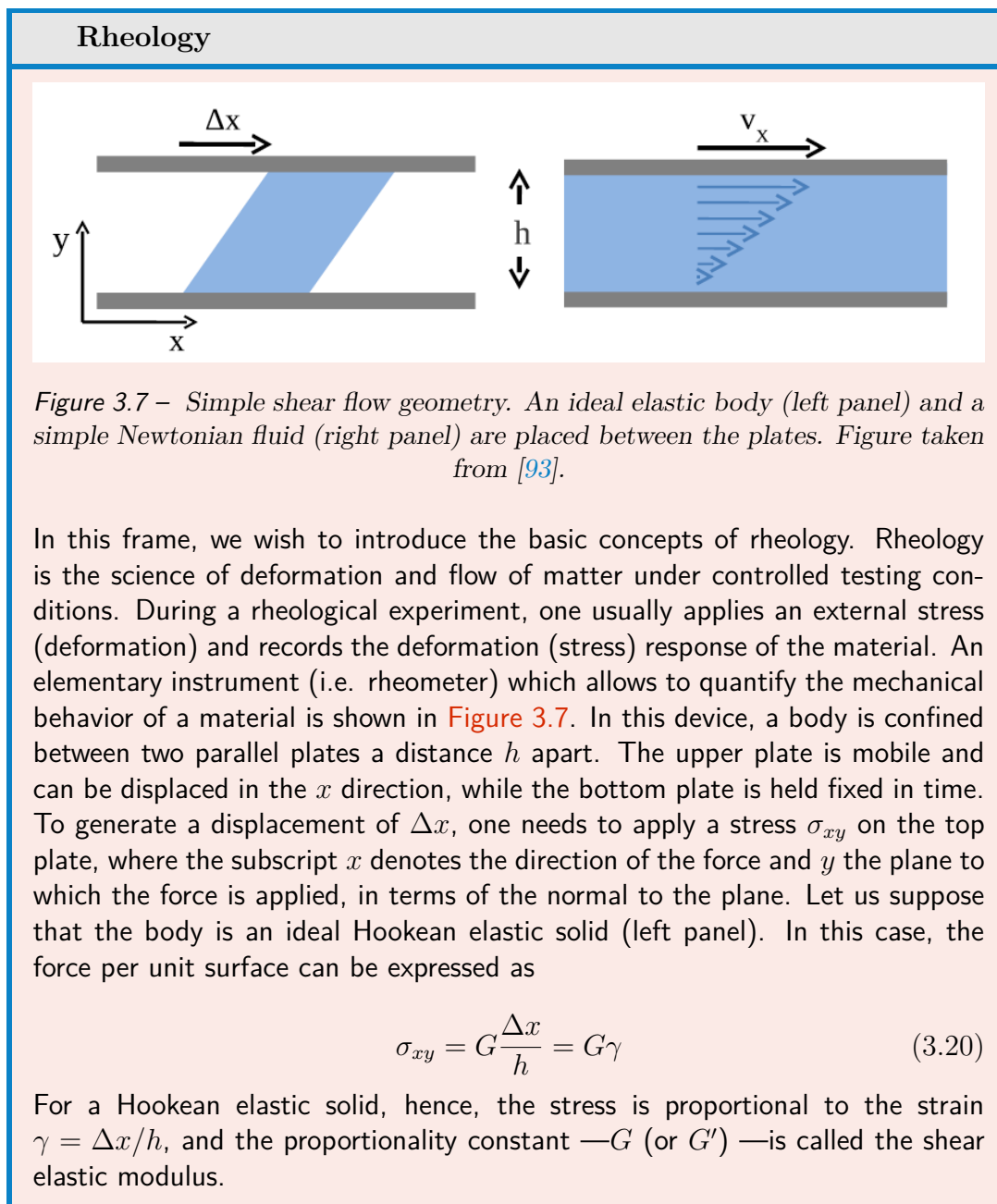
$$\eta_w(T) = 1.790e^{-(1230+T)T/(36100+360T)} \quad (3.19a)$$

$$\eta_g(T) = 12100e^{-(1233-T)T/(9900+70T)} \quad (3.19b)$$

The results are shown in **Figure 3.6(a)**. The viscosity does not increase dramatically for glycerol mass concentrations up to 50%; for instance, for a 60/40 wt% water/glycerol suspension we have $\eta_m = 3.7$ mPas, that is ≈ 4 times the viscosity of pure water, while for $C_m = 70\%$ we obtain $\eta_m \approx 23\eta_w$. According to **Equation (3.14)**, the glycerol mass fraction for which the refractive indexes are matched lies around $C_m = 91\%$, as shown in **Figure 3.6(b)**. Note that in these conditions, however, η_m is about 265 times the viscosity of water. To avoid a strong change of the solvent viscosity, confocal microscopy investigation will be carried out only for $C_m \in [30, 50]\%$. More importantly, this permits to study suspensions for which van der Waals forces are still substantial.

3.2 Macroscopic characterization: Rheometry

In this section, we use rheometry (see frame below) to investigate macroscopic mechanical aging of our suspensions. We first delineate the experimental setup and measurement protocols, and then illustrate the main results of mechanical aging. An important part of the data we report here have been obtained by Jennifer Fusier during her PhD thesis [72]. Using the same experimental protocol, additional data have been acquired during this work, and a similar aging characterization has been carried out with suspensions composed of PMMA particles. We thus only report the main aspects and implications of the macroscopic aging measurements and results, inviting the reader to refer to [72] for a more detailed presentation.



We now replace the perfect elastic material with a simple (Newtonian) fluid, like water, as shown in the right panel of [Figure 3.7](#). Suppose now that the upper plate is displaced at a constant velocity V . In absence of turbulent motion and slip at the wall, the boundary conditions require that the local velocity V_x along x varies linearly across the gap, as indicated by the arrows. In this case, the shear stress needed to maintain the constant velocity of the top plate is given by

$$\sigma = \eta \frac{\partial V_x}{\partial y} = \eta \frac{V_x}{h} = \eta \dot{\gamma}. \quad (3.21)$$

with $\dot{\gamma}$ the shear rate, the derivative over time of the (small) strain. For Newtonian fluids, hence, the stress is proportional to the shear rate; the proportionality constant —the viscosity coefficient η —expresses the resistance to flow in Newtonian fluids. A real material may exhibit both a viscous and an elastic behavior in response to external perturbations; in these conditions, it is termed viscoelastic.

3.2.1 Rheometry in Couette geometry

In the Couette geometry, the suspension is placed in the gap between two co-axial cylinders, as shown in [Figure 3.8](#). In a stress controlled rheometer, a known torque M_i is applied to the inner cylinder of radius r_i , while the outer cylinder of radius r_e remains fixed, and the rotation angle and/or velocity is recorded.

When inertia and edge effects are negligible, the shear stress at a distance r from

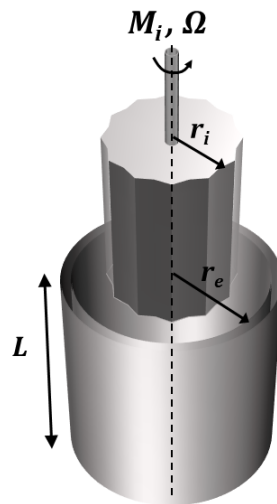


Figure 3.8 – A cartoon of the Couette geometry used in this work.

the axis of symmetry is

$$\sigma(r) = \frac{M_i}{2\pi L r^2} \quad (3.22)$$

where M_i is the prescribed torque to the inner tool and L is the height of the gap. In the gap, the velocity field is

$$v_\theta(r) = \omega(r) \cdot r \quad (3.23)$$

with $v_\theta(r)$ the radial velocity. In the limit of small deformation the strain γ can be written as

$$\gamma(r) = -r \frac{d\delta}{dr} \quad (3.24)$$

where, δ is the local angle of rotation, such as $\omega = \dot{\delta} = v_\theta/r$. Note that both the shear stress σ and the shear strain γ of a particular cylindrical layer of material depend on its distance r to the vertical axis; the shear stress decreases as one goes from the inner cylinder at r_i to the outer cylinder at r_e . This induces a strain heterogeneity in the gap.

The shear rate is

$$\dot{\gamma}(r) = -r \frac{d\omega}{dr} \quad (3.25)$$

where ω is the local angular velocity. The expression for $\dot{\gamma}(r)$ depends on the position of the material point within the gap. When $r_i/r_e > 0.99$, however, the shear rate can be assumed constant within the gap and a simple integration of [Equation \(3.25\)](#) gives

$$\dot{\gamma} = \frac{\Omega r_i}{r_e - r_i} \quad (3.26)$$

where Ω is the angular velocity of the inner tool. Then, the strain, uniform over the gap, can be expressed as

$$\gamma = \frac{\delta_i r_i}{r_e - r_i} \quad (3.27)$$

in which δ_i is the angle of rotation of the inner cylinder. In general, the condition of small gap is not met and stress heterogeneities cannot be neglected. The expression for the shear rate cannot be known unless one makes some hypothesis on the constitutive equation of the material.

3.2.2 Oscillatory rheology

The viscoelastic properties of the material under study are usually probed via oscillatory tests, in which one applies small amplitude strain oscillations

$$\gamma(t) = \gamma_0 \sin(\omega t) \quad (3.28)$$

and simultaneously records the stress response. In the case of an ideal elastic body, the stress follows the strain

$$\sigma(t) = G\gamma_0 \sin(\omega t), \quad (3.29)$$

that is, the response is in phase with the perturbation. For a viscous fluid, σ depends on the instantaneous shear rate $\dot{\gamma}(t) = \gamma_0 \omega \cos(\omega t)$ and one obtains:

$$\sigma(t) = \eta \gamma_0 \omega \sin(\omega t + \pi/2) \quad (3.30)$$

The shear stress response is now shifted by 90° with respect to the strain. In general, viscoelastic materials exhibit a phase shift between the two limit cases, i.e. 0° and 90° . Defining the stress response as

$$\sigma(t) = \sigma_0 \sin(\omega t + \phi) \quad (3.31)$$

where ϕ is the phase shift, and using classical complex notation for oscillatory systems, the response can be expressed as

$$\sigma^*(t) = G^* \cdot \gamma^* \quad (3.32)$$

where

$$G^* = G' + iG'' \quad (3.33)$$

is the so-called complex shear modulus, with:

$$G' = \frac{\sigma_0}{\gamma_0} \cos(\phi) \quad (3.34a)$$

$$G'' = \frac{\sigma_0}{\gamma_0} \sin(\phi) \quad (3.34b)$$

The in-phase or real part G' describes the elastic behavior of the material and is called the storage modulus. The out-of-phase or imaginary part G'' (shifted by 90°), the loss modulus, represents the viscous behavior. For a pure elastic material one recovers $G' = G$ and $G'' = 0$, while for a pure viscous liquid one obtains $G' = 0$ and $G'' = \eta\omega$. It should be pointed out that viscoelastic materials show time-dependency. As a consequence, both G' and G'' might depend on the applied shear frequency ω .

3.2.3 Experimental procedure

Rheometry is performed using a stress-controlled (Malvern Kinexus Ultra +) rheometer, in a thin gap Couette geometry (inner radius $r_i = 12.5 \text{ mm}$, outer cylinder radius $r_e = 13.75 \text{ mm}$, height $L = 37.5 \text{ mm}$) between rough cylinders to avoid slippage. The choice of a Couette geometry results from a compromise between different constraints: despite the need to use a larger experimental volume in comparison with other geometries (cone-plate, plate-plate or cone-plate), the Couette setup permits to reduce sedimentation and migration effects. Whereas in the cone-plate, plate-plate or cone-plate arrangements the load is applied from the top of the sample, i.e. the region the most affected by sedimentation, in the Couette geometry the torque is applied along the entire height of the cylinder. In these conditions, if the gravitational concentration gradient is small, the impact of sedimentation is limited. Measurements of sedimentation profile by MRI (Magnetic Resonance Imaging) of our suspensions can be found in ref. [72]. Thanks to the fact that yield stress stabilizes the suspensions against sedimentation, it was shown

that after a period of about 5h the volume fraction had only slightly increased at the bottom of the sample, while a thin layer of water appeared at the top. In the middle of the sample, however, the concentration was weakly modified. Bearing in mind that the duration of the measurements does not exceed 1h and 30 min, it is concluded that sedimentation does not significantly perturb the results [73].

In this thesis, we focus on two mechanical quantities of practical interest for applications: the elastic shear modulus G' , and the yield stress σ_y . Quite generally, both quantities may depend on a huge number of parameters, such as interaction strength, size, shape and polydispersity of the particles and viscosity of the solvent, to name a few. We use monodisperse spherical particles of radius a in pH neutral water (~ 7), control the interactions by changing the amount of salt in solution I , and study the mechanical properties of the suspensions as a function of resting (or aging) time t . Therefore, in our conditions, both G' and σ_y are a function of 4 main “parameters”:

$$G' = G'(t, I, \phi, a) \quad (3.35a)$$

$$\sigma_y = \sigma_y(t, I, \phi, a) \quad (3.35b)$$

with ϕ the solid volume fraction.

The rheometry protocol is designed to account for the time-dependent behavior of the suspensions. First, each sample is poured in the Couette geometry and pre-sheared at 200 s^{-1} during 5 min, to “erase” the preparation and setting history. In between different G' measurements, the samples are then rejuvenated by shearing, using the same $\dot{\gamma}$ for a duration of 3 min. This procedure permits to obtain a reproducible evolution of the shear modulus. Aging time t is counted after cessation of shearing, i.e., starting when the external torque applied on the Couette cell is set to zero. This slightly overestimates aging time, however, since a modest rotation of the inner cylinder remains measurable for about few (< 5) seconds. Anyway, the evolution of the shear modulus is not effected by this residual flow as long as $t \gg 5\text{s}$. Besides, the shear modulus G' is hardly measurable until about $t \simeq 10\text{s}$. In order to minimize drying effects, the geometry is surrounded by a wet sheet, as shown in Figure 3.9. All tests are conducted at ambient temperature.

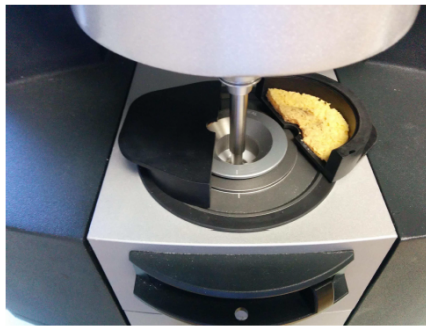


Figure 3.9 – Drying is limited by application of a wet sheet on the top of the Couette geometry.

3.2.4 Shear modulus

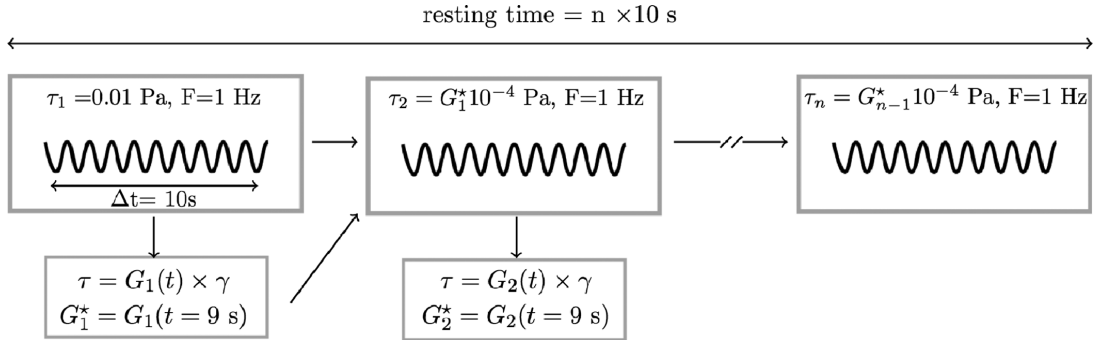


Figure 3.10 – The procedure we use to measure evolution of the elastic modulus as a function of time. F denotes the oscillatory shear stress frequency and n is the number of 10s-cycles in each sequence. Figure taken from [72].

To measure the shear elastic modulus of each suspension, the range of deformations for which strain depends linearly on stress must be known in advance. In addition, since the suspension ages, the extent of the linear domain may evolve during the experiment. The linear elastic domain and its eventual time evolution are identified by applying strain oscillations with increasing amplitude, for three different aging times covering the entire time window of the subsequent aging measurements. After various tests, a strain with amplitude $\gamma_0 = 10^{-4} = 0.01\%$ has been chosen, since this value lies in the linear domain for all resting times and studied formulations [72, 73]. All measurements are conducted at $F = 1$ Hz.

As we work with a stress controlled rheometer, applying strain-controlled oscillations with amplitude $\gamma_0 = 10^{-4}$ is problematic, and we usually observe strong retro-action noise. We thus decide to use an oscillatory shear stress. A constant stress amplitude, however, implies that the corresponding strain varies during the experiments, as our material ages. In these conditions, the suspension may be probed outside its linear regime. In order to remain at that constant amplitude γ_0 during the entire duration of the test, a feedback loop sequence is used [73]. Briefly, the measurement is divided into loops of 10s; at the end of each loop, the applied stress is updated based on the elastic modulus measured in the previous cycle, so that the target strain amplitude remains close to 10^{-4} . The loop sequence is depicted in Figure 3.10.

3.2.5 Yield stress

To quantify the increase in yield stress during material aging, we carry out standard stress sweep tests after different resting times (5-300-600-1200s). We do not use the classical method consisting in recording the stress response while applying a small and constant shear rate, because we observed that the control system of the rheometer was not accurate enough to impose a precise rotation of the inner tool. For each measurement, a stress ramp (from 0 to 200 Pa during 2min) is applied and automatically stopped once a shear rate of 200 s^{-1} is reached, to avoid stronger

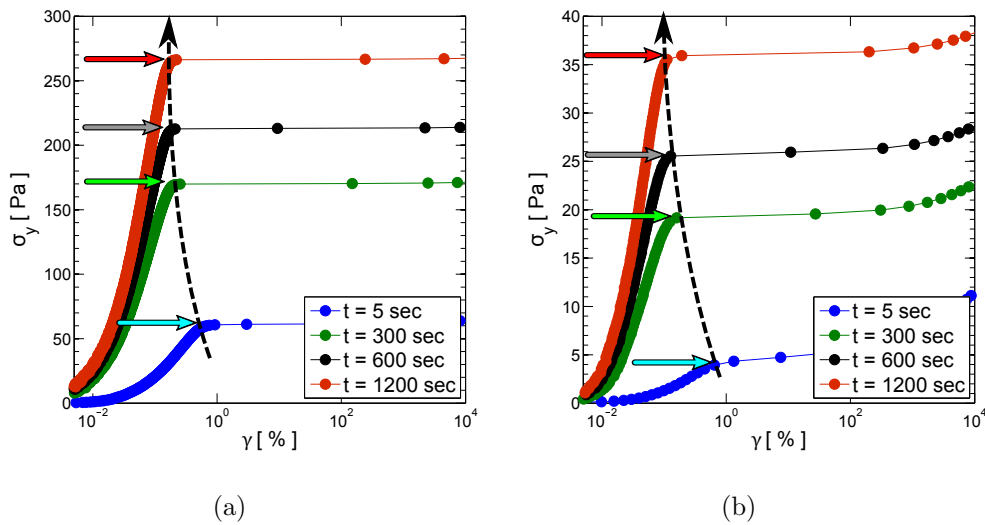


Figure 3.11 – Yield stress aging in dense silica suspensions. Stress ramps for (a) a suspension with $\phi \approx 0.38$, $I = 0.15$ M and $2a = 0.7$ μm , and (b) a suspension with $\phi \approx 0.35$, $I = 0.10$ M and $2a = 1.6$ μm .

shearing than during rejuvenation. In Figure 3.11 we report typical σ data versus deformation during the sweep tests. The yield stress is identified by the rapid increase in shear strain associated with the onset of the stress plateau region (arrows in corresponding brighter colors).

3.2.6 Rheometry cycle

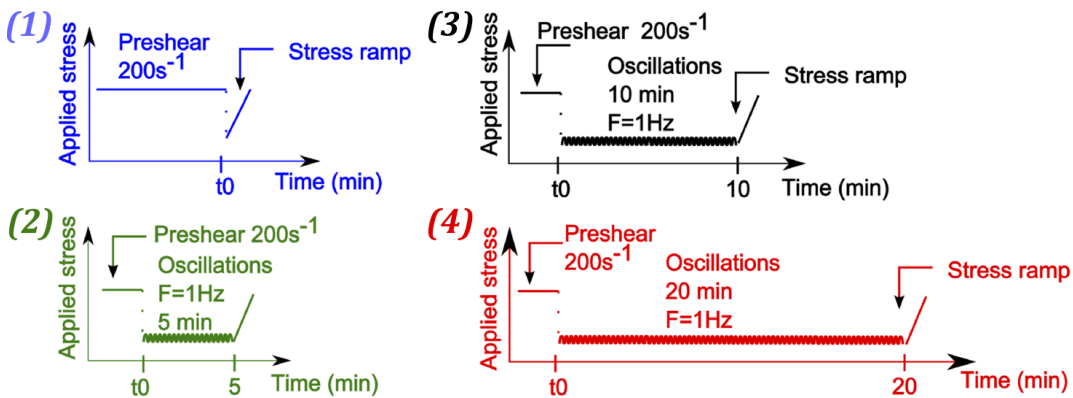


Figure 3.12 – Loading history applied to the sample during rheometric measurements. The numbers denote the chronological order of the rheometry cycle.

For each suspension under study, elastic modulus and yield stress measurements are performed in a unique rheometry cycle, shown in Figure 3.12. The cycle consists in 3 independent measurements of G' with different duration (5-10-20min), complemented by sweep tests at the end of the oscillations. Since the superposition of the G' data indicates that the suspensions are in a reproducible reference state at

the end of the pre-shearing, and since the material is probed in its linear domain, we consider the small-strain oscillations as an effective resting time. We verified this assumption by comparing the yield stress obtained after 5min of oscillatory tests with that obtained after an equivalent interval where the applied stress was set to 0 [72].

3.2.7 Main results: silica suspensions

Shear modulus

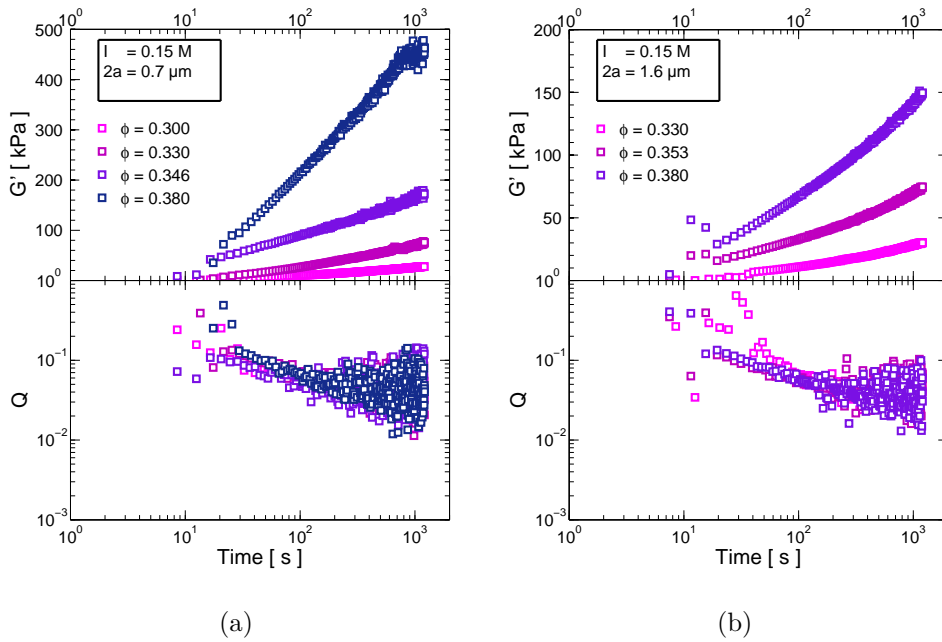


Figure 3.13 – Effect of packing fraction on the time-dependent shear modulus and Q -factor. All data are obtained using $I = 0.15 \text{ M}$ suspensions of silica particles of diameters $2a = 0.7 \mu\text{m}$ (a) and $2a = 1.6 \mu\text{m}$ (b), and for different packing fractions. Top: shear modulus G' vs time t since cessation of pre-shearing; bottom (refer to top frames for legends): the quality factor $Q = G''/G'$ vs t .

Macroscopic rheometry data for silica suspensions in water are presented in Figure 3.13. The left and right columns correspond to different particle sizes, $2a = 0.7 \mu\text{m}$ and $2a = 1.6 \mu\text{m}$ (resp.). For each a (i.e. each column), we plot on the top frame the time-resolved G' data for different packing fractions ϕ . The shear modulus increases monotonically over the accessible time range, and seems to reach asymptotically a quasi-logarithmic growth regime. On the bottom frames, we plot all the corresponding quality factors, $Q = G''/G'$ for the same set of ϕ values. In all cases, Q is of order 0.1 about 10s after cessation of pre-shearing when we start to obtain reliable G' and G'' data. At later times, G'' (not shown) is essentially constant, and therefore Q decays as the inverse of G' . The late times values of Q , which fluctuate around 5×10^{-2} , are usually associated with solid-like behavior.

Our $G'(t)$ data cover a much broader set of conditions, with different particle sizes (from 0.5 to $1.9 \mu\text{m}$) and packing fractions ϕ (29 to 40%). Such experiments,

replicated at different ionic strengths between 0.10 M and 0.20 M, yield the following observations:

- (i) G' is essentially I -independent in this range.
- (ii) G' strongly increases with ϕ , but its magnitude decreases with increasing particle radius a .

The observation of point (i) corroborates with the zeta potential measurements of similar particles in equivalent salt concentrations, in which a substantial saturation of the surface charge is seen for $I > 0.05$ M (see [Figure 3.3](#) in [Section 3.1.4](#)). The behavior in point (ii) is evident if one looks to [Figure 3.14\(a\)](#), where we plot the elastic modulus versus volume fraction for the $2a = 0.7$ μm and $2a = 1.6$ μm data sets at longest aging time (1200s).

Yield stress

The mechanical strengthening of the suspensions is also reflected in the yield stress time evolution, as illustrated in [Figure 3.11](#). Clearly, σ_y is an increasing function of aging time; it usually increases by a factor > 5 in only about 20 minutes after cessation of the pre-shear. Analysis of σ_y data for a wide range of experimental conditions, including different particle sizes a (from 0.5 to 1.9 μm), packing fractions ϕ (29–40%) and ionic strengths I (0.10 to 0.20 M) leads us to two major observations:

- (i) σ_y strongly increases with ϕ and its magnitude decreases with the particle size a .
- (ii) σ_y always increases with t , and is almost I -independent in the studied range.

These observations are summarized in [Figure 3.14\(b\)](#), where we report σ_y vs ϕ for two particle sizes, $2a = 0.7$ and 1.6 μm , and $t = 1200$ s. Observe that σ_y increases with ϕ more slowly than the shear modulus, while, for similar packing fractions, its reduction with a appears more pronounced than that of G' .

From our data set, we can estimate a critical yield strain for the onset of flow as $\gamma_c = \sigma_y/G'$; the results are plotted in [Figure 3.14\(c\)](#). The magnitude of γ_c does not exceed few tenths of % and decreases with ϕ . In addition, γ_c seems to slightly decrease with aging time, as suggested by the dashed black arrows in [Figure 3.11](#).

Water/glycerol mixtures

Finally, in [Figure 3.15](#) we report with open orange circles the time-resolved shear modulus (a) and yield stress (b) of suspensions in a 60/40 wt% water/glycerol mixtures. They clearly age, albeit at a smaller overall amplitude than in the respective pure water systems. This is expected to be caused by the smaller index contrast and hence the reduced scale of van der Waals forces in the glycerol mixture (refer to [Section 3.1.5](#) for more details). Indeed, they are just a factor $c \simeq 3.1$ smaller than the $G'(t)$ and σ_y values measured in the suspensions of identical particles in water at the same corresponding ϕ and I (open blue squares). Additional data confirm that

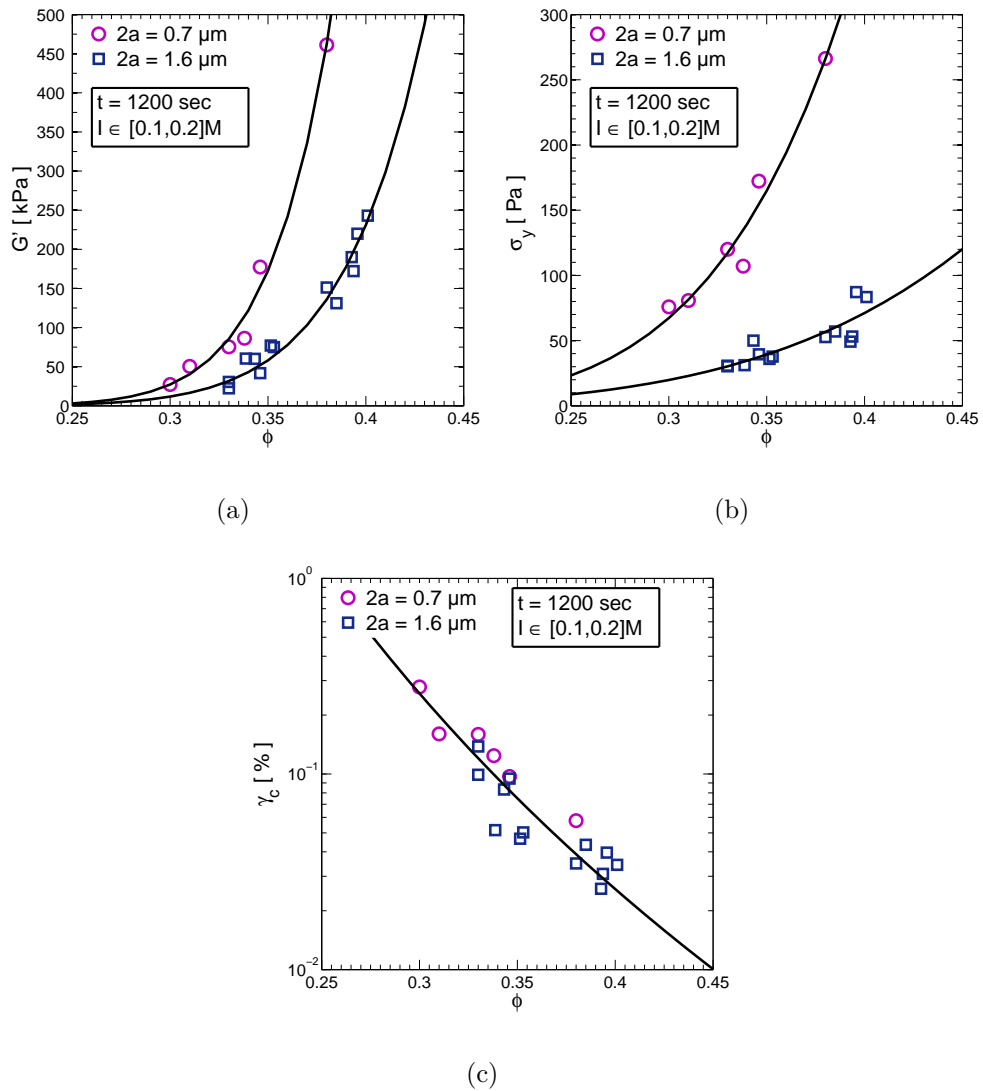


Figure 3.14 – Effect of volume fraction and particle size on the time-dependent shear modulus (a) and yield stress (b). The data are obtained for different ionic strengths in the range 0.1-0.2 M at aging time $t = 1200$ s. (c) Macroscopic critical strain $\gamma_c = \sigma_y/G'$ versus ϕ .

the aging dynamics is not affected by the presence of glycerol at concentrations up to $\sim 50\%$ [72].

3.2.8 Main results: PMMA suspensions

Shear modulus

We report the time-resolved shear elastic modulus of dense PMMA suspensions in CaCl_2 solutions. Due to the limited amount of particles in our possession, we focus on a single volume fraction ≈ 0.35 and study the elastic response for various ionic strengths between 0.20 M and 0.80 M. The results, reported in Figure 3.16(a), show that $G'(t)$ slightly increases with time for all the studied formulations; its magnitude

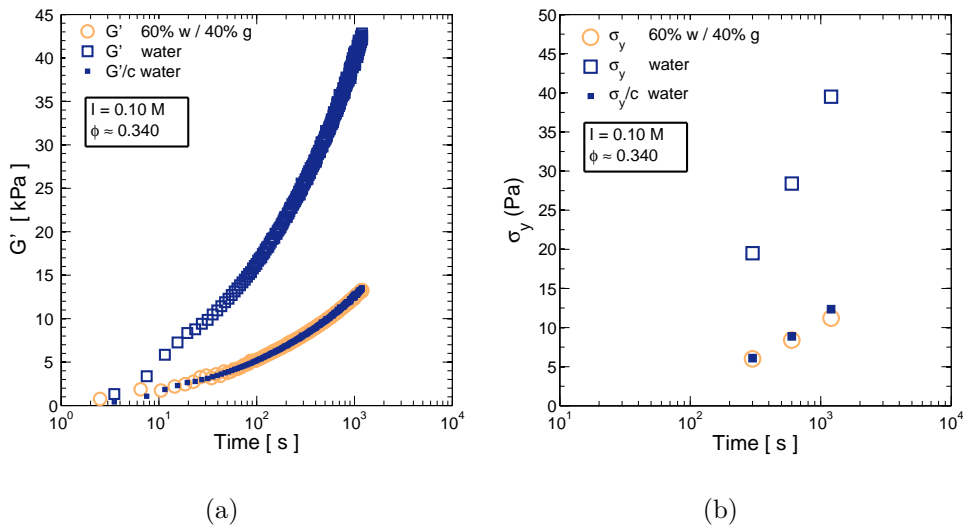


Figure 3.15 – Comparing the shear modulus (a) and yield stress (b) of particle suspensions in water vs in 60/40 wt% water/glycerol mixtures. Shear modulus and yield stress evolution are reported for both water/glycerol mixture (open orange circles) and water (open blue squares), in $2a = 1.6 \mu\text{m}$ particle suspensions at ionic strength $I = 0.1 \text{ M}$ and volume fraction $\phi = 0.34$. When rescaled by a factor $c \approx 3.1$, the water data falls right on top of the water/glycerol curve (filled blue squares).

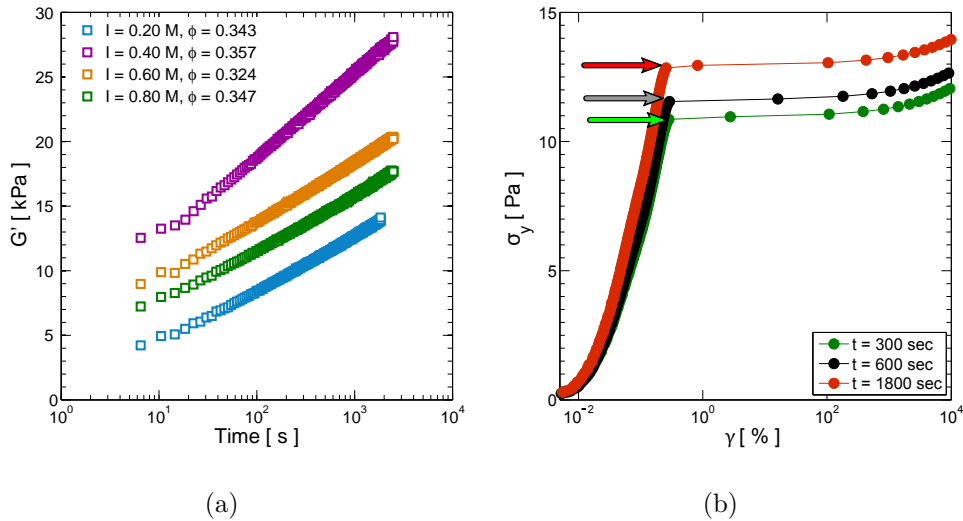


Figure 3.16 – (a) Elastic modulus of $3 \mu\text{m}$ PMMA suspensions at various I . (b) Yield stress of the suspension with $I = 0.20 \text{ M}$.

roughly doubles in about 40 minutes after the cessation of pre-shearing. For clarity, we apply a -3 kPa offset to the $I = 0.20 \text{ M}$ data. From the legend, observe that ϕ is not perfectly equal to 35%, the desired packing fraction, but fluctuates around it. This is due to experimental difficulties we encountered when dispersing the particles in water (Section 3.1.6).

Yield Stress

Using the same rheometry sequence in Section 3.2.3, we also attempt to characterize the yield stress response versus resting time. We show in Figure 3.16(b) the data obtained from a sweep test for a $I = 0.20$ M suspension; we find a slight increase of σ_y with aging time, as expected, and similar trends are observed for the other suspensions. Sometimes, however, σ_y slightly decreases over time, or has a non-monotonic behavior. At this stage, we are not able to determine the causes of this different behavior, and further experiments are much needed to elucidate it. It is worth noting, however, that in contrast with silica suspensions, here the yield stress exhibits variations of few Pa, which are within the limits of instrumental sensitivity (see Figure 3.16(b), for instance). Since it is more difficult for the rheometer to measure small changes in σ_y than an increase of several kPa in G' , the aging characterization of PMMA suspensions will be assessed only through the shear modulus measurements.

3.2.9 Elastic modulus vs yield stress

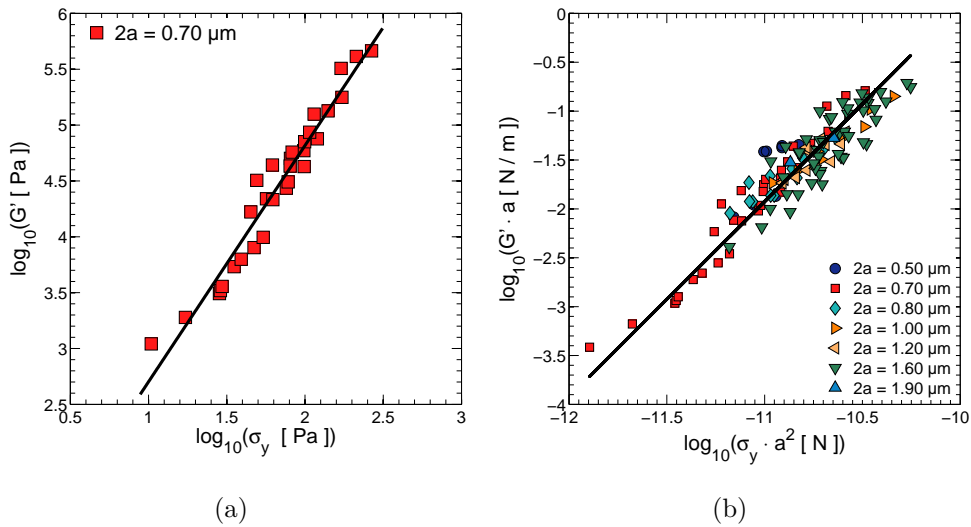


Figure 3.17 – (a) Elastic modulus versus yield stress for a single particle size. (b) For all the studied formulations, the G' data, scaled by the particle size to the power $n_G = 1$ as a function of σ_y , scaled by the particle size to the power $n_\sigma = 2$, showing the emergence of a master curve.

Both elastic modulus and yield stress present similar trends for different suspension formulations. Changing the volume fraction, resting time and particle size has the same effects on their mechanical properties; for example, both G' and σ_y increase with increasing ϕ and resting time, they are almost I -independent in the range 0.10-0.20 M, but decrease with the size of the particles a .

Moreover, if one plots G' versus σ_y for a given particle size, all the data collapse onto a single curve, as illustrated in Figure 3.17(a), indicating that different formulations (ϕ, I) and loading history (t) lead to similar responses. This fact also suggests that

both G' and σ_y , although they describe different material properties, are determined by a “similar” structure when we use different parameters. Additionally, all master curves, each obtained with a different particle size, can be rescaled into a single master curve when we consider the following a -scaling

$$G' = A_{n_G} \cdot a^{-n_G} \quad (3.36a)$$

$$\sigma_y = A_{n_\sigma} \cdot a^{-n_\sigma} \quad (3.36b)$$

where the exponents n_G and n_σ are simple numbers (assumed to be the same for all the silica suspensions) and where the coefficients A_{n_G} and A_{n_σ} depend on the formulation. The existence of a master curve reveals that both quantities are linked by the same relationship whatever the solid volume fraction, the particle size, the ionic strength, or the aging time. As shown in [Figure 3.17\(b\)](#), our data set demonstrates that G' should scale approximately with the inverse of the particle size ($n_G \sim 1$), whereas the yield stress with the inverse of the particle size squared ($n_\sigma \sim 2$), although slight departures from these values cannot be excluded, due to the limited range of explored a and uncertainties in the measurements (indeed, the authors in [\[73\]](#) obtained a good data collapse using $n_G = 1.22$ and $n_\sigma = 1.94$).

Focusing on the exponents in [Equation \(3.36\)](#), our results are in agreement with various experimental works on flocculated colloidal suspensions. Zhou et. al [\[221\]](#) investigated the yield stress of flocculated Al_2O_3 particles for different ϕ and a but under constant surface chemistry conditions. They gathered clear evidences that σ_y is inversely proportional to the square of the particle size, independently from the volume fraction of the suspensions. Similarly, Buscall and co-workers [\[23\]](#) found the same scaling behavior for polystyrene particles ranging from 0.5 to 3.5 μm . Other works [\[113, 131, 68\]](#) reached similar conclusions. The size dependence of the elastic modulus, instead, has been less investigated, although some authors [\[30\]](#) found results in agreement with our a^{-1} scaling.

Until now, there is no consensus about the origin of these experimental results. Most models we found in the literature are based on three major assumptions:

- (i) particles interact solely via centro-symmetric interaction potentials,
- (ii) DLVO theory applies in all conditions, even when particles are in primary minima,
- (iii) the effects of inter-particle forces and volume fraction are decoupled.

As long as the particle content is not too high ($< 40\%$), point (iii) is not problematic. On the other hand, there are more and more evidences that point (i) and (ii) fail in specific conditions ([Sections 2.2.3](#) and [2.2.4](#)), e.g. for small inter-particle separations where the details of the particle surface matter. The prediction of some classical models for both yield stress and elastic modulus are reported in [Table 3.4](#) and [Table 3.5](#), respectively. Without entering in details, none of them is able to predict the observed size dependencies. Scales et al., for instance, predict for the yield stress an a^{-1} scaling. The same is obtained when the DLVO potential is put into the model of Russel and co-workers. With regard to the elastic modulus, using

Table 3.4 – Models from literature expressing yield stress as function of interaction potential.

References	Models	Fitting parameters
Scales et al. [172]	$\sigma_y = \frac{\phi}{12\pi} \frac{C_N(\phi)}{a} \left(\frac{A_H}{h^2} - \frac{24\pi\epsilon\epsilon_0\kappa\zeta^2}{(1+\exp(\kappa h))} \right)$	$h = h_0 e^{-4.5\phi}$ h_0
Flatt and Bowen [63]	$\sigma_y = \frac{1.8}{\sqrt{3}\pi^3} \left(\frac{A_H}{24h^2 a} \right) \phi \frac{\phi^2(\phi-\phi_0)}{\phi_m(\phi_m-\phi)}$	ϕ_m, ϕ_0, h
Russel et al. [165]	$\sigma_y \approx \frac{\phi^2}{4a^2} \left(\frac{\partial V_{int}}{\partial h} \right)_{max}$	

Table 3.5 – Models from literature expressing elastic modulus as function of interaction potential.

References	Models	Fitting parameters
Buscall et al. [23]	$G' = \frac{\alpha}{h} \frac{\partial^2 V_{int}}{\partial h^2}$	α
Russel et al. [165]	$G' \approx \frac{\phi^2 [-(V_{int})_{min}]^{\frac{3}{2}}}{4k_B T a^2} \cdot \left[\left(\frac{\partial^2 V_{int}}{\partial h^2} \right)_{min} \right]^{\frac{1}{2}}$	

the simplified DLVO potential into the predictions of Table 3.5 yields expressions that do not depend on the particle size. Besides, time-dependent effects are not taken into account.

An attempt to explain the yield stress a -scaling has been provided by Flatt and Bowen [63]. The authors suggest that the magnitude of the interparticle (DLVO) forces is not proportional to the radius of the particle, as one would expect from Equation (2.30) (Section 2.2.3), but is best represented by a characteristic radius of curvature \tilde{a} at interparticle contact. Assuming that \tilde{a} does not vary with particle size, the a^{-2} prediction is recovered. The model has been developed for particles with arbitrary shape, i.e. powders, in which the difference between radius of curvature at contact and average particle radius arises from surface morphology. For spherical particles with a narrow size distribution, the authors postulate that \tilde{a} may be related to a typical radius of curvature characterizing the surface roughness, though they do not provide experimental evidences for that.

Recently, Pantina and Furst [146, 147] showed the presence of tangential forces between bonded colloidal particles. With the aid of JKR adhesion theory and fractal models applied to dilute gels [178, 196, 210], they proposed a unified interpretation of the scaling behavior of both G' and σ_y

$$G' \sim \frac{\phi^{\frac{3+d_b}{3-d_f}}}{a} \times k_0 \quad (3.37a)$$

$$\sigma_y \sim \frac{\phi^{\frac{3}{3-d_f}}}{a^3} \times M_c \quad (3.37b)$$

where $k_0 \sim a^{-1/3}$ and $M_c \sim a^{4/3}$ are respectively the rigidity and the critical moment of the bonded particles submitted to torques, and are calculated assuming a circular contact area between the adhesive particles. In Equation (3.37), d_f is

the fractal dimension of the blobs and d_b is the so-called bond dimension, i.e. the fractal dimension of the load-bearing structure through which the load is transmitted [105]. While fractal concepts certainly apply in dilute systems, the extension to dense suspensions is problematic and remains to be demonstrated. Later, Zaccone and co-workers [218, 219] have incorporated central and bond-bending interactions in a model for the elastic shear modulus of denser (glassy) systems comprising adhesive bonds. According to the authors

$$G' = \left(G'^{(CF)} + G'^{(BB)} \right) = \left(\frac{4}{5\pi} z^{(CF)} k_{\parallel} + \frac{124}{270\pi} z^{(BB)} k_{\perp} \right) \cdot \frac{\phi}{a} \quad (3.38)$$

where k_{\parallel} and k_{\perp} are the microscopic bond rigidities for central forces (CF) and bond bending (BB), respectively. The difference in the mean coordination numbers, $z^{(CF)}$ and $z^{(BB)}$, accounts for the fact that the average number of bonds per particle displaying BB resistance may differ from that of purely CF bonds. This is a consequence of the fact that the BB resistance used in the model is based on three-body angular interactions, hence via a quite different mechanism than that proposed by Pantina and Furst [146, 147]. Consequently, the applicability of these concepts in dense suspensions remains to be elucidated, and we emphasize that a multiscale theory of colloidal suspensions able to account for both DLVO and tangential forces, along with time-dependent effects, remains to be completed.

3.3 Structural characterization: Confocal Microscopy

In this part we investigate how the microstructure of the suspension evolves over time, aiming to gain insight into the origin of the observed mechanical aging. Can we understand the macroscopic behavior from the direct visualization of the suspension microstructure? Is aging driven by structural evolution? We attempt to answer these questions.

3.3.1 Working principle

Conventional widefield optical microscopy serves to observe objects of $\sim 1 \mu\text{m}$ size, but, in practice, it cannot yield good quality images of thick samples. The reason is twofold: firstly, multiple scattering from objects that are away from the illuminated region prevents imaging deep within the sample; secondly, in widefield illumination, resolution and image contrast are deteriorated by light originating from areas above and below the focal plane. Confocal microscopy circumvents this problem using two strategies: (i) point illumination of the sample and (ii) rejection of out-of-focus light. The benefit of point illumination lies in the fact that the resolution of an imaging system can be improved at the expense of its field of view (which is nevertheless recovered by scanning), since in point scanning microscopy both the objective and collector lenses contribute to the resolving power [38, 101]. Rejection of out-of-focus light consists in eliminating light originating from regions outside the plane of interest, and it is achieved by inserting a pinhole aperture within the light path. Confocal laser scanning microscopy (CLSM) permits to acquire high-quality images at various depths, and hence offers the possibility to reconstruct 3D volumes of optically dense samples. This represents the most important advantage of CLSM for colloidal studies.

Setup

Figure 3.18 shows the diagram of a typical confocal microscope. To permit the required rather high illumination intensity, the light source is typically a laser, operating at a specific wavelength (usually in the visible spectrum). The use of a monochromatic light is required, since CLSM relies on fluorescence as an imaging mode. First, the excitation light (blue line) impinges on a dichroic mirror. This is constructed to have a critical wavelength above which all incident light is transmitted, and below which it is reflected. The dichroic mirror directs the excitation light towards a steering devices (e.g. a pair of galvo mirrors) to scan the light in x and y . Then, the beam passes through the microscope and is focused by an high numerical aperture (NA) objective toward the fluorescent sample. The fluoresced light (light green) emitted from the illuminated point passes back through the objective and is de-scanned by the same mirrors used to direct the incident beam. As the emitted light has a higher wavelength than the excitation one, it is totally transmitted by the dichroic. A pinhole placed in the conjugate focal plane (hence the term confocal) and positioned just in front of a detector, rejects most of out-of-focus light arriving

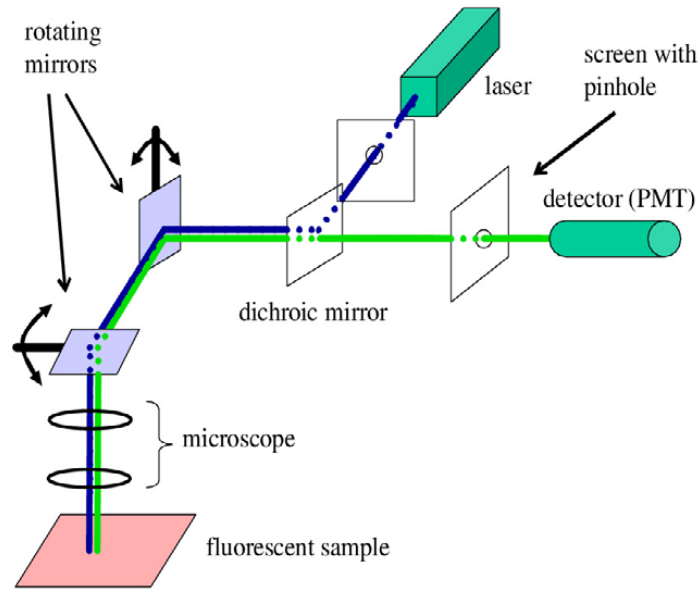


Figure 3.18 – Diagram of a confocal microscope. Figure taken from [159].

from the sample. Finally, the emerging photons are collected by a detector (e.g. a photo-multiplier detector PMT or a CCD camera), digitized by a computer and then displayed on a screen. 3D images are obtained by combining a series of such slices at different depths.

Resolution

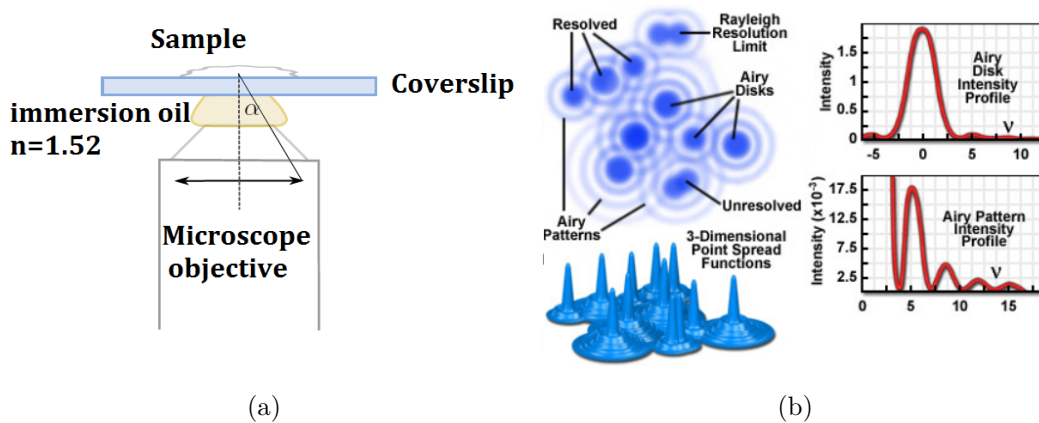


Figure 3.19 – (a) Oil immersion microscope objective. A oil droplet is placed between the objective and the coverslip. (b) Airy disk diffraction pattern and its intensity profile, showing first and higher order maxima, and a schematic representation of a three-dimensional point spread function. Figure taken from [38].

The resolution of a confocal microscope is limited primarily by light diffraction. Like in a conventional optical microscope, even in a perfectly aberration-free one, the image of a point object is not a point image, but consists in a diffraction pattern.

This intensity pattern is known as the Airy disc, and its size ϱ , defined by the position of the first minimum in the intensity distribution, can be expressed as [38]:

$$\varrho = \frac{0.6\lambda}{NA} \quad (3.39)$$

where λ is the laser wavelength and NA is the objective numerical aperture. The latter is proportional to the index of refraction of the medium in which the lens is working, and the angle α of the cone of light that can enter or exit the lens (see Figure 3.19(a))

$$NA = n \sin(\alpha) \quad (3.40)$$

Two illuminated points can be resolved if they are separated by at least the Airy radius. In this condition, indeed, the maximum intensity of one Airy disc coincides with the first minimum intensity of the other, and the points are just resolvable (see Figure 3.19(b)). This is known as the Rayleigh criterion. In 3D, the generalization of the Airy disc is called the Point Spread Function (PSF). The maximum resolution of a confocal microscope is mainly limited by the PSF of the objective lens and the optical setup, albeit other effects such as pixelation and degree of coherence of the illuminating light are important. In most general conditions, due to limitations in the optics, the z resolution of a confocal microscope, typically at best 500 nm, is poorer than the resolution in x and y , which is about 200 nm [159].

Instrument

We use a Zeiss LSM 700 confocal microscope equipped with a 100 \times NA 1.4 oil immersion objective (Zeiss Plan-APOCHROMAT). The laser is a Pigtail-coupled solid-state laser, operating at two wavelengths, $\lambda = 488$ nm and 512 nm. Image are acquired using a CCD camera (AxioCam MRc5). A limitation of our microscope is its low acquisition rate due to the galvo system used to scan the imaging plane. The acquisition speed is limited to 2fps for an image of 512 \times 512 pixels.

Sample cell



Figure 3.20 – A typical sample cell used for imaging. The suspension is inserted into a sealed plastic vial laying on a microscope coverslip.

A typical sample cell is shown in Figure 3.20. It consists of a plastic vial, equipped with a cap, and glued with adhesive (Araldite) to a standard microscope coverslip

at the bottom. The advantage of the cell is that it can be easily filled even with the most viscous suspension and its contents can be reused or adjusted. A small magnetic stirrer bar is inserted inside the vial and allows a controlled suspension shearing before imaging.

Suspension formulation

For good imaging, suspensions are formulated with the addition of glycerol in the range $C_m \in [30, 50]\%$ (see Section 3.1.5). A small amount of fluorescein (0.1 g/L) is added to the suspending phase. This is expected not to affect significantly the surface charge of the particles [73].

3.3.2 Experimental limitations

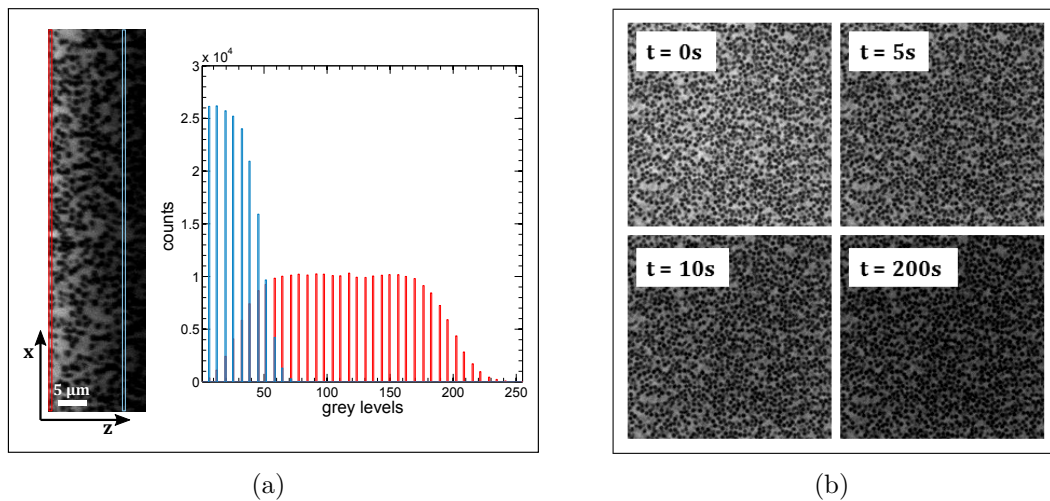


Figure 3.21 – Variation of image contrast as a function of (a) depth and (b) laser exposure time, for a suspension with $\phi \approx 0.35$, $2a = 1.2 \mu\text{m}$ and $I = 0.15 \text{ M}$. In (a) we also report with different colors the gray level histograms of two CLSM images acquired at different depths, as marked in the z-stack to the left.

Contrast variation with depth Our suspensions in water/glycerol mixtures still present a significant index mismatch. Slices taken at increasingly large depths are more and more subjected to multiple scattering. As a consequence, good image contrast is achieved only for a limited range of laser penetrations. Figure 3.21(a) is a typical xOz image of a dense suspension, displaying the complete loss of contrast for only few microns into the sample. The rapid degradation of the signal-to-noise ratio with depth (i) has a profound effect on the estimation of the particle locations, as we will explain in Appendix C, (ii) affects the PSF of the images and consequently (iii) precludes a reliable characterization of the sample in three dimensions.

Photobleaching Another important issue of our confocal experiments is related to the well known photobleaching effect, which refers to the decrease in emitted light

intensity of the dye with exposure time. Quite generally, light emitted by all fluorescent dyes fades during observation. This process is related to chemical or biochemical reactions occurring in the dye and which leads to their rapid degradation and loss of emission ability [49]. The photo-bleaching effect primarily depends on two factors: the exposure time, i.e. the total time during which the laser illuminates the fluorophore, and the light power (for a more detailed presentation of the argument one could refer to [49]). We expect photo-bleaching to be severe in our experiments since the laser beam must be intense enough to obtain a good signal-to-noise ratio (SNR) in our index-mismatched suspensions. The annihilation of the fluorescence ability impacts on the image formation process and leads to a loss of image contrast and hence quality during the measurement, as shown in [Figure 3.21\(b\)](#). Photobleaching impedes a fast and prolonged image acquisition and hence limits the characterization of the dynamics of our suspensions.

Focus drifts Perhaps surprisingly, time-lapse imaging of the suspensions is also hampered by focus drifts. The term describes the inability of a microscope to maintain the selected focal plane over an extended period of time. Note that this phenomenon is common in confocal microscopy and may lead to artifacts and misinterpretations of the dynamics of the sample under study. Axial fluctuations are caused by a number of factors and are generally more pronounced in high-magnification oil-immersion objectives (i.e. with a very shallow depth of focus) [180]. A list of contributing factors includes:

- (1) Temperature variations in the surrounding environment or related to intense illumination sources on the microscope.
- (2) Mechanical instability of the coverslip (gravity might induce a flexion of the coverslip that results in defocusing).
- (3) External vibrations or mechanical vibrations of the microscope and accessories, filter wheels, shutters, automatic stages, filter turrets etc.
- (4) Lateral movements due to the x - y translation of the mechanical stage.
- (5) Immersion media fluctuations, spreading or evaporation, and movements of the sample cell.

We attempted to limit all these factors but, unfortunately, we were not able to definitively fix all problems. Usually, we detect large axial movements ranging between ~ 1 to $3\ \mu\text{m}$ in about 1h.

3.3.3 Results

Due to the experimental limitations discussed above, the suspensions are studied in a single focal plane at depths ranging from ≈ 15 to $20\ \mu\text{m}$. These working distances ensure the absence of wall effects, since they are systematically greater than ~ 10 particle diameters. Sample reconstruction is performed using a standard centroid-based algorithm [41]; the details of the method are reported in [Appendix C](#). The centroid method locates the positions of the particles within a tenth of a pixel, which corresponds to around $12\ \text{nm}$ in our images. Since we work far from ideal conditions, however, the position accuracy should be reduced.

Static properties

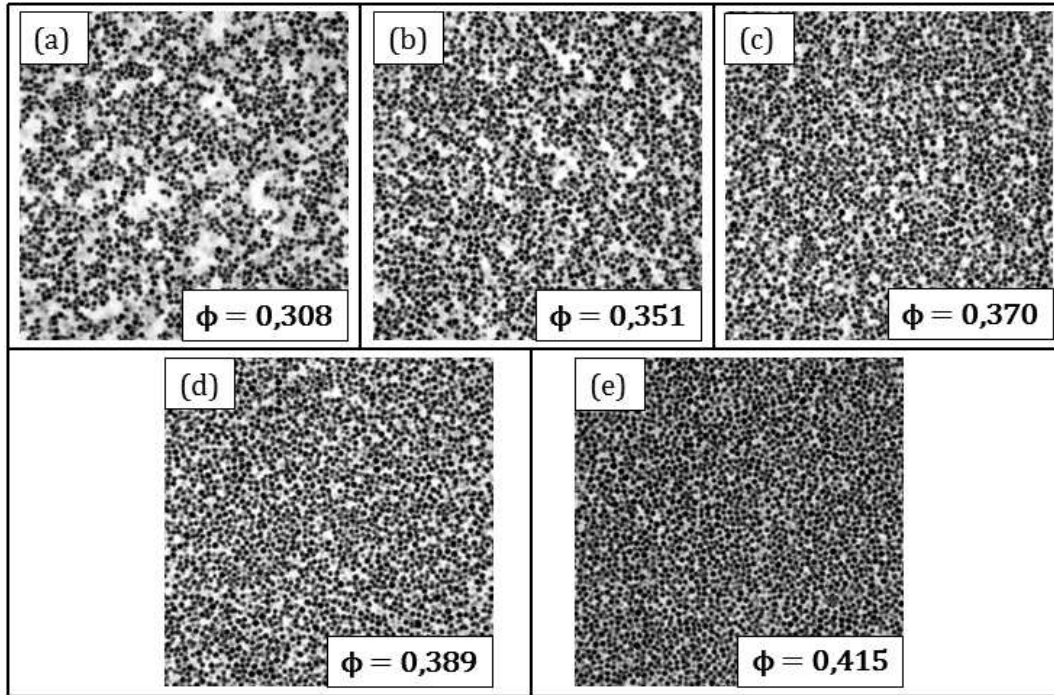


Figure 3.22 – CLSM images of $2a = 1.2 \mu\text{m}$ silica particles in 50/50 wt% water/glycerol mixtures, at different packing fractions. We use a single $I = 0.2 \text{ M}$.

We study the static properties of our suspensions, for several volume fractions, ionic strengths and particle sizes. Figure 3.22 shows 2D images of suspensions in 50/50 wt% water/glycerol mixtures at different packing fractions, $I = 0.2 \text{ M}$ and a single particle size ($2a = 1.2 \mu\text{m}$).

Radial Distribution Function (RDF)

The first structural descriptor we investigate is the radial distribution function $g(r)$, also known as the pair-correlation function. It describes the probability of finding particles at a given center-to-center distance (r) away from a randomly-chosen particle. Once one obtains the locations of all N particles in the field of view, the 2D- $g(r)$ can be computed via

$$g(r) = \frac{1}{2\pi r \Delta r} \frac{1}{N\rho} \sum_{i=1}^N \sum_{j \neq i}^N \langle \delta(r - r_{ij}) \rangle \quad (3.41)$$

where $\rho = N/L^2$ is the number density (L being the linear size of the image), Δr is the thickness of the shell used to count the particles and δ the Dirac function. Equation (3.41) is thus equivalent to counting the number of particles in a shell of size $2\pi r dr$ located at distance r from a test particle, normalized by the same quantity in the ideal gas with same density.

We emphasize that the particle centers in a typical confocal slice are distributed in

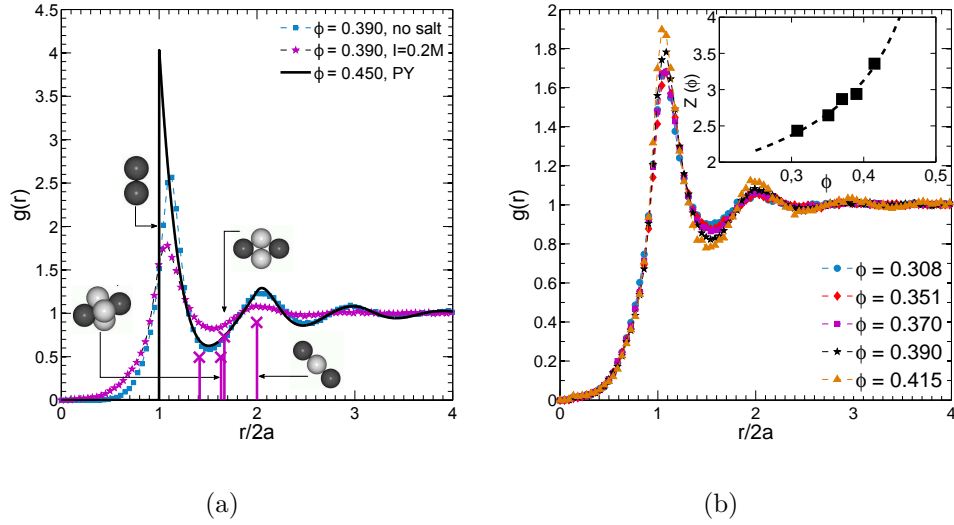


Figure 3.23 – Pair correlation functions measured from the 2D particle positions. (a) $g(r)$ of a suspension in $I = 0.2\text{M CaCl}_2$ (magenta filled stars) and of a stable suspension (blue filled squares). The latter is compared to the radial distribution function of hard spheres [182] (solid black line) at a higher packing fraction (see text). (b) RDF for $I = 0.2\text{M}$ suspensions at various volume fractions; (inset) corresponding coordination number versus ϕ , calculated from Equation (3.43) and using a cutoff separation $r^+ = d + 0.03$. To increase the statistic, all curves result from an average over at least 25 frames taken at the same aging time.

a vertical region of thickness Δz due to the finite depth of focus of the objective. Using all particles located in a x - y image of size L , we calculate $\Delta z \sim 1.5\ \mu\text{m}$, in agreement with known CLSM slice thicknesses [120]. This is done by matching the suspension volume fraction with that determined from the detected particle number N and using $\phi = \pi \rho d^3 / 6$, with $\rho = N / \Omega$, $\Omega = L^2 \Delta z$ and $d = 2a$ the particle diameter.

Since not all particles are located in the same optical plane, the two-dimensional $g(r)$ suffers from a projection error at distances comparable to the thickness of the slice, and that is the reason why it might deviate from an “ideal” 3D- $g(r)$ [136]. This problem can be circumvented by discriminating particles far from the focal plane, based on their intensity [136]. In our case, however, overlaps of intensity of contacting particles, low signal-to-noise ratio and variable image contrast affect the intensity distribution related to individual particles, and induce difficulties in the post-treatment of the images. As a consequence, we underline that the following results are not corrected for projection errors. This fact, combined with the effect of particle polydispersity, leads to a broadening and shift of the peaks in our measured 2D- $g(r)$; this is evident, in particular, from the existence of non-zero contributions to $g(r)$ at distances lower than the particle diameter, as shown in Figure 3.23.

First, we display in Figure 3.23(a) the $g(r)$ computed for a stable suspension (i.e. without salt) with $2a = 1.2\ \mu\text{m}$ and $\phi \approx 39\%$, and compare the results with

a suspension having same a and ϕ , in a $I = 0.2\text{M}$ calcium chloride solution. Let us mention the main conclusions we can draw from this plot. In the stable sample, particles constantly undergo Brownian motion, and the suspension is expected to behave as a viscous liquid. The corresponding pair-correlation function, shown in [Figure 3.23\(a\)](#) with blue filled squares, features characteristics of an homogeneous structure, as we can clearly distinct several peaks associated to the first and higher order coordination shells. For comparison, we also plot the hard spheres (HS) pair-correlation function obtained using the Percus–Yevick closure [\[182\]](#) (solid black line). Apart from a large underestimation of $g(r)$ at contact $r \sim d$, expected from the arguments exposed above, the experimental pair-correlation function appears to be well described by the PY approximation for hard-spheres, but only when we use a packing fraction of 45%, larger than the nominal one. The fact that we need to use a larger ϕ could be explained by considering that the charge-stabilized suspension does not present a yield stress able to hamper sedimentation, which therefore tends to compact particles at the bottom of the vial where images are acquired. Indeed, the volume fraction extrapolated from the CLSM images is greater than the nominal one, confirming this hypothesis. The similarity in the pair-correlation function between the stable sample and the PY calculation suggests that the systems is essentially homogeneous. Note also that the position of the first peak is not located at $r = d$, as expected for perfectly hard sphere particles, but slightly above, at $r = (1.108 \pm 0.02) \cdot d$. The peak shift can be ascribed to the presence of charges at the particle surface [\[93\]](#), and can be roughly estimated via a simple relationship [\[209\]](#):

$$r = \left(\frac{\phi_{rcp}}{\phi} \right)^{1/3} \cdot d \approx 1.12 \cdot d \quad (3.42)$$

where we use $\phi_{rcp} \sim 0.64$, the volume fraction for a random close-packed system, and $\phi = 0.45$.

The effect of ionic strength on the structure of the fluid is seen in the radial distribution function of the corresponding unstable suspension (magenta stars), where now particle aggregation leads to locally denser areas and voids in the microstructure. In particular, the formation of densely packed regions is expected to affect the RDF in the region $1 < r/d < 2$ [\[134\]](#), since, for each cluster geometry, specific center-to-center separations contribute a peak to $g(r)$. Some of these contributions are shown in [Figure 3.23\(a\)](#) with magenta stems. As illustrated, the characteristic peaks correspond to different cluster morphologies and are located at specific interparticle separations ($\sqrt{2}$, $5/3$, etc...). Quite generally, however, the pair correlation functions of the ionic suspensions show little structure; this may be caused by the formation of bonds that disrupt the local cage order [\[174\]](#). This is reflected in the shift towards lower r of the first coordination shell. Bond formation also increases tracking errors, as explained in [Appendix C](#), and leads to a reduction of the first peak height and its broadening in the $r < d$ region.

Coordination Number (CN)

[Figure 3.23\(b\)](#) shows the pair correlation functions of all suspensions in [Figure 3.22](#). Note the change in the first peak height with increasing volume fractions,

indicating increasingly higher average number of bonds per particle (coordination number). The latter can be roughly estimated from the radial distribution function through

$$Z(\phi) = 4\pi\rho \int_0^{r^+} r^2 g(r, \phi) dr \quad (3.43)$$

Where r^+ is a cutoff distance below which particles are assumed to be in contact [159, 50]. The choice of r^+ is controversial, and different strategies can be found in the literature. Here we estimate $Z(\phi)$ using $r^+ = (1 + l^+)d$ with $l^+ = 0.03$ [219], constant for all the studied volume fractions. This value is known to yield $Z \sim 6$ for repulsive hard sphere at random close packing (Maxwell isotacticity criteria) [155]. We compute Equation (3.43) using the experimental $g(r)$ of Figure 3.23(b); the results are shown in the inset of the same figure. As expected, the mean contact number increases with the packing of the particles; we obtain $Z \approx 2.4$ (≈ 3.3) for $\phi \approx 0.31$ (≈ 0.41), respectively. This rough estimate indicates that particles preferentially form string-like structures with low connectivity.

Number Density Fluctuations (NDF)

While the radial distribution function gives useful information on the short-range structure, it is almost insensitive to the long-range degree of heterogeneity of the suspension. We quantify it by measuring the second order fluctuations in particle number N about its average value ($\langle \delta N^2 \rangle$) / $\langle N \rangle$. This quantity, when determined in the thermodynamic limit, is proportional to the isothermal compressibility κ_T^∞ ,

$$\chi_T^\infty = \frac{\kappa_T^\infty}{\kappa_T^0} = \frac{\langle N^2 \rangle - \langle N \rangle^2}{\langle N \rangle} \quad (3.44)$$

where $\kappa_T^0 = 1/\rho k_B T$ is the isothermal compressibility of the ideal gas of same density $\rho = N/\Omega$, and $\langle \dots \rangle$ denotes a grand canonical ensemble average. Note that Equation (3.44) corresponds to the integral over all space of

$$\chi_T^\infty = 1 + 4\pi\rho \int_0^\infty r^2 [g(r) - 1] dr \quad (3.45)$$

and can be further related to the static structure factor $S(q)$ in the low angle limit

$$\chi_T^\infty = S(q=0) = k_B T \left[\frac{\partial \rho}{\partial \Pi} \right]_T. \quad (3.46)$$

where Π is the osmotic pressure. In the theory of liquids Equation (3.45) is known as the compressibility equation.

From the experimental viewpoint, χ_T can be only measured in subsystems with finite size, so that one obtains a so-called finite-size isothermal compressibility. In practice, it is usually computed through the spatial block analysis (SBA) method [170], which consists in subdividing a system of size $\Omega = L^3$ into several squared blocks of

increasing size D^3 , and calculating the average number density fluctuations (NDF):

$$\chi_T^{(D)} = \frac{\kappa_T^{(D)}}{\kappa_T^0} = \frac{\langle N^2 \rangle_D - \langle N \rangle_D^2}{\langle N \rangle_D}, \quad (3.47)$$

where the label (D) emphasizes that χ_T depends on block size D , and $\langle \dots \rangle_D$ denotes an average over all the blocks with same D . Our system consists of two-dimensional images of length L , and the NDF are evaluated by dividing each image into small squares of linear dimension $D = L/M_B$, where M_B is an integer.

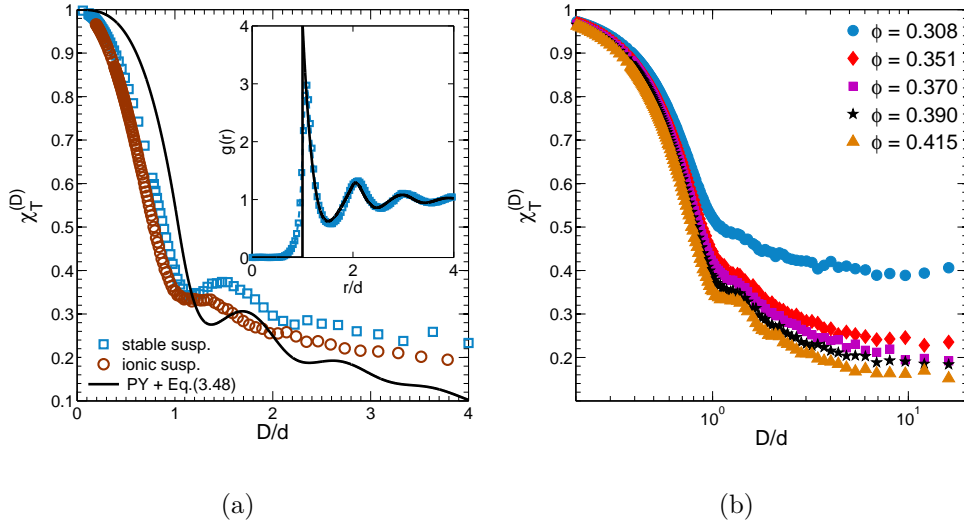


Figure 3.24 – Reduced isothermal compressibility, $\chi_T^{(D)}$, versus size of the block, normalized by the particle diameter. (a) Stable suspension with $d = 1.6 \mu\text{m}$ (open blue squares) and the analytic computation based on Equation (3.48) (solid black line); (inset) ρ in Equation (3.48) is evaluated by matching the experimental and analytic $g(r)$. Open brown circles are obtained for a similar suspension in a $I = 0.2$ M CaCl_2 solution. (b) $\chi_T^{(D)}$ for attractive suspensions in $I = 0.2$ M CaCl_2 solutions.

In Figure 3.24(a) we report with blue open squares $\chi_T^{(D)}$ versus D/d for a liquid suspensions with $d = 1.6 \mu\text{m}$. The data are compared with the analytic calculation based on the compressibility equation for a spherical volume of diameter D [28]:

$$\chi_T^{(D)} = 1 + 4\pi\rho \int_0^D r^2 [g(r) - 1] \left(1 - \frac{3r}{2D} + \frac{r^3}{2D^3} \right) dr \quad (3.48)$$

In Equation (3.48), we use the analytic Percus–Yevick pair-correlation function of hard spheres $g^{PY}(r)$ [182] and the number density ρ is chosen so that $g^{PY}(r)$ matches the experimental $g(r)$, as shown in the inset of Figure 3.24(a). We emphasize that the function $g^{PY}(r)$ used here is truncated to unity past $D/d = 5$, so that the calculation is limited to this range. As shown in the main figure, the trend of the experimental fluctuations is qualitatively consistent with that expected for the hard sphere liquid (black solid line), suggesting again that the structure is homogeneous.

Attractive interactions lead to more disordered structures, as we can deduce from the reduction in the short-ranged oscillations in the density fluctuations of a suspension with similar ϕ and $I = 0.2 \text{ M}$.

We focus on the long-range behavior of $\chi_T^{(D)}$, as well. In [Figure 3.24\(b\)](#) we report [Equation \(3.47\)](#) for the ionic suspensions with $I = 0.2 \text{ M}$. The data show that, quite generally, the long-range fluctuations decrease as the packing fraction of the suspension is increased. This behavior is consistent with [Figure 3.22](#), since the CLSM images clearly display an increasingly homogeneous structure as ϕ grows. In addition, we do not observe any maximum in $\chi_T^{(D)}$ at intermediate-to-large distances, indicating the absence of particle clusters with a characteristic size D less than ~ 20 colloid diameters [\[50\]](#).

[Equations \(3.44\) to \(3.46\)](#) hold in the macroscopic limit, i.e. when $N, \Omega \rightarrow \infty$, such that $\rho = N/\Omega$ remains finite. In principle, the finite-size isothermal compressibility can be extrapolated to the isothermal compressibility in the thermodynamic limit, χ_T^∞ , taking the limits of $D, L \rightarrow \infty$ in $\chi_T^{(D)}$, but in practice, the measured values are affected by finite-size effects [\[170, 166, 91\]](#). In [\[170\]](#), the author proposed that the difference between $\chi_T^{(D)}$ and χ_T^∞ is related to a first-order correction due to the boundaries of the blocks, which can be expressed as:

$$\chi_T^{(D)} = \chi_T^\infty + \frac{c}{D} + \mathcal{O}\left(\frac{1}{D^2}\right) \quad (3.49)$$

By neglecting the $\mathcal{O}(1/D^2)$ terms, [Equation \(3.49\)](#) is rearranged by multiplying both members by $\lambda = D/L = 1/M_B$

$$\lambda \chi_T(\lambda) = \chi_T^\infty \lambda + \frac{c}{L} \quad (3.50)$$

where now the dependence of the finite-size isothermal compressibility on λ is made explicit. [Equation \(3.50\)](#) is directly tested on our $I = 0.2 \text{ M}$ suspensions of [Figure 3.22](#), by plotting the number density fluctuations, multiplied by $\lambda = 1/M_B$, as a function of λ . The results, extensively averaged over several images taken at same aging times, are reported in [Figure 3.25\(a\)](#) with colored filled symbols. Superimposed to the curves, we also show the fits to a linear function, with χ_T^∞ and c as fitting parameters. We have seen that, for very small λ , χ_T may present an oscillating behavior (see [Figure 3.24\(a\)](#), for instance) due to density correlations that reflect the short range structure of the fluid [\[91\]](#), and hence the fit to [Equation \(3.50\)](#) is only valid for $\xi < D < L$, with ξ the correlation length. In our attractive suspensions, short range correlations rapidly decay, as illustrated in the inset of [Figure 3.25\(a\)](#), so that we exclude from the fit only the data for $\lambda < 0.05$. The corresponding estimates of the isothermal compressibilities in the macroscopic limit are then used to calculate the osmotic equation of state:

$$\frac{1}{\chi_T^\infty} = \frac{1}{k_B T} \left[\frac{\partial \Pi}{\partial \rho} \right]_T \quad (3.51)$$

The results, for suspensions with various particle sizes (symbols) and ionic strengths

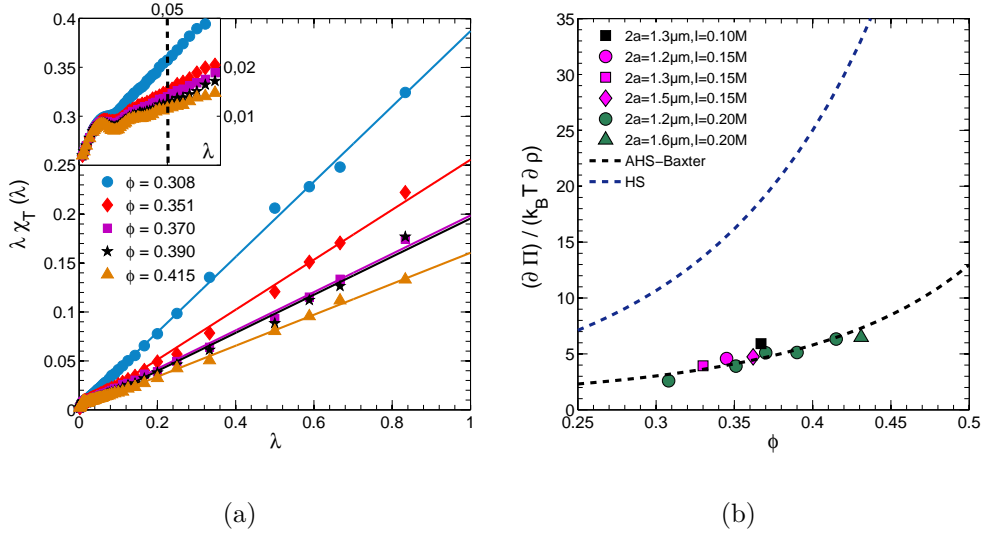


Figure 3.25 – Finite-size effects on the density fluctuations. (a) Finite-size compressibilities times λ versus λ for the data in Figure 3.24(b) (colored filled symbols), fitted according to Equation (3.50) using χ_T^∞ and c as fitting parameters. (b) Inverse of the fitted isothermal compressibilities versus ϕ . Dark blue dotted line is the analytic results for hard spheres using the Percus–Yevick closure [182]. Black dashed line is the analytic results for adhesive hard spheres, Equations (3.54) and (3.55), with stickyness parameter $\tau \sim 0.32$.

(colors) are reported in Figure 3.25(b), as a function of ϕ . For comparison, we also plot the Percus–Yevick expression for the hard sphere system [182]:

$$\frac{1}{k_B T} \left[\frac{\partial \Pi}{\partial \rho} \right]_T^{(HS)} = \frac{(1 + 2\phi)^2}{(1 - \phi)^4} \quad (3.52)$$

The data clearly show the strong departure from ideal HS behavior of our attractive suspensions. Indeed, in our I -conditions, the electrostatic interactions are highly screened, and van der Waals interactions, which become significant at particle surface-to-surface separations of the order of $\sim 0.1d$ [167], can be considered as short ranged compared to the particle size. To check for this hypothesis, we tentatively model the particle interactions using the Baxter adhesive hard-sphere (AHS) potential—the simplest potential with an attractive part—which is the limit for vanishing attraction width Δ of

$$V(r) = \begin{cases} \infty, & \text{if } r \leq d \\ \ln [12\tau\Delta/(d + \Delta)], & \text{if } d < r < d + \Delta \\ 0, & \text{otherwise} \end{cases} \quad (3.53)$$

where τ is called the Baxter temperature and can be regarded as a measure of the interaction strength ($\tau \searrow$ for increasing attractions). The osmotic compressibility

for AHS has been analytically evaluated in the Percus-Yevick approximation [8, 156]:

$$\frac{1}{k_B T} \left[\frac{\partial \Pi}{\partial \rho} \right]_T^{(AHS)} = \frac{(1 + 2\phi - \gamma\phi)^2}{(1 - \phi)^4} \quad (3.54)$$

where

$$\gamma = 6(1 - \tau + \tau/\phi) \cdot \left(1 - \sqrt{1 - \frac{1 + 2/\phi}{6(1 - \tau + \tau/\phi)^2}} \right) \quad (3.55)$$

Note that the osmotic pressure for hard spheres, Equation (3.52), is recovered by taking the limit of $\tau \rightarrow \infty$ in Equations (3.54) and (3.55). Equation (3.54) is tested on our data set, using the stickiness parameter τ as the only free parameter. The data can be well described by the model if one takes $\tau \sim 0.32$, as shown by the dashed black line in Figure 3.25(b). The good agreement of our data with the Baxter model suggests that our interactions can be considered as short-ranged, and confirms that the electrostatic interactions are strongly screened. Additionally, we think that a lower value of τ should be more representative of our suspensions. The reason is that we did not discriminate out-of-focus particles in the computation of the 2D- χ_T , so that we likely underestimate the density fluctuations, and hence overestimate the osmotic pressure.

In order to extrapolate the Baxter temperature to an effective interaction strength u_0 , a common way is to match the second virial coefficient B_2 to that of the square-well potential [141], which can be analytically estimated. For short attraction widths one obtains [141, 156]

$$\frac{u_0}{k_B T} \approx \ln \left(1 + \frac{d/\Delta}{12\tau} \right) \quad (3.56)$$

This mapping procedure can be used to evaluate interaction strengths in depletion gels [50], where Δ is known and set by the polymer radius of gyration, but it is difficult to quantify for colloids interacting through DLVO potential. Moreover, this approach is expected to break down in our suspensions since it is essentially based on the hypothesis that particles interact via centro-symmetric potentials, and thus cannot resist rotations. For this reason, a more accurate investigation is required.

3.3.4 Aging

To test whether aging can be attributed to an evolution of the microstructure, we acquire several images of the suspensions at different aging times and check, at the end of the experiment, that focus drift was negligible. In Figure 3.26(a), we show a typical microscopy image at depth $\approx 15 \mu\text{m}$ for a water/glycerol system, with particle size $2a = 1.6 \mu\text{m}$, ionic strength $I = 0.15 \text{ M}$ and $\phi = 0.39$. In Figure 3.26(b), we draw the particle positions reconstructed from this and later images, which correspond to three different times in the macroscopic aging regime ($t = 1, 5$ and 10 min). Some particles seem to disappear with time, but this is just an effect of the progressive bleaching of the fluorescein—particles that are slightly away from the focal plane become more difficult to distinguish. Quite strikingly, all the particles that can be imaged at the three considered times remain essentially

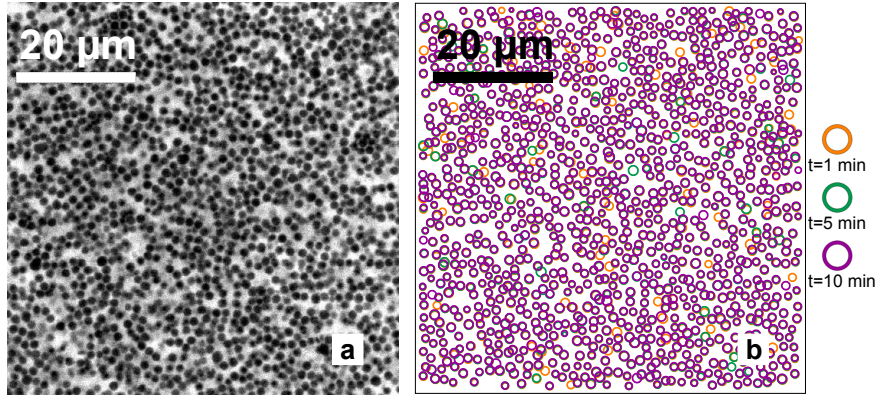


Figure 3.26 – Absence of structural aging in silica concentrated suspensions. (a) Typical CLSM image of a suspension of $2a = 1.6 \mu\text{m}$ silica particles in a 60/40 wt% water/glycerol mixture, with $\phi = 39\%$, $I = 0.15 \text{ M}$, in a plane parallel to the bottom cover slip, at depth $\approx 15 \mu\text{m}$; (b) Reconstructed particle positions at $t = 1$ (red), 5 (green), and 10mn (purple).

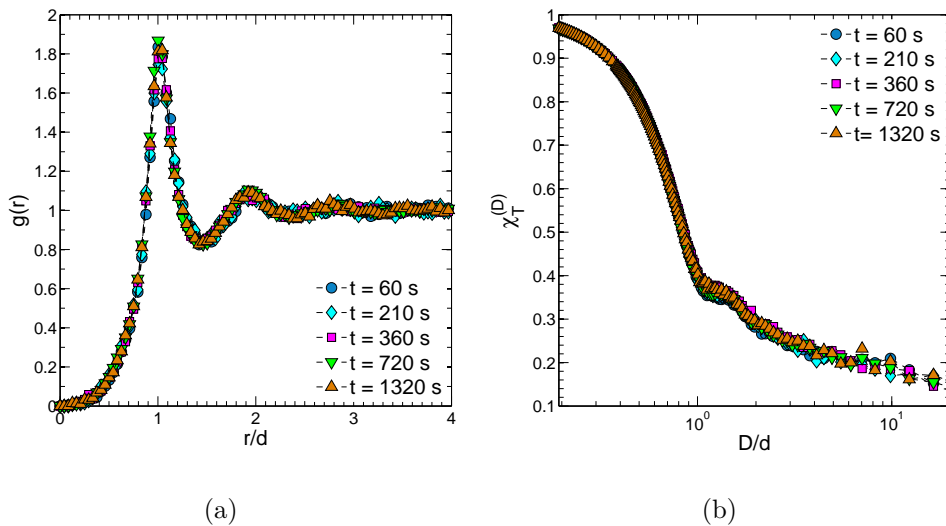


Figure 3.27 – The structure is invariant during mechanical aging. Radial distribution functions (a) and finite-size isothermal compressibilities (b) versus aging time t , for a suspension with $I = 0.1 \text{ M}$ and $d = 1.3 \mu\text{m}$, in a 50/50 wt% water/glycerol mixture. Each curve is obtained by averaging several images taken in $\sim 2 \text{ min}$ time intervals.

fixed at the same positions. To further check whether aging changes the short and long range structure of the suspensions, we also investigate the radial distribution functions and density fluctuations at various aging times. In Figure 3.27, we plot $g(r)$ (a) and χ_T (b) for a suspension that should exhibit the weakest attractive interactions in our explored conditions, i.e. with the lowest ionic strength, $I = 0.1 \text{ M}$, and the highest glycerol content, 50 wt%. The data show that there is no evident correlation between the age of the suspension and its static structure, as evaluated by these quantities. All of these observations establish that the network morphology is constant during mechanical aging and no large structural changes occur. On this basis, we conclude that, in our silica suspensions in glycerol-water mixtures, shear

modulus aging proceeds in the complete absence of structural evolution. This can only happen if solid-solid contacts are formed and evolve over time. In all likelihood, the same happens in silica suspensions in pure water, since they display much larger van der Waals forces, and hence are even more likely to form stable solid-solid contacts.

Part II

Part II

Three-Point Bending Tests with LTs

Contents

4.1	Laser Tweezers (LTs)	94
4.1.1	Optical traps	94
4.1.2	Setup	96
4.1.3	AOD calibration	99
4.1.4	Force calibration	99
4.2	Experimental procedure	102
4.2.1	Materials	102
4.2.2	Sample cell	102
4.2.3	Assembly of particle rods	103
4.2.4	Three-point bending experiments	106
4.2.5	Loading cycle	109
4.3	Elasticity of particle rods	110
4.3.1	SiO ₂ particle rods	110
4.3.2	PMMA particle rods	115
4.4	Yielding of particle rods	117
4.4.1	SiO ₂ particle rods	117
4.5	Interpretation of the results	121
4.5.1	JKR and DMT models	121
4.5.2	Pantina-Furst model	123
4.5.3	Dominik-Tielens model	127
4.5.4	Contact aging	130

4.1 Laser Tweezers (LTs)

Through confocal microscopy, we have observed the rapid near-complete structural arrest of our silica suspensions, which can be explained by the formation of strongly adhesive contacts between the particles. This observation leads us to conclude that, within the conditions explored (medium to high particle concentrations, high salt content), structural evolution of silica suspensions cannot explain their mechanical aging, and therefore it points to the role of contacts. Here we seek to study aging at the level of the contacts, to investigate if their progressive stiffening can drive macroscopic aging in our suspensions. To address this question, we carry out experiments on model particle aggregates using the laser tweezers (LTS) apparatus of Pantina and Furst [145]. We first introduce the standard concepts of optical trapping, and explain how small forces on colloidal particles can be applied and then measured through this technique.

4.1.1 Optical traps

In 1986, Arthur Ashkin and co-workers [6] demonstrated that one could use focused laser beams to trap micrometer-sized dielectric particles. Over the years, the increasing ability in manipulating multiple particles at the same time, the development of stable laser beams with increasing power, three-dimensional piezoelectric stages with unprecedented control over the position of a trapped object, and position detection sensors with nanometer resolution have made optical trapping a standard tool in numerous research areas, ranging from biophysics to microrheology. The most important feature of optical tweezers is perhaps their capability of allowing non-contact force measurements in the order of piconewtons; optical trapping has been successfully used in the characterization of mechanical properties of cells and DNA [206, 110, 140], kinetics properties of viruses, bacteria and molecular motors at the single-molecule level [5, 2], viscoelastic properties of liquids [153, 160, 70] and colloidal interparticle forces [84, 88, 148, 207].

Ray Optics Approximation Laser tweezers take advantage of optical forces acting between a dielectric particle and the laser light. These forces result from the transfer of momentum from the light beam to the particle, when the latter moves away from the center of the focus. To explain qualitatively the operating principle of an optical trap, let us first consider the case when there is no light reflection and absorption from the particle. Let us further assume that the light wavelength λ is much smaller than the particle diameter ($\lambda \ll a$), so that the optical force on the microsphere can be calculated by ray optics. We can imagine a dielectric bead as a positive converging lens, as depicted in [Figure 4.1](#). If the lens center coincides with the focus of the beam (case *a*), the rays are undeviated and the optical force is zero. If the lens is before the focus (case *b*), it increases the convergence of the beam and thus decreases the momentum flux of the light in the direction of propagation. The momentum lost by the beam is gained by the particle, which is pushed back to the focus. On the contrary, if the lens is beyond the focus (case *c*), it decreases the divergence of the beam and therefore increases the momentum of photons, resulting

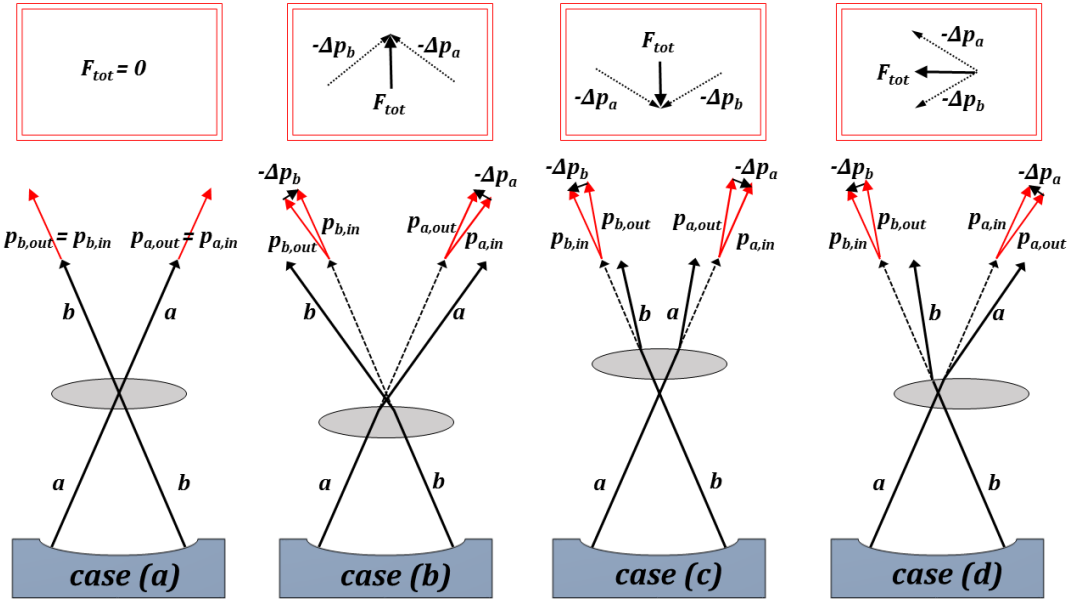


Figure 4.1 – Basic principles of optical trapping. A dielectric sphere acts as a converging lens. The changes in momentum flux result in restoring forces towards the laser focus.

in a restoring force toward the center. When the lens moves sideways—let’s say to the right, for instance—the laser beam is deflected and the counter force from the deflected photons will push it back to the left (case *d*).

Scattering and gradient forces in the Rayleigh limit In real situations, however, the light flux upstream and downstream the particle is not the same due to light reflection and adsorption. Both effects introduce a transfer of moment that pushes the trapped object in the forward direction, away from the focus. The resulting net force is called scattering force, and, in most conventional situations, is larger than the restoring (gradient) force due to refraction—the object cannot be trapped. To efficiently trap a dielectric microsphere, one needs to create a steep intensity gradient near the focus, to increase the convergence of the beam and thus the gradient force; this condition is achieved by sharply focusing the trapping laser beam to a diffraction-limited spot using an objective of high numerical aperture (NA).

In developing a theoretical treatment of optical trapping, it is useful to consider the case where the size of the bead is much smaller than the wavelength of the laser ($\lambda \gg a$). In these conditions, the sphere can be approximated as a dipole and the forces calculated analytically in the Rayleigh limit. According to [140], for a bead of radius a and index of refraction n_p immersed in a solvent of refractive index n_{md} , the scattering force is:

$$\vec{F}_{scat}(\vec{r}) = \frac{128\pi^5 a^6}{3c\lambda^4} \cdot \left(\frac{m^2 - 1}{m^2 + 2} \right)^2 \cdot n_{md}^5 I(\vec{r}) \hat{z} \quad (4.1)$$

where c is the speed of light in vacuum and $m = n_p/n_{md}$. The scattering force \vec{F}_{scat}

is proportional to the intensity of the laser and tends to push the trapped object out of the trap. The gradient force, on the other hand, can be calculated as:

$$\vec{F}_{grad}(\vec{r}) = \frac{2\pi n_{md} a^3}{c} \cdot \left(\frac{m^2 - 1}{m^2 + 2} \right) \cdot \nabla I(\vec{r}) \quad (4.2)$$

It is proportional to the gradient of the laser intensity and tends to attract the bead back to the focus. It forms a trapping potential:

$$V(\vec{r}) = -\frac{2\pi n_{md} a^3}{c} \left(\frac{m^2 - 1}{m^2 + 2} \right) I(\vec{r}) \quad (4.3)$$

Because the scattering force is proportional to a^6 , whereas the gradient force is proportional to a^3 , it follows from [Equations \(4.1\) and \(4.2\)](#) that F_{scat} decreases much faster than F_{grad} when the size of the particle decreases. Therefore, one may conclude that any sufficiently small (non-adsorbing) particle could be trapped. In practice, however, due to Brownian motion it is difficult to durably trap a nanosphere if its size is too small. Although the average kinetic energy $k_B T$ is independent of a , its instantaneous value follows the Maxwell–Boltzmann distribution, and therefore there is a non-vanishing probability that it exceeds by a large factor the mean value. Since the potential well decreases as a^3 ([Equation \(4.3\)](#)), a small particle may be able to escape from the trap by thermal fluctuations.

In practice, especially in micro-rheology experiments, the wavelength of the trapping laser is usually comparable to the diameter of the particle and one cannot use neither ray optics nor Rayleigh’s approximation to model the optical forces—a complete electromagnetic theory of light is called for. In recent years, there have been considerable improvements in the calculation, based on Lorenz-Mie theory [[140](#)], of optical forces in the most general situations. The mathematical calculations involved are quite complex and out of scope of this manuscript. Nevertheless, [Equations \(4.1\) and \(4.2\)](#) provide a simple yet good approximation for the forces at play in optical tweezers, also when the particle sizes is comparable to the laser wavelength.

4.1.2 Setup

The optical tweezers used in this work are a custom-built home made system depicted in [Figure 4.2](#). The instrument has been provided by the research group of Prof. E.M. Furst, from the Department of Chemical & Biomolecular Engineering of the University of Delaware.

The traps are generated by focusing a 4 W CWNd:YAG laser ($\lambda = 1064$ nm, Coherent Compass 1064-400M) to a diffraction limited spot within an inverted microscope (Zeiss Axiovert 200), to allow for simultaneous trapping and imaging with video microscopy. In order to increase the trapping efficiency and stability, the laser is expanded and collimated at the entrance of an high NA water immersion objective. To collimate the beam, the laser is firstly passed through two lenses (L_2 and L_3) of focal length $f = 100$ mm. A pair of orthogonal acousto-optic deflectors AODs

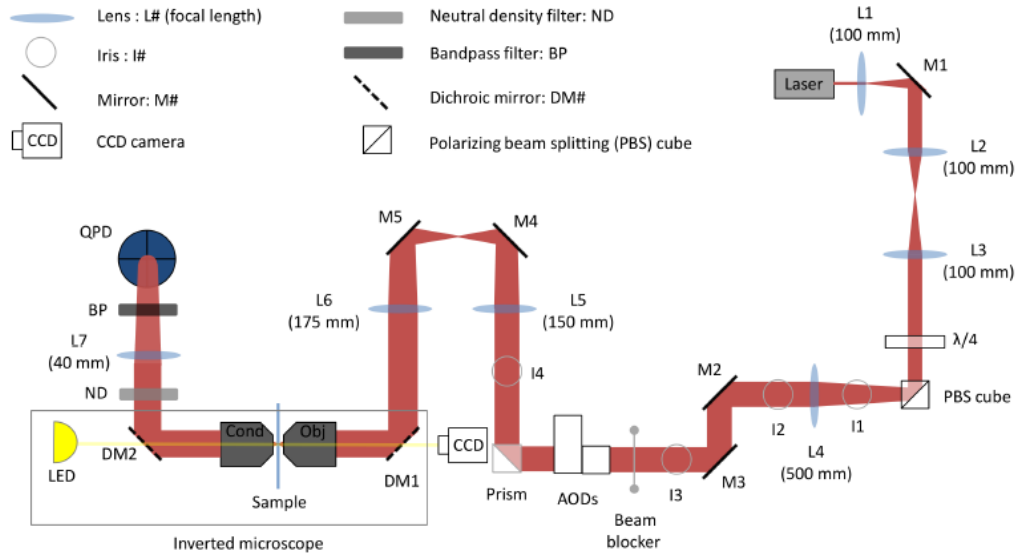


Figure 4.2 – Laser tweezers setup used in this thesis.

(Optoelectronics, AA.DTX.XU-400) are placed in the beam path to control the trap position within the trapping plane of the sample, by directing the angle of the beam at the back aperture of the objective. Briefly, an AOD consists of a transparent crystal (generally TeO_2) acting as an optical diffraction grating. The laser impinging the AOD is deviated due to density changes associated with the acoustic traveling wave inside the material. The angle of deflection depends on the frequency of the acoustic wave through:

$$\Delta\theta = \lambda f / v \quad (4.4)$$

where λ is the optical wavelength, and v and f are the velocity and frequency of the acoustic wave. The fast response times of the AODs enable us to reposition the beam in the focal plane with a minimum delay of $10 \mu\text{s}$, corresponding to a maximum scanning frequency of 100 kHz . This high-frequency and high-precision steering of a single beam allows us to simultaneously hold multiple particles by time-sharing the location of the trap. The laser is repeatedly scanned in a desired pattern of discrete locations with a return frequency faster than the characteristic Brownian diffusion time, resulting in a stable trapping of the particles [135].

After the AODs, another pair of lenses (L_5 with $f = 150 \text{ mm}$ and L_6 with $f = 75 \text{ mm}$) are arranged as a keplerian telescope. These lenses collimate and raise the level of the beam to reach the microscope and are arranged in such a way that the beam slightly overfills the back aperture of the objective to maximize the trapping efficiency [138]. The objective is a $63 \times \text{NA } 1.2$ water immersion microscope objective (Zeiss Objective CApochromat $63 \times / 1.2 \text{ W Cor } 441777-9970$). The use of a high numerical aperture water immersion objective presents a series of benefits; it maximizes the gradient force produced by the laser while reducing the effect of spherical aberrations in aqueous samples and increasing the working distance up to $200 \mu\text{m}$ from the cover-slip. The laser beam is a linearly polarized Gaussian beam

(TEM₀₀), with the polarization perpendicular to the propagation direction, and a beam waist that spreads next to the trapping plane as

$$\omega(z) = \omega_0 \left[1 + \left(\frac{z}{z_R} \right)^2 \right]^{\frac{1}{2}} \quad (4.5)$$

where ω_0 is the waist radius at the focus and $z_R = (\pi\omega_0^2)/\lambda_{md}$ the Rayleigh range, defined as the distance over which the beam radius spreads by a factor of $\sqrt{2}$, λ_{md} being the laser wavelength in the medium (see Figure 4.3). Note that the beam waist ω_0 is inversely proportional to the objective numerical aperture:

$$\omega_0 = \frac{\lambda_{md}}{\pi \text{NA}} \quad (4.6)$$

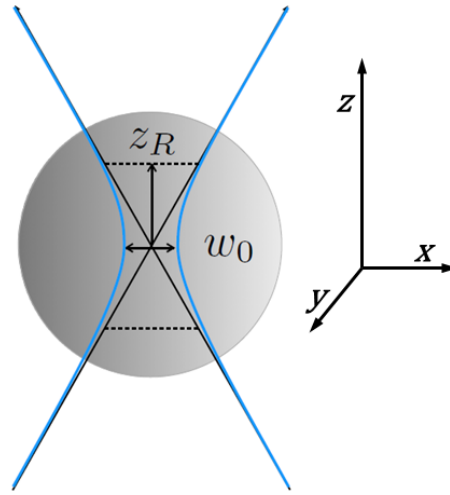


Figure 4.3 – Beam waist in the vicinity of the laser focus.

A long working distance objective (Zeiss Objective LD Plan-Neouar 40x/0.6 Corr M27 421360-9970) is positioned after the sample to act as a condenser to collect and recollimate the laser light after it passes through the sample. A dichroic mirror reflects the light collected from the back focal plane of the condenser onto a relay lens which projects the beam onto a quadrant photodiode (QPD; First Sensor, QP45-Q-HVSD) for particle position detection using back focal plane interferometry (BFPI). Sample positioning is achieved using a motorized microscope stage (Applied Scientific Instrumentation MS-2000-XY). A light emitting diode (LED) is used to illuminate the sample for imaging of the trapping plane. Images are acquired by a coupled device (CCD) camera (Hitachi, KP-M1AN), stored with an S-VHS video recorder (JVC HR-S9800U) at a rate of 30 frames/s, digitalized and then transferred to a computer using an image acquisition board (National Instruments NI-IMAQ 2.5.1). The same data acquisition card (DAQ; National Instrument, NI PCI-6221), controlled through custom software written in LABVIEW, is used to simultaneously control the input voltage across the AODs and the data acquisition from the QPD, resulting in a nearly perfect synchronization of the two tasks.

4.1.3 AOD calibration

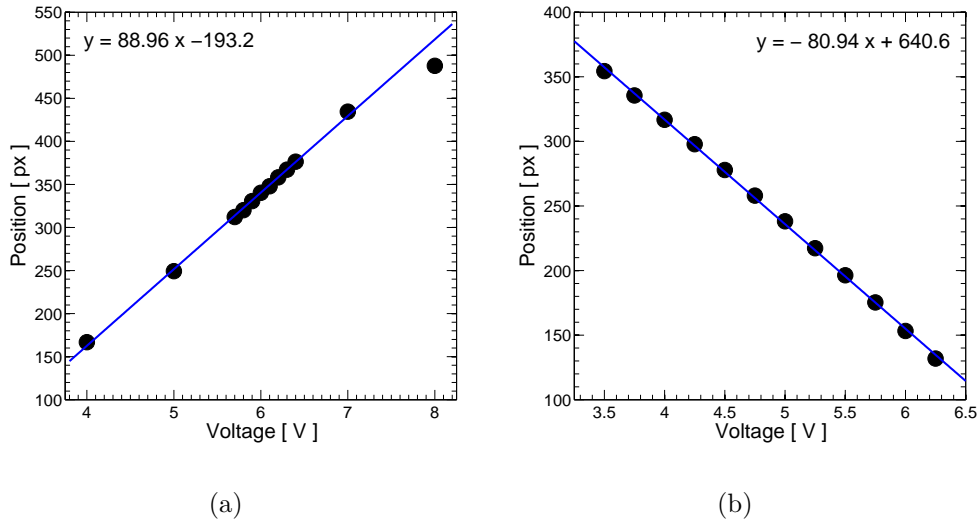


Figure 4.4 – Calibration of the AOD along the x (a) and y (b) directions. The retrieved sensitivities are respectively 88.96 pixel/V (10.40 $\mu\text{m}/\text{V}$) and -80.94 pixel/V (-9.47 $\mu\text{m}/\text{V}$).

A pair of AODs are placed orthogonally in the beam train to manipulate the position of the trap in both x and y directions. The AODs must be calibrated in order to know the relationship between the input voltage sent to the device and the displacement of the trap within the sample. To do that, we start by holding a particle in a stationary trap. Then, the voltage input to the AOD controlling the y -position is kept constant, while that provided to the AOD controlling the x -position is gradually changed in the desired range. For each voltage, we record ~ 100 images, enough to average out the effect of Brownian motion. The position of the trap versus input voltage is then estimated by the average position of the particle. The same procedure is repeated in the orthogonal direction, by changing the signal associated to the y axis and keeping a constant voltage for the x -controlling AOD. Calibration curves are shown in Figure 4.4; the slopes of the linear fit indicate the AOD sensitivities in the x (a) and y (b) directions. Note that the displacement of the trap in pixel units can be converted to a real displacement by knowing the pixel resolution of the camera, which is 0.117 $\mu\text{m}/\text{pixel}$ for the used 63 x water immersion objective.

4.1.4 Force calibration

To measure the optical forces on the trapped bead, one needs to determine separately the trap stiffness k_t and the displacement Δr of the particle from the equilibrium trap position. Under the assumption of a parabolic potential well, which hold for relative small displacements ($\Delta r \lesssim 0.5$ μm) [138], the force can be calculated through Hooke's law: $F = -k_t \Delta r$.

A large number of methods can be used to measure k_t ; we can classify them in two categories: active and passive ones. Active calibration techniques involve

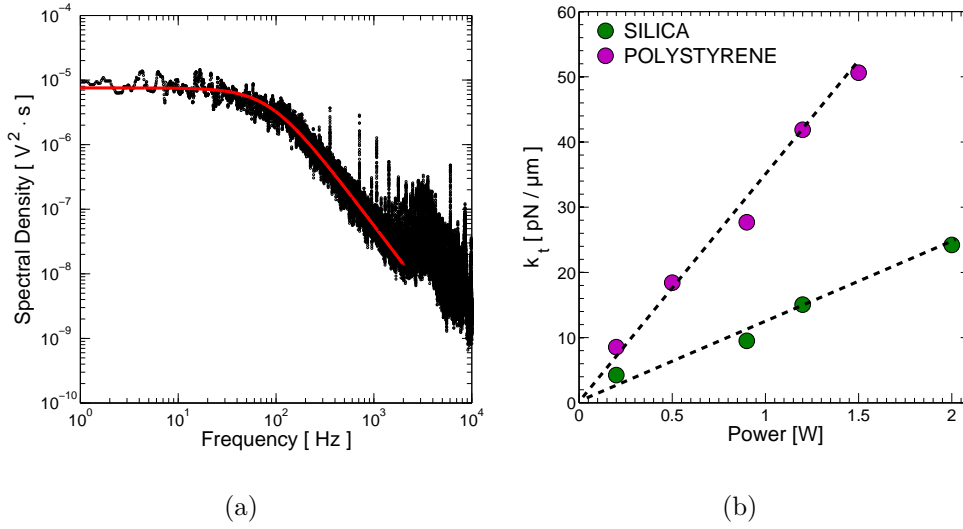


Figure 4.5 – (a) Power spectrum of a 3.27 μm PS bead recorded with a QPD in the back focal plane (black circles) and a fit to a Lorentzian (red line). The input laser power was set at 0.2 W and the measured trap stiffness is 8.53 pN/μm. (b) Radial stiffness of polystyrene (red circles) and silica (green circles) particles as a function of input laser power.

the application of known external forces on the trapped object until it experiences an identical and opposite restoring force. The most popular and direct method is the drag force technique, which consists in measuring the particle displacement in response to known viscous forces, *viz.* generated by moving the stage at known velocity. The sample holder can be displaced statically, *i.e.* with a constant speed, or dynamically, by applying a sinusoidal/square wave [138, 192]. A variant of this method consists in applying small step displacements of the laser (instead of the stage) and simultaneously recording the damped trajectory of the bead relaxing towards the new equilibrium position [179, 75].

Passive calibration techniques take advantage of the thermal energy supplied by the medium surrounding the particle. One approach involves measuring the power spectrum of the thermal-induced displacements, which is well described by a Lorentzian function for particles lying in an harmonic potential:

$$SS(f) = \frac{k_B T}{\pi^2 \beta (f_0^2 + f^2)} \quad (4.7)$$

where the roll-off frequency f_0 is related to the stiffness by $f_0 = k_t/2\pi\beta$, $\beta = 6\pi\eta a$ being the hydrodynamic drag coefficient. An example of a typical power spectrum, acquired by means of the QPD for a polystyrene particle of 3.27 μm in diameter, is reported in Figure 4.5(a). Note that one does not need to calibrate the QPD signal in order to measure the trap stiffness. Observe also that the power spectrum is sensitive to various noise sources. At high frequencies, analog signal processing circuits, power electronics, and AOD controller give rise to characteristic spikes, while in the low-frequency regime the noise contribution comes from laser wobble, drift, and statistical artifacts. This limits the frequency range of the fit to a small

interval, usually $[f_0/7, f_0/4]$ [179], and causes difficulties in the measure of the roll-off frequency when the trap stiffness is too small.

Thermal fluctuations of a trapped object can also be used to obtain k_t through the equipartition theorem:

$$\frac{1}{2}k_B T = \frac{1}{2}k_t \langle x^2 \rangle \quad (4.8)$$

where $\langle x^2 \rangle$ is the positional variance of the trapped object. In addition to the easiness of implementation, the main advantage of the equipartition method is that one does not need to know in advance the viscosity η of the solvent. However, the variance alone does not provide any information about the shape of the potential and eventual misalignment of the system.

In this work, the radial trap stiffness is measured by the power spectrum and equipartition methods. In each technique, we use a different strategy to find the positions of the trapped particle; in the former, they are estimated by the intensity fluctuations of the QPD signal, in the latter, they are inferred by measuring the centroid of the particle intensity distribution [41] in the CCD images. We usually find a good agreement between the values deduced from the two techniques.

Equation (4.3) indicates that k_t depend on three main parameters: the laser power, the bead diameter and the refractive index mismatch between the particle and the surrounding medium n_p/n_{md} [140]. To find the optimal working conditions for our silica particles, we measure the trapping stiffness as a function of the laser power supplied by the dedicated module and report the results in Figure 4.5(b). Note that the effective power arriving at the back aperture of the objective is typically reduced by $\sim 30\%$, due to losses in the beam path, especially within the AODs [140]. In addition, we compare the trapping efficiency versus refractive index using polystyrene beads with $2a = 3.27 \mu\text{m}$ ($n_p = 1.57$). As expected, the trap stiffness k_t is proportional to the supplied laser power for both particles, and is lower for the $1.9 \mu\text{m}$ silica bead ($n_p = 1.45$).

The maximum trapping force of n time shared traps depends linearly on the fraction of time per scanning cycle that the laser spends at the individual trap location [145]. This means that it decreases when one manipulates multiple particles at the same time. Since in the following bending experiments we shall use a three-point geometry, k_t is measured using three time-shared traps. For $1.9 \mu\text{m}$ silica beads, we achieve a maximum trapping stiffness of $(6.50 \pm 0.15) \mu\text{m}$, while for PMMA particles ($2a = 3.0 \mu\text{m}$) we obtain $(3.50 \pm 0.30) \mu\text{m}$. Later, we will use these values in the calculation of the forces acting on our particles.

4.2 Experimental procedure

In [145] Pantina and Furst used Laser Tweezers to directly assemble colloidal aggregates and study their mechanical response under tensile stresses. Interestingly, they found that the strength of the bonds between poly(methyl methacrylate) PMMA particles in divalent salts solutions was ≈ 10 times greater than that predicted by the Derjaguin-Landau-Verwey-Overbeek theory. Later [146, 147, 71], by measuring the elasticity of particle rods in response to a bending moment, they also provided the first experimental evidence that colloidal particles in contact are capable of transmitting torques. The above observations were in sharp contrast with DLVO theory, for which free rotation of the particles was expected, since only central forces can be transmitted through contact. Inspired by these pioneering studies, in this work we replicate similar three-point bending tests on silica and PMMA particle rods to evidence the formation of solid-solid contacts and their aging dynamics.

4.2.1 Materials

For the silica system, we focus on beams formed using a single particle size $2a^* = 1.9 \mu\text{m}$. The choice of this value results from a compromise between different constraints: on the one hand, the higher a , the broader the range of accessible forces (given the silica/water optical index contrast [140]) and the better the evaluation of particle positions at sub-pixel accuracy; on the other, it is difficult to synthesize large monodisperse particles. The chosen a value limits polydispersity to 5%, while allowing us to access the desired rod properties.

The particles are dispersed in MilliQ water and diluted to a volume fraction of $\phi \approx 10^{-4}$, low enough to easily manipulate multiple traps without interference of stray particles. Before each micro-mechanical experiment, the particle solution is vigorously stirred and left in ultrasonic bath for 2 minutes. The double-layer repulsion is screened through the addition of calcium chloride (CaCl_2 , Sigma-Aldrich) at various ionic strengths, $I = 0.05, 0.10, 0.15$ and 0.20 M. The same procedure is applied to test the response of silica particle rods in monovalent salt solutions (KCl) at a single I , namely $I = 0.20$ M.

We also form and follow in time PMMA particle beams using the same protocol. Particle sizes are distributed around $3 \mu\text{m}$ with a 15% polydispersity. We use various CaCl_2 ionic strengths, $I = 0.05, 0.20, 0.40, 0.60$ and 0.80 M and NaCl concentrations ($I = 0.20, 0.30, 0.50$ M).

4.2.2 Sample cell

The sample cells are made using a double-sided adhesive spacer to create a gap between a microscope slide (Fisher, size $25 \times 75 \times 1\text{mm}^3$) and a coverslip (Fisher, size $22 \times 30 \times 0.17\text{mm}^3$). A difficulty we encountered is that, at the targeted salt concentrations, both SiO_2 and PMMA particles, which sediment due to density contrast, stick so strongly to the coverslip that they cannot be detached with the tweezers. To be able to manipulate these particles, we need to postpone the time when particles enter in the saline solution. We achieve this by dividing

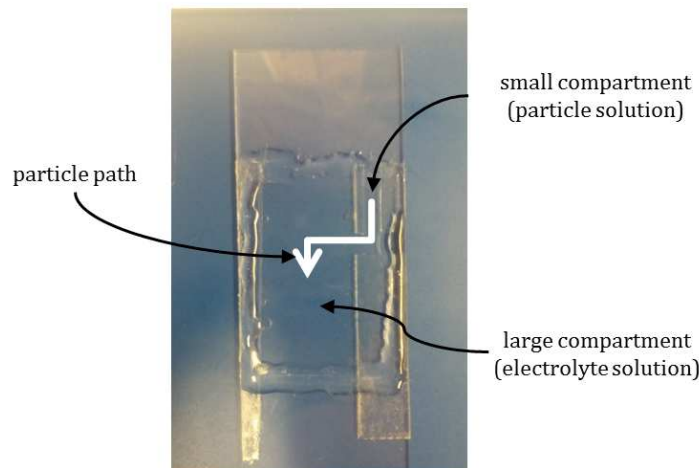


Figure 4.6 – Photograph of the sample cell. The black arrows indicate the different regions of the cell while the white arrow displays the path of the traps before beam assembly. For more details, see the text.

the cell into two compartments carved in the adhesive spacer: a small ($\sim 7 \mu\text{L}$) one, where the diluted suspension of particles in pure water is introduced; a large one ($\sim 50 \mu\text{L}$), where the electrolyte solution is introduced. To prevent drying, the whole cell is sealed using a fast UV-curing epoxy (Norland Products, NOA 81) immediately after the introduction of the ionic solution and suspended particles. The two compartments are in open contact with each other through a small aperture, which sufficiently slows down salt diffusion that particles, although they sediment, do not stick to the coverslip, and can be handled, for nearly 2 hours. The size difference between the two compartments guarantees that even after the complete diffusive dispersion of salt the relative error in the ionic strength remains smaller than $\approx 5\%$. A photograph of the sample cell is shown in [Figure 4.6](#).

4.2.3 Assembly of particle rods

We form beams of 11 or 13 particles using a method similar to that described in [\[146\]](#). First, an array of n traps, where n is the number of particles in the rod, is created by time-sharing a single laser beam. The traps are separated by a distance much larger than the particle diameter, to avoid interactions ([Figure 4.7\(a\)](#)). Thereafter, they are filled by actively seeking particles in the small compartment by translating the microscope stage. Once the array completed, it is moved at approximately half of the depth of the sample cell ($\approx 100 \mu\text{m}$), and then towards the ionic solution (large compartment) by means of the motorized microscope stage (white arrow in [Figure 4.6](#)). This requires a very small amount of time, but care must be employed to avoid losing particles due to drag forces; positioning the traps in the center of the electrolyte compartment is achieved in less than 2 minutes. Thanks to the cell design, the experiments are carried out in a region where stray particles entering the trapping plane during the measurements are absent.

Differently from [\[146\]](#), where the rods are formed by reducing the distance be-

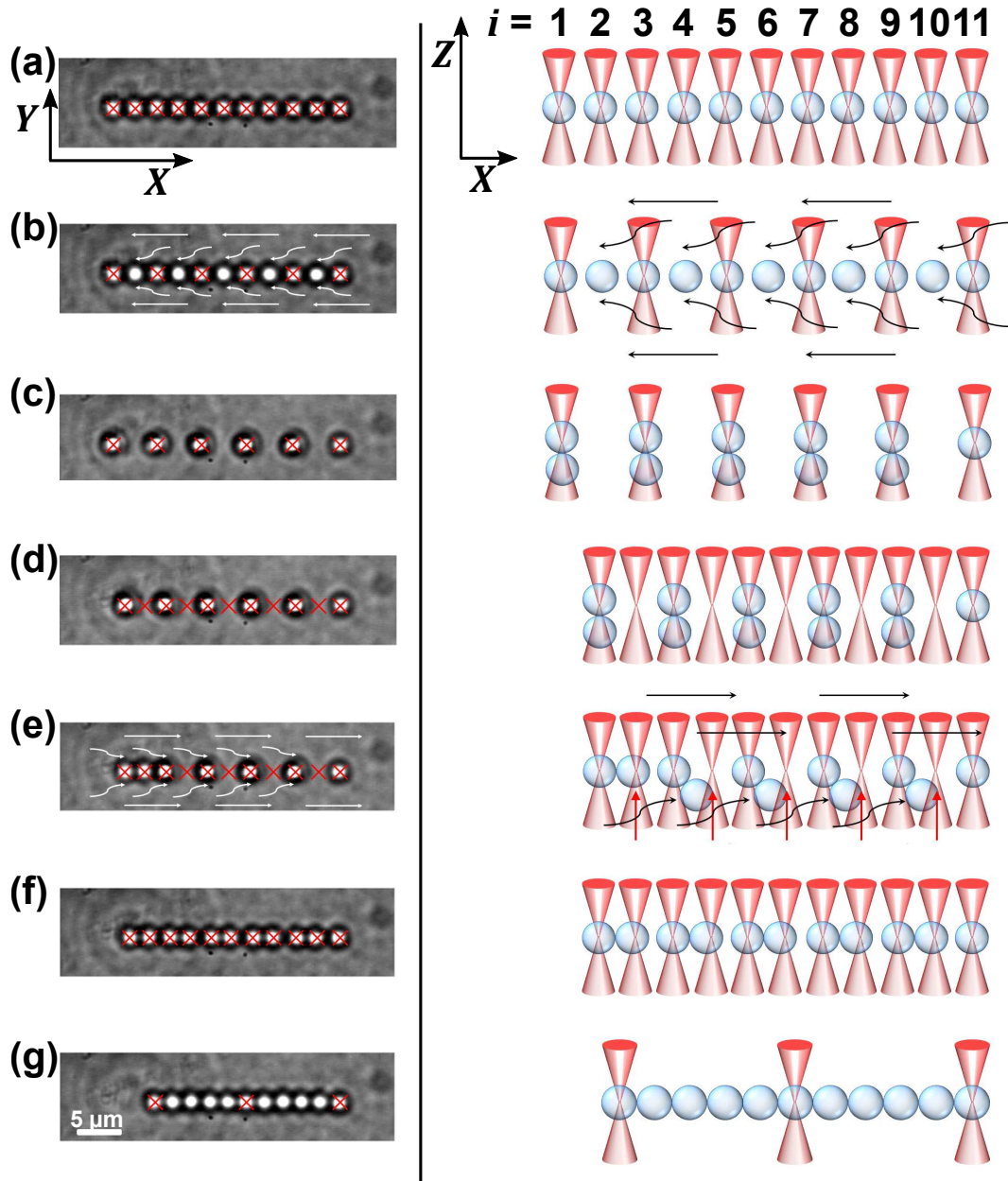


Figure 4.7 – Typical rod assembly. Images of the particles (left panel) and their position in the XOZ plane (right panel) during the formation of the beams. In the real images, the traps are drawn with red crosses.

tween the traps until vdW forces induce aggregation, the assembly of silica rods adopted here consists in simultaneously trapping two particles in a single trap. It presents various benefits: on the one hand, it permits to better control the assembly time, thus reducing scatter between different rods. On the other hand, it reduces the rod tortuosity that inevitably arises in the assembly process, as the pairs are more stable than isolated particles against fluctuations caused by Brownian motion. The proposed method can be understood looking at Figure 4.7. In the first column we report the photographs taken with the CCD camera in the XOY trapping plane, while in the second column we plot a schematic representation of the traps and par-

ticles in the XOZ plane, parallel to the laser propagation direction. Each line [(a) to (f)], instead, describes a step of the process. The traps (particles) are ordered according to the X axes as shown on the top of the figure.

Starting from well separated $n = 11$ traps (particles), stage (a), we rapidly remove the traps in the $i = \text{even}$ ($i = 1, \dots, n$) positions and simultaneously apply a drag force to the left, by moving the motorized microscope stage, as shown by arrows in (b). This forces the $i = \text{even}$ particles to move (instantaneously) toward the respective neighboring traps to the left. We thus end-up in (c) with 5 pairs (bonds) filling the leftmost odd traps and an isolated particle within the rightmost trap. This moment defines the time origin for the assembly process. Note that the pairs are oriented along the vertical axis and that their centers of mass lie slightly below the focus of the laser due to gravity. Then, we slightly reduce the distance between the traps, yet by an amount which still guarantees that their separation remains much larger than the particle diameter, and the $n = 11$ traps are restored, stage (d). Stage (e) consists in applying a drag force to all the particles in the right direction, which, together with the scattering force of the laser of the empty traps, imparts a torque to the pairs that are able to realign with the trapping plane. Once all the pair are re-positioned in the XOY plane, stage (f), the distance between the traps is reduced until all the remaining bonds form due to vdW forces. The formation of the last contact is taken as the origin of (aging) time for the beam evolution. The full aggregation of a beam takes a time of order a minute after the formation of the first bonds, i.e. between stages (c) and (f). Finally, the beam is held only by three traps: two at its extremities, one at its center (Figure 4.7(g)).

For the PMMA particles, we are not able to simultaneously hold two particles in the same trap, probably due to their larger size and refractive index. To form the rods, therefore, we simply apply the standard procedure described in [146].

In Figure 4.8(a) we report the particle center-to-center distance ($\Delta_i x = x_{i+1} - x_i$) during the stage (f) of the silica beam assembly, *viz.*, when we reduce the separation between the traps. We recall that 5 bonded pairs ($i = 1, 3, 5, 7, 9$) are already formed during this stage, and hence we expect their center-to-center distance to remain constant. This is indeed the case, as shown in the left panel of Figure 4.8(a), where we add a $1 \mu\text{m}$ offset to each curve to avoid superposition of the data. Conversely, the curves corresponding to the $\Delta_i x$ with $i = \text{even}$, display a very different behavior, since now large discontinuities, associated with the formation of the bonds, are clearly visible (black arrows in right hand panel of the same figure). We replot in Figure 4.8(b) the same data without offset to highlight the bond formation; due to large vdW attractive forces, the particles suddenly jump into contact, so rapidly that their motion cannot be resolved by our high acquisition rate camera (30fps). The mean jump is of the order of 80 nm , around 2-3 times the resolution of the centroid tracking algorithm in the confocal experiments. This large value supports that one can exclude the formation of new contacts during time in the macroscopic suspensions, as these jumps should be resolved by confocal image analysis.

Once formed, a rod remains stable for hours when held by just three traps acting on the particles (Figure 4.7(g)): this establishes that particles form cohesive contacts that do not break by thermal activation over the considered timescales. All

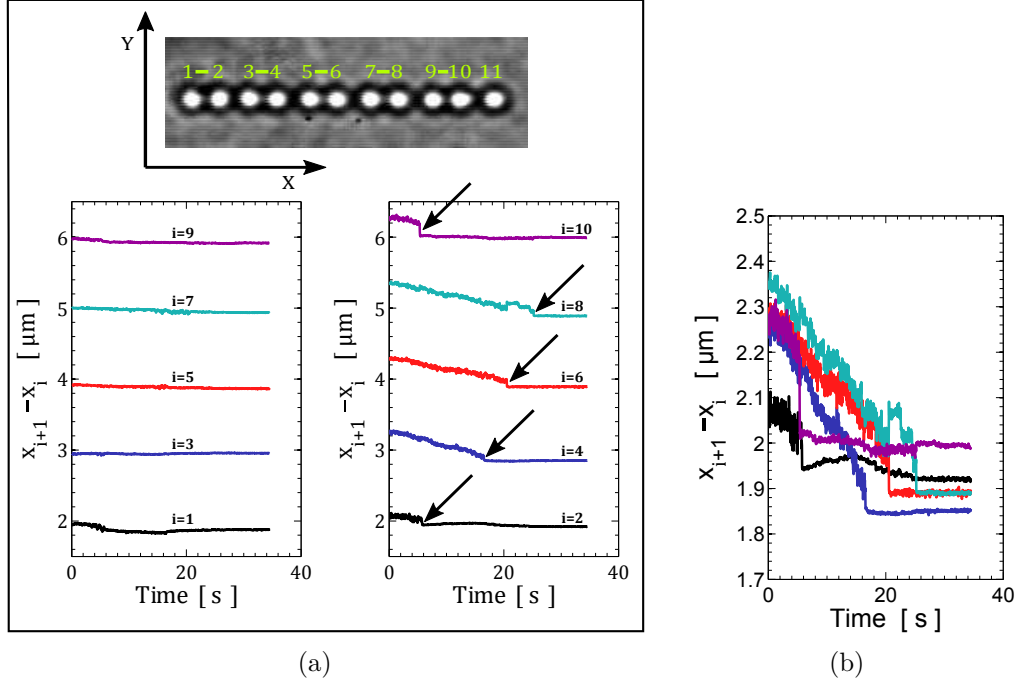


Figure 4.8 – Formation of the bonds between pairs during stage (f) of rod assembly. (a) We report the particle center-to-center distance as a function of time, during which the traps separation is reduced. Curves are offset by 1 μm. The $\Delta_i x$ of particles already at contact during this stage are denoted with odd i . The contacts, (even i , right panel) are formed when vdW forces overcome the trapping restoring forces, and are indicated by black arrows. Upper panel shows a photograph of the particle disposition at $t = 0$ (particles already in contact are joined with a dash). (b) Same data as in the right panel of (a), without offset.

these observations bring decisive support to the idea that suspension microstructure stabilizes shortly after cessation of pre-shearing.

4.2.4 Three-point bending experiments

Bending is enforced by translating the center trap perpendicularly to the chain, at a velocity slow enough for the hydrodynamic drag to remain negligible, while the two other traps are held fixed. The center trap is moved either with a sinusoidal or a triangular wave, with a maximum amplitude of ≈ 3.8 μm and velocity ranging between 10 and 40 nm/s. We do not find significant changes in the results for these different loading conditions.

We collect a series of images at a rate of 30fps during each loading ramp and, using a centroid algorithm [41], compute the particle positions at sub-pixel precision, at least of ≈ 35 nm. In Figure 4.9(a), we show typical microscopy images of a rod of SiO₂ particles at different bending levels. As illustrated, X is the axis passing apparently (on the image) through the centers of end particles and Y the perpendicular direction. Both axes lie by definition in the focal plane of the microscope. Since we know the trap stiffness, the bending force $F = k_{trap} \cdot \Delta Y$ is essentially obtained by monitoring the Y -displacements of the end particles from their initial positions, i.e.,

from the positions of the associated (fixed) traps; the deflection Ξ may be accessed from the differences in Y of the end and central particles.

For the SiO_2 particles rods, however, the raw data thus inferred from Y displacements

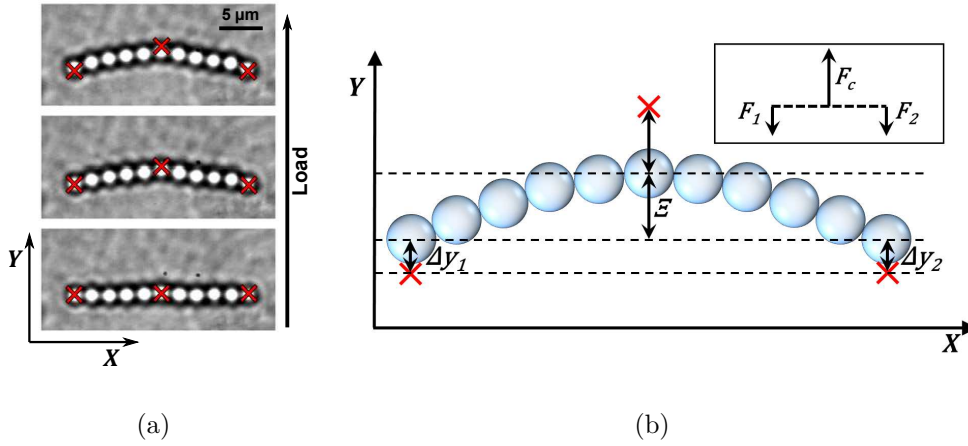


Figure 4.9 – Microscope images (a) and a sketch (b) of the three-point bending experiment. The bending moment is applied by translating the central trap along the Y direction. Two stationary traps are positioned on the two end particles and used as force sensors.

ments alone have to be corrected to take into account mainly two problems:

- (I) rods are not strictly linear,
- (II) the optical traps and microscope focal planes are not perfectly aligned.

In [Section 5.1](#) we will explain in detail how we can correct the data and access more accurate values of the force (f) and deflection (δ). For the moment, let us start by assuming that the trap plane is perfectly aligned with the focal plane of the microscope. A sketch of the three-point bending geometry is reported in [Figure 4.9\(b\)](#). As illustrated, we denote F_c , F_1 and F_2 the forces exerted, along axis Y , by optical traps, on the center and end particles (resp.). In mechanical equilibrium, $F_c = -F_1 - F_2$ and $F_1 \simeq F_2$ (slight departures from this equality may arise from misalignment). The center particle, hence, sustains a force $|F_c| \simeq 2|F_1| \simeq 2|F_2|$, which is twice larger than the end ones. For all the studied beams, since the forces F_1 and F_2 are twice smaller than F_c , the displacements of the end particles remain within the range where the trapping potential is harmonic [\[181\]](#). This allows us to estimate the bending force $F = |F_c| = |F_1| + |F_2|$ as $F = 2k_{\text{trap}} \Delta Y_{\text{end}}$ with k_{trap} the trap stiffness, and $\Delta Y_{\text{end}} = (\Delta Y_1 + \Delta Y_2)/2$ the average displacement of the end particles from the corresponding trap centers. The latter are identified by image analysis as the positions at rest of end particles. Note that the Y -displacements in [Figure 4.9\(b\)](#) are exacerbated for visual inspection.

Typical bending force data as a function of $\Xi = Y_c - (Y_1 + Y_2)/2$, the apparent rod deflection, are shown in [Figure 4.10\(a\)](#), in blue. Clearly the rod does develop a force but only when Ξ increases beyond some threshold Ξ_0 , which we found to vary significantly between 0 and $2 \mu\text{m}$ depending on the rod. We understand this feature as arising from the fact that rods are not perfectly straight, but present in general

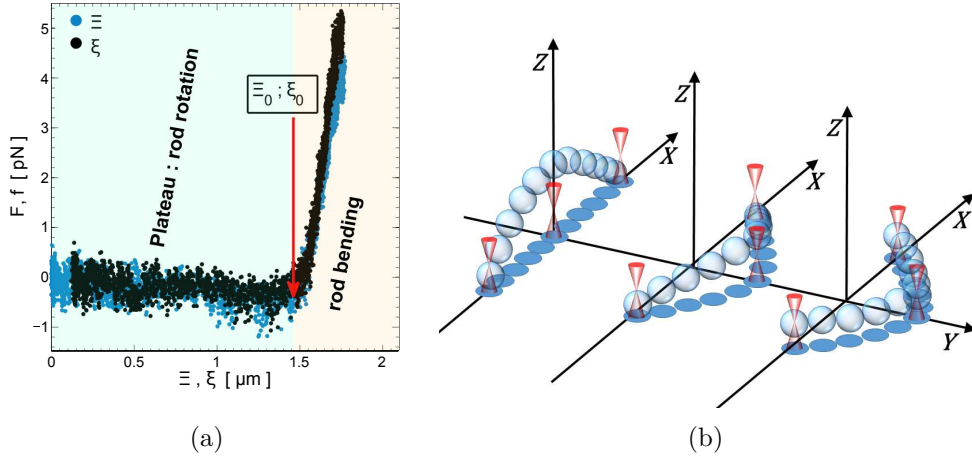


Figure 4.10 – (a) Raw (blue) and alignment-corrected (black) force vs relative displacement data. (b) 3D particle beam rotation in the force plateau region of (a).

a curvature at rest. Since the relative weight of a rod is about 0.04 pN , the torque induced by gravity and the lack of linearity, remains below experimental resolution, so that the rod rotates as a rigid body without showing a measurable force before it lies in the plane of the three traps, which happens when $\Xi = \Xi_0$, as schematically shown in Figure 4.10(b).

Direct evidences for this are reported in Section 5.1. Moreover, we will explain how the brightness of each particles can be used to reconstruct the full 3D trajectory of the rod. This enable us also to correct for misalignment between the optical traps and microscope focal plane. We label x, y, z the new axes after this correction: x is now aligned with the centers of the end particles, and y the perpendicular axis in the plane of the traps. We also label with f and ξ the recalculated bending force and deflection. The corrected f versus ξ curve is reported in Figure 4.10(a), in black. Unlike the SiO_2 particle beams, PMMA rods did not show substantial rotation during loading, probably due to the their lower density.

Next, in order to associate the measured force with the bending of the rod, we need to subtract the initial curvature from the particle positions in the load state, and show that the subsequent deformation is consistent with a bending response. To proceed, we take as reference the particle coordinates y_i^0 ($i = 1, \dots, n$) when $\xi = \xi_0$ (i.e at the onset of the load), and calculate the values of the displacements $\delta y_i = y_i - y_i^0$ at different higher loading levels. Hence, we define the true rod deflection as:

$$\delta = \xi - \xi_0 \quad (4.9)$$

Let us note that we cannot exclude the existence of an initial pair of opposite (tensile or compressive) forces acting on the end particles and aligned along the x axis. We have checked that these forces remain negligible, however. Indeed, during the whole test, the leftmost trap is left at a fixed position. We checked the absence of significant drift by observing that the associated particle fluctuates around the corresponding stationary trap position before it becomes engaged in the rod. After the rod is

fully formed, this particle has sustained along the x axis a certain displacement, of order ± 60 nm at most. The associated initial residual force (tensile or compressive) is thus of amplitude at most $\simeq 0.4$ pN, which is within the error bar of our force measurement. Note also that the bending test is not strictly performed in pure flexion because the end traps are held at fixed positions and thus exert a force along x on the associated particles. These forces, however, remain negligibly small: their maximum amplitude, reached only at the highest bending level, is of order 0.3 pN. This guarantees the validity of our flexural measurement.

4.2.5 Loading cycle

To investigate the relevance of contact aging, three-point bending experiments are replicated with the same rod, at different aging time after its assembly (between ~ 20 to ~ 1900 s). After each loading ramp, the center trap is gently repositioned collinear with the other ones, according to the imposed waveform. The images are analyzed at the end of the full loading cycle. In some tests, the f vs ξ curve shows drops associated with non elastic rearrangements. To make sure that we access the elastic regime of rods in which the interparticle contacts have similar aging time, i.e. that have not rearranged during the several loading ramps of each experiment, the bending data are sorted by applying the following criteria:

- (1) rods with large initial defects (curvature) and strong deviation in shape from the Euler-Bernoulli theory are ignored.
- (2) the data of the first ramp R_1 are always kept. Possible rearrangements are counted and stored.
- (3) the second ramp R_2 is kept only if no rearrangement is present in the previous (first) ramp R_1 . In this case, the data are considered and eventual rearrangements are counted and stored.
- (4) the subsequent ramps R_i are kept only in the absence of rearrangements in all the previous ramps $R_{j < i}$, like in (2). However, the data can be retained, even in the presence of rearrangements, if another condition is met. This corresponds to cases where the time difference between the considered ramp R_i and the last ramp in which we detected some rearrangements, R_k , exceeds about $20 \times t_k$, where t_k is the aging time of R_k . For our data set, this happens only when $t_i > 20$ min, so that t_k do not exceed 1–2 minutes, a time comparable to that elapsed during the beam assembly. Due to uncertainties in defining a time origin for the beam evolution (recall that not all the bonds are formed exactly at the same instant), the aging time of ramp R_i is little affected by rearrangements in R_k ; hence we decided to preserve the same time origin for both ramps.

4.3 Elasticity of particle rods

4.3.1 SiO₂ particle rods

Divalent salt (CaCl₂)

Previously, we showed (Figure 4.10(a)) that the rods develop a force only beyond a critical deflection value ξ_0 , past which f increase with deformation $\delta = \xi - \xi_0$. A typical force-deflection curve, after subtraction of the initial curvature, is reported in Figure 4.11(a). At the beginning of the load, f increases linearly with δ . Eventually, when the force reaches a critical value f_c , the stress in the aggregate is relaxed via small-scale movement of adjacent particles and f abruptly drops to lower values, while the deflection continues to increase. For the moment, we focus on the linear domain below f_c .

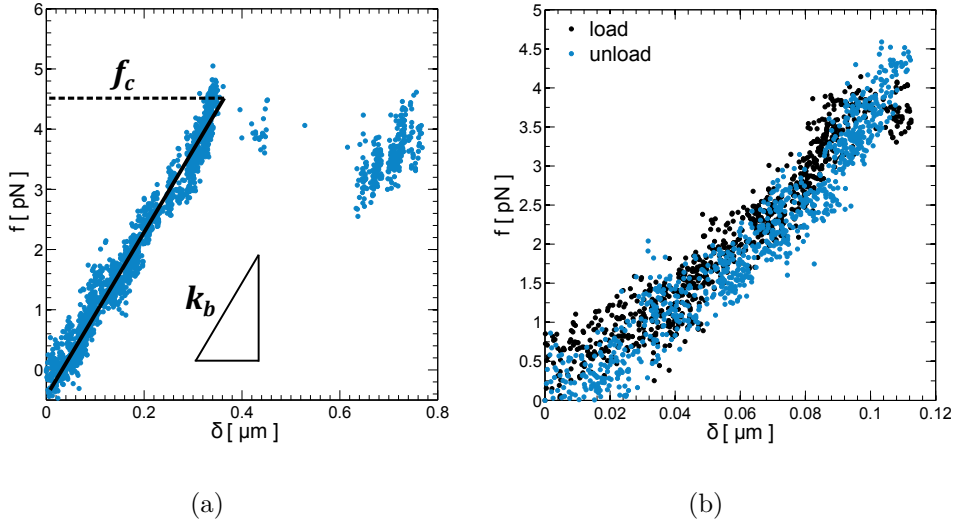


Figure 4.11 – (a) A typical f versus δ curve, after corrections for misalignment between the optical traps and microscope focal plane. (b) Elastic response of the rods. Load (black points) and unload (blue points) data, for a $n = 13$ particle beam with $I = 0.20$ M and $t \approx 1870$ s.

The first question we want to address is if the observed behavior is related to an elastic response of the rods. We investigate the beam response during a loading-unloading ramp. As shown in Figure 4.11(b), we obtain a nearly perfect superposition of the load (black points) and unload (blue points) data. This confirms that the rods respond elastically as the process is reversible. Secondly, we want to demonstrate that the measured force can be related to a bending resistance. We thus examine the shape of the rods under increasing bending loads. Remarkably, as shown in Figure 4.12, the δy_i vs x_i curves systematically fit very well the Euler-Bernoulli expression (dashed lines):

$$y(x) = \frac{-f}{2E\hat{I}} \left(\frac{Lx^2}{4} - \frac{|x|^3}{6} \right) \quad (4.10)$$

where E is Young's modulus, \hat{I} is the area moment of inertia, and $L = 2a(n - 1)$ is the length of the aggregate, i.e. the distance between the centers of the end particles (a is the particle radius). The curvature of the rods does demonstrate the existence of tangential restoring forces that prevent particles from undergoing free rotation in response to a bending moment. Otherwise, we should have obtained a triangular structure with a pivot point at the center particle. Note that Equation (4.10) holds for a continuum beam, wherein the deformations are uniformly distributed. In our aggregates, we expect the deformations to be primarily localized at the contacts, whereas the bulk of the particles remains substantially inactive. We could model our system with a discrete chain of rigid segments, connected by torsion springs of stiffness k_r . In Appendix E we demonstrate that such a discrete chain assumes a shape that is fully in accordance with Equation (4.10), providing that the number of segments is not too small.

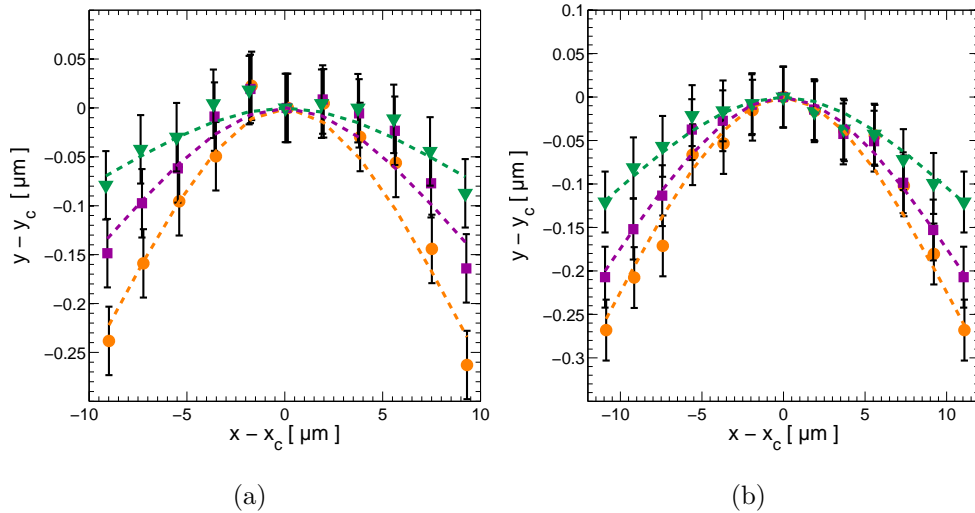


Figure 4.12 – Reconstructed rod deflection in the trapping plane at various increasing (green-purple-orange) loading levels for (a) an 11 particles beam, $I = 0.15$ M and (b) a 13 particles beam and $I = 0.10$ M. Dashed lines are the best fits of the data with the Euler-Bernoulli equation.

We collected a large number of data by performing such three-point bending tests on different particle rods and ionic strengths between 0.05 M and 0.20 M. The data are then sorted using the criteria described in the previous section. Such experiments yield the first substantial observation:

- (l) **rods bend according to the Euler-Bernoulli equation in the linear elastic regime.**

The chain elasticity can be described by the bending rigidity k_b :

$$k_b = \frac{f}{\delta} = \frac{f}{y(L/2)} = \frac{48E\hat{I}}{L^3}, \quad (4.11)$$

which is inferred from the force-deflection data, by performing a linear regression with both errors in x and y , following the method in York et al. [212]. Due to the large number of experimental points, the confidence intervals of the fits usually correspond to very small error bars; the main source of uncertainties, however, is related to the choice of the set of data points to include in the fit, as sometimes the transition between the force plateau and the linear domain is not well defined. We disregarded all the data where this transition was not clearly identifiable. Point (I) suggests that the single bond bending stiffness is independent of the rod length. Hence, we can define an effective single-bond rigidity through [105, 107]

$$k_0 = k_b \times \left(\frac{L}{a}\right)^3 \quad (4.12)$$

Using Equation (4.11) for k_b , one obtains

$$k_0 = \frac{48E\hat{I}}{a^3} \quad (4.13)$$

which is indeed independent from L . Note also that k_0 has the same dimension of k_b (N/m). In the following analysis we will use this elastic constant, instead of a torsion rigidity k_r (in N · m). This choice will not influence the subsequent results, since the two elastic constants are proportional (see Appendix D):

$$k_0 \sim \frac{96k_r}{a^2} \quad (4.14)$$

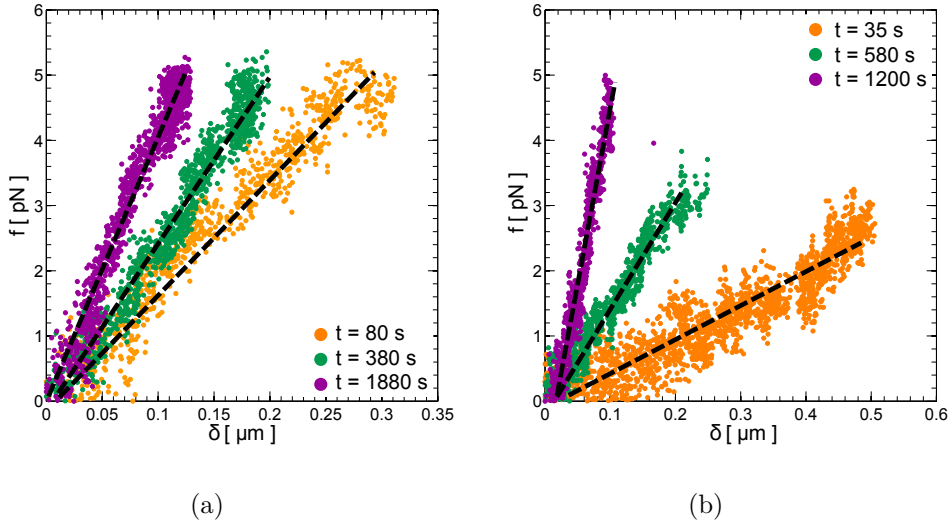


Figure 4.13 – Force f vs beam deflection δ after three aging times for (a) $n = 11$ particle beams with $I = 0.15$ M and (b) a $n = 13$ particle beams with $I = 0.10$ M

In Figure 4.13 we plot typical force-deflection curves at various aging times, for two different ionic strengths. Strikingly, the bending modulus increases over time, suggesting that the rods strengthen when held at rest in the optical traps. By analyzing our full data set, we conclude that:

(II) k_b grows over time.

Since $k_b(t) \propto k_0(t)$, we conclude that the strengthening of the rods results from the stiffening of the bonds between particles. We collect in [Figure 4.14\(a\)](#) both 11 and 13 particles rod data to assess that indeed the bond-stiffness k_0 is independent of L . This plot furthermore demonstrates that:

(III) flexural rigidity reaches a roughly logarithmic growth regime at late times.

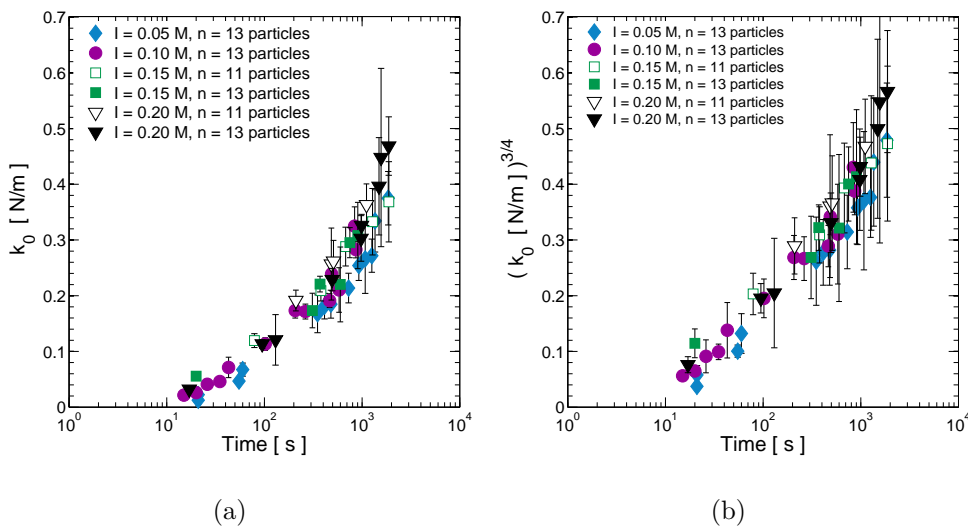


Figure 4.14 – (a) Bond stiffness k_0 as a function of time t for different ionic strengths, as measured from three-points bending tests with different rod lengths L , with error bars showing the confidence interval of the linear fit of f vs δ data. (b) Log-lin plot of $[k_0]^{3/4}$ vs t supporting that asymptotic growth is rather $\simeq [\log(t/\tau)]^{4/3}$ as suggested by our arguments (see later in the text for details).

Observe, however, that $k_0(t)$ shows an upward curvature, so that a logarithm can only be fitted over less than a decade. Curiously, we find that the logarithmic growth can be extended to all studied decades by plotting $[k_0]^{3/4}$ vs t —see [Figure 4.14\(b\)](#). Arguments supporting this scaling will be presented later in the text. Note also that our data set covers different I values and supports that k_0 is I -independent over the considered range, although a slight increase with salt concentration cannot be excluded. This observation can be ascribed to the fact that, above $I \approx 0.05$ M, the zeta potential of our particles saturates (to $\simeq -10$ mV), i.e. that the surface charge is essentially I -independent (see [Section 3.1.4](#)).

Let us emphasize two key conclusions we may already draw from our above observations. First of all, point (I) demonstrates the formation of solid-solid contacts between particles as non-adhesive bonds cannot show elastic restoring forces in response to rotational motion. Indeed, the fact that these contacts are able to support

torques can be attributed only to the pinning of the solid-solid contact line. Secondly, the evolution of the effective flexural rigidity of bonds, point (II), can only be ascribed to an evolution occurring inside these adhesive contacts. Such a contact aging between colloidal silica particles in CaCl_2 solutions has never been directly observed before. We also stress that these observations are not consistent with the DLVO framework, for which the forces are centro-symmetric and time-invariant.

Monovalent salt (KCl)

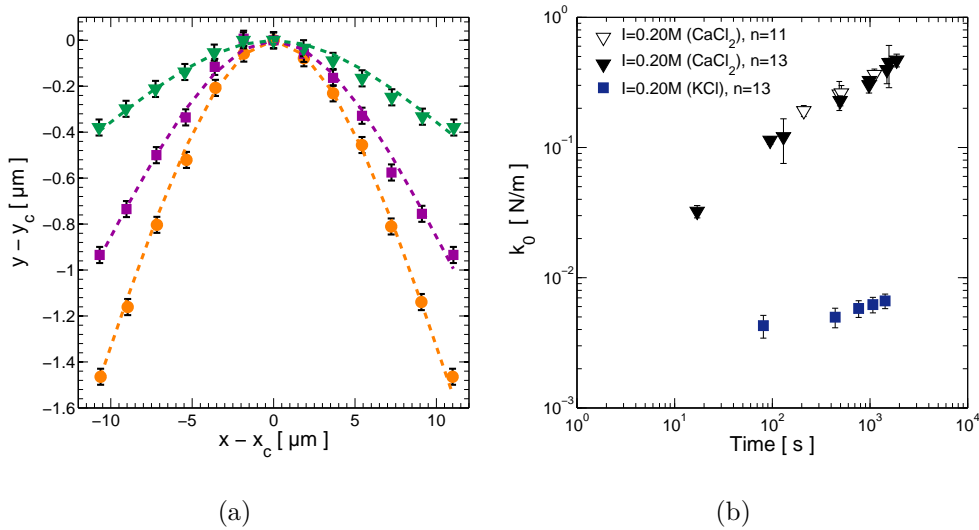


Figure 4.15 – (a) Shape progression at increasing bending loads for a rod in KCl solution. (b) Log-log plot of the bond stiffness vs time for CaCl_2 (black symbols) and KCl (blues symbols) at the same ionic strength.

We perform also bending tests on SiO_2 rods in KCl electrolyte solutions at a single $I = 0.20$ M. Interestingly, for lower salt concentrations we are unable to form stable rods. At $I = 0.20$ M or higher, instead, we do not find beam ruptures for time interval of about 1h, indicating the formation of strong thermally irreversible bonds. Moreover, in these conditions the rods follow the Euler-Bernoulli bending theory in analogy with the divalent salt (Figure 4.15(a)). The above observations suggest the existence of a critical ionic concentration below which electrostatic repulsion prevents the beads to form contacts.

In Figure 4.15(b) we report the k_0 vs t data for the considered I and compare them with the values in the divalent salt solution. With KCl the bond rigidity is about an order of magnitude lower than that found with CaCl_2 . Note also that the KCl salt concentration at this ionic strength corresponds to 3 times the divalent salt concentration. This highlights the dramatic effects of divalent electrolytes on the potential and counter-ion distribution at the surface of the particles. These data also indicate that the valency of the salt may have a substantial effect on the aging dynamics of the contacts, as k_0 appears to increase more slowly in the presence of K^+ cations. These findings underline the potential relevance of ion species in the formation and subsequent aging dynamics of the contacts between silica particles.

4.3.2 PMMA particle rods

Divalent salt (CaCl_2)

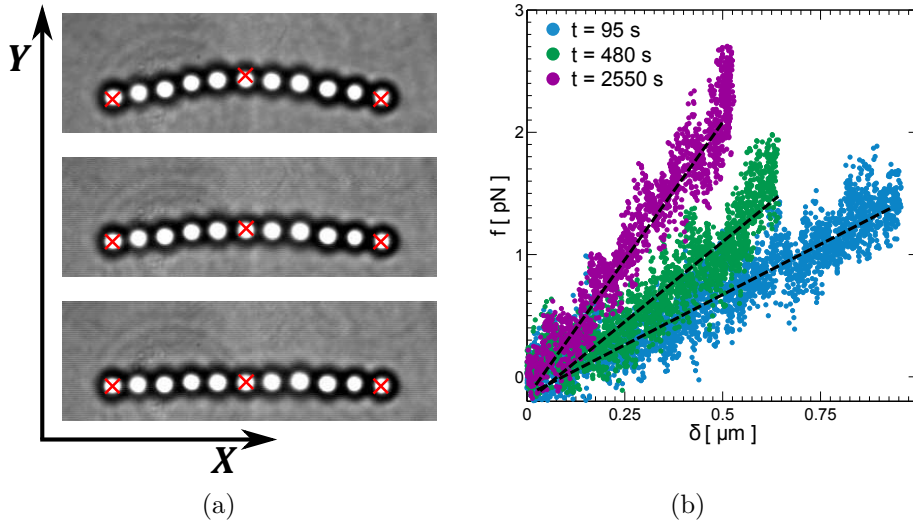


Figure 4.16 – (a) Typical microscope images of a PMMA rod under increasing bending levels. (b) Bending stiffness k_b for three aging times and $I = 0.40$ M.

We have also studied (poly(methyl methacrylate)) PMMA particle rods in CaCl_2 salt solutions for a single particle size $2a = 3 \mu\text{m}$ and several I values between 0.05 and 0.8 M. In all cases, we are able to form rods that are stable when held by their extremities. Moreover, the beams show the existence of a flexural modulus between the particles, as they bent according to the Euler-Bernoulli equation. In Figure 4.16 we report typical microscope images of a 11-particle rod under bending (left panel) and force-deflection curves at three different aging times (right panel). We clearly observe the formation of solid-solid contacts that age, with k_b approximately an order of magnitude lower than for silica particle despite the higher electrolyte concentrations used.

As shown in Figure 4.17(a), in all studied cases except when $I = 0.05$ M (in which case the flexural modulus is small — $\simeq 0.0015$ N/m—and does not appear to evolve in time), k_0 does age quasi-logarithmically. Yet, in contrast with the case of silica, the PMMA bending stiffness depends significantly and non-monotonically (see the legend of Figure 4.17(a)) on ionic strength. In particular, k_0 monotonically increases until 0.60 M and then shows a downturn at higher salt concentrations. This feature is in agreement with similar results obtained by Pantina and Furst [147], who attributed it to a charge reversal of the particles caused by the adsorption of Ca^{++} cations on the PMMA surface.

Monovalent salt (NaCl)

Remarkably, changing the salt valency leads to a very different response also for the PMMA system. Here we used potassium chloride (NaCl) as a monovalent salt, at three ionic strengths. The results for the bond stiffness are reported in

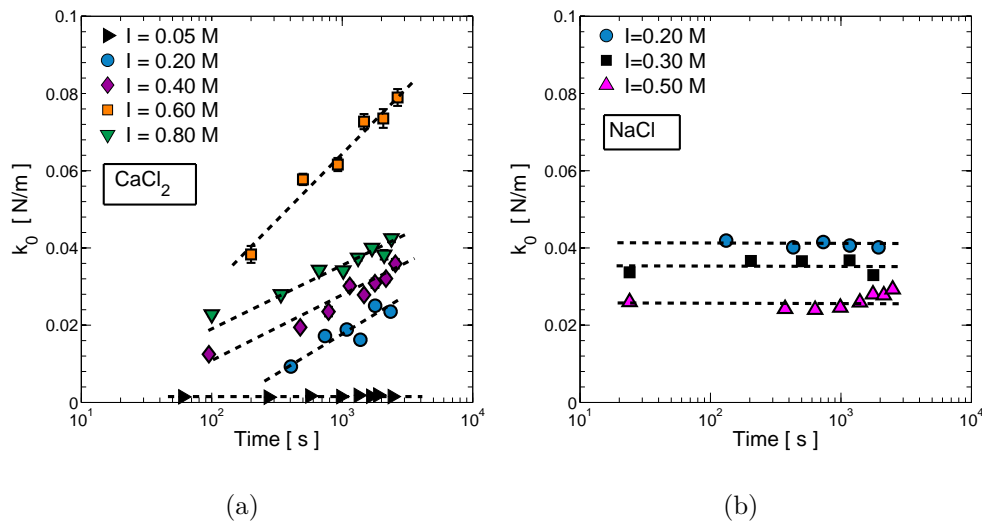


Figure 4.17 – Bond rigidity k_0 versus aging time for calcium chloride (a) and sodium chloride (b) solutions.

Figure 4.17(b). Surprisingly, k_0 does not appear to age in the considered range of salt concentrations, in sharp contrast with the divalent electrolyte. Furthermore, the magnitude of k_0 is of the same order of that found in CaCl_2 solutions, and slightly decrease with the addition of salt as the maximum is now found at $I = 0.20$ M (blue points).

All these observations indicate a non-trivial dependence of contact formation and aging on the salt used to screen the electrostatic energy barrier. For silica particles, divalent salts seem to be more efficient in promoting contacts and they also accelerate their aging dynamic compared to a monovalent salt as KCl . In the PMMA system, both CaCl_2 and NaCl promote the formation of contacts to the same extent, yet with a different dependence with ionic strength. In addition, monovalent (sodium) cations appear to reduce, indeed interrupt contact aging.

We will not use the results for the monovalent electrolytes in the rest of the manuscript. The main reason is that a more thorough experimental characterization must be conducted in order to assess their effects on contact aging. Note that the k_0 data of Figure 4.14 are a result of experiments and subsequent analysis of more than 50 different particle rods, because a huge number of them cannot be exploited due to their shape strongly deviating from the Euler-Bernoulli prediction (either by defects arising from the beam assembly, or from particle rearrangements). Due to experimental difficulties and the limited time for the tweezers experiments, we will focus on the divalent salt, for which a larger number of rheology, as well as bending, data, have been acquired.

4.4 Yielding of particle rods

4.4.1 SiO₂ particle rods

Divalent salt (CaCl₂)

Although in our experiments the contacts are able to support significant torques, small-scale rearrangements within the silica rods can occur. Conversely, with PMMA rods we do not observe rearrangements before the center particle is released from its trap, which implies that critical thresholds lie beyond the force we can exert. Therefore, here we examine the non-linear mechanical response of our $2a^* = 1.9 \mu\text{m}$ silica particles in CaCl₂ solutions.

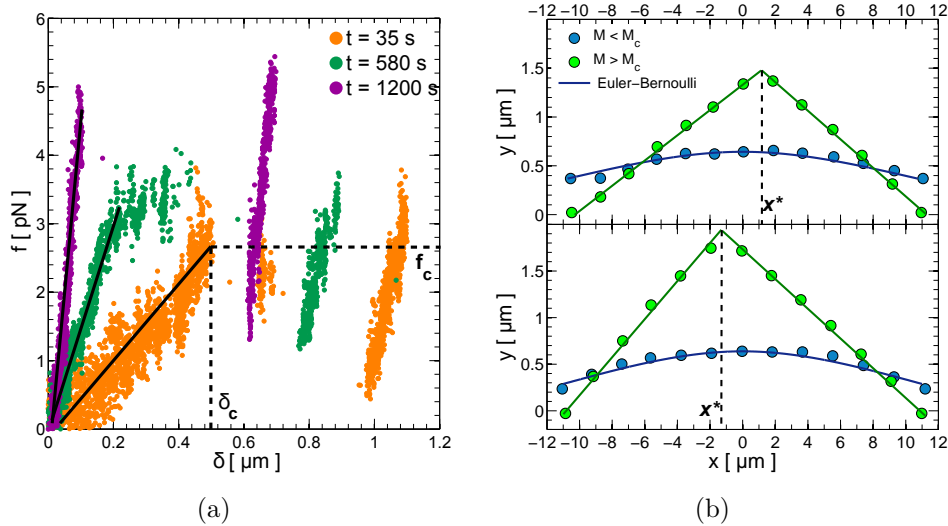


Figure 4.18 – (a) Same force f vs deflection δ curves in Figure 4.13(b). Here we report also the non linear response. (b) Particle positions immediately prior to the rearrangement (blue circles) and at a time after M_c had been exceeded (green circles) for two beams with $I = 0.10 M$ and $I = 0.20 M$.

In the three-point bending geometry, the aggregates experience an uniformly distributed shear force of amplitude $|f/2|$, and a bending moment M , which instead varies with the position, assuming its maximum value at the center $x = 0$, while symmetrically decreasing towards 0 at the end of the rod ($x = \pm L/2$):

$$M(x) = \frac{f}{2} \left[\frac{L}{2} - |x| \right], \quad (4.15)$$

Note that for a chain composed of n particles, the torques are transmitted almost entirely by the contacts, hence the maximum bending moment $M_a = f(n - 2)a/2$ is reached at $|x| = a$. If rearrangements are induced by rolling motion, the rupture occurs when the maximum value of the bending moment in the aggregate reaches a critical value M_c , which is related to the maximum tangential force f_c supported by

the contacts and the position of the bond x^* that undergoes the rearrangement by:

$$M_c = \frac{f_c}{2} \left[\frac{L}{2} - |x^*| \right], \quad (4.16)$$

The critical force can be directly measured from the f versus δ curves. As an example, we plot in [Figure 4.18\(a\)](#) the same force-deflection data in [Figure 4.13\(b\)](#), but we also include the remaining part of the curves after M_c has been exceeded; f_c corresponds to the maximum force marking the limit of linear elastic response (dashed lines). The location of the rupture is identified by the particle positions immediately prior and after the rearrangement. As illustrated in [Figure 4.18\(b\)](#), below M_c the rods present an upward curvature that signals the presence of tangential restoring forces; when $M > M_c$, the stress relaxes and the aggregate assumes a triangular shape with a pivot point at x^* .

We focus on the longer aggregates, i.e. those composed of 13 particles, for which we collected a thorough set of M_c data as a function of ionic strength (between 0.05 and 0.20 M) and aging time. We make the following observations: first, approximately 90% of the rearrangements takes place at x^* smaller than 2 particle diameters from the center of the aggregate, and 70% at distances smaller than a particle diameter, as shown in [Figure 4.19\(a\)](#). In the histogram, we plot the number of yielding events as a function of the bond number, which is counted starting from the leftmost particle (see upper panel). Clearly, the events are grouped around the 6th and 7th bond and correspond to rearrangements occurring near the center particle. This fact supports that rolling motion is the main mechanism of particle rearrangements, since the rod yields near the center where the moment is the greatest. Otherwise, if the bond failure was caused by the shear force exceeding the critical force of static friction, we should have observed an equally-distributed rupture probability.

In [Figure 4.19\(b\)](#) we report the time evolution of M_c for the rods in which rearrangements occurred within $2a$ from the rod center. This ensure that the data are self-consistent with [Equation \(4.16\)](#). First, we observe that M_c is essentially I -independent in the studied range, like the bending stiffness k_0 . Secondly, it strongly increases with aging time, reaching a nearly logarithmic regime at later times. The data bring a decisive support to our idea that stiffening is occurring within the particle solid-solid contacts.

At the same time, [Figure 4.18\(a\)](#) shows that the rupture occurs sharply, so that we can identify a specific yield deflection δ_c . This fact suggests a ‘brittle-like’ behavior of the rods, inasmuch the breakage initiates without significant plastic deformation. Since δ_c is related to the maximum radius of curvature of the aggregate, which in turn is related to the maximum rolling angle supported by the contacts, and since we observe a linear elastic response everywhere for $\delta < \delta_c$, we can define a critical rolling angle through the following equation:

$$M_c(t, a^*) = k_r(t, a^*) \cdot \vartheta_c(t, a^*) = \frac{k_0(t, a^*) \cdot a^{*2}}{96} \cdot \vartheta_c(t, a^*) \quad (4.17)$$

where we use [Equation \(4.14\)](#) to relate the torsion stiffness k_r to the bond stiffness k_0 . Our data set permits to characterize the behavior of ϑ_c versus aging time. To

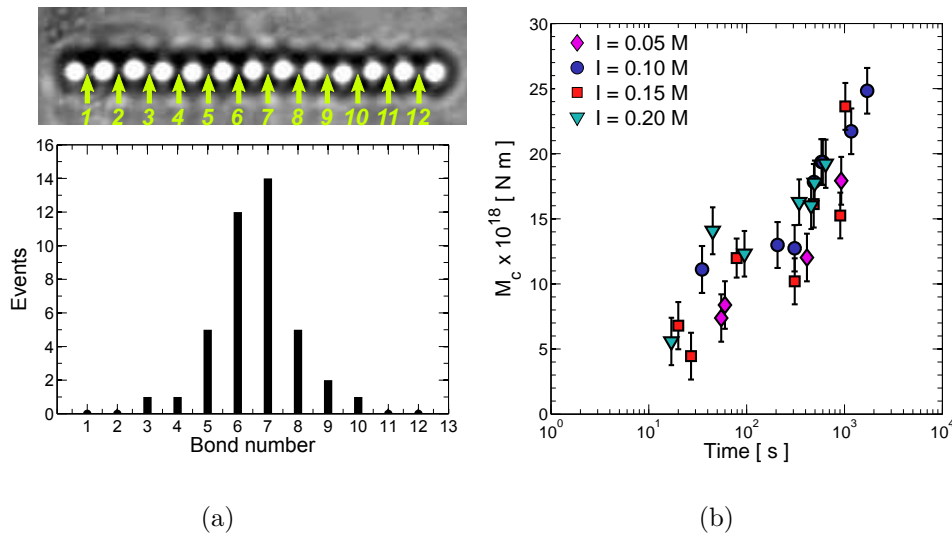


Figure 4.19 – (a) Histogram of the yielding events as a function of the bond number in the 13 particles rods. (b) Log-lin plot of the critical bending moment M_c versus aging time, for different ionic strengths and as measured from three-points bending tests with $n = 13$ particles. Error bars are deduced from uncertainties in f_c and x^* .

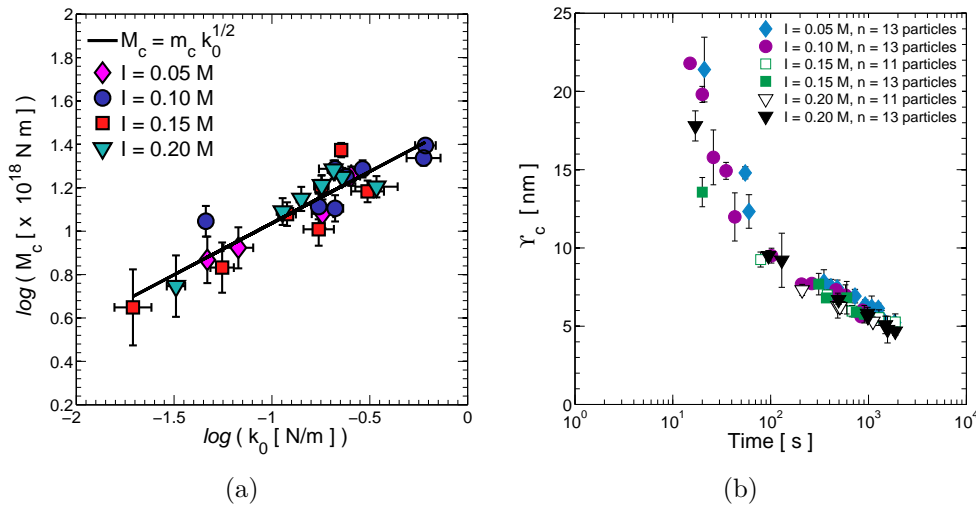


Figure 4.20 – (a) Critical moment versus bond stiffness parametrized by aging time, for all ionic strengths. (b) Critical rolling displacement versus t computed from Equation (4.20) and the $k_0(t)$ data set.

show that, we plot in Figure 4.20(a) for all I the critical moments versus bond stiffnesses obtained at the same t , i.e. measured during the same loading ramp. Interestingly, we find a power-law relationship $M_c \propto k_0^p$, with $p = 0.47 \pm 0.1$, as inferred from a direct fit. Taken into account experimental uncertainties, we expect the exponent to be $1/2$ and thus write:

$$M_c(t, a^*) = m_c \sqrt{k_0(t, a^*)}, \quad (4.18)$$

From the fit we find a constant prefactor $m_c = (0.32 \pm 0.1) \cdot 10^{-16} \text{N}^{1/2} \text{m}^{3/2}$ (black solid line). It is worth noting that an identical relationship has already been found by Pantina and Furst for PMMA and polystyrene particles in divalent salt solutions [71], but its origin remains to be elucidated. Combining Equation (4.17) with Equation (4.18) yields:

$$\vartheta_c(t, a^*) \propto \frac{96 \cdot m_c}{[a^*]^2 \sqrt{k_0(t, a^*)}} \approx \frac{3.4 \times 10^{-3}}{\sqrt{k_0(t, a^*)}} \quad (4.19)$$

where we used the the experimental values for m_c and a^* . According to Equation (4.19), the growth of k_0 during aging is accompanied by a reduction of the maximum angle supported by the bonds. Hence, particle-particle contacts are able to transmit increasingly larger torques, but, at the same time, the extent of flexural elastic deformation shrinks. This was already evident in Figure 4.18(a), wherein δ_c decreased from 500 to 100 nm in ≈ 20 min. The contacts break when a critical rolling displacement Υ_c is reached:

$$\Upsilon_c(t, a^*) \sim a^* \vartheta_c(t, a^*) = \frac{96 m_c}{a^* \sqrt{k_0(t, a^*)}} \approx \frac{3.2 \times 10^{-9}}{\sqrt{k_0(t, a^*)}} \quad (4.20)$$

The predictions of Equation (4.20) as a function of contact time, are reported in Figure 4.20(b), according to the bond stiffness data set. As illustrated, Υ_c varies from 27 nm to 4 nm—a very plausible range of variations, in accordance with recent AFM studies on micron-sized particles [92, 52].

4.5 Interpretation of the results

To explore in detail the possible origin of contact aging and its consequences in terms of macroscopic aging, we model the solid-solid contacts using adhesion theories. This approach provides a way to directly link the energy of adhesion between the particles and their bending elasticity [147].

4.5.1 JKR and DMT models

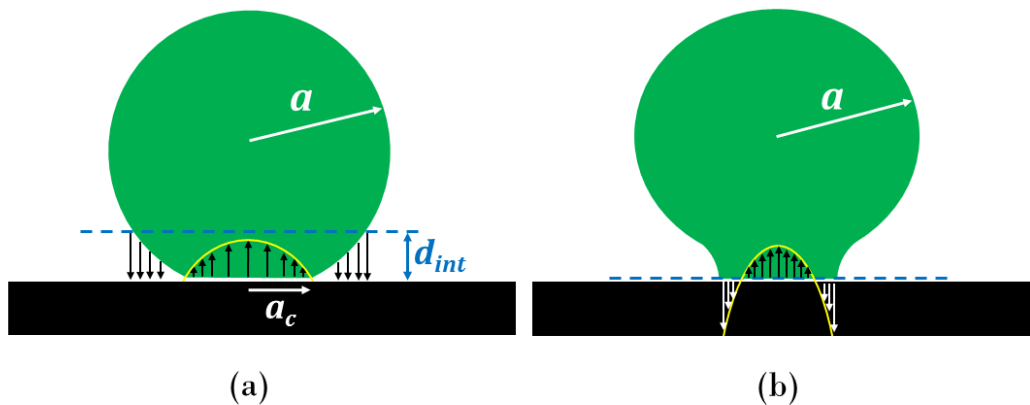


Figure 4.21 – Adhesion theory in the DMT (a) and JKR (b) limit. In the DMT model the contact area is determined by Hertz theory with the external load acting only outside it. The range of the interaction d_{int} tends to infinity. In the JKR limit the interaction forces are assumed to have infinitesimal spatial range, and are operative only in the contact area. The resulting pressure distribution has a (tensile) divergence at the contact edges.

The determination of the adhesion forces between small particles and/or particles and solid surfaces is a longstanding problem in contact mechanics [46], and is a topic of considerable interest in diverse disciplines, including physics and biology. We briefly review two well established theories that account for the coupling between surface adhesion and contact mechanics: the Derjaguin-Muller-Toporov (DMT) [48] and Johnson-Kendall-Roberts (JKR) models [102], inviting the reader to refer to ref. [10] for a recent review on this and related topics. The range of applicability of each theory depends on material properties and contact conditions. From a physical point of view, they differ in their predictions for the distribution of pressures within the contact zone and around it, and the profile of the bodies in the vicinity of the contact (see Figure 4.21). For the DMT model, the magnitude of the compressive contact stresses largely exceeds the interaction stresses so that the latter do not bring about deformation on the sphere. The punch shape then remains the same as in the adhesionless Hertz problem. The adhesion is assumed to result from long-range attractive forces and is computed in the manner of the Derjaguin approximation, by integrating the adhesion stress over the sphere non-contact area. In these conditions, the relevant parameter is the extent of the long-range interaction potential, and the

size of the contact zone has a little impact on the pull-out force [125], i.e. the force needed to separate the bodies in contact:

$$F_{DMT} = 2\pi\hat{a}W \quad (4.21)$$

with $\hat{a} = a_1a_2/(a_1 + a_2)$ the reduced radius, and $W = 2\gamma_{SL}$ the work of adhesion. JKR theory, on the other hand, neglects the range of the interaction potential and considers the interaction forces as purely contact ones. The adhesion force is assumed to apply only in the contact area of radius a_c and corresponds to an interfacial binding energy $E_{ad} = W\pi a_c^2$. The shape of the elastic body is obtained by minimizing $-E_{ad} + U_{el}$, where U_{el} is the elastic deformation energy. The solution of the JKR problem shows that the profile of the particle approaches the contact edges with a vertical tangent. This shape entails that an infinite pressure is exerted on the contact perimeter, with an inverse root singularity akin to that found in fracture mechanics, ahead of a sharp crack. As long as the height of the neck is much larger than the spatial extent of the surface interactions, a variation in a_c results in a complete transfer of work from the contact zone. In the JKR theory, thus, the relevant parameter for the determination of the contact zone is the adhesion energy required to create surfaces. It can be shown that the pull-out force is reduced with respect to the DMT case:

$$F_{JKR} = \frac{3}{2}\pi\hat{a}W \quad (4.22)$$

The contact region between two equal-size elastic spheres in the absence of normal applied load is a flat circular area. In both theories its radius is estimated as:

$$a_c = A \left(\frac{3\pi a^2 W}{8E^*} \right)^{1/3} \quad (4.23)$$

where A is a prefactor that ranges from 1 to $3^{1/3} \simeq 1.44$ between the DMT and JKR limits [48, 102, 188], $E^* = E/(1 - \nu^2)/2$ is the reduced modulus, with E and ν respectively the Young's modulus and the Poisson's ratio of the material.

Tabor parameter In 1977 Tabor [188] introduced the so-called Tabor parameter:

$$\lambda = \left(\frac{W^2 a}{8 [E^*]^2 h^3} \right)^{1/3} . \quad (4.24)$$

to define the range of applicability of each theory. Quite generally, JKR theory holds for $\lambda \gg 1$ and applies when interaction stresses are large and the materials compliant. DMT, on the contrary, is the limit for $\lambda \ll 1$ and is suitable for small, rigid spheres and long range interactions.

For the SiO₂ particles, taking $W = 200 \text{ mJ/m}^2$ [95] and $2a^* \simeq 1.9 \mu\text{m}$ as upper bounds for the adhesion energy and particle radii, a lower limit $h = 0.3 \text{ nm}$ [86] for the gap between the surfaces, $E \simeq 30 \text{ GPa}$ [150] and $\nu = 0.17$, the Tabor parameter [188] is estimated to be $\lambda \simeq 0.9$. Although far from the pure DMT case, this

leads us to use $A \simeq 1$ in Equation (4.23). The use of the DMT estimation is popular in works dealing with Stöber silica, so we will follow this idea. This will appear self-consistent, as our oncoming analysis will support that the stiffening of contacts results from a growth of W , yet within a range that remains below 200 mJ/m^2 so that the upper bound $\lambda \lesssim 0.9$ remains valid. One should keep in mind that, all things being equal, the Tabor parameter is strongly affected by the adhesion energy W , which we cannot directly measure in our bending tests. Therefore, it remains problematic (and out of the scope of this work) to assess the most rigorous choice of A , since, additionally, W is time-dependent. Moreover, we emphasize that the choice of A will not significantly change the main results.

For the $2a = 3.0 \mu\text{m}$ PMMA particles, standard values for the Young's modulus and Poisson ratio are $E \simeq 3.1 \text{ GPa}$ and $\nu = 0.40$, whereas an upper bound for the surface energy can be estimated as $W = 100 \text{ mJ/m}^2$ [147]. Keeping the same minimal gap h between the surfaces, Equation (4.24) yields $\lambda \simeq 2.7$; similar values are generally representative of intermediate cases between DMT and JKR behavior.

It is worth noting that rolling friction is strictly absent in the adhesive theories proposed so far. The contact is able to transmit a non-vanishing torque only if the pressure distribution P within the contact zone is asymmetric with respect to the center of the contact area, which is not the case neither for JKR nor DMT. It is clear, hence, that other effects, such as surface roughness, adhesion hysteresis etc. must be evoked to explain the observed rolling friction. We will come back later on this point. The strengthening of the interparticle bonds, evidenced in our three-point bending experiments, can only be associated to a phenomenon occurring inside this zone of radius $\approx a_c$. In the following, we will use two strategies to relate the growth in time of k_0 and M_c to the contact radius.

4.5.2 Pantina-Furst model

Elastic response

In a first approach, which we denote with the superscript PF , we tentatively write k_0 as that of a beam of radius a_c [147]. As for such a circular cross section the area moment of inertia is

$$\hat{I} = \frac{\pi a_c^4}{4}, \quad (4.25)$$

using Equations (4.13) and (4.23) with $A = 1$ we obtain:

$$k_0^{PF}(t) = \frac{12 \pi E a_c^4(t)}{a^3} = \frac{(3\pi)^{7/3} E}{4 a^{1/3}} \left(\frac{W(t)}{E^*} \right)^{4/3} \quad (4.26)$$

Since E and E^* are bulk properties that do not change over time, this expression suggests that contact aging arises due to an increase of interaction energy W between the silica surfaces, which causes a_c and thus k_0 to grow. Equation (4.26) also predicts that the effective flexural rigidity depends on particle size only via the geometric pre-factor $a^{-1/3}$.

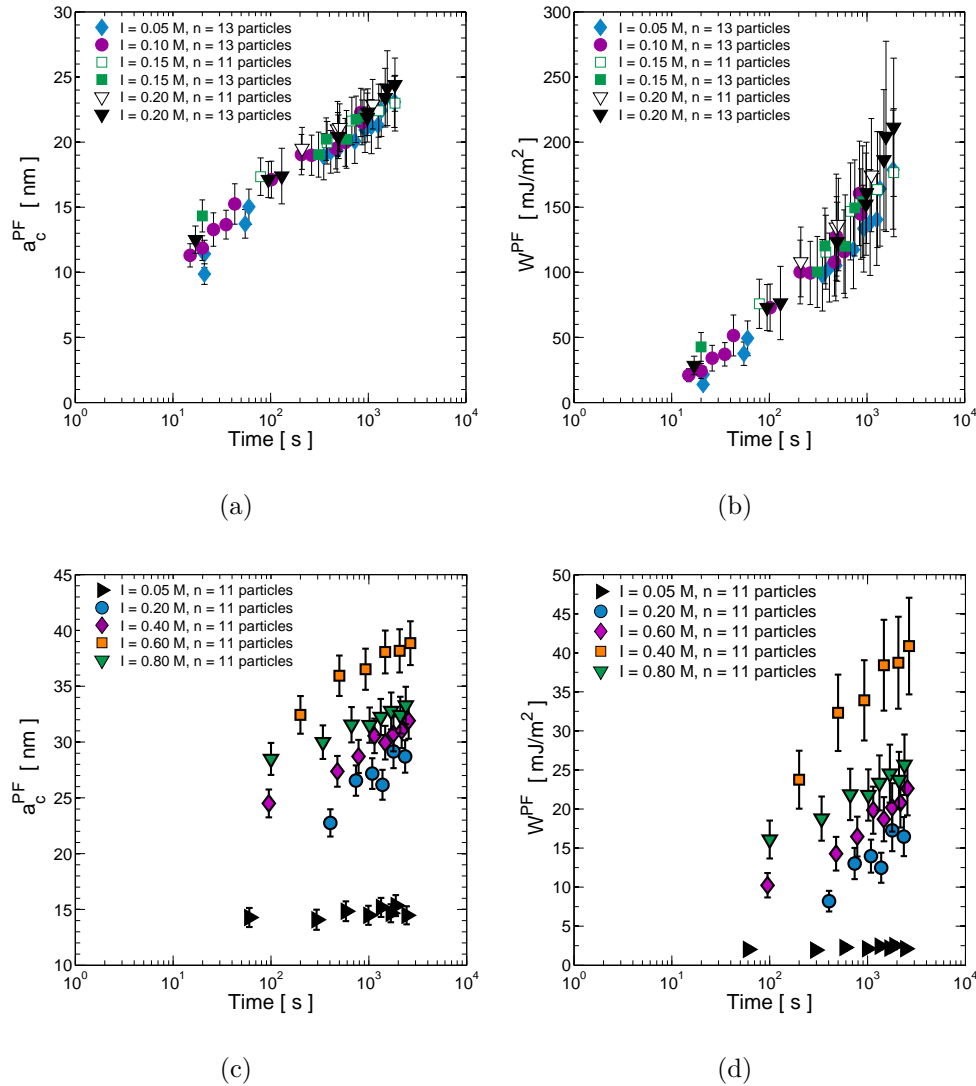
SiO₂ and PMMA in CaCl₂ solutions

Figure 4.22 – Log-lin plot of a_c and W versus time for silica (a,b) and PMMA particles (c,d) in CaCl₂ aqueous media, using the measured k_0 and the Pantina-Furst model.

SiO₂ particles We use our k_0 measurements together with Equation (4.26) to estimate contact radii and adhesion energies in our particle rods. For the asymmetric electrolyte CaCl₂, we find a_c to vary from ~ 10 to ~ 25 nm—which are not unreasonable values—while W grows from ~ 20 to 200 mJ/m². The data are reported in Figure 4.22. Note that the van der Waals contribution to the work of adhesion can be estimated as:

$$W = \frac{A_H}{12\pi D_0^2} \quad (4.27)$$

where $D_0 = 0.165$ nm is the surface-surface separation at contact [98] and $A_H = 8.3 \times 10^{-21}$ J is the non-retarded Hamaker constant of silica in water. A simple

calculation leads to $W \approx 9 \text{ mJ/m}^2$, a value that may be consistent with our data at short aging times ($< 10\text{s}$). Hence, [Figure 4.22\(b\)](#) suggests the presence of additional age-dependent contributions to W . We shall see later that these contributions may be related to the silica surface chemistry (formation of Si-O-Si bridges).

It should be pointed out, however, that adhesion energies of few hundreds of mJ/m^2 are more in accordance with values reported by Atomic Force Microscope (AFM) and Surface Force Apparatus (SFA) studies for silica surfaces in ambient (humid) air [204, 92], but are far larger than those obtained for similar surfaces in electrolyte solutions [128, 26, 198, 55, 86, 195] (in the few mJ/m^2 range, as reported in [Table 4.1](#)). The beam model, thus, appears to overestimate a_c and thus the adhesion forces. One should keep in mind, however, that the mentioned works show a great variability of results. This fact may be ascribed to the surface properties of the particles [211], which may depend on a number of factors, such as the synthesis process, how the particles are post-treated and/or stored, the presence of impurities, etc. For instance, in these works a careful procedure is typically required to attach the particle to the AFM cantilever, which is likely to change its surface properties. First, both surfaces must be cleaned, which is achieved by oxygen plasma treatment for several minutes. Then, to remove the glue, the particles are usually treated with UV curing [55] or heated at high temperature ($> 1000^\circ\text{C}$) in an oven [199]. It is known that heating changes the state of surface hydroxylation [204, 222], which in turn may alter the adhesion forces.

In our case, we find large differences in the rheology responses of our synthesized silica particles and commercial ones (Spherometer CA). In the same physio-chemical conditions, the mechanical strength of the suspensions is relatively high for the former, while it is strongly reduced for the latter [72]; this fact may partially explain the large values reported in [Figure 4.22\(b\)](#).

PMMA particles Using a similar approach, we compute contact radii and adhesion energies for the PMMA particles and report them in [Figure 4.22](#). These values are again in reasonable agreement with those found in adhesion studies in ambient environment, $W \approx 30 - 50 \text{ mJ/m}^2$ [147].

Non-linear response

SiO₂ particles According to the Euler-Bernoulli theory, as long as linear elasticity applies, a “fiber” of the material parallel to the neutral axis (i.e. the axis passing through the center of the cross section) and distant r from it, experiences a stress:

$$\sigma = \frac{Er}{R} = \frac{Mr}{\hat{I}} \quad (4.28)$$

where R is the radius of curvature of the rod, and M the external bending moment. The stress is zero at the center and reaches its maximum value σ_m at the edges of the contact area $r = \pm a_c$. In these conditions, the rods may yield when σ_m exceeds a critical value σ_c characteristic of the material ($\sigma_m > \sigma_c$). Substituting

Table 4.1 – Typical adhesion energy between silica surfaces in aqueous electrolyte solutions measured by AFM.

Authors	Salt	I [M]	pH	F/a [mN/m]	W [mJ/m ²]
Chapel et al. [26]	NaCl	0.1	5.5	5.8	0.92
Dishon et al. [55]	KCl	0.1	5.5	0.65	0.10
	KCl	0.2	5.5	0.90	0.14
Meagher [128]	CaCl ₂	0.3	5.5	0.2	0.03
	CaCl ₂	0.03	5.3	6.1	0.97
	CaCl ₂	1.00	4.1	1.2	0.19
Troncoso et al. [195]	NaCl	0.001	5.1	7.96	1.27
	NaCl	0.01	5.1	9.09	1.45
	CaCl ₂	0.0003	5.1	6.79	1.08
	CaCl ₂	0.003	5.1	7.51	1.20
	CaCl ₂	0.03	5.1	9.33	1.49
Guleryuz et al. [86]	NaCl	0.01	5.3	0.61	0.1
	NaCl	0.1	12.5	6.97	1.11
	NaCl	0.5	12.5	8.85	1.41
	NaCl	1.0	12.5	7.51	1.20

Equation (4.25) for \hat{I} into Equation (4.28) gives for the critical moment:

$$M_c \sim \frac{\pi}{4} \sigma_c a_c^3 \quad (4.29)$$

Thus, M_c should be proportional to a_c^3 . This is not supported by our experiments on silica particles, since from the previous expression and Equation (4.26) one would obtain $M_c \propto k_0^{3/4}$, while our data suggest $M_c \propto k_0^{1/2}$ (see Figure 4.20(a)). Therefore, simple bending theory seems not able to describe our critical moment versus bond stiffness curve for the SiO₂ particles. One possibility to account for this behavior is to consider that stress may localize at the contact edges; in this case, the assumption that stress is linearly distributed across the beam section fails.

Combining Equation (4.26) with $M_c \propto k_0^{1/2}$ yields, instead:

$$M_c^{PF}(t) = \eta^{PF} a_c^2(t) \sim a^{4/3} \cdot W^{2/3}(t) \quad (4.30)$$

where the fitted proportionality factor is equal to $\eta^{PF} = (0.039 \pm 0.003)$ N/m. To account for this observation, Pantina and Furst [71] related the yielding of the colloidal bonds to the applied load f exceeding the static friction force between the particle surfaces $F_{||} = \mu_s L_0$, where $L_0 \sim \pi a W$ is the adhesion force. If the critical shear force f_c for a bond to slip is $f_c \sim M_c / \delta$, where $\delta \simeq a_c^2 / a$ is the contact indentation associated with the formation of the contact zone with radius a_c [102], the $M_c \propto a_c^2$ simply derives from the requirement that f_c is independent of the contact area, as usually observed in macroscopic friction. The bond yields when

$f_c = F_{||}$ and the friction coefficient can then be estimated as:

$$\mu_s(t) = \frac{\eta^{PF}}{\pi W(t)} \quad (4.31)$$

Interestingly, if contact aging derives from an increase of W , μ_s would then decrease with time. This may reflect the flattening and plastic deformation of surface asperities as the adhesive load increases, and may account for the observed reduction with age of the critical rolling displacement Υ_c . If we now use the extrapolated W values we can estimate the friction coefficient to decrease from 0.90 to 0.05 — a plausible range of variation. However, the above hypothesis may be at variance with our experimental observations. Indeed, the shear force in a three-point bending tests is independent from the bond position and would then cause an equal distribution of rearrangement along the particle chain, if static friction is the main mechanism of yielding. Although sliding of adjacent particles is observed in our bending experiments, our data demonstrate that rolling is predominant.

The scaling properties deduced from [Equation \(4.26\)](#) and from the empirical relation, [Equation \(4.30\)](#), are summarized in [Table 4.2](#).

Table 4.2 – Scaling of k_0 and M_c with a and W according to the P-F model.

	a	$W(t)$
k_0	$a^{-1/3}$	$W^{4/3}$
M_c	$a^{4/3}$	$W^{2/3}$

Table 4.3 – Scaling of k_0 and M_c with a and W according to the D-T model.

	a	$W(t)$
k_0	/	W
M_c	a	$W^{1/2}$

4.5.3 Dominik-Tielens model

Elastic response

The second model we consider is that of Dominik and Tielens and will be denoted with the superscript DT. In [57] the authors derived an expression for the rolling moment of a spherical particle attached to a flat substrate, in absence of sliding. The main features of the rolling resistance calculation are illustrated in [Figure 4.23\(a\)](#). Under an external torque and/or a lateral displacement Υ , adhesion hysteresis, i.e. the energy dissipated in the making and breaking of bonds at the leading and trailing edge of the contact, causes the pinning of the solid-solid line. In these conditions, a_c is no longer centered around the center of the original contact circle (see star and plus symbols in [Figure 4.23\(b\)](#)). When an external shear force F or displacement Υ is applied to the center of the particle, the restoring moment M can be computed by decomposing this shifted contact area into two circles of different radii $a_c + \Upsilon$ and $a_c - \Upsilon$. The variation of a_c can be related to a change in the pressure distribution between the two half circles, $P(r, a_c + \Upsilon)$ and $P(r, a_c - \Upsilon)$ and results in a finite rolling moment. In the calculation, the JKR estimation for P is used, and it turns out

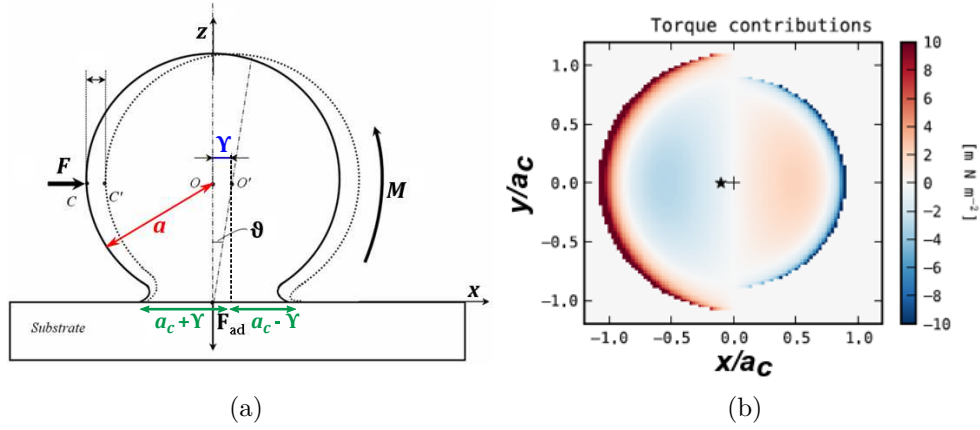


Figure 4.23 – (a) Sketch of the rolling motion of a sphere in adhesion with a flat substrate (figure adapted from [52]). (b) Contact area and torque contribution used in the calculation of M (figure adapted from [108]).

that only the term associated with the JKR neck contributes to the non-vanishing torque [57]. For a spherical particle on a flat substrate, the integration of $P(r, a_c \pm \Upsilon)$ with respect to the contact surface leads to:

$$M = 6\pi W \hat{a} \Upsilon \quad (4.32)$$

where $\hat{a} = a$ is the sphere-substrate reduced radius and $\Upsilon \sim \vartheta a$ the rolling displacement. For two equal sized spheres, we have $\hat{a} = a/2$ and

$$M = 3\pi W a^2 \vartheta \quad (4.33)$$

Hence, for small displacements, the torque is proportional to the rolling angle. The proportionality constant, the rolling stiffness $k_r = 3\pi W a^2$, can be further related to k_0 through Equation (4.14), and we finally obtain:

$$k_0^{DT}(t) = 288\pi W(t) \quad (4.34)$$

The model suggest that k_0 is independent of the elastic bulk properties (E, E^*) and radius of the particles. Note that, using Equation (4.23), we can rewrite the bond stiffness as:

$$k_0^{DT}(t) = \frac{256E^* a_c^3(t)}{a^2} \quad (4.35)$$

This elastic constant thus differs from Equation (4.26) by a factor a_c/a .

SiO₂ and PMMA in CaCl₂ solutions

SiO₂ particles For the silica particles, the predictions of the model are displayed respectively in Figures 4.24(a) and 4.24(b). Noticeably, both a_c^{DT} and W^{DT} are much lower than a_c^{PF} and W^{PF} , since they now vary from ~ 1.5 to ~ 5 nm and from ~ 0.01 to ~ 0.5 mJ/m², respectively. These adhesion energy values, which correspond to pull off forces of few nN, are comparable with those displayed in Table 4.1,

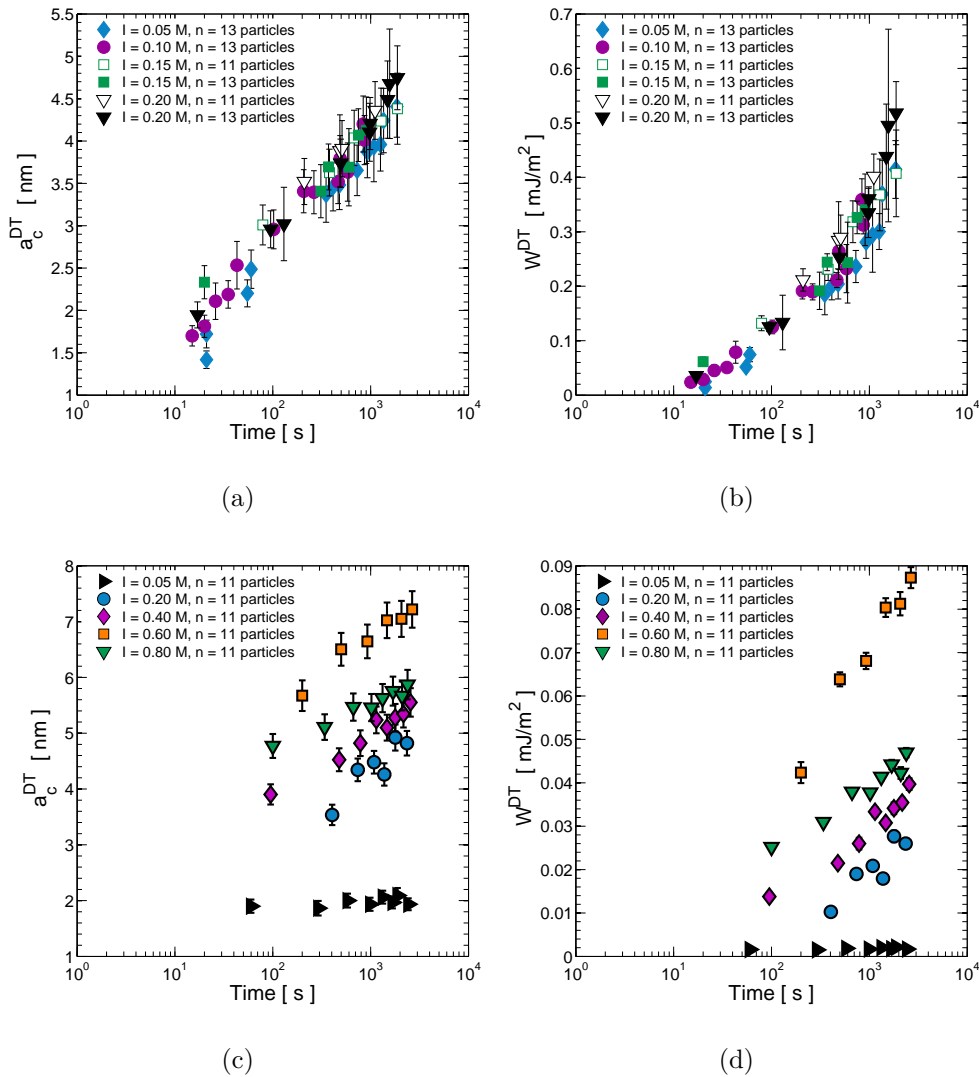


Figure 4.24 – Log-lin plot of a_c and W versus time for silica (a,b) and PMMA particles (c,d) in CaCl_2 aqueous media, using the measured k_0 and the Dominik-Tielens model.

even though a direct comparison remains difficult as time-dependent effects are not considered in these works.

PMMA particles Similar considerations hold for the PMMA system, for which a_c varies from ~ 2 to ~ 7 nm and W from ~ 0.001 to ~ 0.09 mJ/m², depending on contact time and I (Figures 4.24(c) and 4.24(d)).

Non-linear response

SiO₂ particles According to ref. [57], the linear elastic response is lost and the contact area starts to move when a critical rolling displacement Υ_c is reached. Dominik and Tielens suggested that a lower bound for Υ_c is of the order of the distance between atoms in the material, e.g. 0.2 nm [57]. More recently, describing the contact zone as a Mode I opening crack, Krijt et al. [108] related Υ_c to the adhe-

sion energy hysteresis $\Delta W = W_{opening} - W_{closing}$ associated to the breakage and formation of bonds during rolling:

$$\Upsilon_c = \frac{a_c \Delta W}{12 W} \quad (4.36)$$

If $\Delta W/W$ is constant, Υ_c represents a fixed fraction of the contact radius, and is expected to scale with $a^{2/3}$. In this case, with [Equations \(4.32\)](#) and [\(4.36\)](#), the critical moment is predicted to scale as:

$$M_c = \frac{\pi}{4} \Delta W \cdot a \cdot a_c \propto a^{5/3} \cdot \Delta W \cdot W^{1/3} \quad (4.37)$$

The description of the rolling resistance based on the Dominik-Tielens model presents various debatable aspects. First of all, we should mention that the computation involves the splitting of the contact area in two half circles with different contact radii, a very strong hypothesis which (i) leads to a discontinuity in the pressure distribution at $x = 0$ and (ii) has never been supported by experimental evidences. Additional problems emerge if one considers the particle rearrangements in our bending tests and the upper bound for Υ_c predicted by the theory. The latter is set by the condition $\Upsilon_c < a_c$, as suggested by the calculation itself (see [Figure 4.23](#)). From our bending tests, we estimated the critical displacements (angles) and observed that Υ_c varied approximately in the range ~ 4 to ~ 25 nm (refer to [Figure 4.20\(b\)](#)). If we compare these values with the contact radii displayed in [Figure 4.24\(a\)](#), we find $\Upsilon_c > a_c$, which is strongly in contrast with the computation. Additionally, if we substitute the estimated upper limit of $W \sim 0.5$ mJ/m² —in [Equation \(4.24\)](#), we obtain $\lambda = 0.015$. This small value suggests that P should be estimated by the DMT theory, while the D-T calculation uses JKR. These two observations lead us to rule out the Dominik-Tielens description for the rolling resistance between our silica particles.

Nevertheless, one may still find instructive to look at the scaling laws predicted by the model. Assuming $M_c \propto k_0^{1/2}$, from [Equation \(4.35\)](#) we obtain:

$$M_c(t) = \eta^{DT} a_c^{3/2}(t) \sim a \cdot W^{1/2}(t) \quad (4.38)$$

where $\eta^{DT} = (7.1 \pm 0.5) \cdot 10^{-5}$ N/m^{1/2}, as measured from a direct fit. We summarize the Dominik-Tielens predictions in [Table 4.3](#).

4.5.4 Contact aging

We now discuss the possible origin of contact aging for silica and PMMA surfaces. We recall that the time-dependent behavior of k_0 and M_c can be associated with an increase of a_c . There are various phenomena that may be responsible for this evolution.

One possibility is an increase of the size of the neck through mass transfer. For the silica particles, this mass transfer may be attributed to solubility variations due to the difference in radius of curvature between the neck and the particles [95]. For spheres in the micron range, however, the rate of dissolution is essentially negligible. Other mass transfers such as grain boundary or surface diffusion are too slow at

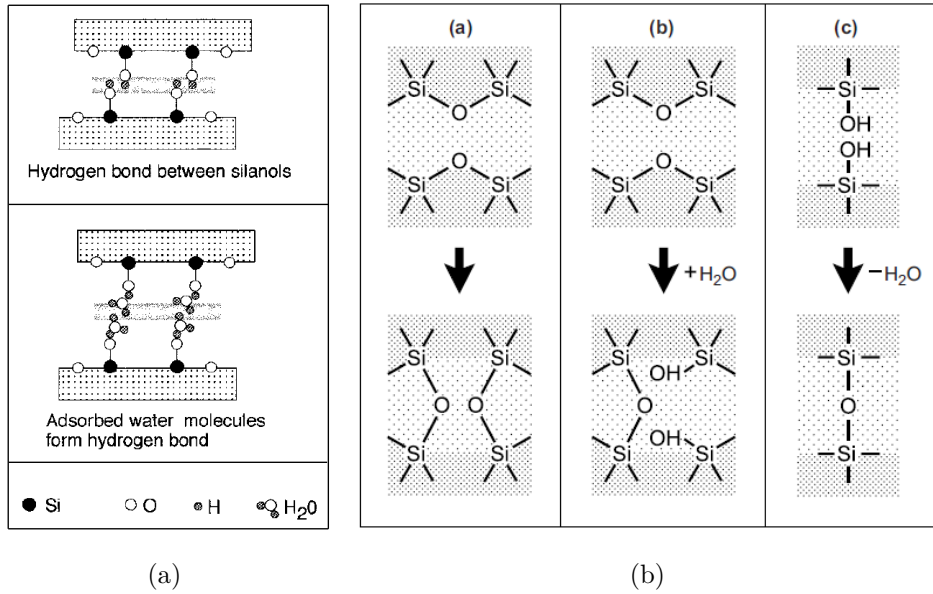
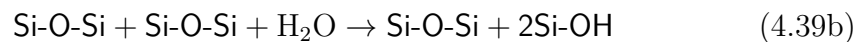


Figure 4.25 – (a) Hydrogen bonding between silanols of touching surfaces. Figure adapted from [69]. (b) Formation of siloxane bridges at the interface during time. Figure taken from Israelachvili [98].

ordinary temperatures to capture the time behavior of the bond stiffness, thus we ruled out sintering as a possible process. Besides, hydrogen bonding between the silanol groups of opposite surfaces [127, 69] (Figure 4.25(a)) is too rapid to explain the protracted increase at later times.

There is, however, clear evidence in the literature that, at room temperature, the interface between two silica surfaces ages by the formation of siloxanes [204, 114, 119, 191, 115], as shown in Figure 4.25(b):



These works support that W grows logarithmically in time. Interestingly, a logarithmic increase of W is evident also in our extrapolated data in Figure 4.22(b), using the P-F estimates of a_c . When combined with Equation (4.26), it suggests that $k_0^{3/4}$ —and not k_0 —would grow logarithmically. This leads us to replot our three-point bending data as $k_0^{3/4}$ vs t , in Figure 4.14(b): we do find the logarithmic scaling to be much more evident than in Figure 4.14(a) as it now extends over two decades in time. Clearly, more evidence is needed to confirm this aging mechanism for our particles, and the empirical scaling do not constitute an unambiguous evidence for the applicability of the beam model.

The strengthening of the contacts has been also attributed to the condensation of the surface gel layers during time [204]. It could be accounted for by considering a time-dependent Young's modulus [123]. However, it remains very unclear how to define a “local” Young's modulus and how it would affect the bonded region.

The contact aging of PMMA particles poses different questions. In fact, they are known to dissolve and swell upon contact with water [190]. In these conditions, their surface is usually covered by a layer of polymeric chains, and contact aging may be ascribed to chain interdigitation occurring at the interface [98], hence via a quite different mechanism than in the case of silica. Indeed, it is known that molecules of polymeric materials can interpenetrate and flow with time across the interface, resulting in an increase of the effective contact area or number of interfacial bonds and in aging effects. Eventually, the interface can disappear, leading to the formation of a continuous neck, as sketched in Figure 4.26(b). Moreover, the non-monotonic increase of W with the addition of CaCl_2 (Figure 4.17(a)) could be ascribed to the formation of ion-bridges at the interface, as suggested by Pantina and Furst in ref. [147]. Yet, it has never been investigated how these effects are coupled with surface dissolution, swelling and interdigitation.

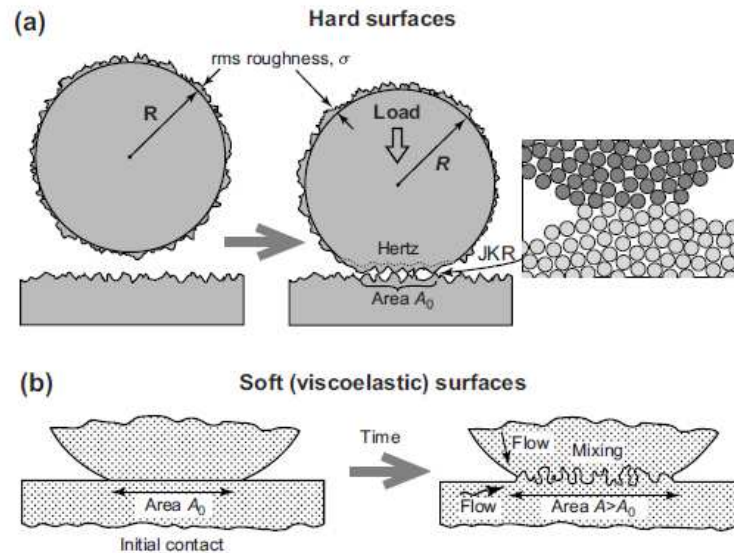


Figure 4.26 – Difference in contact formation and aging for hard elastic (a) and soft viscoelastic (b) particles. Figure taken from [98].

Another issue is that surface roughness strongly affects adhesion, either by reducing the effective contact area relative to the nominal one, or by altering the balance between compressive and tensile stresses in the asperities [151]. For hard elastic materials like silica, local junctions can be JKR-like even if the average deformation remains close to the Hertzian profile, as shown in Figure 4.26(a). Surface roughness can reduce adhesion, and this fact can partially explain the lower k_0 values of PMMA particles vs silica ones. Indeed, scanning electron micrographs in Figure 4.27 evidence substantial differences in surface roughness between the two types of particles.

In addition, the possible existence of non-DLVO interactions at contact [83, 98], associated to the presence of layers of adsorbed cations and water molecules on the particle surfaces, may lead to time-dependent effects (see Section 2.2.4). Vakarelski

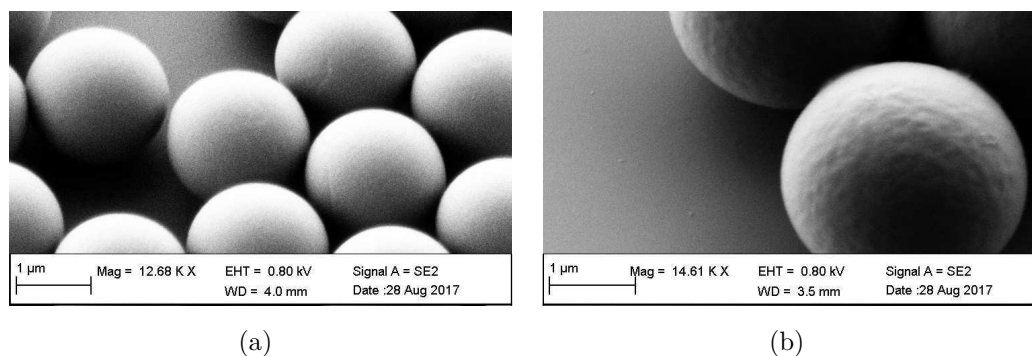


Figure 4.27 – Surface roughness of SiO_2 (a) and PMMA (b) particles imaged by SEM.

et al. [198, 197] investigated the effect of contact time and salt species in the adhesion of silica micro-particles and mica surfaces. Interestingly, they found a strong increase of W with contact time, even in pure water. Adding low concentrations of LiCl, NaCl, KCl, or CsCl leads to little changes in the time behavior of the adhesive force, which roughly increased from 5 to 25 mN/m in about 50s. On the contrary, at higher salt content, the adhesive force strongly depended on the ionic strength and on the type of cation used. In some cases, it decreased with increased electrolyte concentration, in analogy with our results for PMMA particles in NaCl (see Figure 4.17(b)). Remarkably, adhesion was usually high for ions with large hydration enthalpy, following the order $\text{Li}^+ > \text{Na}^+ > \text{K}^+ > \text{Cs}^+$. To account for these findings, they proposed that there exists a thin surface layers of water molecules, cations and hydrated cations that govern how closely the surfaces can approach each other, and thus the extent of adhesion. Highly hydrated ions form a thick but “weak” layer that can be easily destroyed, and, therefore, the adhesion can vary rapidly with the time of contact. Cations with low hydration enthalpy, on the other hand, form a thin but “strong” structured layer, that slows down particle approach and results in a lower growth rate. The proposed mechanism is schematically reported in Figure 4.28. Although our results on contact aging with different salt valencies may be in agreement with this picture, and generally with ion-dependent effects, an accepted theory comprising these effects is still lacking.

Our analysis underlines the absence of compelling theories describing the effects of adhesion, DLVO interactions, surface roughness and interface chemistry, and then emphasizes that further theoretical progress on the modelling of the contact region between colloidal particles and aging dynamics remains much needed.

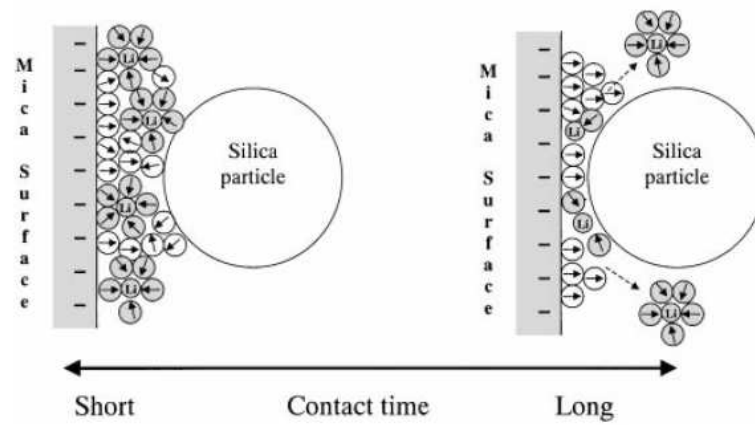


Figure 4.28 – Cation-induced adhesion aging proposed by ref. [198].

Three-Point Bending Tests: Behind the Scene

Contents

5.1 Rigid body rotation	136
5.1.1 Force-deflection curves	136
5.1.2 Simulated motion of the rods in 3D	137
5.1.3 Misalignment correction	140

In this Chapter, we describe how the force-deflection data, obtained in the three-point bending tests, are analyzed and corrected for misalignment between the focal and the trapping planes. Although this topic is not essential for the physical interpretation of our results, it represents an important part of the analysis of the contact aging data. The reader not primarily interested in these technical details should feel free to skip this section, but may still find it valuable to refer back to it at her/his convenience.

5.1 Rigid body rotation

5.1.1 Force-deflection curves

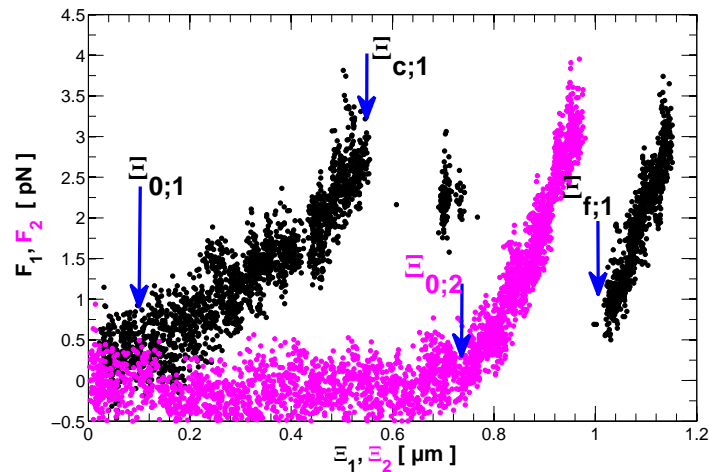


Figure 5.1 – Force versus deflection at two consecutive aging times, showing different extents of the zero-force plateau region due to particle rearrangements.

As shown in Figure 4.10(a) and in the rest of Chapter 4, the force vs deflection data can be split into three regimes. Usually, at the beginning of the load, no force is detected although the deflection of the chains increases (in fact, sometimes the force goes toward slightly negative values). At a critical deflection Ξ_0 , we enter a linear elastic regime where the bending force is proportional to the deformation. Occasionally, when the deflection reaches a threshold Ξ_c , particle rearrangements within the chain may occur.

Before, we postulated that the plateau region is associated with a rigid body rotation of the rods due to their curvature at rest and the torque induced by gravity. Here we report clear evidence that bring decisive support to this interpretation. The first indirect hint can be found by looking at Figure 5.1, where we report the raw data related to two loading ramps carried out on the same rod and at two consecutive aging times. Clearly, any possible curvature is not seen at rest because, when the three traps are aligned along the X axis, the rod tends to lie in the plane perpendicular to the trapping plane due to gravity, and hence the microscope images represent a “2D projection” of the real particle positions. In the first ramp (black points), the regime

of zero-force extends up to $\Xi_{0;1} \sim 0.1 \mu\text{m}$. We expect that, after a rotation around the X axis, at $\Xi_{0;1}$ the rod is coplanar with the trapping plane. When $\Xi > \Xi_{0;1}$, the rod develops a force until it yields at $\Xi_{c;1} \sim 0.5 \mu\text{m}$ (in the following analysis we can neglect the presence of a second, short rupture that appears at approximately $0.7 \mu\text{m}$). The deflection increases up to a new value $\Xi_{f;1} \sim 1.1 \mu\text{m}$ and the force falls down to $\sim 0.5 \text{pN}$, before eventually increasing again. At the end of the first loading ramp, the three traps are re-positioned along X , and again no curvature can be detected by visual inspection. However, if the failure of the aggregate occurred next to the center particle, the initial curvature should have increased by an amount approximately equal to $\Xi_{f;1} - \Xi_{c;1}$. Thus, in the subsequent loading ramp, the rod should reach the trapping plane only when $\Xi_{0;2} \simeq \Xi_{0;1} + (\Xi_{f;1} - \Xi_{c;1}) \sim 0.7 \mu\text{m}$. This is indeed evident from the plateau in the second ramp (light purple points) of [Figure 5.1](#). This entails that the rods bent only when they are aligned with the trapping plane and the presence of a critical deflection is related to their curvature at rest.

5.1.2 Simulated motion of the rods in 3D

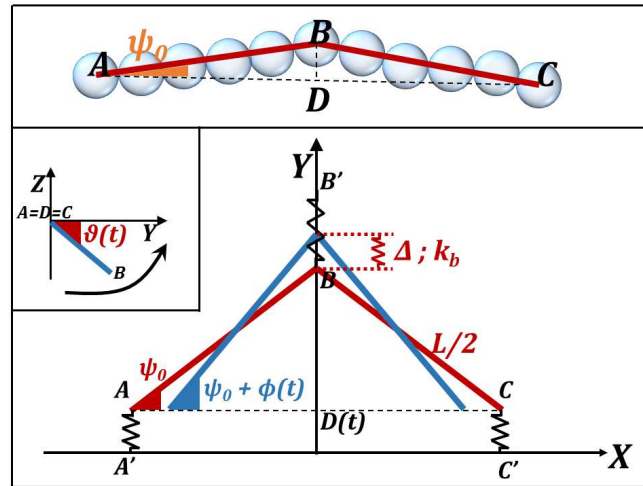


Figure 5.2 – System used to simulate the motion of our particle rods.

To confirm the above arguments, we also performed a numerical simulation with Maple. Since in the plateau region the rods are assumed to behave as rigid bodies, we can apply Euler-Lagrange mechanics to retrieve their equations of motion. We approximate the particle beam with two identical rigid cylinders of length $L/2$, arranged to form a triangle with a common vertex in B , as shown in the upper panel of [Figure 5.2](#). This triangular shape is assumed to roughly represent the initial defect of the rods. The fundamental parameter describing the curvature is thus the height of the triangle, or, identically, the angle $\widehat{BAD} = \Psi_0$. During motion, the cylinders are forced to maintain contact in B , to ensure the cohesion of the rod. To simulate the optical traps in the three-point bending geometry, we define 2 fixed points, $A' = (-X_{trap}, 0, 0)$ and $C' = (X_{trap}, 0, 0)$, and a movable point $B' = (0, A_L \sin(\omega t), 0)$, as shown in the lower panel of [Figure 5.2](#). Note that all these points lie in the (trapping) XOY plane. Then, they are linked through springs with

the corresponding vertexes of the rod, i.e. A with A' , B with B' and C with C' . For each point, the restoring elastic force is decomposed into in-plane and perpendicular components; this results in 3 identical radial springs (acting in the XOY plane) of elastic constant k_{trap} , and in a same amount of springs acting in the Z direction and having stiffness $k_z < k_{trap}$ [138], but large enough to sustain the rod weight. Note that we neglect variations of the radial stiffness with depth Z . As the beam is rigid, the bending is approximated by a rotation of the cylinders with a pivot point in B that results in a variation over time of the angle $\widehat{BAD} = \Psi_0 + \phi(t)$. Such a change corresponds to a Y -displacement $\Delta = L/2(\sin(\Psi_0 + \phi(t)) - \sin(\Psi_0))$, provided that point B is constrained to remain in $X = 0$. To mimics the elastic response of the rods, therefore, a spring with rigidity k_b , applying a restoring force $F = -k_b\Delta$, is used. Taking for simplicity the position of point D as $\vec{D}(t) = (0, Y_D(t), Z_D(t))$ and calling $\theta(t)$ the polar angle formed by the plane of the beam with the trapping plane (see small inset in Figure 5.2), we thus end up with 4 generalized coordinates $\phi(t)$, $\theta(t)$, $Y_D(t)$, $Z_D(t)$.

The Lagrangian of the problem is:

$$L = T - V \quad (5.1)$$

where V is the total potential energy due to elastic and gravitational potential energies, and T is the sum of the rotational and kinetic energies. The equation of motions are computed by applying the well-known formalism:

$$\frac{d}{dt} \left(\frac{\partial L}{\partial \dot{q}_j} \right) = \frac{\partial L}{\partial q_j} \quad (5.2)$$

where q_j and \dot{q}_j are the generalized coordinates and velocity (resp.). A Maple script allows to resolve numerically the above non linear differential equations with respect to the q_j . Considering the density of silica $\rho = 2 \text{ g/cm}^3$, we use the mass of 11 particles ($2a = 1 \mu\text{m}$) in water and use a standard expression for the moment of inertia of cylinders. At rest, the position of the rod is assumed parallel to the vertical plane (i.e. $\theta(0) = -\pi/2$), and, due to equilibrium of gravitational and trapping forces, we compute the initial value for $Z_D(0)$. We finally set $Y_D(0)$ and $\phi(0)$ equal to 0, as expected in the real experiments. Typical results as a function of time are reported in Figure 5.3, here for a rod with initial triangle height $1.55 \mu\text{m}$ and $k_b = 18.5 \text{ pN}/\mu\text{m}$. Note that, approximately at $t=55\text{s}$, the polar angle $\theta(t)$ (Figure 5.3(a)) reaches 0 and then oscillates around it, while, at the same time, $\phi(t)$ starts to increase (Figure 5.3(b)). This indicates that (i) the beam is aligned with the trapping plane and (ii) begins to experience a bending force. Since at every time $Y_D = Y_A = Y_C$, the motion of D , illustrated in Figure 5.3(c) and Figure 5.3(d), reflects the trajectories of the end particles in a real experiment. Surprisingly, in analogy with our data, the Y displacement (and thus the measured force in this direction) decreases to slightly negative values until the rod lie in the $Z = 0$ plane. This fact can be ascribed to a competition between the torque induced by gravity and the trapping restoring forces in the Z direction acting at different points in the beam. Thereafter, the beam starts to bent as both $Y_D(t)$ and $\phi(t)$ increase.

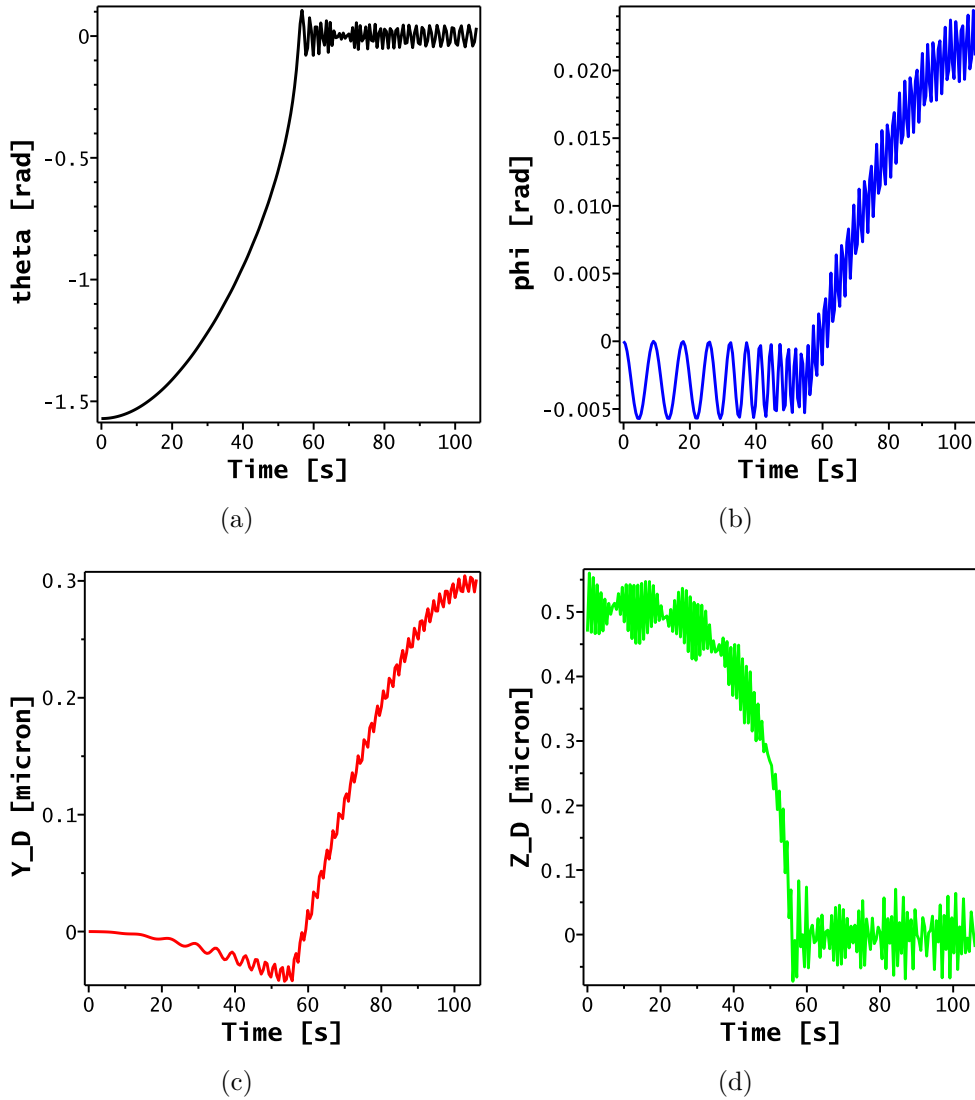


Figure 5.3 – Solutions of the Euler-Lagrange generalized coordinates for the simulated beam. See text for more details.

From the generalized coordinates, we can reconstruct the 3-D motion of our silica rods, using the experimental values for L , k_{trap} , Ψ_0 , k_b and the known displacement of the center laser. Referring to the results of Figure 5.3, we have used $L = 19 \mu\text{m}$ ($n = 11$ particle rod), $k_{trap} = 6.5 \text{ pN}/\mu\text{m}$, initial plateau $1.55 \mu\text{m}$ corresponding to $\Psi_0 = 0.16 \text{ rad}$ and a measured bending stiffness $k_b \sim 18.5 \text{ pN}/\mu\text{m}$. The laser is moved with amplitude $A_L = 2.65 \mu\text{m}$ and frequency $\omega = 0.0295 \text{ rad/s}$. With these parameters, we compute the Y positions of point A (equivalent to the rod end particles, green solid line) and point B (equivalent to the rod center particle, black solid line) during the loading ramp, and show them in Figure 5.4(a), superimposed to real data.

Despite the rudimentary model, the results are in perfect agreement with the ex-

periments. It is worth noting that the observed oscillations have a different source. Whereas in the simulation they originate from the undamped dynamics encompassed in the Lagrangian (Equation (5.1)), in the other case, they are only due to experimental noise. The excellent agreement is reflected in the force-deflection curve, as illustrated in Figure 5.4(b), where the simulation (dark red line) falls in top of the raw data obtained in the real three-point bending test (blue points). As expected, the center and end particles reach the trapping plane when Ξ_0 equals the height of the triangle, $1.55 \mu\text{m}$. This is also evident in Figure 5.4(c) where we show the parametric trajectories of the end (green) and center (black) vertexes (particles). Blue arrows indicate their motion during the ramp.

5.1.3 Misalignment correction

To obtain the direct evidence for this, we recall that the brightness of each particles depends on its distance from the focal plane of the microscope. We access the integrated brightness of each particle using Crocker's centroid algorithm [41], and report in Figure 5.5(a) the values measured for the end and center particles as a function of Y during a loading ramp. Blue arrows indicate the motion of particles during loading; dashed lines show the Y coordinates of particles when $\Xi = \Xi_0$; large filled circles mark the points reached at the maximum flexion. Before loading, the brightness levels of the center particle is clearly different from those of the two end particles. That is clear evidence that the particles are not at the same height, i.e. that the rod is bent. When $\Xi \geq \Xi_0$, the three particles have similar brightness levels, consistently with the expectation that they then are coplanar with the traps. However, even then, the brightness levels are not exactly equal, which points to a small misalignment between the microscope and trapping plane.

To correct for misalignment, we assume that the measured intensity is a linear function of Z , which is expected to be valid because the Z differences between particles are at most equal to Ξ_0 which is below $2 \mu\text{m}$. To obtain the prefactor of the Z vs intensity relation, we first identify Ξ_0 for each rod from the force-deflection curve; we then observe that before loading the end particles (subscript 1 and 2) and the center one (subscript c) lie in a nearly vertical plane, due to gravity (see colored crosses in Figure 5.5(a)); therefore Ξ_0 can be identified with $(Z_1 + Z_2)/2 - Z_c$. Comparing Ξ_0 with the corresponding difference in intensities yields the desired proportionality coefficient. The consequent estimates of Z values (up to an arbitrary origin) are reported in Figure 5.5(a) on the right vertical axis. For each rod, the trap plane is identified using the positions of end and center particles at the maximum flexion (large circles in Figure 5.5(a)). Using our estimated Z coordinates, we then operate a rotation to access displacements and thus forces in the plane of optical traps. This operation does not change significantly our results, but slightly reduces their scatter. We label x, y, z the new axes: x is now aligned with the centers of the end particles, and y the perpendicular axis in the plane of the traps. The computed y, z trajectories of the end and center particles of the rod of Figure 5.5(a) are reported in Figure 5.5(b). We also show in Figure 5.5(c) the reconstructed 3D structure of the considered rod. Finally, according to the new

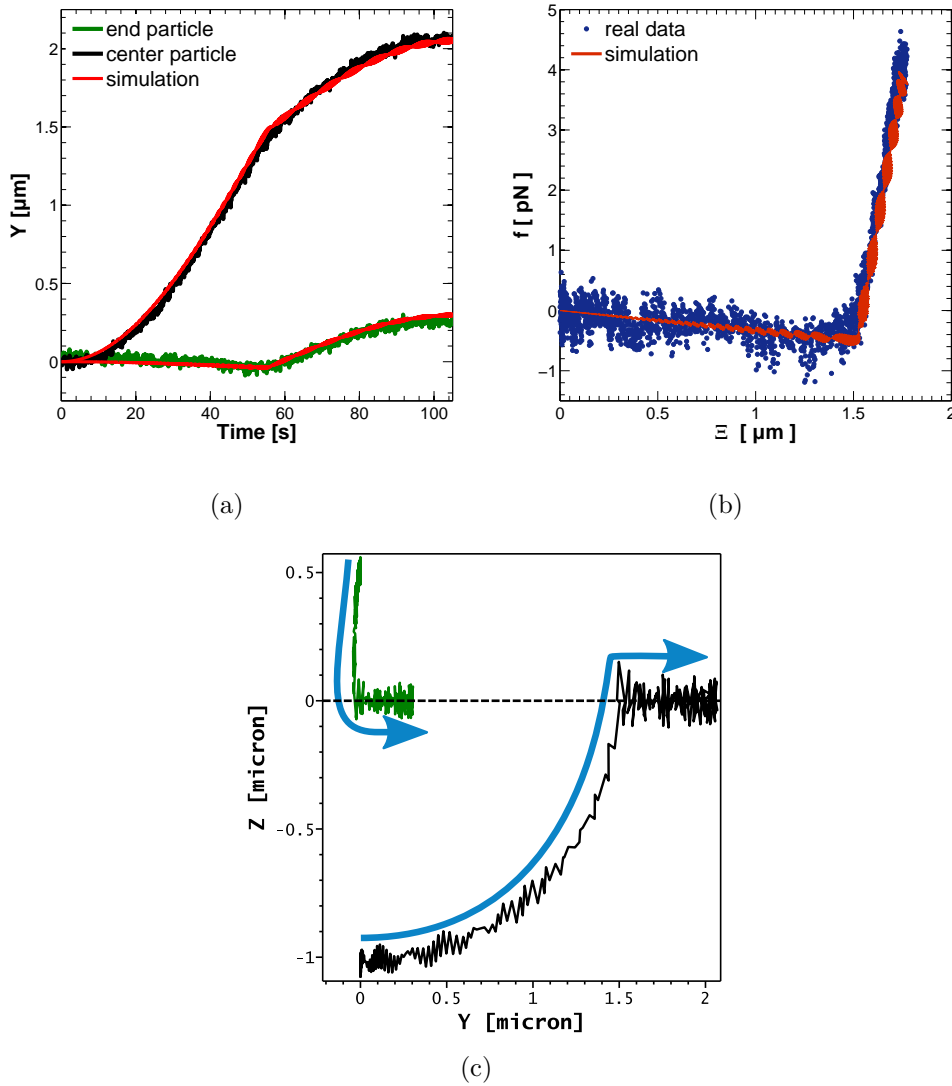


Figure 5.4 – (a) Experimental Y -displacement of the end particle (green solid line) and of the center particle (black solid line) during time, for a beam with initial defect of $1.55 \mu\text{m}$. Red solid lines are computations for point A (equivalent to the rod end particle) and point B (equivalent to the rod center particle). Force versus deflection curve (blue points) for the same beam in (a). The red curve is the result of the simulated data. (c) Simulated trajectories in the YOZ plane of points A and B.

reconstructed coordinates x and y , the corrected force (now labeled f) and deflection (now labeled ξ) are computed according to the procedure described in [Chapter 4](#).

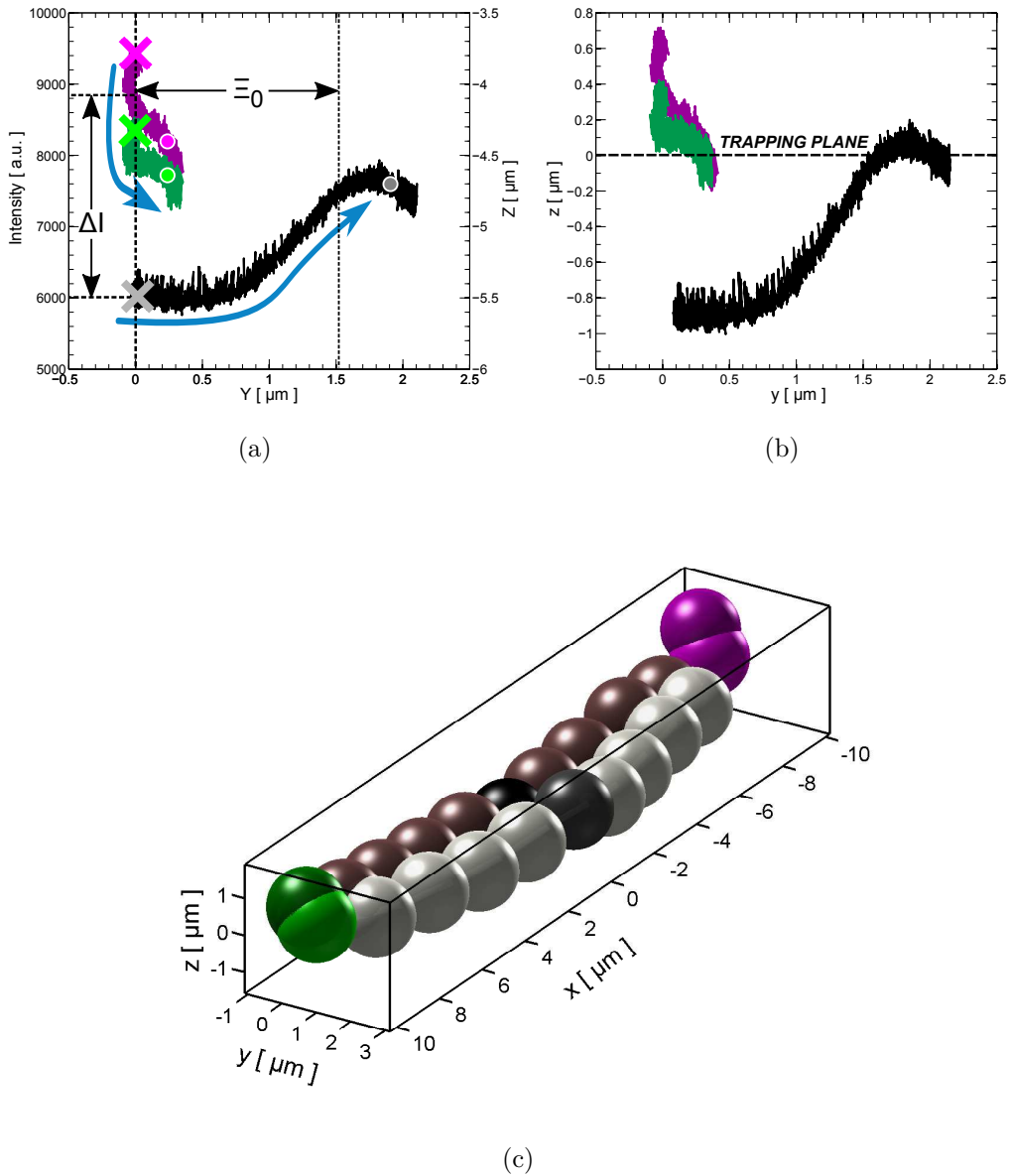


Figure 5.5 – Reconstructing the 3D structure of a rod. (a) Intensity of the end (green and purple) and center (black) particles vs Y ; the curves are parametrized by the loading level which increases as indicated by the blue arrows. On the right axis, we display the estimated Z coordinates deduced by linearizing the intensity vs height relation. (b) Vertical z vs horizontal y particle displacements in the laser plane after reconstruction of the 3D trajectories (see text). (c) Reconstructed 3D image of a rod in both unloaded (brown) and loaded (grey) states.

6

From Micro to Macro

Contents

6.1	Elastic modulus	144
6.1.1	SiO ₂ particle suspensions	144
6.1.2	PMMA particle suspensions	148
6.2	Yield stress	151
6.3	Elastic modulus vs yield stress	153
6.4	Discussion	156

In [Section 3.2](#), we studied the macroscopic aging of dense silica and PMMA suspensions, flocculated with addition of CaCl_2 . We performed bulk rheological measurements for different physio-chemical conditions, and we found, whatever the formulation, a strong growth over time of both the storage modulus G' and the yield stress σ_y . Besides, we carried out a confocal microscopy investigation of similar suspensions and demonstrated the absence of significant changes in the network morphology occurring over the same time interval.

In [Chapter 4](#), using laser tweezers, we performed three point flexural tests on beams formed by identical silica and PMMA particles and demonstrated that, in these moderate-to-high ionic strengths conditions, the particles form irreversible solid-solid contacts that resist rolling. Moreover, their bending rigidity, as well as the maximum moment prior to particle rearrangements, grew quasi-logarithmically in time and with a characteristic time-scale akin to that found in the macroscopic mechanical responses. This fact can only be imputed to the aging of these inter-particle solid-solid contacts.

In this Chapter, we will try to answer to the following question: **can we predict mechanical aging from contact aging, by assuming that the microstructure is rapidly fixed after flow arrest?**

6.1 Elastic modulus

6.1.1 SiO_2 particle suspensions

Let us start with the shear modulus aging for the SiO_2 particle suspensions. We recall that, in the tweezers experiments, we investigated contact aging using a single particle size $2a^* = 1.9 \mu\text{m}$. For now on, we denote $k_0(a^*, t)$ the corresponding bending modulus. Moreover, when attempting to separate particles with our tweezers setup in direct contact, we realized that, in our conditions, the bonds were too strong to be broken by tensile forces, whereas the rods respond elastically when small bending forces are applied. Since the floppiest elastic modes are likely to dominate the macroscopic behavior, it is reasonable to expect that G' is determined, primarily, by the bending rigidity k_0 . Assuming further the complete absence of any structural evolution, all these considerations lead us to propose a simple relationship between the bending rigidity and the elastic modulus:

$$G'(a, \phi, t) = \frac{S(\phi)}{a} \times k_0(a, t) \quad (6.1)$$

with S a t -independent dimensionless quantity, characterizing the structure. Note that we do not explicitly consider the effect of the ionic strength, as we demonstrated that both k_0 and G' are essentially I -independent in the studied range. This expression is tested directly in [Figure 6.1\(a\)](#) (blue symbols) by plotting $G'(t)$ versus $k_0(t)$ data for the particles of size a^* , where t denotes aging times as measured in the three-point bending tests. The linear relation between these two quantities demonstrates experimentally that [Equation \(6.1\)](#) holds, i.e., that, in the explored ionic strength conditions, macroscopic aging can be attributed solely to the progressive stiffening of interparticle contacts, the microstructure being essentially constant shortly after

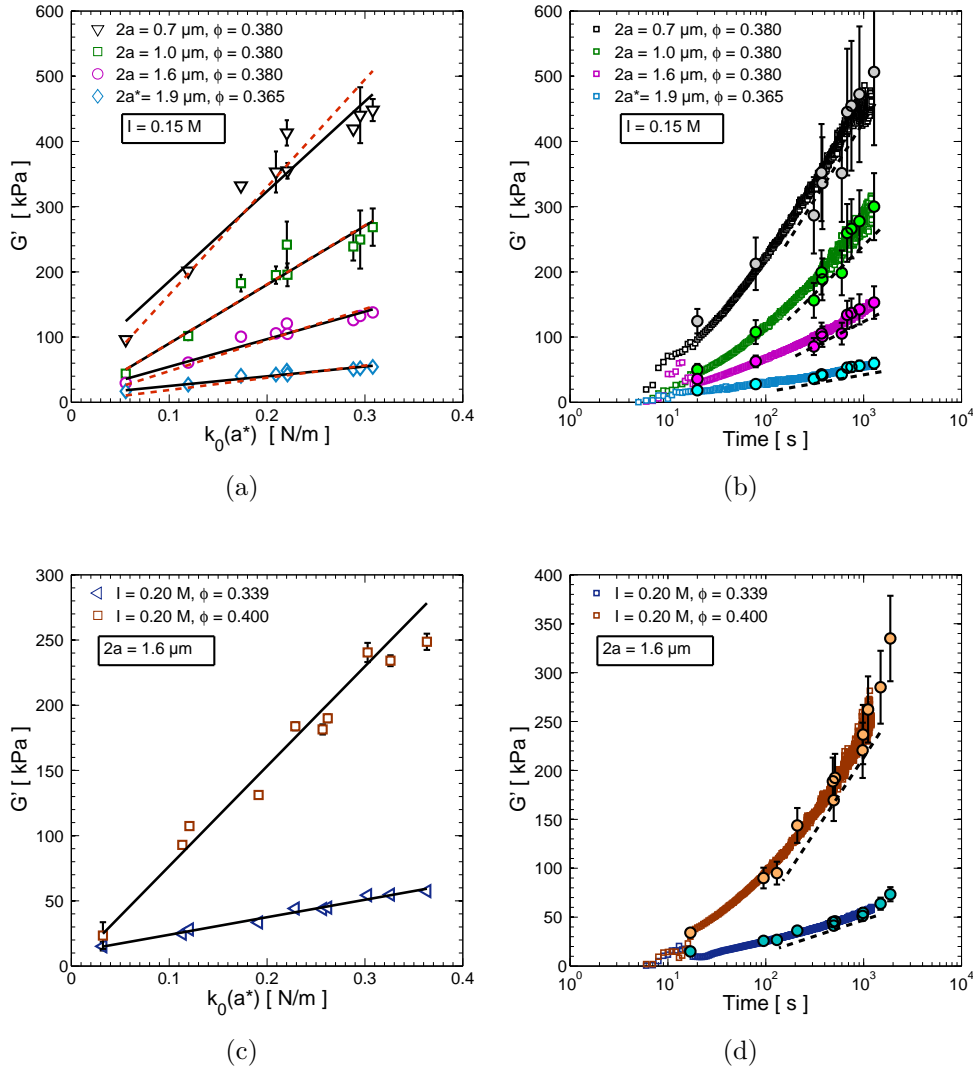


Figure 6.1 – Matching microscopic and macroscopic data. **(a)** $G'(t)$ for suspensions of ionic strength $I = 0.15$ M, for (i) $\phi \simeq 38\%$ and particle diameters, $2a = 0.7$ (black), 1 (green), and $1.6 \mu\text{m}$ (purple) and (ii) $\phi \simeq 36.5\%$ and $2a \simeq 1.9 \mu\text{m}$ (blue), versus the effective flexural rigidity $k_0(a^*; t)$ at the same aging time t ; error bars show the standard deviation of G' data over centered 5s intervals. **(b)** The shear modulus G' (squares) for the same suspensions in **(a)** as a function of aging time. Filled circles (in lighter corresponding colors) are the predictions obtained by extrapolating (see text) the aging data from our three-point bending tests. **(c-d)** Similar plots, but for suspensions with $I = 0.20$ M, $2a = 1.6 \mu\text{m}$ and two packing fractions.

cessation of shearing. The linearity between G' and k_0 , thus, reflects the structural arrest of the suspension network on time scales of few seconds, and demonstrates further that the network deformation is essentially dominated by bond bending.

To further test the above relation, we tentatively analyzed plots of $G'(a, t)$ vs $k_0(a^*; t)$ parametrized by aging time t . Interestingly, as illustrated in [Figure 6.1\(a\)](#) (black-green-purple data) and [Figure 6.1\(c\)](#), the linear relationship systematically applies also when the shear modulus data, obtained at different particle sizes, are compared with the bond stiffness for the given radius a^* , no matter the ionic strength or packing fraction. We thus are able to fit the $G'(a, t)$ vs $k_0(a^*, t)$ by a linear expression:

$$G' = C + N \times k_0 \quad (6.2)$$

for each of our macroscopic data set, i.e. for each a , I , and ϕ . In some cases, the G' vs $k_0(a^*)$ line intercepts the y axis at a small finite value, always $< 50kPa$. These intercepts should be attributed to experimental errors as: (i) they do not appear to correlate with any of our parameters (a , I , or ϕ); (ii) they correspond to the indeterminacy of the origin of aging time in either rheometry or flexural bending experiments, and (iii) they lie below our experimental error bars ($0.03N/m$) on $k_0(a^*)$. As a consequence, assuming $C \simeq 0$ in [Equation \(6.2\)](#) provides equally acceptable fits, as demonstrated by red dashed lines in [Figure 6.1\(a\)](#). The remarkable collapse demonstrates that macroscopic aging can be predicted using just our contact aging data for a single particle size. Thereafter, using the fit parameters, we can reconstruct the time evolution of macroscopic modulus (brightly colored symbols in [Figure 6.1\(b\)](#) and [Figure 6.1\(d\)](#)) from the $k_0(a^*)$ time series.

We now focus on suspensions with ionic strength $I = 0.15\text{ M}$, and report in [Figure 6.3\(a\)](#) the proportionality factors N as a function of ϕ , extrapolated from the linear fits. Since we use the same ionic strength, the emergence of different curves can only be imputed to the an effect of the particle size. Clearly, one wishes to find a function that collapses all the data into a single master curve, thus eliminating the effect of a . To do so, in the following section we will use the Pantina-Furst model for k_0 , in combination with [Equation \(6.1\)](#).

Pantina-Furst model Remember that in [Section 4.5.2](#) we used Euler-Bernoulli beam theory to express the bending stiffness k_0 as a function of the contact area between particles. [Equation \(4.26\)](#) predicts $k_0 \propto a^{-1/3}$, which, combined with [Equation \(6.1\)](#) yields for the macroscopic shear modulus:

$$G'(a, t) = \frac{S \cdot (3\pi)^{7/3} E}{4 a^{4/3}} \left(\frac{W(t)}{E^*} \right)^{4/3} = S \frac{(a^*)^{1/3}}{a^{4/3}} k_0(a^*, t) \quad (6.3)$$

If this relation holds, we now expect that, since $[k_0(a^*)]^{3/4}$ does, $(G')^{3/4}$ —and not G' —grows logarithmically in time. We check this by plotting in [Figures 6.2\(a\)](#) and [6.2\(b\)](#) the G' data of [Figures 6.1\(b\)](#) and [6.1\(d\)](#), respectively, as $(G')^{3/4}$ vs t . There is a considerable improvement on this representation of the range where a

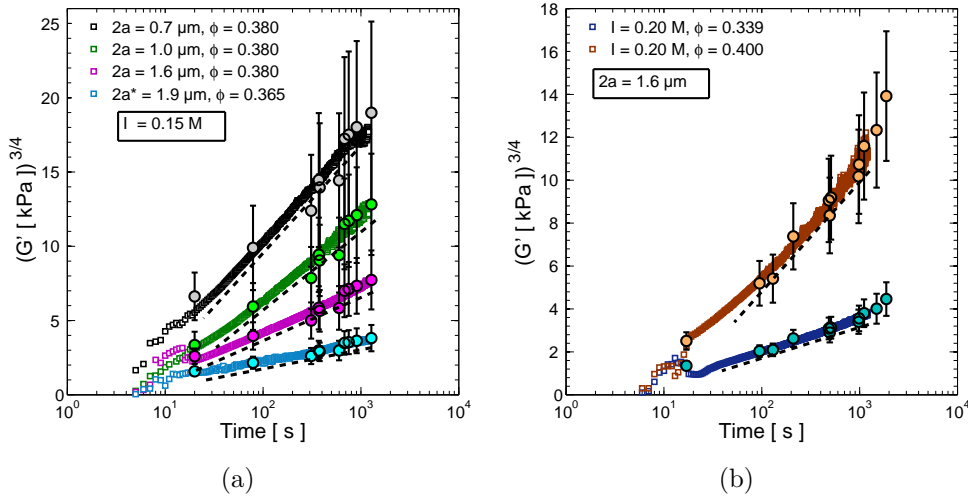


Figure 6.2 – Log-lin plot of $[G']^{3/4}$ vs t supporting that asymptotic growth is rather $\simeq [\log(t/\tau)]^{4/3}$ as suggested by our arguments (see text for details).

logarithmic growth is observed, which supports strikingly well the scaling predicted by our simple relation.

Next, for each of our macroscopic data set, we take the slope N of the linear fit, and estimate the structural parameter S of equation (6.3) as:

$$S^{PF} \simeq \frac{a^{4/3}}{(a^*)^{1/3}} N \quad (6.4)$$

All of our S^{PF} data, when plotted vs ϕ (see Figure 6.3(b)) remarkably collapse on a single curve. This confirms the prediction of the beam model for the $a^{-4/3}$ particle size scaling of G' , and supports that the dimensionless prefactor S depends neither on particle size, nor on ionic strength. Unsurprisingly, S rapidly increases with ϕ . The data are consistent with its diverging at a packing fraction ϕ_c , as it fits reasonably well an expression of the form $S = S_0/(\phi_c - \phi)^\alpha$, for example with $\phi_c \simeq 0.52$ and $\alpha = 4$, as shown.

We find quite striking that our silica data support that both k_0 and G' age asymptotically as $\propto [\log(t/\tau)]^{4/3}$, and furthermore verify the predicted a -scaling. Indeed, we expect this analysis to explain qualitatively the origin of the growth of network rigidity, but not to provide consistent predictions at such a level of detail. Thus, while the data bring compelling experimental evidence for Equation (6.3), we also tested the possibility that k_0 is independent from the particle size, like in the Dominik-Tielens model. In this case, Equation (6.1) is not affected by the particular value of a^* , and the particle radius enters only as a linear proportionality constant between N and S :

$$S^{DT} \simeq a N \quad (6.5)$$

(the label DT is used to remind that a similar scaling would have been obtained with the Dominik-Tielens rolling model). Note that, even though Equations (6.4) and (6.5)

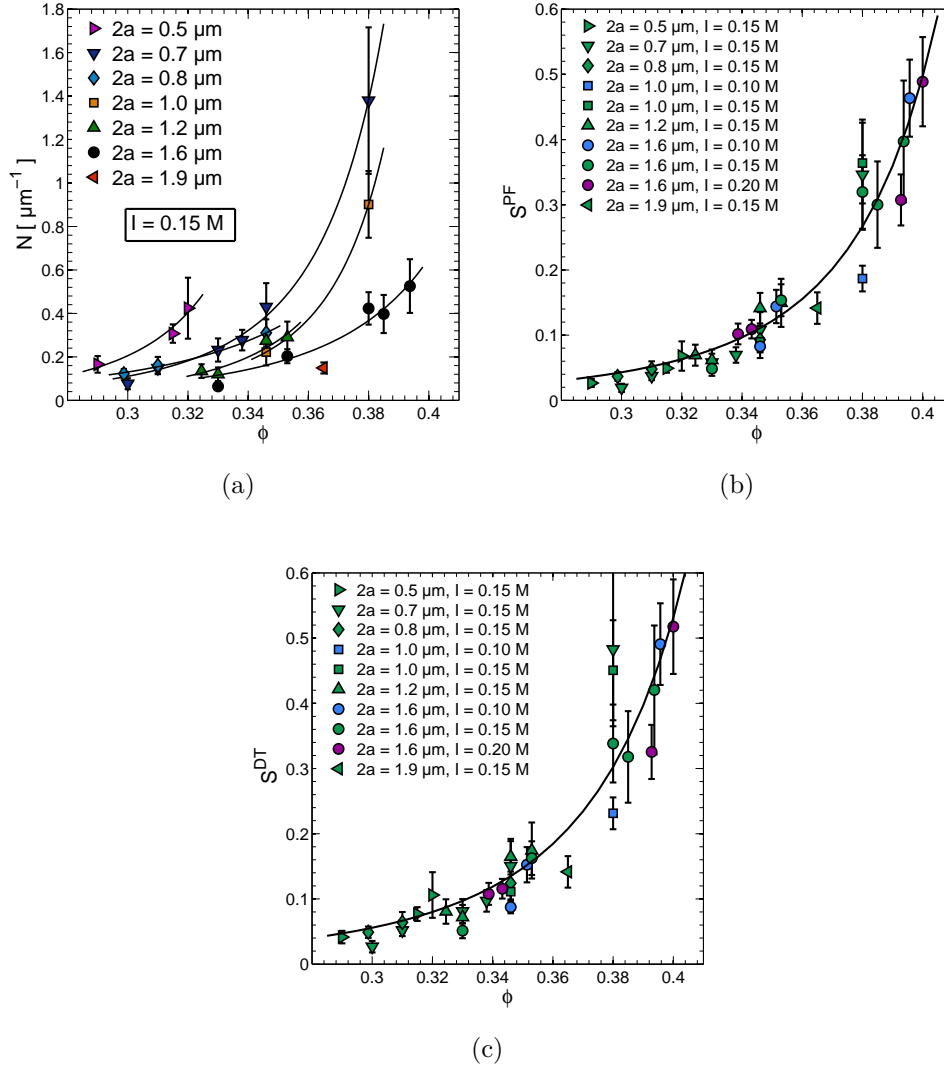


Figure 6.3 – (a) Proportionality prefactor N versus ϕ for the same I but different particle sizes; error bars show the confidence intervals of the G' vs k_0 linear fit. (b) Structural parameter S^{PF} expected from the Pantina-Furst model, Equation (6.4); different a (I) are shown with contrasting symbols (colors). (c) Structural parameter calculated from the scaling in Equation (6.5), akin to the Dominik-Tielens predictions. Solid lines are fits with $S = S_0/(\phi_c - \phi)^\alpha$, with fixed $\alpha = 4$ and (b) $\phi_c \simeq 0.518$ and (c) $\phi_c \simeq 0.532$.

only differ by a factor $(a/a^*)^{1/3}$, which is a small contribution in the (restricted) range of particle sizes used in our experiments, the collapse shown in Figure 6.3(c) appears less convincing.

6.1.2 PMMA particle suspensions

To support the generality of our findings, we now examine the results for the $2a = 3\mu\text{m}$ PMMA suspensions in CaCl_2 solutions. Equation (6.1) between macroscopic and contact aging can be tested directly as we used the same particle size in both

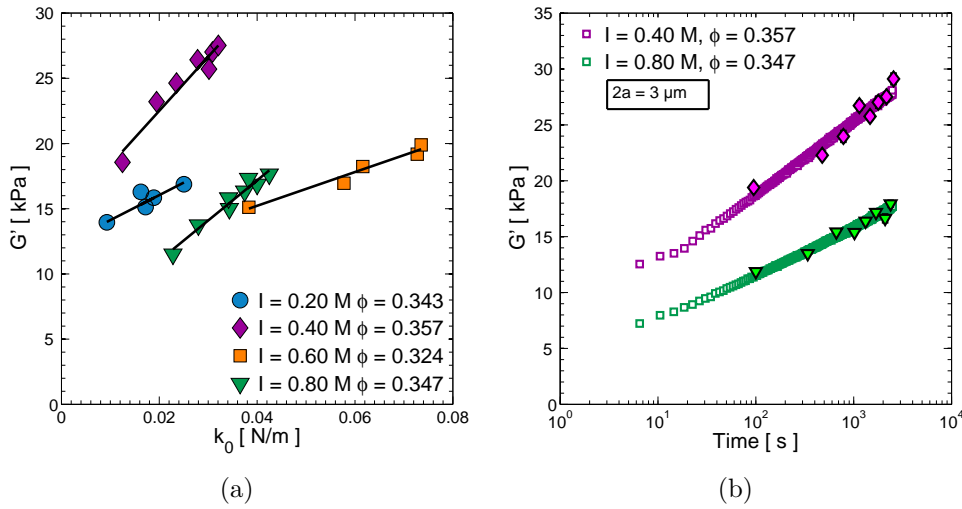


Figure 6.4 – Macroscopic and contact aging in PMMA suspensions. (a) Shear modulus G' vs k_0 for the same aging times, showing that the two quantities are well described by a linear relationship. (b) Macroscopic shear modulus G' (colored squares) for two suspensions with $\phi \simeq 0.35$ and different ionic strengths along with the modulus reconstructed from the k_0 time series (brightly colored circles) using a linear fit.

type of experiments. We report in Figure 6.4(a) our $G'(t)$ vs $k_0(t)$ data for different ionic strength conditions ($I = 0.20$ - 0.80 M). Quite remarkably, all of these plots are very clearly linear, namely of the same form $G' \simeq C + N \times k_0$. However, in sharp contrast with the case of silica, the intercepts are rather large and cannot arise from experimental errors. This entails that at very early times, when the bending rigidity is still negligibly small, PMMA suspensions already present an initial measurable macroscopic modulus $G'_0 \simeq C$ associated with the network of attractive interparticle bonds. The linearity of the G' vs k_0 plots supports that G' is just the sum of two contributions: G'_0 , which does not age, and $N \times k_0$, which does, due to contact aging.

$$G'(a, \phi, I, t) = G'_0(a, \phi, I) + \frac{S(\phi, I)}{a} \times k_0(a, I, t) \quad (6.6)$$

Our PMMA data thus demonstrate that, just as with silica suspensions, the growth of G' can solely be attributed to that of k_0 , irrespective of the initial modulus G'_0 . The time evolution of G' can then be reconstructed from the k_0 times series, using just the two constant parameters G'_0 and N of the linear fits —see the brightly colored symbols in Figure 6.4(b), which fall right on top of the G' curve.

We do not have for the moment a clear explanation for the physical origin of G'_0 , and why the overall suspension aging is only related to an increase of the rolling stiffness, whereas the total macroscopic elasticity appears to depend also on additional local time-independent rigidities. Observe also that G'_0 is almost identical —around 12 kPa —for all the suspensions with $I \leq 0.60$ M, and sharply falls to ~ 4 kPa for the higher ionic strength. At this stage, we are not able to explain this behavior,

nor if we can attribute it to the charge reversal of the particles observed at 0.6 M in ref. [147]. Additionally, a single structure factor S can not be retrieved by our data, as both G' and k_0 strongly depend on I .

6.2 Yield stress

In the previous section we demonstrated that the G' aging of our suspensions can be imputed solely to the aging of the particle-particle contacts, considering the microstructure essentially frozen over time. Here, we extend these findings to the non-linear rheological response of the suspensions, by establishing, for the first time, a direct link between the strengthening of the contacts and the time evolution of σ_y . The quantitative agreement between microscopic and macroscopic measurements enable us to elucidate the origin of the yield stress aging in our concentrated colloidal suspensions.

SiO₂ particle suspensions

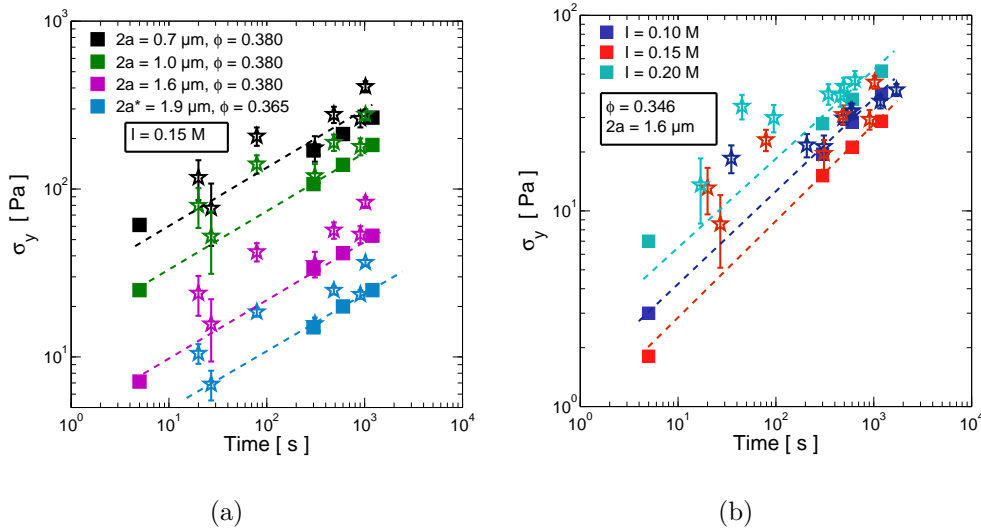


Figure 6.5 – Yield stress aging in a dense silica suspensions. (a) Colored filled squares are the σ_y results for suspensions with ionic strength $I = 0.15$ M, $\phi \simeq 38\%$ and $2a = 0.7$ (black), 1 (green), 1.6 μm (purple), $\phi \simeq 36.5\%$ and $2a \simeq 1.9$ μm (blue). Stars (in corresponding colors) are the predictions obtained by multiplying by a constant proportionality factor the M_c data set at the same I . (b) Similar plot for suspensions with $\phi \simeq 35\%$, $2a = 1.6$ μm and $I = 0.10$ M (blue), $I = 0.15$ M (red) and $I = 0.20$ M (light blue).

Recently, it has been argued [71] that the yield stress of diluted colloidal gels, made of aggregated particles, should be essentially determined by the bending (as opposed to elongational) micro-mechanics of the particle bonds. We now tentatively apply this idea to our dense suspensions. From a microscopic viewpoint, this is supported by various empirical observations. Recall that the rods yield in a “brittle-like” fashion, with the critical moment M_c marking an abrupt transition between elastic and non linear response. A similar behavior is found in the macroscopic suspensions, since critical strains of few tenths of % suggest that the structure is not strongly strained prior to flow. Besides, the linear elastic domain measured in the tweezers experiments shrinks with age and an analogous behavior can be observed by the

analysis of the σ_y data (see Section 3.2). It is thus reasonable to believe that, as we showed that the elastic shear modulus is essentially determined by the bending rigidity of the contacts, the macroscopic yielding behavior is similarly determined by the failure of the bonds under external torques.

In Section 4.4.1 we also demonstrated that the growth in time of M_c in our silica rods can only be attributed to a strengthening process occurring within the inter-particle contacts. Such contact aging, together with the observation of structural arrest, leads us to ask whether the macroscopic yield stress growth can be related to the time evolution of M_c , i.e. whether we can write:

$$\sigma_y(a, \phi, t) = \frac{Q(\phi)}{a^3} \times M_c(a, t) \quad (6.7)$$

where Q is again a time- and I -independent prefactor associated to the microstructure (the analogous of S).

To test this hypothesis, we first focus our attention to a suspension made of $2a^* = 1.9 \mu\text{m}$ silica particles at $\phi = 0.365$. Macroscopic yield stress measurements at three different aging times — $t=300-600-1200$ s— give $\sigma_y(a^*, t) \sim 12-20-25$ Pa, respectively, as illustrated in Figure 6.5(a) (filled blue squares). We now wish to compare these data with the time-dependent critical moments obtained from bending tests on identical particles. Observe that, in contrast with the case of elasticity, a direct fit between σ_y and M_c is not possible due to the small number of data acquired during the rheology cycle (Section 3.2.3). However, since at the same aging time, $M_c(a^*, t) \sim (10-19-21) \cdot 10^{-18} \text{Nm}$ (see also Section 4.4.1), it is easy to show that the ratio σ_y/M_c remains almost constant during the considered time interval, which suggests, hence, that the time evolution of the yield stress and the critical moment are proportional, i.e. that Equation (6.7) holds. Hence, a rough calculation of the structure factor could be performed via

$$Q(\phi) = a^{*3} \left\langle \frac{\sigma_y(a^*, t)}{M_c(a^*, t)} \right\rangle_t \quad (6.8)$$

where $\langle \dots \rangle_t \sim 1.15 \pm 0.10 \mu\text{m}^{-3}$ denotes the average over the three aging times $t=300-600-1200$ s. Using $a^* = 0.95 \mu\text{m}$, Equation (6.8) yields $Q \sim 1$. With this value, we reconstruct the time evolution of the yield stress from the $M_c(a^*, t)$ time series, as shown in Figure 6.5(a) with blue stars. The remarkable correlation between microscopic and macroscopic measurements represents a direct evidence that the yield stress growth is determined solely by the strengthening of the particle-particle solid contacts.

We now check whether the full set of σ_y vs t can be predicted only on the basis of the critical moments M_c obtained with the particular particle size used in the bending tests. To calculate the proportionality prefactor N , however, we need to know how M_c scales with a . To do so without invoking a model, N is characterized using a statistical approach to relate the yield stress to the critical moment time series. The method is based on the Fréchet distance $F(A, B)$ between two (discrete) curves

A and B , a particular proximity (scalar) measure that takes into account (i) the location and ordering of the points along the curves and (ii) the different dimensions of the time series [60]. The proportionality factor N is simply found by firstly defining a range of multiplication constants c , usually $c = [0.01, 20] \mu\text{m}^{-3}$ and, then, by searching for the c that minimizes the distance $F(\sigma_y, c \times M_c)$ between σ_y and $c \times M_c$. The yield stress data are subsequently reconstructed from the M_c time series through $N \times M_c$, and then plotted in Figure 6.5(a).

Unsurprisingly, we are able to predict the σ_y time evolution of suspensions with different a , only using Equation (6.7) with the M_c data obtained for a^* —see colored stars in Figures 6.5(a) and 6.5(b). To our knowledge, such a relationship between contact and yield stress aging has never been directly observed before.

6.3 Elastic modulus vs yield stress

In Section 3.2 we illustrated that the elastic modulus of our suspensions, whatever the solid volume fraction, the particle size, the ionic strength or the resting time, can be rescaled into a single master curve if one plots $G' \cdot a^{n_G}$ versus $\sigma_y \cdot a^{n_\sigma}$, where the exponents n_G and n_σ are simple numbers assumed to be the same for all the silica suspensions. We now would like to explain the emergence of this master curve on the basis of our microscopic data, as this would represent an additional stringent support to our previous findings. First, we rewrite the shear modulus and yield stress a -scaling as:

$$G'(a) = G'(a^*) \left[\frac{a^*}{a} \right]^{n_G} \quad (6.9a)$$

$$\sigma_y(a) = \sigma_y(a^*) \left[\frac{a^*}{a} \right]^{n_\sigma} \quad (6.9b)$$

where a^* is a reference particle size (and, for now on, is assumed to coincide with the size of the beads used in the bending tests). We then observe that in the tweezers experiments we found:

$$M_c(a^*, t) = m_c \cdot [k_0(a^*, t)]^p \quad (6.10)$$

with $p \sim 1/2$ (see Figure 4.20(a) and Section 4.4.1) and m_c a constant proportionality factor. Note that, if the time evolution of σ_y (through Equation (6.7)) and G' (through Equation (6.1)) are determined by adhesion energy $W(t)$, i.e. by contact aging, Equation (6.10) suggests that the yield stress increases more slowly than the shear modulus. Since the linear elastic behavior roughly extends everywhere below the yield stress — $\sigma_y = G' \gamma_c$, with γ_c a critical macroscopic strain — Equation (6.10) confirms, hence, that the critical strain $\gamma_c = \sigma_y / G'$ is a decreasing function of time, in agreement with our rheology measurements.

Using Equations (6.1), (6.7), (6.9) and (6.10) it is easy to show that:

$$G' \cdot a^{n_G} = \left\{ \frac{S(\phi)}{Q^{1/p}(\phi)} \cdot \left[\frac{[a^*]^{3-n_\sigma+p(n_G-1)}}{m_c} \right]^{1/p} \right\} \times [\sigma_y \cdot a^{n_\sigma}]^{1/p} \quad (6.11)$$

From the bulk measurements of G' and σ_y (Section 3.2), we already know that the

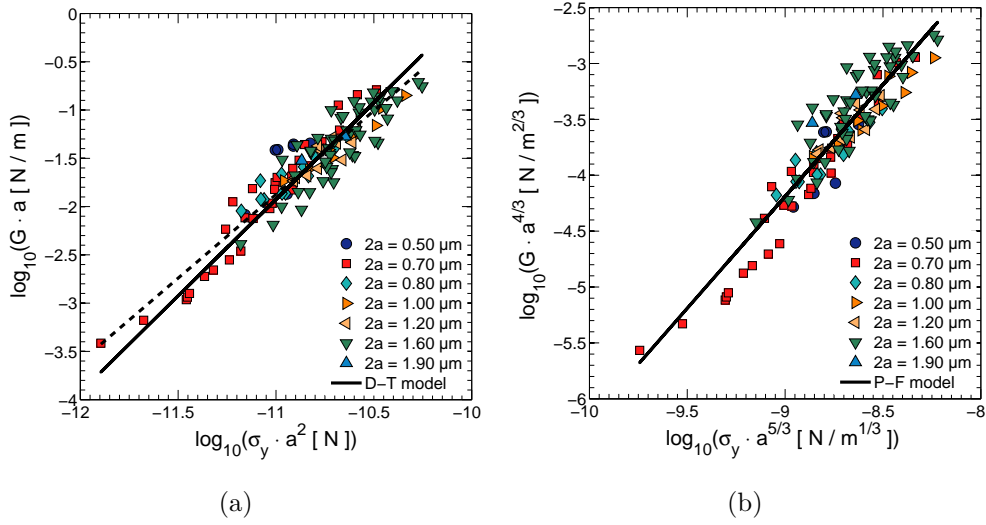


Figure 6.6 – (a) Elastic modulus versus yield stress scaled with $n_G = 1$ and $n_\sigma = 2$, respectively. (b) Same thing, using the P-F estimations ($n_G = 4/3$ and $n_\sigma = 5/3$, respectively).

shear elastic modulus should scale approximately with the inverse of the particle size, whereas the yield stress with the inverse of the particle size squared. This suggests $n_G = 1$ and $n_\sigma = 2$ in the previous expression. According to Equation (6.7), n_σ is equal to 2 only if $M_c \propto a$. More precisely, it turns out that these exponent values are those predicted by the Dominik-Tielens rolling model, in view of Equation (6.10) (refer to Section 4.5.3 and Table 4.3) and, for this reason, we will refer to the D-T model when using $n_G = 1$ and $n_\sigma = 2$. Summing up, with the above values and $p = 1/2$, Equation (6.11) reduces to:

$$G' \cdot a = \left\{ \frac{S(\phi)}{Q^2(\phi)} \cdot \left[\frac{a^*}{m_c} \right]^2 \right\} \times [\sigma_y \cdot a^2]^2, \quad (6.12)$$

The above relationship can be tested directly upon our macroscopic data, by plotting $\log(G' \cdot a)$ as a function of $\log(\sigma_y \cdot a^2)$. The results, for all the studied packing fraction, ionic strengths, resting times and particle sizes are reported in Figure 6.6(a). The macroscopic data are then fitted by a power-law relationship $G' \cdot a = C \times [\sigma_y \cdot a^2]^u$ with C and u as fitting parameters, as predicted by Equation (6.12). The fit yields $u = 1.75 \pm 0.15$ (dashed black line), which is close, but not equal to the expectation of the model (i.e. 2). Observe, however, that if one forces the fit using $u = 2$ and leave C as a free parameter (solid black line), one still obtains a reasonable agreement; the goodness of the two fits can be roughly compared by taking their R -squared values, $R = 0.866$ and $R = 0.846$ in the two cases, respectively. The results of the fits are reported in Table 6.1.

The good agreement between the macroscopic data and Equation (6.12) indicates that the term between curly brackets in the latter is constant. Since both a^* and m_c are constant in our tweezers experiments, this is possible only if $S(\phi) \sim Q(\phi)^2$.

Table 6.1 – Power-law fits to the G' versus σ_y curves in Figure 6.6. Errors are confidence intervals of the fit.

Model	C	u	R-squared
$G' \cdot a = C \times [\sigma_y \cdot a^2]^u$	$1.55 \cdot 10^{17} \text{J}^{-1}$	1.75 ± 0.15	0.866
$G' \cdot a = C \times [\sigma_y \cdot a^2]^2$	$1.20 \cdot 10^{20} \text{J}^{-1}$	/	0.846
$G' \cdot a^{4/3} = C \times [\sigma_y \cdot a^{5/3}]^u$	$1.30 \cdot 10^{14} \text{N}^{-1}$	2.04 ± 0.15	0.870

Using the experimental values for m_c and a^* , and the fitted $C \approx 1.20 \cdot 10^{20} \text{J}^{-1}$, we then obtain

$$\left[\frac{a^*}{m_c} \right]^2 \sim 9 \cdot 10^{20} \text{J}^{-1}, \quad (6.13)$$

and, hence

$$Q(\phi) \approx 2.75 \times \sqrt{S(\phi)} \quad (6.14)$$

Let us reflect on two consequences of Equation (6.14). From Equations (6.1), (6.7) and (6.14) one obtains:

$$\gamma_c(t, \phi) \sim \frac{2.75 \cdot \Upsilon_c(t)}{96 \cdot a \sqrt{S(\phi)}} \sim \frac{2.75 \cdot \vartheta_c(t)}{96 \cdot \sqrt{S(\phi)}} \quad (6.15)$$

where Υ_c and ϑ_c are the interparticle critical rolling displacements and angles (resp.). This relation is able to capture two main features of our rheology data. Indeed, since S grows with ϕ and $\Upsilon_c(t)$ decreases with age of the contacts (Figure 4.20(b)), $\gamma_c(t, \phi)$ is a decreasing function of (i) packing fraction and (ii) aging time, as we indeed observed in Section 3.2. Note also that a similar γ_c vs ϕ behavior has been reported in diverse experimental works [196, 22, 29] and shares some similarity with the reduction of the limit of elastic linearity discussed in [178].

Pantina-Furst model We now analyze our scenario on the basis of the scaling laws predicted by Pantina and Furst, and Equation (6.10) with $p = 1/2$. In Section 4.5.2 we have seen that the bond stiffness and the critical bending moment should scale as:

$$(I) \quad k_0^{PF}(a, t) \propto a^{-1/3} \cdot W^{4/3}$$

$$(II) \quad M_c^{PF}(a, t) \propto a^{4/3} \cdot W^{2/3}$$

Thus, $n_G = 4/3$. Since M_c is proportional to $a^{4/3}$, from Equation (6.7) one obtains $\sigma_y(t) \propto a^{-5/3}$, i.e. $n_\sigma = 5/3$. Upon inserting these values in Equation (6.11), we get:

$$G' \cdot a^{4/3} = \left\{ \frac{S(\phi)}{Q^2(\phi)} \cdot \left[\frac{a^* \cdot 3/2}{m_c} \right]^2 \right\} \times [\sigma_y \cdot a^{5/3}]^2, \quad (6.16)$$

Of course, the data collapse predicted by the model differs from that obtained previously. Yet, despite this different a -scaling, the results are still compatible with a

power-law function $G' \cdot a^{4/3} = C \times [\sigma_y a^{5/3}]^u$. A direct fit with C and u as free parameters yields $C \sim 1.3 \cdot 10^{14} \text{N}^{-1}$ and $u = 2.04 \pm 0.15$, as shown in [Figure 6.6\(b\)](#) (black solid line). The fit results and the corresponding R -squared value ($R = 0.87$) are reported in [Table 6.1](#). Therefore, the P-F expectations nicely agree with the empirical G' versus σ_y curve, since one gets $u \sim 2$. Moreover, since we have:

$$\left[\frac{a^{*3/2}}{m_c} \right]^2 \sim 8.35 \cdot 10^{14} \text{ N}^{-1} \quad (6.17)$$

and $C \sim 1.3 \cdot 10^{14} \text{N}^{-1}$, we obtain a similar relationship to [Equation \(6.14\)](#):

$$Q(\phi) \approx 2.5 \times \sqrt{S(\phi)} \quad (6.18)$$

Note that the scaling exponents, n_G and n_σ , are based on the particular model used to characterize the rolling properties of the contacts (P-F or D-T), while the power-law exponent ~ 2 is determined only by $p \sim 1/2$ in [Equation \(6.10\)](#), i.e. by the empirical relationship obtained in our tweezers experiments. The fact that [Equations \(6.12\)](#) and [\(6.16\)](#) with $u \approx 2$ appear to well describe our macroscopic data, hence, gives an additional support to our scenario, *viz.* a shear modulus and yield stress aging that is proportional to the time-evolution of k_0 and M_c , respectively, with S and Q two time-independent quantities characterizing the microstructure.

We now study the predictions of the P-F model in terms of critical rolling angles. Recalling that $M_c = \eta^{PF} a_c^2$, with $\eta^{PF} = 0.039 \pm 0.003 \text{N/m}$, the critical rolling angle decreases with particle size and adhesion energy as:

$$\vartheta_c^{PF}(a, t) = \frac{32\eta^{PF}}{\pi(3\pi)^{2/3} E a^{1/3}} \cdot \left(\frac{E^*}{W(t)} \right)^{2/3} \approx \frac{1.85 \cdot 10^{-5}}{a^{1/3} W^{2/3}(t)} \quad (6.19)$$

From our bending data we first evaluate $W(t)$ at a particular aging time, e.g. $t = 300\text{s}$, and then assess ϑ_c versus a from [Equation \(6.19\)](#), as illustrated in [Figure 6.7](#) (black solid line). We compare this estimate with the critical angles computed from [Equation \(6.15\)](#), averaging $\gamma_c(\phi) \cdot \sqrt{S(\phi)}$ over all suspensions with same particle size and different pairs (ϕ, I) , and using the fitted S^{PF} values (filled symbols). The superposition of the data indicates, as expected, that the model describes qualitatively well our bulk rheology data.

6.4 Discussion

It would be clearly desirable to find an unambiguous scaling behavior. Unfortunately, this is hardly achievable only on the basis of our rheology data in [Figures 6.6\(a\)](#) and [6.6\(b\)](#). We repeat that the reason is quite simple: our study, like many others in colloidal suspensions [[221](#), [23](#), [113](#), [131](#), [68](#)], suffer from the small range of a which is experimentally accessible (usually in the 50nm - $3\mu\text{m}$ interval). Besides, the results are likely to be altered by experimental issues as particle polydispersity, shape, surface roughness, etc.

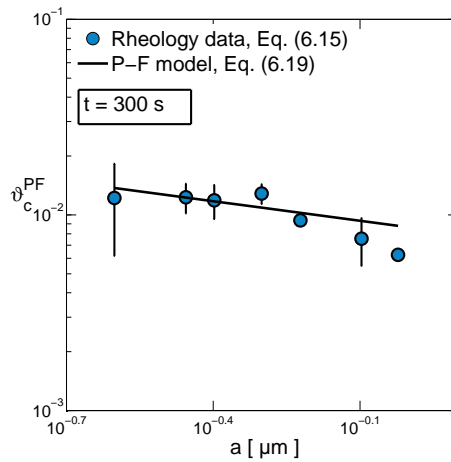


Figure 6.7 – Average critical rolling angle versus particle radius computed from rheology measurements (γ_c) and Equation (6.15) (solid symbols). Solid line is the prediction of Equation (6.19).

Nevertheless, our analysis suggests scaling exponent values that are similar to those found in strongly flocculated colloidal suspensions where contacts may be relevant [221, 23, 113, 131, 68]. Focusing on σ_y , for instance, we obtained $\sigma_y \propto a^{-2}$ and $\sigma_y \propto a^{-5/3}$ when we used the D-T or the P-F models, respectively. Attempts to rationalize the yield stress behavior as a function of particle size, on the other hand, are generally based on the idea that the solid-liquid transition arises from the tensile failure of the colloidal bonds [172, 63], in agreement with centro-symmetric interactions. These models usually predict $\sigma_y \propto a^{-1}$, in contrast with the experimental $\sigma_y \sim a^{-2}$ dependence found in the mentioned works.

We emphasize that the core of our results is the experimental demonstration that contact aging is determinant in shaping the mechanical properties of dense suspensions of strongly flocculated colloidal particles. Our scenario is very clearly supported by the combination of our observations at particle and macroscopic scales. In particular, (i) we directly observe flexural aging using our tweezers experiment and (ii) we establish a linear relation with macroscopic aging.

7

Conclusions and Perspectives

In this work, we have studied two ionic suspension models involving particles of sharply different natures. In both cases, we observed the same scenario: first, the microstructure rapidly stabilizes due to the formation of irreversible contacts; then, macroscopic aging proceeds due to the growth of flexural rigidity between particles, i.e. the stiffening of contacts. We have analyzed this scenario through contact models based on adhesion theories [102, 48], and we have attempted to provide an interpretation for contact aging at the microscopic scale. We stress, however, that our conclusions do not depend on the aging mechanisms at these scales, which is a system-specific issue. Using two systems with drastically different aging mechanisms at sub-contact level, we have indeed shown that the existence of a relationship between contact and macroscopic aging does not depend on the microscopic mechanisms of aging inside the contact. Although what is actually causing contact aging is an important and interesting problem, it is just not the goal of the present work.

It may be argued that macroscopic aging could proceed via a different mechanism than the one we propose. One possibility could be that the structure is rapidly stabilized by attractive forces bringing pairs within short distances, below about 20nm, without actual contact formation for times comparable to aging. This requires contact formation to be limited by energy barriers. More precisely, the above scenario could be valid in the conditions when the interparticle forces present two closely energy minima: that associated with contacts and a secondary one within 20nm. The DLVO potential may present such a structure depending on conditions. In such a case the structure could be rapidly stabilized by the pairs accessing secondary minima; and the progressive formation of contacts could drive aging. The barriers limiting contact formation would then need to correspond to activation timescales of order comparable with the onset of aging, which is about 10s. However, we have clear evidence that such barriers are absent. First, we have identified all the parameters of the DLVO interaction for our system; we showed that the ionic strengths at which we work are well within the domain where no barrier, and no secondary minimum exist. Second, this is directly supported by our observation that contact cannot be reopened immediately after their formation. Hence, the key condition for the aging scenario is that the formation of solid-solid contacts is essentially not barrier-limited. Indeed, van der Waals contact energies lie typically in the $1000kT$ [98] range. So, in general, solid-solid contacts cannot be opened by thermal activation at room temperature [187, 207]. Therefore, at moderate or high packing fractions, the corresponding suspensions are expected to rapidly freeze into thermally irreversible structures. Moreover, solid-solid contacts generically display roll-resistance [44], because particle surfaces are non-ideally smooth. Since, roll-resistance and aging are ubiquitous contact properties, our whole scenario follows from the absence of barriers limiting the formation of contacts.

It is noteworthy that our silica particles, being micron-sized, should sediment over seconds if they were not interacting. Yet, they stabilize at rather moderate volume fractions (at least down to 33% [73]): this degree of stability is a signature of the rapid formation of attractive contacts. Also, in our two systems (silica and PMMA suspensions), rejuvenation may be achieved by a sufficiently strong preshearing, which entails that the solid-solid contacts, although irreversible under thermal activation,

are broken by mechanical forcing. Therefore suspensions may be both homogeneous and easily reshuffled by shearing, even though solid-solid contacts are formed and are stable at rest. Stability and homogeneity hence may be facilitated by contact formation. For these reasons, our scenario—rapid stabilization by contact formation followed by contact-controlled mechanical aging—is expected to be common in suspensions as soon as the ionic concentration is sufficient to screen out Coulombic repulsion. This is likely to be the case of many materials of practical importance, such as cements at the young age [169], sediments, ceramics, sewage sludges, mine tailings, etc, which present ionic concentrations that are typically larger than those considered here. The precise domain of relevance of this scenario, of course, will need to be assessed case-by-case. In the relevant situations, the quantitative link we have established between contact and mechanical aging is a plausible starting point for the construction of predictive models.

We should also contemplate the possibility that, under certain conditions, contact aging may compete with structural aging. This may occur if, for example, the formation of contacts is not as rapid as here—i.e. is limited by non-vanishing but small barriers—or if van der Waals contacts are weak enough to open by thermal activation. The fact that the contacts may stiffen in time may be not incompatible with the additional presence of rearrangements. Such rearrangements appear absent in our concentrated suspensions, due to the formation of strong, irreversible bonds and the “high” packing fractions used. In these conditions, it has been possible to clearly identify it. But contact strengthening must apply also in more diluted suspensions, or gels, comprising similar particles and physio-chemical conditions, i.e. as soon as contact formation can not be avoided. At such lower densities, however, demonstrating a relationship between contact aging and structural relaxation is rendered much harder by the fact that other possible sources of rearrangements can not be disregarded. We discussed in the introduction that the development of internal stresses in dilute gels is one of the main causes determining the unusual faster than exponential relaxation dynamics in these systems [35, 16, 37, 87]. A stiffening of interparticle contacts may be a source of such internal stresses, because it can change the local force balance. Indeed, an heuristic explanation for the observed phenomena is based on the emergence of dipole forces (and long range elastic responses) associated with the *syneresis* of the gel, that is, the local shrink of the microstructure due to the sintering of aggregate particles [35, 20]. Additionally, we have also demonstrated in our three-point bending experiments the existence of a critical bending moment M_c above which small-scale rearrangements are observed. Even when contacts are weak enough that these yield events can be thermally activated, the time growth of the energetic barrier of the critical moment is expected to have important implications for the dynamics of the colloidal gel, as small-scale rearrangements will occur on increasingly larger time scales [62]. The present work, thus, may provide additional insights on the interpretation of structural aging in more diluted systems.

From a theoretical point of view, some open questions that we were not able to fully assess, still remain. They concern the mechanics of the adhesive contacts under external torques. In this regard, future works could be focused on the development of micro-mechanical bending models of aggregate colloidal particles. In this work we

have used two models that likely overlook the complexity of the contacts, and we have shown, indeed, that they are not appropriate to describe the bending mechanics of our colloidal particles.

Additional bending experiments are needed to understand the role of the salt valency on the formation and aging of the adhesive contacts. Our preliminary results show that the amplitude and time-evolution of the bending stiffness are considerably affected by the addition of a monovalent, rather than a divalent, salt, and may also depend on the hydration enthalpy or hydrated size of the cations. Moreover, it might be interesting to investigate the role of the solution pH in the adhesion between the particles, especially in the case of silica, for which it is known that the surface dissociation may strongly depend on it [211, 127]. Lastly, it will be of considerable interest for practical applications the study of the effects of adsorbing polymers on adhesion, contact and macroscopic aging. Some preliminary rheology experiments (not shown here) on suspensions of polymer grafted silica particles show that their mechanical aging is substantially reduced. Progress on these and related questions will open the route towards the possibility to tune mechanical aging by controlling and tailoring the surface chemistry of particles, a fascinating perspective in many applications.

Appendices

A

Dynamic Light Scattering

In DLS, a dilute suspension of Brownian particles is illuminated by a monochromatic laser, and the quasi-elastic scattered light (which implies that the magnitude of wave vector is constant $k_f = k_i$) is detected at a scattering angle θ related to the scattering vector $\mathbf{q} = \mathbf{k}_f - \mathbf{k}_i$ by $q = 2k \sin(\theta/2)$. The light scattered by a set of N independent particles produces a random interference pattern on a screen, provide that the light reaching the detector has not been scattered a significant number of times (single-scattering regime). The pattern is in general formed by numerous, irregularly spaced bright spots called speckles. If the particles positions are fixed in time, the pattern remains unchanged. When particle positions change over time, instead, the speckle field or interference pattern starts to fluctuate depending upon the scatterer dynamics. In general, the intensity fluctuations are recorded for a single speckle (fixed q) as a function of time and analyzed by means of the intensity auto-correlation function (ACF).

$$g_2(q, \tau) = \frac{\langle I(q, 0)I(q, \tau) \rangle_t}{\langle I(q, t) \rangle_t} \quad (\text{A.1})$$

where $\langle \dots \rangle_t$ denotes an average over time and τ is the lag time. Typical raw data and correlation function are reported in [Figure A.1](#). The intensity auto-correlation function is linked to the normalized electromagnetic field correlation function $g_1(q, \tau) = \langle E(q, 0)E^*(q, \tau) \rangle / \langle |E(q, 0)|^2 \rangle$ by the Siegert formula:

$$g_2(q, \tau) = 1 + \beta |g_1(q, \tau)|^2 \quad (\text{A.2})$$

where β is the Siegert factor which is inherently linked to the detection optics. It can be shown [\[220\]](#) that, for a mono-size particle dispersion of Brownian particles, the field correlation is a single exponential decay function of the form:

$$g_1(q, \tau) = e^{-q^2 \cdot \langle \Delta r^2(\tau) \rangle / 6} \quad (\text{A.3})$$

where $\langle \Delta r^2(\tau) \rangle = 6D\tau$ is the mean square displacement. Thus,

$$g_1(q, \tau) = e^{-Dq^2\tau} = e^{-\tau/\tau_c} \quad (\text{A.4})$$

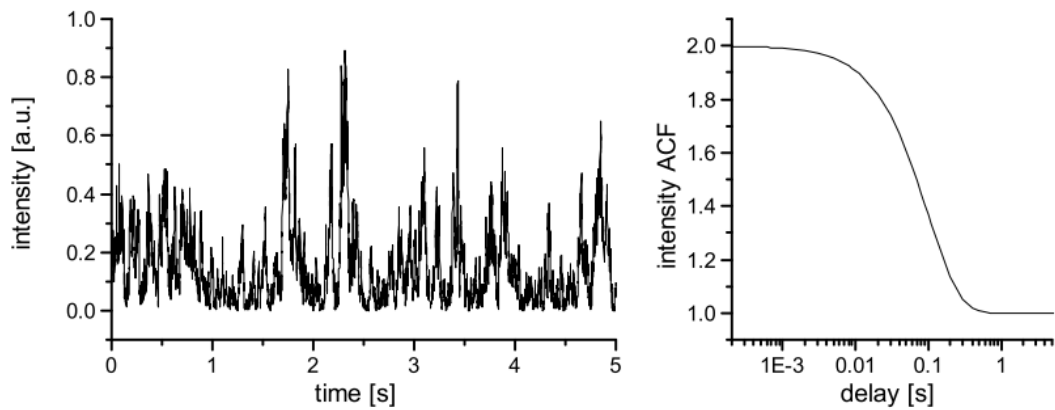


Figure A.1 – Intensity fluctuations in a single speckle as a function of time (left) and corresponding intensity auto-correlation function ACF (right).

where $\tau_c(q) = 1/(Dq^2)$ is the relaxation time. Hence, encompassed within the correlation curve is all of the information regarding the diffusion of particles within the sample being measured. By fitting the correlation curve to an exponential decay function, the diffusion coefficient D can be calculated and the radius of the particles deduced from

$$D = \frac{k_b T}{6\pi\eta a} \quad (\text{A.5})$$

where, $k_b T$ is the thermal energy and η the solvent viscosity.

For a polydisperse sample, the situation is relatively more complicated, as the correlogram is now a sum of exponential decays. The size distribution of the polydisperse sample can be deduced using two main fitting procedures:

- (a) the cumulant (z-average) analysis,
- (b) the single distribution analysis.

In the cumulant method, one assumes that there is one overall average size and one overall average polydispersity. Thus, the ACF is forced to fit a simple Gaussian distribution where the z-average is the mean and the polydispersity index (PDI) is related to the width of this simple distribution. In the other method, the distribution by intensity is obtained from an entirely different fitting scheme; an algorithm-based approach to resolving a mixture of exponential functions into a number of intensity values each associated with a discrete size band [96]. The result is composed of different intensity peaks which possess each their own distribution. It is worth noting that, using Mie theory, the intensity distribution can be converted to a volume/number distribution which describes the relative proportion of each particle size population, provide that:

- (a) all particles are spherical,
- (b) all particles have the same density,
- (c) the real and imaginary part of the refractive index are known.

When the sample is composed by two populations, the cumulant fit is biased because of the assumption of a single size distribution. The results are generally in between the two distributions. Thus, especially in the presence of even a small amount of aggregation between particles, the z-average gives a mean size and a distribution width which are bigger than the true ones. At the same time, also the single intensity distribution can be somewhat misleading, in that a small amount of aggregates or larger particles can dominate the distribution [96]. Tacking into account the above considerations, we decide to analyze the DLS data in terms of number density distributions, since it is less affected by the presence of aggregates [96]. Additionally, DLS technique is strongly sensitive to sedimentation, as the intensity fluctuation of the scattered light are affected by the presence of drift velocities.

Scanning Electron Microscopy

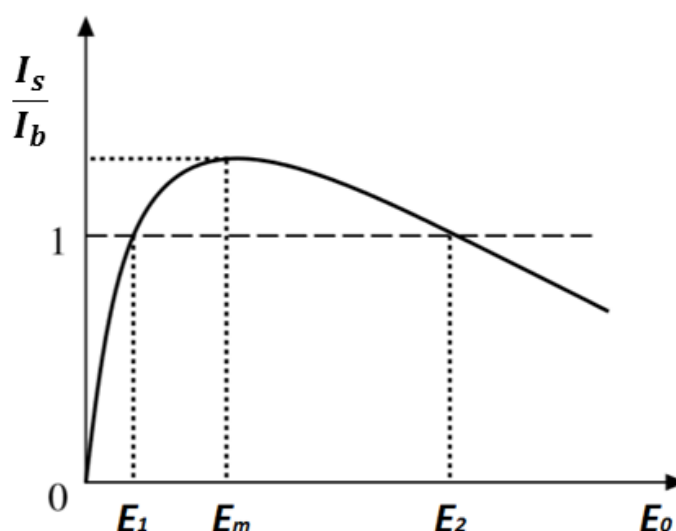


Figure B.1 – Emission curve of an insulator versus energy of the beam electrons, according to the Total Yield Approach (TYA).

When an insulator is imaged inside a SEM environment, the electron bombardment results in a continuous charging of the surface. The charge accumulation alters the surface potential, induces leakage currents and gives rise to hole-electron recombination; all these effects preclude the acquisition of good images.

To avoid the formation of charge artifacts, here we use a strategy based on the Total Yield Approach (TYA) [19], i.e the total emission curve of the material under electron bombardment. According to the TYA, there are two beam energies (crossover energies) at which the total incoming current is perfectly balanced by the emission current. For an insulator, a typical TYA curve as a function of electron beam energy is plotted in Figure B.1. When the beam energy E_0 equals the two crossover energies E_1 and E_2 , the sample current I_s is identical to the beam current I_b and no net charge accumulates. However, the charging process is a dynamic effect, while the TYA describes only stationary conditions [61]. During a continuous electron

exposure, strong negative surface potentials develop and deviate the impinging beam electrons from the sample surface. This not only results in poor quality images, but modifies also the crossover energies. As these effects are stronger for larger E_0 , charge artifacts can be efficiently reduced only working at $E_0 \sim E_1$ [19, 103].

Particle tracking

Particle tracking is at the core of our data analysis, both for the confocal microscopy and the optical tweezers experiments. Over recent years, numerous tracking algorithms have been developed to monitor the sub-pixel displacement of fluorescent particles, depending on the details of the sample and the imaging system [101]. In general, nanometer resolution can be achieved in very ideal samples, where particles are not in touch and the signal to noise ratio (SNR) is high. In this section we will briefly explain the strategy used to extrapolate the particle trajectories from our images.

Centroid algorithm

In colloidal studies, the most popular tracking algorithm is the centroid one, developed by Crocker et al. [41]. The first step of the centroid method consists in searching for local maxima (pixels) of the images, as they correspond to the nearest pixels to the 'true' particle centers. Subsequently, the position estimations are refined based on the moments of the object intensity distribution, through single or multiple iteration steps.

In this work, we use the centroid method proposed by Kilfoil and co-workers [77]. It was claimed that the algorithm provides particle positions with resolution of $1/10$ of a pixel, also in dense colloidal suspensions. Let us explore in more detail the fundamental characteristics of this tracking scheme. Although the results are given for the two dimensional case, they can be easily extended to three dimensions.

Image restoration

Contrast gradient The first step of the algorithm involves image restoration, as digital images typically suffer from various shortcomings, like geometric distortion, nonuniform contrast, and noise [41]. Contrast gradients, which usually arises from nonuniform pixel sensitivity, can be modeled by a boxcar average over a region of extent $2w_1 + 1$, where w_1 is an integer larger than the particle apparent radius in

pixels, but smaller than the typical interparticle separation.

$$I_1(x, y) = \frac{1}{(2w_1 + 1)^2} \sum_{i, j=-w_1}^{w_1} I_0(x + i, y + j) \quad (\text{C.1})$$

where $I_0(x, y)$ is the raw image. Despite interparticle distances in concentrated suspensions are usually greater than w_1 , the results of Equation (C.1) remain useful to suppress contrast gradients [101].

Single pixel noise Digitization of the CCD camera is an additional source of noise. As the typical correlation length of such a digital noise is $\lambda_n \sim 1$ pixel [41], a common strategy is to convolve the image with a Gaussian kernel of linear size $2w_1 + 1$:

$$I_2(x, y) = \frac{1}{B} \sum_{i, j=-w_1}^{w_1} I_1(x + i, y + j) \exp\left(\frac{-(i^2 + j^2)}{4\lambda_n^2}\right) \quad (\text{C.2})$$

where $B = \left[\sum_{i=-w_1}^{w_1} \exp(-i^2/(4\lambda_n^2))\right]^2$. This convolution removes the noise without unduly blurring the image [41].

Particle tracking

Candidate particle location After filtering the raw image, the locations of the candidate particles are computed by identify the local maxima within the image. The corresponding integers (x_m, y_m) correspond to the nearest pixels to the “true” position. To avoid the overlapping of more than one local maximum per particle, a pixel is considered a candidate only if it is the brightest point within a region of size $2w_2 \times 2w_2$, with w_2 an integer equal to (or larger than) the particle radius in pixel.

Position refinement The location refinement is achieved by computing the centroid of the intensity distribution around each local maxima [41]. To do that, a mask of linear size $2w_3 + 1$ is considered around each candidate particle location. The shift of the center $(\varepsilon_x, \varepsilon_y)$ for integrated intensity under this mask is calculated as:

$$\begin{pmatrix} \varepsilon_x \\ \varepsilon_y \end{pmatrix} = \frac{1}{m_0} \cdot \sum_{i^2+j^2 \leq w_3^2} \begin{pmatrix} i \\ j \end{pmatrix} I_2(x + i, y + j) \quad (\text{C.3})$$

where $m_0 = \sum_{i^2+j^2 \leq w_3^2} I(x + i, y + j)$ is the integrated intensity of the feature. The particle position is finally updated to $(x_0, y_0) = (x_m + \varepsilon_x, y_m + \varepsilon_y)$. Similarly, the second moment of the intensity distribution, which corresponds to the particle radius of gyration, can be computed as

$$m_2 = \frac{1}{m_0} \sum_{i^2+j^2 \leq w_3^2} (i^2 + j^2) \cdot I_2(x + i, y + j). \quad (\text{C.4})$$

Further position refinements The main improvement of Kilfoil and co-workers [77] consists in using an iterative refinement algorithm, based on Equation (C.3). In the k -th iteration, the position refinement $(\varepsilon_x^k, \varepsilon_y^k)$ is obtained using a window centered

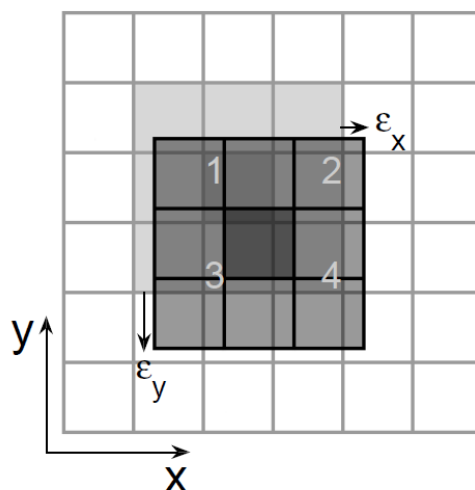


Figure C.1 – Sketch of the intensity interpolation routine used in each refinement iteration. Light filled gray squares belongs to the mask used for the computation of the shift $(\varepsilon_x, \varepsilon_y)$. The mask for further refinement is shown with darker gray squares and is centered on $(x + \varepsilon_x, y + \varepsilon_y)$. Figure taken from [77].

on the previously estimated center $(x^{k-2} + \varepsilon_x^{k-1}, y^{k-2} + \varepsilon_y^{k-1})$ (i.e. obtained in the $k - 1$ iteration). Note that for $k > 1$, both $x^{k-2} + \varepsilon_x^{k-1}$ and $y^{k-2} + \varepsilon_y^{k-1}$ are not integers, hence the new mask is not in registry with the pixels of the underlying image. To overcome this problem, the intensity of each pixels in the window is calculated by a linear interpolation, using the intersection area between the mask and the original underlying image. In Figure C.1 we report, for a 3×3 window, an example of such interpolation routine, according to which the intensity I of the center pixel (dark gray square) is:

$$I = I_1 \cdot (1 - |\varepsilon_x|) \cdot (1 - |\varepsilon_y|) + I_2 \cdot |\varepsilon_x| \cdot (1 - |\varepsilon_y|) + I_3 \cdot (1 - |\varepsilon_x|) \cdot |\varepsilon_y| + I_4 \cdot |\varepsilon_x| \cdot |\varepsilon_y| \quad (\text{C.5})$$

Tracking generation Once the particles have been located in a sequence of consecutive images, a standard algorithm can be used to determine the trajectories. The details of this procedure can be found in [41].

Limits of the centroid algorithm

The centroid technique has been widely used for the characterization of colloidal systems. The reason is twofold. On the one hand, it is a relatively simple technique, and numerous routines have been implemented in recent years. On the other hand, the calculations it involves are not computationally demanding, so that a huge number of images with a large number of particles can be processed in a relative small amount of time.

Despite the centroid algorithm is known to give good results even for relatively low quality images [101], it works better in quite dilute samples, where the intensity distribution of different particles does not interfere. We report in Figure C.2 a typical

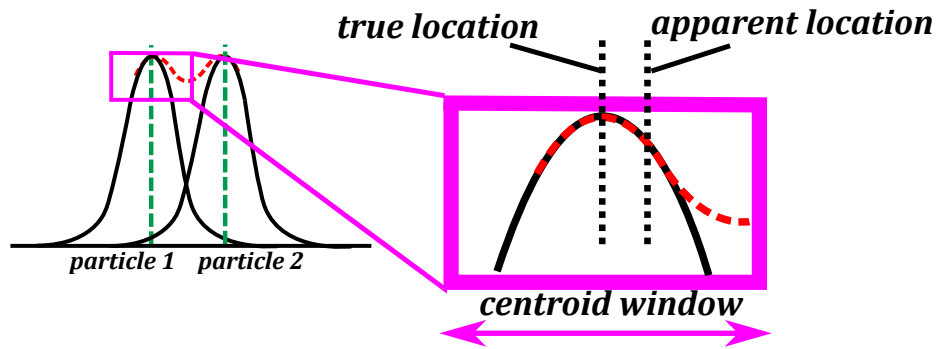


Figure C.2 – Intensity distribution overlap for two particles in contact.

problem that arises when two particles are in contact, or in close proximity to each other. In these conditions, due to the point spread function of the microscope and to light diffraction, the intensity distributions of the particles overlap (red dashed line). Suppose that we are still capable to resolve the local maxima (i.e. the center candidates) associated with each particle (green dashed lines). In the position refinement step, one needs to open a window around these candidates to converge to sub-pixel resolution. As shown in [Figure C.2](#), however, the intensity distribution in the such a window is asymmetric, and the extent of this asymmetry depends on (i) how close the particles are and (ii) on image quality. In these conditions, the computed centroids do not correspond, in all likelihood, to the true particle positions, but should be biased towards the line connecting the centers. Reducing the size of the window to exclude the overlapping region, on the other hand, results in under-sampling and other artifacts. The technique may thus give biased results in dense suspensions with a large number of particles in contact and low SNR.

D

Relation between k_r and k_0

Analytic approximate calculation

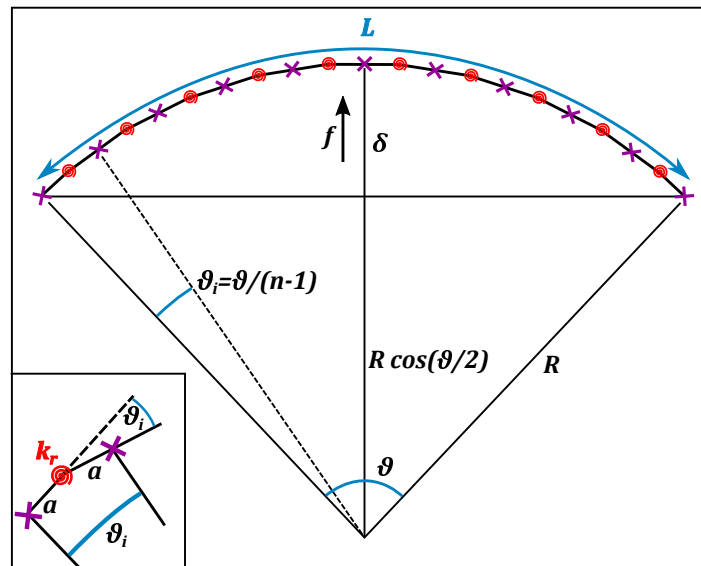


Figure D.1 – Schematic geometry of an eleven-particles rod which bends under the action of a bending moment M . The large magenta crosses are the particle centers. Red spirals represent the particle-particle contacts where rotation occurs. For clarity, the deflection has been exaggerated.

Let us consider a rod made of n particles of radius a , such that its length (the distance between the centers of the end particles) is:

$$L = 2a(n - 1) \quad (\text{D.1})$$

Suppose that under an external bending moment the rod shape can be depicted as in Figure D.1, where the red spirals represent the bonds undergoing rotation, and the crosses the particle centers. Each bond (i.e. contact) can be ideally replaced by a torsion spring of elastic constant k_r .

If the deflection δ is considerably smaller than the length of the beam, the radius of curvature R is $R \sim L/\vartheta$. The elastic energy stored in the rod can be expressed as

a sum of the elastic energies associated with the rotations of the particles:

$$E_{el} = \frac{1}{2}k_r \sum_{i=1}^{n-1} \vartheta_i^2 = \frac{n-1}{2}k_r \left(\frac{\vartheta}{n-1} \right)^2 \quad (\text{D.2})$$

where we assume that all the particles rotate of the same angle $\vartheta_i \sim \vartheta/(n-1)$. Now, since the deflection at the center is $\delta = R - R \cos(\vartheta/2)$ and being

$$\cos\left(\frac{\vartheta}{2}\right) = \sqrt{1 - \sin^2\left(\frac{\vartheta}{2}\right)} \approx \sqrt{1 - \left(\frac{\vartheta^2}{4}\right)} \approx 1 - \frac{\vartheta^2}{8} + \mathcal{O}(\vartheta^4) \quad (\text{D.3})$$

in the limit of small angles, we obtain:

$$\delta = \frac{R\vartheta^2}{8} \Rightarrow \vartheta = \frac{8\delta}{L} \quad (\text{D.4})$$

in which we used $R\vartheta \sim L$. Combining [Equations \(D.1\), \(D.2\) and \(D.4\)](#), we can rewrite the elastic energy as:

$$E_{el} \sim \frac{64k_r a \delta^2}{L^3} \quad (\text{D.5})$$

The bending force associated with this elastic deflection δ is:

$$F_{bend} = \frac{\partial E_{el}}{\partial \delta} = \left(\frac{128k_r a}{L^3} \right) \delta = k_b \delta \quad (\text{D.6})$$

where k_b is the bending stiffness we used throughout the manuscript. Hence:

$$k_r \sim \left(\frac{L^3}{128a} \right) k_b \quad (\text{D.7})$$

In this work we have considered the single bond bending rigidity k_0 , defined as:

$$k_0 = k_b \left(\frac{L}{a} \right)^3 \quad (\text{D.8})$$

Thus, the relationship between the rolling stiffness k_r and the effective bond rigidity k_0 is:

$$k_r = \frac{k_0 a^2}{\Gamma} \quad (\text{D.9})$$

where $\Gamma = 128$ for this approximate calculation.

Numeric solution

The prefactor of [Equation \(D.9\)](#) can be calculated using an optimization technique based on energy minimization. To proceed, we schematically plot our bent chain as in [Figure D.2](#). As illustrated, each particle is attached to its nearest one by a torsion spring of rigidity k_r (red spirals) and is rotated by an angle $\vartheta_i = |\varphi_{i+1} - \varphi_i|$, with φ_i the angle of particle i with axis x . Defining the origin of the axes at the

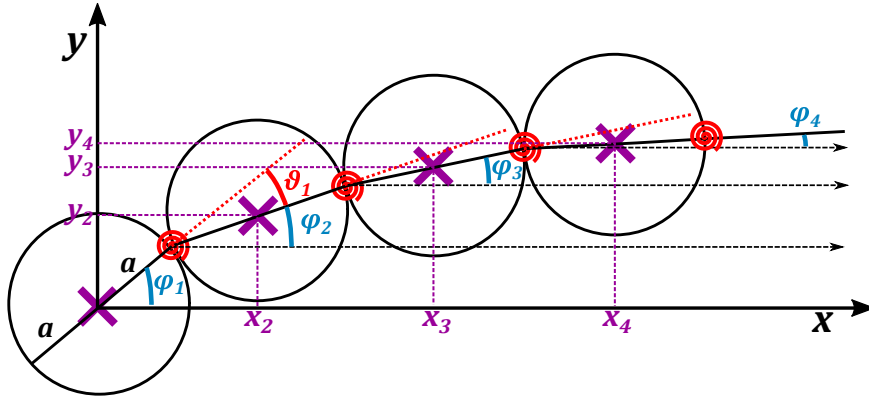


Figure D.2 – Sketch for the calculation of the prefactor Γ .

center of the leftmost bead, the position of particle i can be computed as follow:

$$x_i = a \cdot \sum_{j=1}^{i-1} (\cos \varphi_j + \cos \varphi_{j+1}) \quad (\text{D.10a})$$

$$y_i = a \cdot \sum_{j=1}^{i-1} (\sin \varphi_j + \sin \varphi_{j+1}) \quad (\text{D.10b})$$

In the limit of small angles $\sin \varphi \sim \varphi$, the rod deflection reads:

$$\delta = y_{(n+1)/2} = a \cdot \sum_{j=1}^{(n-1)/2} (\varphi_j + \varphi_{j+1}) \quad (\text{D.11})$$

The stored elastic energy is:

$$E_{el} = \frac{1}{2} k_r \sum_{i=1}^{n-1} (\vartheta_i)^2 = \frac{1}{2} k_r \sum_{i=1}^{n-1} (\varphi_{i+1} - \varphi_i)^2 \quad (\text{D.12})$$

Using the technique of Lagrangian multiplier we must minimize the quantity:

$$\mathcal{L} = E_{el} - W - \lambda \cdot g \quad (\text{D.13})$$

where $W = F_{bend} \delta$ is the work of the external bending force, λ is the Lagrangian multiplier and

$$g = \sum_{j=1}^{i-1} (\varphi_j + \varphi_{j+1}) = 0 \quad (\text{D.14})$$

is the equality constrain. An analytical approximate solution of Equation (D.13) can be found in [12], when the number of particle in the chain $\rightarrow \infty$. The computation being quite tedious, here we solve it numerically with Maple. The script directly returns the bending stiffness k_b as a function of n , k_r and a . Using again Equations (D.1) and (D.8), we can extrapolate the prefactor Γ of Equation (D.9). The results are reported in Table D.1:

Table D.1 – Prefactor Γ of Equation (D.9) computed with the Lagrange multiplier technique.

n	11	13	15	21	51	99	501
Γ	96.969	96.671	96.492	96.240	96.038	96.009	96.000

When the number of particle in the chain tends to infinity, we obtain

$$k_r = \frac{k_0 a^2}{96}. \quad (\text{D.15})$$

E

Equilibrium shape of a bent chain of particles

In this section we demonstrate that, in response to a bending moment, a chain of rigid particles, connected with torsion springs of elastic constant k_r , behaves as a thin, continuous rigid rod. As a consequence, the particle positions are in agreement with the prediction of Euler-Bernoulli beam theory under similar load conditions. Remember that in our three-point bending tests, the two optical traps at the end of the chain are fixed, while the center one is slowly displaced in the y direction. Consider a chain composed of n particles of radius a . We denote with (x_l, y_l) and (x_r, y_r) the equilibrium positions of the left and right particles, and with (x_c, y_c) the equilibrium positions of the center one ($c = (n + 1)/2$). Let us also denote with capital letters the corresponding positions of the trap centers. Hence (X_l, Y_l) , (X_r, Y_r) and (X_c, Y_c) correspond to the leftmost, rightmost and center traps, respectively. In mechanical equilibrium, the force F_c exerted on the center is compensated by a force $F_c/2$ acting on each end particles. The elastic energy associated with these optical forces is:

$$E_{trap} = \frac{1}{2}k_t \left\{ \left[(x_l - X_l)^2 + (y_l - Y_l)^2 \right] + \left[(x_r - X_r)^2 + (y_r - Y_r)^2 \right] + \left[(x_c - X_c)^2 + (y_c - Y_c)^2 \right] \right\} \quad (\text{E.1})$$

where k_t is the trap (radial) stiffness. Without loss of generality, we can set $(X_l, Y_l) = (0, 0)$, which obviously leads to $(X_c, Y_c) = (L/2, Y_c)$ and $(X_r, Y_r) = (L, 0)$, where L is the chain length (Equation (D.1)). The previous equation reduces to:

$$E_{trap} = \frac{1}{2}k_t \left\{ \left[x_l^2 + y_l^2 \right] + \left[(x_r - L)^2 + y_r^2 \right] + \left[(x_c - L/2)^2 + (y_c - Y_c)^2 \right] \right\} \quad (\text{E.2})$$

In the elastic regime, when the center trap is at $Y_c > 0$, the applied force results in a deformation of the chain, i.e. a change in the equilibrium angles between the particles. In these conditions, the bead positions are parametrized by an expression akin

to Equation (D.10), where the only difference is that x_l and y_l are not constrained to lie in the origin of the reference frame, and can therefore take any particular value (x^*, y^*) . Thus, we have:

$$\begin{cases} x_l = x^* \\ y_l = y^* \end{cases} \quad \text{if } i = 1$$

$$\begin{cases} x_i = x_{i-1} + a \cdot (\cos \varphi_{i-1} + \cos \varphi_i) \\ y_i = y_{i-1} + a \cdot (\sin \varphi_{i-1} + \sin \varphi_i) \end{cases} \quad \text{if } 2 \leq i \leq n$$
(E.3)

where the angles φ_i are illustrated in Figure D.2. With these relationships, the position of the center and end particles in Equation (E.2) can be expressed only as a function of (x^*, y^*) and $\{\varphi_i\}_{i=1..n}$. The equilibrium shape can be found via energy minimization, given the total elastic energy

$$E = E_{trap} + E_{chain} \quad (\text{E.4})$$

where E_{chain} is the elastic energy stored in the chain (see Equation (D.12) and Figure D.2):

$$E_{chain} = \frac{1}{2} k_r \sum_{i=1}^{n-1} (\varphi_{i+1} - \varphi_i)^2 = \frac{k_0 a^2}{192} \sum_{i=1}^{n-1} (\varphi_{i+1} - \varphi_i)^2 \quad (\text{E.5})$$

where we used Equation (D.15) to switch from k_0 to k_r , and E_{trap} is given by Equation (E.2) with Equation (E.3).

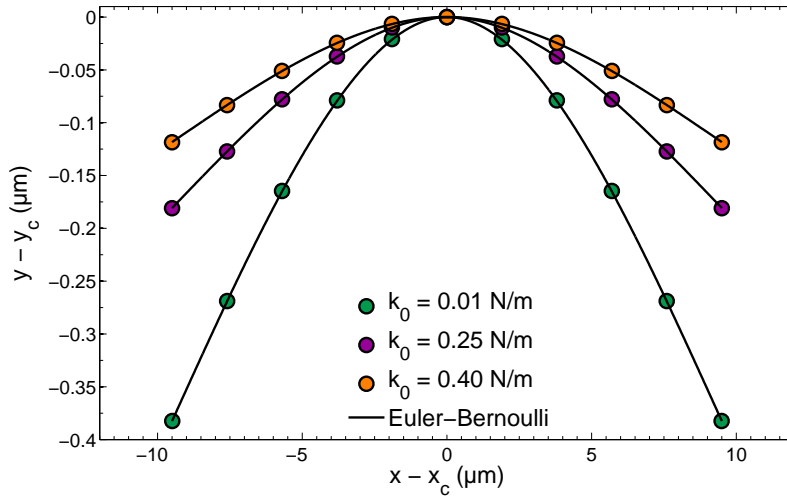


Figure E.1

A maple script allows us to perform the computation. The results (solid filled circles) for $k_t = 6.5 \text{ pN}/\mu\text{m}$, $2a = 1.9 \mu\text{m}$, $n = 11$, $Y_c = 1.5 \mu\text{m}$ and three different flexural stiffnesses of the contacts $k_0 = 0.01, 0.25$ and 0.4 N/m , are reported in Figure E.1. Clearly, the data are in excellent agreement with the predictions of the

Euler-Bernoulli beam theory (black solid lines):

$$y(x) = \frac{-F_{bend}}{2EI} \left(\frac{Lx^2}{4} - \frac{|x|^3}{6} \right) \quad (\text{E.6})$$

with EI the flexural rigidity of the rod.

Bibliography

- [1] ABOU, B., BONN, D., AND MEUNIER, J. Aging dynamics in a colloidal glass. *Phys. Rev. E* 64 (Jul 2001), 021510.
- [2] ALLERSMA, M. W., GITTES, F., DECASTRO, M. J., STEWART, R. J., AND SCHMIDT, C. F. Two-dimensional tracking of ncd motility by back focal plane interferometry. *Biophysical Journal* 74, 2 (1998), 1074 – 1085.
- [3] AMIRI, A., ØYE, G., AND SJÖBLOM, J. Influence of ph, high salinity and particle concentration on stability and rheological properties of aqueous suspensions of fumed silica. *Colloids and Surfaces A: Physicochemical and Engineering Aspects* 349, 1 (2009), 43 – 54.
- [4] ASAKURA, S., AND OOSAWA, F. Interaction between particles suspended in solutions of macromolecules. *Journal of Polymer Science* 33, 126 (1958), 183–192.
- [5] ASHKIN, A., AND DZIEDZIC, J. Optical trapping and manipulation of viruses and bacteria. *Science* 235, 4795 (1987), 1517–1520.
- [6] ASHKIN, A., DZIEDZIC, J. M., BJORKHOLM, J. E., AND CHU, S. Observation of a single-beam gradient force optical trap for dielectric particles. *Opt. Lett.* 11, 5 (May 1986), 288–290.
- [7] BANDYOPADHYAY, R., LIANG, D., YARDIMCI, H., SESSOMS, D. A., BORTHWICK, M. A., MOCHRIE, S. G. J., HARDEN, J. L., AND LEHENY, R. L. Evolution of particle-scale dynamics in an aging clay suspension. *Phys. Rev. Lett.* 93 (Nov 2004), 228302.
- [8] BARBOY, B. On a representation of the equation of state of fluids in terms of the adhesive hard-spheres model. *The Journal of Chemical Physics* 61, 8 (1974), 3194–3196.
- [9] BARNES, H. A. Thixotropy—a review. *Journal of Non-Newtonian Fluid Mechanics* 70, 1 (1997), 1 – 33.

- [10] BARTHEL, E. Adhesive elastic contacts: JKR and more. *Journal of Physics D: Applied Physics* 41, 16 (jul 2008), 163001.
- [11] BAUMBERGER, T., AND CAROLI, C. Solid friction from stick–slip down to pinning and aging. *Advances in Physics* 55, 3-4 (2006), 279–348.
- [12] BECKER, V., AND BRIESEN, H. Tangential-force model for interactions between bonded colloidal particles. *Phys. Rev. E* 78 (Dec 2008), 061404.
- [13] BEHRENS, S. H., AND BORKOVEC, M. Electrostatic interaction of colloidal surfaces with variable charge. *The Journal of Physical Chemistry B* 103, 15 (1999), 2918–2928.
- [14] BERGENHOLTZ, J., AND FUCHS, M. Nonergodicity transitions in colloidal suspensions with attractive interactions. *Phys. Rev. E* 59 (May 1999), 5706–5715.
- [15] BERGENHOLTZ, J., POON, W. C. K., AND FUCHS, M. Gelation in model colloid-polymer mixtures. *Langmuir* 19, 10 (2003), 4493–4503.
- [16] BISSIG, H., ROMER, S., CIPELLETTI, L., TRAPPE, V., AND SCHURTENBERGER, P. Intermittent dynamics and hyper-aging in dense colloidal gels. *PhysChemComm* 6 (2003), 21–23.
- [17] BITTER, J. L., DUNCAN, G. A., BELTRAN-VILLEGAS, D. J., FAIRBROTHER, D. H., AND BEVAN, M. A. Anomalous silica colloid stability and gel layer mediated interactions. *Langmuir* 29, 28 (2013), 8835–8844.
- [18] BOGUSH, G., TRACY, M., AND ZUKOSKI, C. Preparation of monodisperse silica particles: Control of size and mass fraction. *Journal of Non-Crystalline Solids* 104, 1 (1988), 95 – 106.
- [19] BONACCI, F., MICHELE, A. D., CAPONI, S., COTTONE, F., AND MATTARELLI, M. High charge density silica micro-electrets fabricated by electron beam. *Smart Materials and Structures* 27, 7 (jun 2018), 075052.
- [20] BOUCHAUD, J.-P., AND PITARD, E. Anomalous dynamical light scattering in soft glassy gels. *The European Physical Journal E* 6, 3 (Nov 2001), 231–236.
- [21] BOUZID, M., COLOMBO, J., BARBOSA, L. V., AND DEL GADO, E. Elastically driven intermittent microscopic dynamics in soft solids. *Nature Communications* 8 (June 2017), 15846.
- [22] BUSCALL, R., MILLS, P., AND YATES, G. Viscoelastic properties of strongly flocculated polystyrene latex dispersions. *Colloids and Surfaces* 18, 2 (1986), 341 – 358.
- [23] BUSCALL, R., MILLS, P. D. A., GOODWIN, J. W., AND LAWSON, D. W. Scaling behaviour of the rheology of aggregate networks formed from colloidal particles. *J. Chem. Soc., Faraday Trans. 1* 84 (1988), 4249–4260.

- [24] C. K. POON, W., STARRS, L., P. MEEKER, S., MOUSSAÏD, A., M. L. EVANS, R., N. PUSEY, P., AND M. ROBINS, M. Delayed sedimentation of transient gels in colloid-polymer mixtures: dark-field observation, rheology and dynamic light scattering studies. *Faraday Discuss.* 112 (1999), 143–154.
- [25] CATES, M. E., FUCHS, M., KROY, K., POON, W. C. K., AND PUERTAS, A. M. Theory and simulation of gelation, arrest and yielding in attracting colloids. *Journal of Physics: Condensed Matter* 16, 42 (oct 2004), S4861–S4875.
- [26] CHAPEL, J.-P. Electrolyte species dependent hydration forces between silica surfaces. *Langmuir* 10, 11 (1994), 4237–4243.
- [27] CHAPMAN, D. L. Li. a contribution to the theory of electrocapillarity. *The London, Edinburgh, and Dublin Philosophical Magazine and Journal of Science* 25, 148 (1913), 475–481.
- [28] CHAY, T. R., AND FRANK, H. S. Density fluctuations in water and in simple fluids. *The Journal of Chemical Physics* 57, 7 (1972), 2910–2919.
- [29] CHEN, M., AND RUSSEL, W. Characteristics of flocculated silica dispersions. *Journal of Colloid and Interface Science* 141, 2 (1991), 564 – 577.
- [30] CHEN, S., OYE, G., AND SJOBLUM, J. Rheological properties of aqueous silica particle suspensions. *Journal of Dispersion Science and Technology* 26, 4 (2005), 495–501.
- [31] CHENG, N.-S. Formula for the viscosity of a glycerol-water mixture. *Industrial and Engineering Chemistry Research* 47, 9 (2008), 3285–3288.
- [32] CHUNG, B., RAMAKRISHNAN, S., BANDYOPADHYAY, R., LIANG, D., ZUKOSKI, C. F., HARDEN, J. L., AND LEHENY, R. L. Microscopic dynamics of recovery in sheared depletion gels. *Phys. Rev. Lett.* 96 (Jun 2006), 228301.
- [33] CIANCI, G. C., COURTLAND, R. E., AND WEEKS, E. R. Correlations of structure and dynamics in an aging colloidal glass. *Solid State Communications* 139, 11 (2006), 599 – 604. *Soft Condensed Matter*.
- [34] CIANCI, G. C., COURTLAND, R. E., AND WEEKS, E. R. Invariance of structure in an aging colloidal glass. *AIP Conference Proceedings* 832, 1 (2006), 21–25.
- [35] CIPELLETTI, L., MANLEY, S., BALL, R. C., AND WEITZ, D. A. Universal aging features in the restructuring of fractal colloidal gels. *Phys. Rev. Lett.* 84 (Mar 2000), 2275–2278.
- [36] CIPELLETTI, L., AND RAMOS, L. Slow dynamics in glassy soft matter. *Journal of Physics: Condensed Matter* 17, 6 (jan 2005), R253–R285.

- [37] CIPELLETTI, L., RAMOS, L., MANLEY, S., PITARD, E., WEITZ, D. A., PASHKOVSKI, E. E., AND JOHANSSON, M. Universal non-diffusive slow dynamics in aging soft matter. *Faraday Discuss.* 123 (2003), 237–251.
- [38] CLAXTON, N. S., FELLERS, T. J., AND DAVIDSON, M. W. *Microscopy, Confocal*. American Cancer Society, 2006.
- [39] COURTLAND, R. E., AND WEEKS, E. R. Direct visualization of ageing in colloidal glasses. *Journal of Physics: Condensed Matter* 15, 1 (dec 2002), S359–S365.
- [40] COUSSOT, P., TABUTEAU, H., CHATEAU, X., TOCQUER, L., AND OVARLEZ, G. Aging and solid or liquid behavior in pastes. *Journal of Rheology* 50, 6 (2006), 975–994.
- [41] CROCKER, J. C., AND GRIER, D. G. Methods of digital video microscopy for colloidal studies. *Journal of Colloid and Interface Science* 179, 1 (1996), 298 – 310.
- [42] DAWSON, K., FOFFI, G., FUCHS, M., GÖTZE, W., SCIORTINO, F., SPERL, M., TARTAGLIA, P., VOIGTMANN, T., AND ZACCARELLI, E. Higher-order glass-transition singularities in colloidal systems with attractive interactions. *Phys. Rev. E* 63 (Dec 2000), 011401.
- [43] DE HOOG, E. H. A., KEGEL, W. K., VAN BLAADEREN, A., AND LEKKERKERKER, H. N. W. Direct observation of crystallization and aggregation in a phase-separating colloid-polymer suspension. *Phys. Rev. E* 64 (Jul 2001), 021407.
- [44] DEL GADO, E., AND KOB, W. A microscopic model for colloidal gels with directional effective interactions: network induced glassy dynamics. *Soft Matter* 6 (2010), 1547–1558.
- [45] DEREK, C., DUCOURET, G., AJDARI, A., AND FRANCOIS, L. Aging and nonlinear rheology in suspensions of polyethylene oxide-protected silica particles. *Phys. Rev. E* 67 (Jun 2003), 061403.
- [46] DERJAGUIN, B. Untersuchungen über die reibung und adhäsion, iv. *Kolloid-Zeitschrift* 69, 2 (Nov 1934), 155–164.
- [47] DERJAGUIN, B., AND LANDAU, L. Theory of the stability of strongly charged lyophobic sols and of the adhesion of strongly charged particles in solutions of electrolytes. *Progress in Surface Science* 43, 1 (1993), 30 – 59.
- [48] DERJAGUIN, B., MULLER, V., AND TOPOROV, Y. Effect of contact deformations on the adhesion of particles. *Journal of Colloid and Interface Science* 53, 2 (1975), 314 – 326.
- [49] DIASPRO, A., CHIRICO, G., USAI, C., RAMOINO, P., AND DOBRUCKI, J. *Photobleaching*. Springer US, Boston, MA, 2006, pp. 690–702.

- [50] DIBBLE, C. J., KOGAN, M., AND SOLOMON, M. J. Structure and dynamics of colloidal depletion gels: Coincidence of transitions and heterogeneity. *Phys. Rev. E* 74 (Oct 2006), 041403.
- [51] DIETERICH, J. H., AND KILGORE, B. D. Imaging surface contacts: power law contact distributions and contact stresses in quartz, calcite, glass and acrylic plastic. *Tectonophysics* 256, 1 (1996), 219 – 239.
- [52] DING, W., HOWARD, A. J., PERI, M. M., AND CETINKAYA, C. Rolling resistance moment of microspheres on surfaces: contact measurements. *Philosophical Magazine* 87, 36 (2007), 5685–5696.
- [53] DINSMORE, A. D., WEEKS, E. R., PRASAD, V., LEVITT, A. C., AND WEITZ, D. A. Three-dimensional confocal microscopy of colloids. *Appl. Opt.* 40, 24 (Aug 2001), 4152–4159.
- [54] DINSMORE, A. D., AND WEITZ, D. A. Direct imaging of three-dimensional structure and topology of colloidal gels. *Journal of Physics-Condensed Matter* 14 (2002), 7581–7597. Times Cited: 82.
- [55] DISHON, M., ZOHAR, O., AND SIVAN, U. Effect of cation size and charge on the interaction between silica surfaces in 1:1, 2:1, and 3:1 aqueous electrolytes. *Langmuir* 27, 21 (2011), 12977–12984.
- [56] DO, K. K., AND TAIK, K. H. New process for the preparation of monodispersed, spherical silica particles. *Journal of the American Ceramic Society* 85, 5 (2002), 1107–1113.
- [57] DOMINIK, C., AND TIELENS, A. G. G. M. Resistance to rolling in the adhesive contact of two elastic spheres. *Philosophical Magazine A* 72, 3 (1995), 783–803.
- [58] DURI, A., AND CIPELLETTI, L. Length scale dependence of dynamical heterogeneity in a colloidal fractal gel. *Europhysics Letters (EPL)* 76, 5 (dec 2006), 972–978.
- [59] ECKERT, T., AND BARTSCH, E. Re-entrant glass transition in a colloid-polymer mixture with depletion attractions. *Phys. Rev. Lett.* 89 (Aug 2002), 125701.
- [60] EITER, T., AND MANNILA, H. Computing discrete fréchet distance. Tech. rep., Technische Universität Wien, 1994.
- [61] FAKHFAKH, S., JBARA, O., RONDOT, S., RAU, E. I., AND FAKHFAKH, Z. An experimental approach for measuring surface potential and second crossover energy in insulators. *Journal of Physics D: Applied Physics* 41, 10 (apr 2008), 105402.
- [62] FERRERO, E. E., MARTENS, K., AND BARRAT, J.-L. Relaxation in yield stress systems through elastically interacting activated events. *Phys. Rev. Lett.* 113 (Dec 2014), 248301.

- [63] FLATT, R. J., AND BOWEN, P. Yodel: A yield stress model for suspensions. *Journal of the American Ceramic Society* 89, 4 (2006), 1244–1256.
- [64] FLORY, P. J. Molecular size distribution in three dimensional polymers. gelation. *Journal of the American Chemical Society* 63, 11 (1941), 3083–3090.
- [65] FOFFI, G., MICHELE, C. D., SCIORTINO, F., AND TARTAGLIA, P. Scaling of dynamics with the range of interaction in short-range attractive colloids. *Phys. Rev. Lett.* 94 (Feb 2005), 078301.
- [66] FOFFI, G., ZACCARELLI, E., BULDYREV, S., SCIORTINO, F., AND TARTAGLIA, P. Aging in short-ranged attractive colloids: A numerical study. *The Journal of Chemical Physics* 120, 18 (2004), 8824–8830.
- [67] FRANKS, G. V., JOHNSON, S. B., SCALES, P. J., BOGER, D. V., AND HEALY, T. W. Ion-specific strength of attractive particle networks. *Langmuir* 15, 13 (1999), 4411–4420.
- [68] FRANKS, G. V., AND LANGE, F. F. Mechanical behavior of saturated, consolidated, alumina powder compacts: effect of particle size and morphology on the plastic-to-brittle transition. *Colloids and Surfaces A: Physicochemical and Engineering Aspects* 146, 1 (1999), 5 – 17.
- [69] FUJI, M., MACHIDA, K., TAKEI, T., WATANABE, T., AND CHIKAZAWA, M. Effect of wettability on adhesion force between silica particles evaluated by atomic force microscopy measurement as a function of relative humidity. *Langmuir* 15, 13 (1999), 4584–4589.
- [70] FURST, E. M. Applications of laser tweezers in complex fluid rheology. *Current Opinion in Colloid & Interface Science* 10, 1 (2005), 79 – 86.
- [71] FURST, E. M., AND PANTINA, J. P. Yielding in colloidal gels due to nonlinear microstructure bending mechanics. *Phys. Rev. E* 75 (May 2007), 050402.
- [72] FUSIER, J. *Suspensions floculées modèles : de la caractérisation à la modélisation*. PhD thesis, 2016. Thèse de doctorat dirigée par Chateau, Xavier Sciences des Matériaux Paris Est 2016.
- [73] FUSIER, J., GOYON, J., CHATEAU, X., AND TOUSSAINT, F. Rheology signature of flocculated silica suspensions. *Journal of Rheology* 62, 3 (2018), 753–771.
- [74] GADO, E. D., FIERRO, A., DE ARCANGELIS, L., AND CONIGLIO, A. A unifying model for chemical and colloidal gels. *Europhysics Letters (EPL)* 63, 1 (jul 2003), 1–7.
- [75] GALL, A. L., PERRONET, K., DULIN, D., VILLING, A., BOUYER, P., VISSCHER, K., AND WESTBROOK, N. Simultaneous calibration of optical tweezers spring constant and position detector response. *Opt. Express* 18, 25 (Dec 2010), 26469–26474.

- [76] GAO, W., AND RIGOUT, M. O. Facile control of silica nanoparticles using a novel solvent varying method for the fabrication of artificial opal photonic crystals. *Journal of Nanoparticle Research* 18, 12 (Dec 2016), 387.
- [77] GAO, Y., AND KILFOIL, M. L. Accurate detection and complete tracking of large populations of features in three dimensions. *Opt. Express* 17, 6 (Mar 2009), 4685–4704.
- [78] GAO, Y., KIM, J., AND HELGESON, M. E. Microdynamics and arrest of coarsening during spinodal decomposition in thermoreversible colloidal gels. *Soft Matter* 11 (2015), 6360–6370.
- [79] GASSER, U., WEEKS, E. R., SCHOFIELD, A., PUSEY, P. N., AND WEITZ, D. A. Real-space imaging of nucleation and growth in colloidal crystallization. *Science* 292, 5515 (2001), 258–262.
- [80] GORDON, M. B., KLOXIN, C. J., AND WAGNER, N. J. The rheology and microstructure of an aging thermoreversible colloidal gel. *Journal of Rheology* 61, 1 (2017), 23–34.
- [81] GOTZE, W., AND SJOGREN, L. Relaxation processes in supercooled liquids. *Reports on Progress in Physics* 55, 3 (mar 1992), 241–376.
- [82] GOUY, M. Sur la constitution de la charge électrique à la surface d'un électrolyte. *J. Phys. Theor. Appl.* 9, 1 (1910), 457 – 468.
- [83] GRASSO*, D., SUBRAMANIAM, K., BUTKUS, M., STREVETT, K., AND BERGENDAHL, J. A review of non-dlvo interactions in environmental colloidal systems. *Reviews in Environmental Science and Biotechnology* 1, 1 (Mar 2002), 17–38.
- [84] GRIER, D. G. Optical tweezers in colloid and interface science. *Current Opinion in Colloid & Interface Science* 2, 3 (1997), 264 – 270.
- [85] GÖTZE, W. Recent tests of the mode-coupling theory for glassy dynamics. *Journal of Physics: Condensed Matter* 11, 10A (jan 1999), A1–A45.
- [86] GULERYUZ, H., RØYSET, A. K., KAUS, I., FILIÀTRE, C., AND EINARSRUD, M.-A. Afm measurements of forces between silica surfaces. *Journal of Sol-Gel Science and Technology* 62, 3 (Jun 2012), 460–469.
- [87] GUO, H., RAMAKRISHNAN, S., HARDEN, J. L., AND LEHENY, R. L. Gel formation and aging in weakly attractive nanocolloid suspensions at intermediate concentrations. *The Journal of Chemical Physics* 135, 15 (2011), 154903.
- [88] GUTSCHE, C., KEYSER, U. F., KEGLER, K., KREMER, F., AND LINSE, P. Forces between single pairs of charged colloids in aqueous salt solutions. *Phys. Rev. E* 76 (Sep 2007), 031403.

- [89] H. J. HERRMANN, J.-P. HOVI, S. L. *Physics of Dry Granular Media*. Springer, Dordrecht, 2013.
- [90] HAMAKER, H. The london—van der waals attraction between spherical particles. *Physica* 4, 10 (1937), 1058 – 1072.
- [91] HEIDARI, M., KREMER, K., POTESTIO, R., AND CORTES-HUERTO, R. Fluctuations, finite-size effects and the thermodynamic limit in computer simulations: Revisiting the spatial block analysis method. *Entropy* 20, 4 (2018).
- [92] HEIM, L.-O., BLUM, J., PREUSS, M., AND BUTT, H.-J. Adhesion and friction forces between spherical micrometer-sized particles. *Phys. Rev. Lett.* 83 (Oct 1999), 3328–3331.
- [93] HUNTER, G. L., AND WEEKS, E. R. The physics of the colloidal glass transition. *Reports on Progress in Physics* 75, 6 (may 2012), 066501.
- [94] HUNTER, R. J. Chapter 2 - charge and potential distribution at interfaces. In *Zeta Potential in Colloid Science*, R. J. HUNTER, Ed. Academic Press, 1981, pp. 11 – 58.
- [95] ILER, K. *The Chemistry of Silica: Solubility, Polymerization, Colloid and Surface Properties and Biochemistry of Silica*. John Wiley and Sons Inc, Jun 1979.
- [96] INSTRUMENTS, M. Inform white paper: Dynamic light scattering, common terms defined. *Malvern Guides* 1, 6 (2011).
- [97] IOANNIDOU, K., KANDUC, M., LI, L., FRENKEL, D., DOBNIKAR, J., PELLENQ, R., AND DEL GADO, E. Gelation of calcium-silicate-hydrate in cement. In *APS Meeting Abstracts* (2016), p. F37.011.
- [98] ISRAELACHVILI, J. N. In *Intermolecular and Surface Forces (Third Edition)*, J. N. Israelachvili, Ed., third edition ed. Academic Press, San Diego, 2011.
- [99] ISRAELACHVILI, J. N. 14 - electrostatic forces between surfaces in liquids. In *Intermolecular and Surface Forces (Third Edition)*, J. N. Israelachvili, Ed., third edition ed. Academic Press, San Diego, 2011, pp. 291–340.
- [100] ISRAELACHVILI, J. N. Chapter 13 - van der waals forces between particles and surfaces. In *Intermolecular and Surface Forces (Third Edition)*, J. N. Israelachvili, Ed., third edition ed. Academic Press, San Diego, 2011, pp. 253 – 289.
- [101] JENKINS, M., AND EGELHAAF, S. Confocal microscopy of colloidal particles: Towards reliable, optimum coordinates. *Advances in Colloid and Interface Science* 136, 1 (2008), 65 – 92.
- [102] JOHNSON, K. L., KENDALL, K., AND ROBERTS, A. D. Surface energy and the contact of elastic solids. *Proceedings of the Royal Society of London A: Mathematical, Physical and Engineering Sciences* 324, 1558 (1971), 301–313.

- [103] JOY, D. C., AND JOY, C. S. Low voltage scanning electron microscopy. *Micron* 27, 3 (1996), 247 – 263.
- [104] KANG, S., HONG, S. I., CHOE, C. R., PARK, M., RIM, S., AND KIM, J. Preparation and characterization of epoxy composites filled with functionalized nanosilica particles obtained via sol-gel process. *Polymer* 42, 3 (2001), 879 – 887.
- [105] KANTOR, Y., AND WEBMAN, I. Elastic properties of random percolating systems. *Phys. Rev. Lett.* 52 (May 1984), 1891–1894.
- [106] KAUFMAN, L. J., AND WEITZ, D. A. Direct imaging of repulsive and attractive colloidal glasses. *The Journal of Chemical Physics* 125, 7 (2006), 074716.
- [107] KRALL, A. H., AND WEITZ, D. A. Internal dynamics and elasticity of fractal colloidal gels. *Phys. Rev. Lett.* 80 (Jan 1998), 778–781.
- [108] KRIJT, S., DOMINIK, C., AND TIELENS, A. G. G. M. Rolling friction of adhesive microspheres. *Journal of Physics D: Applied Physics* 47, 17 (apr 2014), 175302.
- [109] KROY, K., CATES, M. E., AND POON, W. C. K. Cluster mode-coupling approach to weak gelation in attractive colloids. *Phys. Rev. Lett.* 92 (Apr 2004), 148302.
- [110] KUO, S. C. Using optics to measure biological forces and mechanics. *Traffic* 2, 11 (2001), 757–763.
- [111] LAXTON, P. B., AND BERG, J. C. Investigation of the link between micromechanical interparticle bond rigidity measurements and macroscopic shear moduli of colloidal gels. *Colloids and Surfaces A: Physicochemical and Engineering Aspects* 301, 1 (2007), 137 – 140.
- [112] LAZZARI, S., NICOUD, L., JAQUET, B., LATTUADA, M., AND MORBIDELLI, M. Fractal-like structures in colloid science. *Advances in Colloid and Interface Science* 235 (2016), 1 – 13.
- [113] LEONG, Y., SCALES, P., HEALY, T., AND BOGER, D. Interparticle forces arising from adsorbed polyelectrolytes in colloidal suspensions. *Colloids and Surfaces A: Physicochemical and Engineering Aspects* 95, 1 (1995), 43 – 52.
- [114] LI, Q., TULLIS, T. E., GOLDSBY, D., AND CARPICK, R. W. Frictional ageing from interfacial bonding and the origins of rate and state friction. *Nature* 480 (Nov 2011), 233 EP –.
- [115] LI, Z., PASTEWKA, L., AND SZLUFARSKA, I. Chemical aging of large-scale randomly rough frictional contacts. *Phys. Rev. E* 98 (Aug 2018), 023001.
- [116] LIFSHITZ, E. The theory of molecular attractive forces between solids. *Soviet Phys. JETP* 2 (1 1956).

- [117] LINDBERG, R., SUNDHOLM, G., PETTERSEN, B., SJOBLUM, J., AND FRIBERG, S. E. Multivariate analysis of the size dependence of monodisperse silica particles prepared according to the sol-gel technique. *Colloids and Surfaces A: Physicochemical and Engineering Aspects* 123-124 (1997), 549 – 560. *Frontiers in Colloid Chemistry an International Festschrift to Professor Stig E. Friberg.*
- [118] LIU, A. J., AND NAGEL, S. R. Jamming is not just cool any more. *Nature* 396, 6706 (1998), 21–22.
- [119] LIU, Y., AND SZLUFARSKA, I. Chemical origins of frictional aging. *Phys. Rev. Lett.* 109 (Nov 2012), 186102.
- [120] LU, P. J., GIAVAZZI, F., ANGELINI, T. E., ZACCARELLI, E., JARGSTORFF, F., SCHOFIELD, A. B., WILKING, J. N., ROMANOWSKY, M. B., WEITZ, D. A., AND CERBINO, R. Characterizing concentrated, multiply scattering, and actively driven fluorescent systems with confocal differential dynamic microscopy. *Phys. Rev. Lett.* 108 (May 2012), 218103.
- [121] LU, P. J., ZACCARELLI, CIULLA, E., SCHOFIELD, F., B., A., SCIORTINO, F., AND WEITZ, D. A. Gelation of particles with short-range attraction. *Nature* 453 (May 2008), 499–503.
- [122] LÖWEN, H. Colloidal soft matter under external control. *Journal of Physics: Condensed Matter* 13, 24 (may 2001), R415–R432.
- [123] MANLEY, S., DAVIDOVITCH, B., DAVIES, N. R., CIPELLETTI, L., BAILEY, A. E., CHRISTIANSON, R. J., GASSER, U., PRASAD, V., SEGRE, P. N., DOHERTY, M. P., SANKARAN, S., JANKOVSKY, A. L., SHILEY, B., BOWEN, J., EGGERS, J., KURTA, C., LORIK, T., AND WEITZ, D. A. Time-dependent strength of colloidal gels. *Phys. Rev. Lett.* 95 (Jul 2005), 048302.
- [124] MASSCHAELE, K., FRANSAER, J., AND VERMANT, J. Direct visualization of yielding in model two-dimensional colloidal gels subjected to shear flow. *Journal of Rheology* 53, 6 (2009), 1437–1460.
- [125] MAUGIS, D. Adhesion of spheres: The jkr-dmt transition using a dugdale model. *Journal of Colloid and Interface Science* 150, 1 (1992), 243 – 269.
- [126] MCLEISH, T. C. B., CATES, M. E., HIGGINS, J. S., OLMSTED, P. D., KILFOIL, M. L., PASHKOVSKI, E. E., MASTERS, J. A., AND WEITZ, D. A. Dynamics of weakly aggregated colloidal particles. *Philosophical Transactions of the Royal Society of London. Series A: Mathematical, Physical and Engineering Sciences* 361, 1805 (2003), 753–766.
- [127] MCNAMEE, C. E., AND HIGASHITANI, K. Time dependence of silica surfaces on their interactions in water and alkaline solutions. *Langmuir* 31, 22 (2015), 6064–6071.

- [128] MEAGHER, L. Direct measurement of forces between silica surfaces in aqueous CaCl_2 solutions using an atomic force microscope. *Journal of Colloid and Interface Science* 152, 1 (1992), 293 – 295.
- [129] MENG, B., WU, J., LI, Y., AND LOU, L. Aging process of the bond between colloidal particles measured using laser tweezers. *Colloids and Surfaces A: Physicochemical and Engineering Aspects* 322, 1 (2008), 253 – 255.
- [130] MEWIS, J., AND WAGNER, N. J. *Colloidal Suspension Rheology*. Cambridge Series in Chemical Engineering. Cambridge University Press, 2011.
- [131] MILLER, K. T., MELANT, R. M., AND ZUKOSKI, C. F. Comparison of the compressive yield response of aggregated suspensions: Pressure filtration, centrifugation, and osmotic consolidation. *Journal of the American Ceramic Society* 79, 10 (1996), 2545–2556.
- [132] MILLER, M. A., AND FRENKEL, D. Competition of percolation and phase separation in a fluid of adhesive hard spheres. *Phys. Rev. Lett.* 90 (Apr 2003), 135702.
- [133] MILLER, M. A., AND FRENKEL, D. Phase diagram of the adhesive hard sphere fluid. *The Journal of Chemical Physics* 121, 1 (2004), 535–545.
- [134] MILLER, M. A., AND FRENKEL, D. Simulating colloids with baxter's adhesive hard sphere model. *Journal of Physics: Condensed Matter* 16, 42 (oct 2004), S4901–S4912.
- [135] MIO, C., AND MARR, D. W. M. Tailored surfaces using optically manipulated colloidal particles. *Langmuir* 15, 25 (1999), 8565–8568.
- [136] MOHANTY, P. S., PALOLI, D., CRASSOUS, J. J., ZACCARELLI, E., AND SCHURTENBERGER, P. Effective interactions between soft-repulsive colloids: Experiments, theory, and simulations. *The Journal of Chemical Physics* 140, 9 (2014), 094901.
- [137] NAKABAYASHI, H., YAMADA, A., NOBA, M., KOBAYASHI, Y., KONNO, M., AND NAGAO, D. Electrolyte-added one-pot synthesis for producing monodisperse, micrometer-sized silica particles up to 7 μm . *Langmuir* 26, 10 (2010), 7512–7515.
- [138] NEUMAN, K. C., AND BLOCK, S. M. Optical trapping. *Review of Scientific Instruments* 75, 9 (2004), 2787–2809.
- [139] NEVILLE, A. M. *Properties of concrete. 4th and final edition*. Harlow, Essex, 1995.
- [140] NIEMINEN, T. A., KNÖNER, G., HECKENBERG, N. R., AND RUBINSZTEIN-DUNLOP, H. Physics of optical tweezers. In *Laser Manipulation of Cells and Tissues*, vol. 82 of *Methods in Cell Biology*. Academic Press, 2007, pp. 207 – 236.

- [141] NORO, M. G., AND FRENKEL, D. Extended corresponding-states behavior for particles with variable range attractions. *The Journal of Chemical Physics* 113, 8 (2000), 2941–2944.
- [142] NOZAWA, K., GAILHANOU, H., RAISON, L., PANIZZA, P., USHIKI, H., SELLIER, E., DELVILLE, J. P., AND DELVILLE, M. H. Smart control of monodisperse stöber silica particles - effect of reactant addition rate on growth process. *Langmuir* 21, 4 (2005), 1516–1523. PMID: 15697302.
- [143] OVARLEZ, G., AND CHATEAU, X. Influence of shear stress applied during flow stoppage and rest period on the mechanical properties of thixotropic suspensions. *Phys. Rev. E* 77 (Jun 2008), 061403.
- [144] OVARLEZ, G., AND COUSSOT, P. Physical age of soft-jammed systems. *Phys. Rev. E* 76 (Jul 2007), 011406.
- [145] PANTINA, J. P., AND FURST, E. M. Directed assembly and rupture mechanics of colloidal aggregates. *Langmuir* 20, 10 (2004), 3940–3946. PMID: 15969383.
- [146] PANTINA, J. P., AND FURST, E. M. Elasticity and critical bending moment of model colloidal aggregates. *Phys. Rev. Lett.* 94 (Apr 2005), 138301.
- [147] PANTINA, J. P., AND FURST, E. M. Colloidal aggregate micromechanics in the presence of divalent ions. *Langmuir* 22, 12 (2006), 5282–5288.
- [148] PARK, B. J., LEE, B., AND YU, T. Pairwise interactions of colloids in two-dimensional geometric confinement. *Soft Matter* 10 (2014), 9675–9680.
- [149] PASHLEY, R., AND ISRAELACHVILI, J. A comparison of surface forces and interfacial properties of mica in purified surfactant solutions. *Colloids and Surfaces* 2, 2 (1981), 169 – 187.
- [150] PAUL, J., ROMEIS, S., TOMAS, J., AND PEUKERT, W. A review of models for single particle compression and their application to silica microspheres. *Advanced Powder Technology* 25, 1 (2014), 136 – 153.
- [151] PERSSON, B. N. J., AND SCARAGGI, M. Theory of adhesion: Role of surface roughness. *The Journal of Chemical Physics* 141, 12 (2014), 124701.
- [152] PERSSON, B. N. J., AND TOSATTI, E. Qualitative theory of rubber friction and wear. *The Journal of Chemical Physics* 112, 4 (2000), 2021–2029.
- [153] PESCE, G., LUCA, A. C. D., RUSCIANO, G., NETTI, P. A., FUSCO, S., AND SASSO, A. Microrheology of complex fluids using optical tweezers: a comparison with macrorheological measurements. *Journal of Optics A: Pure and Applied Optics* 11, 3 (jan 2009), 034016.
- [154] PHAM, K. N., PUERTAS, A. M., BERGENHOLTZ, J., EGELHAAF, S. U., MOUSSAID, A., PUSEY, P. N., SCHOFIELD, A. B., CATES, M. E., FUCHS, M., AND POON, W. C. K. Multiple glassy states in a simple model system. *Science* 296, 5565 (2002), 104–106.

- [155] PHILLIPS, J. C. Topology of covalent non-crystalline solids I: Short-range order in chalcogenide alloys. *Journal of Non Crystalline Solids* 34, 2 (Oct 1979), 153–181.
- [156] PIAZZA, R., PEYRE, V., AND DEGIORGIO, V. “sticky hard spheres” model of proteins near crystallization: A test based on the osmotic compressibility of lysozyme solutions. *Phys. Rev. E* 58 (Sep 1998), R2733–R2736.
- [157] PORUS, M., LABBEZ, C., MARONI, P., AND BORKOVEC, M. Adsorption of monovalent and divalent cations on planar water-silica interfaces studied by optical reflectivity and monte carlo simulations. *The Journal of Chemical Physics* 135, 6 (2011), 064701.
- [158] POTANIN, A. A., AND RUSSEL, W. B. Fractal model of consolidation of weakly aggregated colloidal dispersions. *Phys. Rev. E* 53 (Apr 1996), 3702–3709.
- [159] PRASAD, V., SEMWOGERERE, D., AND WEEKS, E. R. Confocal microscopy of colloids. *Journal of Physics: Condensed Matter* 19, 11 (feb 2007), 113102.
- [160] PREECE, D., WARREN, R., EVANS, R. M. L., GIBSON, G. M., PADGETT, M. J., COOPER, J. M., AND TASSIERI, M. Optical tweezers: wideband microrheology. *Journal of Optics* 13, 4 (mar 2011), 044022.
- [161] PUERTAS, A. M., FUCHS, M., AND CATES, M. E. Aging in attraction-driven colloidal glasses. *Phys. Rev. E* 75 (Mar 2007), 031401.
- [162] PUSEY, P., PIRIE, A., AND POON, W. Dynamics of colloid-polymer mixtures. *Physica A: Statistical Mechanics and its Applications* 201, 1 (1993), 322 – 331.
- [163] PUSEY, P. N., AND VAN MEGEN, W. Phase behaviour of concentrated suspensions of nearly hard colloidal spheres. *Nature* 320 (1986), 340–342.
- [164] PUSEY, P. N., AND VAN MEGEN, W. Observation of a glass transition in suspensions of spherical colloidal particles. *Phys. Rev. Lett.* 59 (Nov 1987), 2083–2086.
- [165] ROBINS, M., AND FILLERY-TRAVIS, A. Colloidal dispersions. edited by w. b. russel, d. a. saville & w. r. schowalter, cambridge university press, cambridge, uk, 1989, xvii + 506 pp., price: £60.00. isbn 0 521 34188 4. *Journal of Chemical Technology & Biotechnology* 54, 2 (1992), 201–202.
- [166] ROMÁN, F. L., WHITE, J. A., AND VELASCO, S. Block analysis method in off-lattice fluids. *Europhysics Letters (EPL)* 42, 4 (may 1998), 371–376.
- [167] ROSENBAUM, D., ZAMORA, P. C., AND ZUKOSKI, C. F. Phase behavior of small attractive colloidal particles. *Phys. Rev. Lett.* 76 (Jan 1996), 150–153.

- [168] ROUSSEL, N., LEMAÎTRE, A., FLATT, R. J., AND COUSSOT, P. Steady state flow of cement suspensions: A micromechanical state of the art. *Cement and Concrete Research* 40, 1 (2010), 77 – 84.
- [169] ROUSSEL, N., OVARLEZ, G., GARRAULT, S., AND BRUMAUD, C. The origins of thixotropy of fresh cement pastes. *Cement and Concrete Research* 42, 1 (2012), 148 – 157.
- [170] ROVERE, M., NIELABA, P., AND BINDER, K. Simulation studies of gas-liquid transitions in two dimensions via a subsystem-block-density distribution analysis. *Zeitschrift für Physik B Condensed Matter* 90, 2 (Jun 1993), 215–228.
- [171] RUSSEL, W. B., SAVILLE, D. A., AND SCHOWALTER, W. R. *Colloidal Dispersions*. Cambridge Monographs on Mechanics. Cambridge University Press, 1989.
- [172] SCALES, P. J., JOHNSON, S. B., HEALY, T. W., AND KAPUR, P. C. Shear yield stress of partially flocculated colloidal suspensions. *AIChE Journal* 44, 3 (1998), 538–544.
- [173] SCIORTINO, F., BULDYREV, S. V., MICHELE, C. D., FOFFI, G., GHOFraniHA, N., NAVE, E. L., MORENO, A., MOSSA, S., SAIKA-VOIVOD, I., TARTAGLIA, P., AND ZACCARELLI, E. Routes to colloidal gel formation. *Computer Physics Communications* 169, 1 (2005), 166 – 171. Proceedings of the Europhysics Conference on Computational Physics 2004.
- [174] SCIORTINO, F., AND TARTAGLIA, P. Glassy colloidal systems. *Advances in Physics* 54, 6-7 (2005), 471–524.
- [175] SEDGWICK, H., EGELHAAF, S. U., AND POON, W. C. K. Clusters and gels in systems of sticky particles. *Journal of Physics: Condensed Matter* 16, 42 (oct 2004), S4913–S4922.
- [176] SEGRÈ, P. N., PRASAD, V., SCHOFIELD, A. B., AND WEITZ, D. A. Glasslike kinetic arrest at the colloidal-gelation transition. *Phys. Rev. Lett.* 86 (Jun 2001), 6042–6045.
- [177] SEGUR, J. B., AND OBERSTAR, H. E. Viscosity of glycerol and its aqueous solutions. *Industrial & Engineering Chemistry* 43, 9 (1951), 2117–2120.
- [178] SHIH, W.-H., SHIH, W. Y., KIM, S.-I., LIU, J., AND AKSAY, I. A. Scaling behavior of the elastic properties of colloidal gels. *Phys. Rev. A* 42 (Oct 1990), 4772–4779.
- [179] SHINDEL, M. M., SWAN, J. W., AND FURST, E. M. Calibration of an optical tweezer microrheometer by sequential impulse response. *Rheologica Acta* 52, 5 (May 2013), 455–465.
- [180] SILFIES, J. S., LIESER, E. G., AND SCHWARTZ, S. A. Correcting focus drift in live-cell microscopy. *Nikon Instruments, Inc.*

- [181] SIMMONS, R., FINER, J., CHU, S., AND SPUDICH, J. Quantitative measurements of force and displacement using an optical trap. *Biophysical Journal* 70, 4 (1996), 1813 – 1822.
- [182] SMITH, W., AND HENDERSON, D. Analytical representation of the Percus-Yevick hard-sphere radial distribution function. *Molecular Physics* 19, 3 (1970), 411–415.
- [183] SMOLUCHOWSKI, M. *Handbook of Electricity and Magnetism*. Barth, Leipzig, 1921, p. 366.
- [184] SOLLICH, P. Rheological constitutive equation for a model of soft glassy materials. *Phys. Rev. E* 58 (Jul 1998), 738–759.
- [185] STERN, O. Zur theorie der elektrolytischen doppelschicht. *Zeitschrift für Elektrochemie und angewandte physikalische Chemie* 30, 21-22 (1924), 508–516.
- [186] STOBER, W., FINK, A., AND BOHN, E. Controlled growth of monodisperse silica spheres in the micron size range. *Journal of Colloid and Interface Science* 26, 1 (1968), 62 – 69.
- [187] SWAN, J. W., SHINDEL, M. M., AND FURST, E. M. Measuring thermal rupture force distributions from an ensemble of trajectories. *Phys. Rev. Lett.* 109 (Nov 2012), 198302.
- [188] TABOR, D. Surface forces and surface interactions. *Journal of Colloid and Interface Science* 58, 1 (1977), 2 – 13. International Conference on Colloids and Surfaces.
- [189] TANAKA, H., MEUNIER, J., AND BONN, D. Nonergodic states of charged colloidal suspensions: Repulsive and attractive glasses and gels. *Phys. Rev. E* 69 (Mar 2004), 031404.
- [190] TATEISHI, Y., KAI, N., NOGUCHI, H., UOSAKI, K., NAGAMURA, T., AND TANAKA, K. Local conformation of poly(methyl methacrylate) at nitrogen and water interfaces. *Polym. Chem.* 1 (2010), 303–311.
- [191] TIAN, K., GOSVAMI, N. N., GOLDSBY, D. L., LIU, Y., SZLUFARSKA, I., AND CARPICK, R. W. Load and time dependence of interfacial chemical bond-induced friction at the nanoscale. *Phys. Rev. Lett.* 118 (Feb 2017), 076103.
- [192] TOLIĆ-NØRRELYKKE, S. F., SCHÄFFER, E., HOWARD, J., PAVONE, F. S., JÜLICHER, F., AND FLYVBJERG, H. Calibration of optical tweezers with positional detection in the back focal plane. *Review of Scientific Instruments* 77, 10 (2006), 103101.
- [193] TRAPPE, V., PRASAD, V., CIPOLLETTI, L., SEGRE, P. N., AND WEITZ, D. A. Jamming phase diagram for attractive particles. *Nature* 411, 6839 (2001), 772–775.

- [194] TRAPPE, V., AND SANDKÜHLER, P. Colloidal gels—low-density disordered solid-like states. *Current Opinion in Colloid & Interface Science* 8, 6 (2004), 494 – 500.
- [195] TRONCOSO, P., SAAVEDRA, J. H., ACUÑA, S. M., JELDRES, R., CONCHA, F., AND TOLEDO, P. G. Nanoscale adhesive forces between silica surfaces in aqueous solutions. *Journal of Colloid and Interface Science* 424 (2014), 56 – 61.
- [196] URIEV, N., AND LADYZHINSKY, I. Fractal models in rheology of colloidal gels. *Colloids and Surfaces A: Physicochemical and Engineering Aspects* 108, 1 (1996), 1 – 11.
- [197] VAKARELSKI, I. U., AND HIGASHITANI, K. Dynamic features of short-range interaction force and adhesion in solutions. *Journal of Colloid and Interface Science* 242, 1 (2001), 110 – 120.
- [198] VAKARELSKI, I. U., ISHIMURA, K., AND HIGASHITANI, K. Adhesion between silica particle and mica surfaces in water and electrolyte solutions. *Journal of Colloid and Interface Science* 227, 1 (2000), 111 – 118.
- [199] VALMACCO, V., ELZBIECIAK-WODKA, M., HERMAN, D., TREFALT, G., MARONI, P., AND BORKOVEC, M. Forces between silica particles in the presence of multivalent cations. *Journal of Colloid and Interface Science* 472 (2016), 108 – 115.
- [200] VAN MEGEN, W., AND UNDERWOOD, S. M. Glass transition in colloidal hard spheres: Mode-coupling theory analysis. *Phys. Rev. Lett.* 70 (May 1993), 2766–2769.
- [201] VANDAMME, M., AND ULM, F.-J. Nanogranular origin of concrete creep. *Proceedings of the National Academy of Sciences* 106, 26 (2009), 10552–10557.
- [202] VARADAN, P., AND SOLOMON, M. J. Direct visualization of flow-induced microstructure in dense colloidal gels by confocal laser scanning microscopy. *Journal of Rheology* 47, 4 (2003), 943–968.
- [203] VERWEY, E. J. W. Theory of the stability of lyophobic colloids. *The Journal of Physical and Colloid Chemistry* 51, 3 (1947), 631–636.
- [204] VIGIL, G., XU, Z., STEINBERG, S., AND ISRAELACHVILI, J. Interactions of silica surfaces. *Journal of Colloid and Interface Science* 165, 2 (1994), 367 – 385.
- [205] VON GRÜNBERG, H. H., HELDEN, L., LEIDERER, P., AND BECHINGER, C. Measurement of surface charge densities on brownian particles using total internal reflection microscopy. *The Journal of Chemical Physics* 114, 22 (2001), 10094–10104.

- [206] WANG, K., FORBES, J. G., AND JIN, A. J. Single molecule measurements of titin elasticity. *Progress in Biophysics and Molecular Biology* 77, 1 (2001), 1 – 44. Single Molecule Biochemistry and Molecular Biology, Part II.
- [207] WHITAKER, K. A., AND FURST, E. M. Bond rupture between colloidal particles with a depletion interaction. *Journal of Rheology* 60, 3 (2016), 517–529.
- [208] WHITAKER, K. A., VARGA, Z., HSIAO, L. C., SOLOMON, M. J., SWAN, J. W., AND FURST, E. M. Colloidal gel elasticity arises from the packing of locally glassy clusters. *Nature Communications* 10, 2237 (May 2019), 2041–1723.
- [209] WYSS, H. M., TERVOORT, E., MEIER, L. P., MÜLLER, M., AND GAUCKLER, L. J. Relation between microstructure and mechanical behavior of concentrated silica gels. *Journal of Colloid and Interface Science* 273, 2 (2004), 455 – 462.
- [210] WYSS, H. M., TERVOORT, E. V., AND GAUCKLER, L. J. Mechanics and microstructures of concentrated particle gels. *Journal of the American Ceramic Society* 88, 9 (2005), 2337–2348.
- [211] YAMINSKY, V. V., NINHAM, B. W., AND PASHLEY, R. M. Interaction between surfaces of fused silica in water. evidence of cold fusion and effects of cold plasma treatment. *Langmuir* 14, 12 (1998), 3223–3235.
- [212] YORK, D., EVENSEN, N. M., MARTINEZ, M. L., AND DE BASABE DELGADO, J. Unified equations for the slope, intercept, and standard errors of the best straight line. *American Journal of Physics* 72, 3 (2004), 367–375.
- [213] ZACCARELLI, E. Colloidal gels: equilibrium and non-equilibrium routes. *Journal of Physics: Condensed Matter* 19, 32 (jul 2007), 323101.
- [214] ZACCARELLI, E., FOFFI, G., SCIORTINO, F., AND TARTAGLIA, P. Activated bond-breaking processes preempt the observation of a sharp glass-glass transition in dense short-ranged attractive colloids. *Phys. Rev. Lett.* 91 (Sep 2003), 108301.
- [215] ZACCARELLI, E., FOFFI, G., SCIORTINO, F., TARTAGLIA, P., AND DAWSON, K. A. Gaussian density fluctuations and mode coupling theory for supercooled liquids. *Europhysics Letters (EPL)* 55, 2 (jul 2001), 157–163.
- [216] ZACCARELLI, E., AND POON, W. C. K. Colloidal glasses and gels: The interplay of bonding and caging. *Proceedings of the National Academy of Sciences* 106, 36 (2009), 15203–15208.
- [217] ZACCARELLI, E., VALERIANI, C., SANZ, E., POON, W. C. K., CATES, M. E., AND PUSEY, P. N. Crystallization of hard-sphere glasses. *Phys. Rev. Lett.* 103 (Sep 2009), 135704.

- [218] ZACCONE, A. The shear modulus of metastable amorphous solids with strong central and bond-bending interactions. *Journal of Physics: Condensed Matter* 21, 28 (jun 2009), 285103.
- [219] ZACCONE, A., WU, H., AND DEL GADO, E. Elasticity of arrested short-ranged attractive colloids: Homogeneous and heterogeneous glasses. *Phys. Rev. Lett.* 103 (Nov 2009), 208301.
- [220] ZAKHAROV, P., AND SCHEFFOLD, F. *Advances in dynamic light scattering techniques*. Springer Berlin Heidelberg, Berlin, Heidelberg, 2009, pp. 433–467.
- [221] ZHOU, Z., SOLOMON, M. J., SCALES, P. J., AND BOGER, D. V. The yield stress of concentrated flocculated suspensions of size distributed particles. *Journal of Rheology* 43, 3 (1999), 651–671.
- [222] ZHURAVLEV, L. The surface chemistry of amorphous silica. zhuravlev model. *Colloids and Surfaces A: Physicochemical and Engineering Aspects* 173, 1 (2000), 1 – 38.